



UvA-DARE (Digital Academic Repository)

Optical properties of circumstellar and cometary grains

Min, M.

Publication date

2005

Document Version

Final published version

[Link to publication](#)

Citation for published version (APA):

Min, M. (2005). *Optical properties of circumstellar and cometary grains*.

General rights

It is not permitted to download or to forward/distribute the text or part of it without the consent of the author(s) and/or copyright holder(s), other than for strictly personal, individual use, unless the work is under an open content license (like Creative Commons).

Disclaimer/Complaints regulations

If you believe that digital publication of certain material infringes any of your rights or (privacy) interests, please let the Library know, stating your reasons. In case of a legitimate complaint, the Library will make the material inaccessible and/or remove it from the website. Please Ask the Library: <https://uba.uva.nl/en/contact>, or a letter to: Library of the University of Amsterdam, Secretariat, Singel 425, 1012 WP Amsterdam, The Netherlands. You will be contacted as soon as possible.

Optical properties of circumstellar and cometary grains

ISBN: 90-5776136-X

Cover: Absorption contours (like in Figs. 2.3, 2.4, 3.2, 3.3, 3.4, and 5.1) of small, randomly oriented particles shaped like the Maxwell equations (front) and like little aliens (back).

Optical properties of circumstellar and cometary grains

Optische eigenschappen van vaste deeltjes in
circumstellaire schijven en kometen

Academisch Proefschrift

ter verkrijging van de graad van doctor aan de Universiteit van Amsterdam op gezag van de Rector Magnificus prof. mr. P.F. van der Heijden ten overstaan van een door het college voor promoties ingestelde commissie, in het openbaar te verdedigen in de Aula der Universiteit op donderdag 12 mei 2005, te 14:00 uur

door

Michiel Min

geboren te Hoorn

Promotiecommissie

Promotores	prof. dr. J. W. Hovenier prof. dr. L. B. F. M. Waters
Co-promotor	dr. A. de Koter
Overige leden	prof. dr. Th. Henning prof. dr. T. de Jong prof. dr. A. C. Levasseur-Regourd dr. C. Dominik dr. A. G. Hoekstra dr. M. I. Mishchenko

Faculteit der Natuurwetenschappen, Wiskunde en Informatica

Simplicity is the ultimate sophistication.

Leonardo da Vinci

Contents

Contents	i
1 Introduction	1
1.1 Cosmic dust	1
1.1.1 The dust life-cycle	1
1.1.2 Why do we study cosmic dust?	2
1.2 The interaction of radiation and dust	3
1.2.1 Thermal emission	3
1.2.2 Scattering	4
1.2.3 Extinction	5
1.3 Dust grain characteristics	5
1.3.1 Grain composition and lattice structure	5
1.3.2 Grain size	8
1.3.3 Grain shape and structure	10
1.4 Computing the optical properties of dust grains	11
1.4.1 The statistical approach	12
1.5 Applications to astronomical observations	12
1.5.1 The formation of planetary systems	13
1.5.2 Circumstellar dust	14
1.5.3 Cometary dust	15
1.6 Summary and conclusions	16
1.7 A look into the future	19
2 Shape effects in scattering and absorption by randomly oriented particles small compared to the wavelength	21
2.1 Introduction	21
2.2 Light scattering by ellipsoids small compared to the wavelength	23
2.3 Distributions of shapes, the statistical approach	25
2.3.1 Continuous Distribution of Ellipsoids (CDE)	26
2.3.2 Continuous Distribution of Spheroids (CDS)	27
2.3.3 Uniform Distribution of Spheroids (UDS)	28
2.3.4 Distribution of Hollow Spheres	29
2.4 Spectral features	31
2.4.1 Shape dependence of spectral features	31
2.4.2 An example: Forsterite (20-40 μm)	36
2.5 Conclusions	39

3	Absorption and scattering properties of arbitrarily shaped particles in the Rayleigh domain	41
	A rapid computational method and a theoretical foundation for the statistical approach	41
3.1	Introduction	41
3.2	The absorption properties of very small particles	43
3.2.1	General equations in the Rayleigh domain	43
3.2.2	The Discrete Dipole Approximation (DDA)	45
3.2.3	The distribution of form-factors	47
3.2.4	Summary of the procedure	48
3.3	Application to various shapes	49
3.3.1	Homogeneous spheres and spheroids	49
3.3.2	Gaussian random sphere	50
3.3.3	Aggregates with various fractal dimensions	53
3.4	Discussion	55
3.4.1	Comparison with distributions of simple shapes	55
3.4.2	Absorption spectra	56
3.4.3	The statistical approach	58
3.4.4	Extrapolation to larger particles	58
3.5	Conclusions	59
4	Scattering and absorption cross sections for randomly oriented spheroids of arbitrary size	61
4.1	Introduction	61
4.2	Theoretical aspects	62
4.2.1	General	62
4.2.2	Particles small compared to the wavelength	64
4.2.3	Particles large compared to the wavelength	65
4.3	Computational results	66
4.4	Conclusions	72
	Appendix A: Anomalous Diffraction	74
5	Modeling optical properties of cosmic dust grains using a distribution of hollow spheres	75
5.1	Introduction	75
5.2	Dust shape models	77
5.2.1	Distribution of Hollow Spheres (DHS)	77
5.2.2	Uniform Distribution of Spheroids (UDS)	78
5.3	The absorption, extinction and emission spectra	78
5.3.1	Example: amorphous silicates	80
5.3.2	Example: crystalline silicates	83
5.4	The degree of linear polarization	86
5.4.1	Example: the polarization of small quartz particles	87
5.5	Discussion	93
5.6	Conclusions	94

6	The 10 μm amorphous olivine feature of fractal aggregates and compact particles with complex shapes	97
6.1	Introduction	97
6.2	Absorption and emission spectra	98
6.2.1	The Discrete Dipole Approximation	99
6.3	Particle shapes	100
6.3.1	Gaussian Random Spheres	100
6.3.2	Fractal aggregates	101
6.4	Results	103
6.4.1	The 10 μm amorphous silicate feature	103
6.4.2	Fractal aggregates versus Gaussian random spheres	103
6.5	Implications for grain growth and dust modeling	106
6.6	Conclusions	109
7	Spectroscopic diagnostic for the mineralogy of large dust grains	111
7.1	Introduction	111
7.2	Infrared emission spectra	112
7.3	The spectrum of Vega	114
7.4	Discussion	115
7.4.1	Grain composition	115
7.4.2	Grain structure	115
7.5	Conclusions	116
8	The composition and size distribution of the dust in the coma of comet Hale-Bopp	117
8.1	Introduction	118
8.2	Method	119
8.2.1	Size and shape of the dust grains	119
8.2.2	Thermal emission	121
8.2.3	Degree of linear polarization of scattered light	122
8.2.4	Least squares fitting procedure	123
8.2.5	Dust components	125
8.2.6	Chemical abundance constraints	127
8.3	Results	128
8.3.1	Observations	128
8.3.2	Best fit model	129
8.3.3	Dust composition and size distribution	134
8.4	Discussion: Origin and evolution of cometary dust	138
8.5	Conclusions	140
9	A 10 μm spectroscopic survey of Herbig Ae star disks: grain growth and crystallization	143
9.1	Introduction	143
9.2	The sample stars	146
9.2.1	Selection effects	148

9.2.2	Classification of the sources	148
9.3	Observations and data reduction	151
9.3.1	Atmospheric correction	152
9.3.2	Flux calibration	154
9.4	Description of the observations	154
9.4.1	Description of the spectra	154
9.4.2	The shape and strength of the silicate feature	158
9.5	Analysis	159
9.5.1	Compositional fits	159
9.5.2	Results	165
9.5.3	Observed trends in the fits	169
9.6	Discussion	173
9.6.1	The active disk phase	174
9.6.2	The passive disk phase	175
9.6.3	New constraints on dust processing	176
9.6.4	Global picture that emerges	179
9.7	Conclusions	180
10	The building blocks of planets in the ‘terrestrial’ region of protoplanetary disks	183
	Supplementary material of chapter 10	191
	Samenvatting in het Nederlands	195
	Kosmisch stof	195
	De wisselwerking van straling en stof	200
	Dit proefschrift	203
	Bibliography	206
	Dankwoord	219

1

Introduction

1.1 Cosmic dust

In this thesis the characteristics of cosmic dust are studied. The first question that arises is what is meant by the term *cosmic dust*. In astronomy dust does not mean the usual dust that we find in houses. This dust consists of, among other things, textile fibers, decomposing insect parts, human and animal hair, food leftovers, mold spores and skin flakes. Of course, these ingredients are not found in astronomical environments. What we call cosmic dust are small solid state particles composed of, for example, silicates, sulfides, or carbonaceous species. Cosmic dust can form from the gas phase when gas cools down below the dust condensation temperature. Cosmic dust particles are also called *grains*. This thesis deals with the properties of grains in orbit around young stellar objects and in the comae and tails of comets. In Fig. 1.1 two typical examples of cosmic dust grains are shown.

Dust has its bad sides. It can, for example, obscure relatively distant stars located in the plane of the Galaxy or those hidden inside molecular clouds. Dust also has its good sides. Dusty reflection nebulae, for instance, can create spectacular images. Dust released by comets can sometimes be viewed with the naked eye, and is something that fascinated mankind throughout the ages.

1.1.1 The dust life-cycle

Cosmic dust grains go through a cycle of creation and destruction. To our knowledge, a large fraction of the cosmic dust is formed in the outflows of old stars, where the conditions to form dust are optimal. When a star of intermediate mass (up to ~ 8 times the mass of the Sun) nears the end of its life, it expands and a massive outflow can occur. When the gas expands away from the star, it cools and solid material may condense, forming small dust grains. The dust shell expands further and finally a planetary nebula forms. An example of a planetary nebula is shown in the left panel of Fig. 1.2. The dust formed in this way is ejected into the interstellar medium (ISM), where it can reside for hundreds of millions of years. It can be processed by the interstellar radiation field, causing changes in the dust lattice structure (the ordering of the atoms) or even destroying it. In the ISM, regions of higher density – so-called molecular clouds – can occur. In the middle panel of Fig. 1.2 an example of a molecular cloud, the Orion nebula, is shown. Such clouds are dominated by molecular gas, but are interspersed with a small component of solid state particles. Fragments of the cloud can collapse under their own

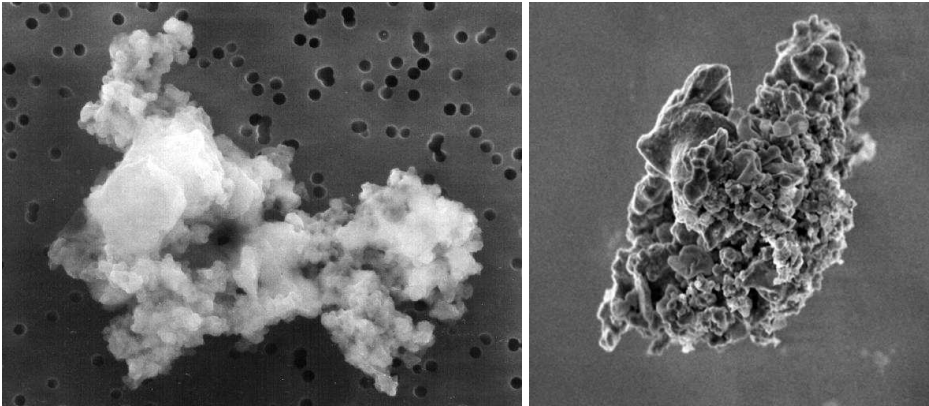


Figure 1.1: Two examples of cosmic dust grains. The grains shown here have been captured by special airplanes in the stratosphere (at ~ 20 km altitude) and have typical sizes of about $10\ \mu\text{m}$. The shape and structure of these particles is probably similar to those of cometary grains. Picture credits: NASA.

gravity, forming protostars. The interstellar dust is at some point incorporated in a gas dominated disk from which the central protostar accretes matter. A large part of the dust will be destroyed when it is incorporated into the new star. In the circumstellar disk the dust can undergo severe processing due to heating close to the star, shocks in the disk, and perhaps even lightning. The densities in the disk are high enough for the grains to stick together to form larger dust particles and eventually even comets and asteroids, possibly even planets. In the right panel of Fig. 1.2 we show an image of the protoplanetary disk surrounding the young star HD 163296, which is one of the objects studied in chapters 9 and 10. To make the dust cycle complete, when the central star is near the end of its life, it will lose a large fraction of its mass, for example through a dense outflow and/or a supernova explosion. From this initially gaseous material flowing into the interstellar medium, dust can form, starting a new life-cycle.

1.1.2 Why do we study cosmic dust?

Cosmic dust provided the building blocks of all solid material we find on Earth and in our solar system. Planets are believed to accumulate from small dust grains. How this exactly happens is not entirely clear. We also have very limited knowledge of the composition of the building blocks of planets. This too is an interesting issue, the answer of which cannot be obtained by studying material found on Earth. Because the entire Earth has been molten in the past (and most of it still is molten) terrestrial material has been reprocessed several times, erasing information on its original structure and composition. One way to study the material that formed the Earth and other planets is by studying the dust in the planet forming disks around other stars. A second possibility is to study the dust in tails of solar system comets. These topics will be addressed in Sect. 1.5.2 and 1.5.3 respectively.

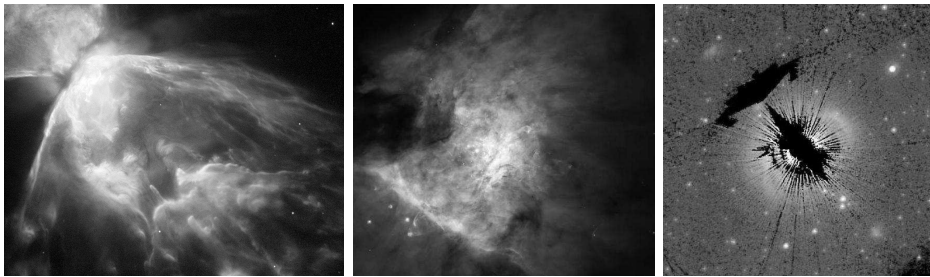


Figure 1.2: *Dust in astronomical environments.* In the left picture a closeup of the inner part of the planetary nebula NGC 6302 is shown. A planetary nebula is a leftover of the mass a solar-type star loses when it dies. The dust that is created by these dying stars is injected into the interstellar medium. Part of this dust ends up in molecular clouds. An example of such a molecular cloud, the Orion nebula M42 in the Orion molecular cloud is shown in the middle picture. In molecular clouds stars form. These new stars are surrounded by a dusty protoplanetary disk. An example, the disk around the young star HD 163296, is shown in the right picture. The central part in the picture is black because the central star is covered such that the weak emission from the disk can be observed. The black part towards the upper black corner is due to missing data. The disk feeds the star, so part of the dust will be incorporated into the star and destroyed. Part of the dust may also be incorporated in planets. Picture credits: A. Zijlstra et al. (UMIST), ESA, NASA (left); C. R. O’Dell et al. (Rice University), NASA (middle); C. A. Grady et al. (Nat. Opt. Astron. Obs.), NASA (right).

1.2 The interaction of radiation and dust

When studying astronomical objects, the only information that is usually available is the radiation we receive on Earth. When studying cosmic dust, one therefore has to know how it interacts with radiation, i.e. its *optical properties*. Note that with the term optical properties we refer to the scattering and absorption properties of a particle at arbitrary wavelengths, *not* only in the visible part of the spectrum. There are three main types of diagnostics on the characteristics of the dust particles; thermal emission, scattering, and extinction.

1.2.1 Thermal emission

Every object emits thermal radiation. The spectrum of the emitted radiation is determined by the characteristics of the emitting body as well as by its temperature. An object which absorbs all radiation that is incident on it, a so-called perfect blackbody, will thermally re-emit radiation in a distribution over wavelength that is given by the Planck function. The maximum of this function shifts towards shorter wavelengths when the temperature of the body increases.

Dust grains are not perfect blackbodies. The radiation emitted by a non-perfect blackbody is a Planck curve multiplied by the emission efficiency of the emitting object. Therefore, to compute the thermal emission of a dust grain we have to compute its emission efficiency. A particle in thermal equilibrium emits the same amount of energy

as it absorbs. Kirchhoff's law states that *at any wavelength the emission efficiency is equal to the absorption efficiency*. A rigorous derivation of this law for an isothermal sphere is given by Kattawar & Eisner (1970). This result is extended for an ensemble of randomly oriented nonspherical particles forming a macroscopically isotropic and mirror-symmetric medium by Mishchenko et al. (2002). Thus in order to compute the emission spectrum of a dust grain it suffices to compute its absorption spectrum which can be obtained in general by using numerical procedures like the ones discussed in this thesis.

The shape of the emission spectrum of a dust grain strongly depends on its characteristics, as will be discussed in Sect. 1.3. This enables us to derive, to a certain extent, the characteristics, like size, shape and composition, of the dust grains from observations of the thermal emission spectrum.

Cosmic dust grains can in general have temperatures ranging up to ~ 1500 K. Above this temperature the grains will evaporate. This corresponds to an emission spectrum peaking at wavelengths longwards of $\sim 3 \mu\text{m}$. In most cases, the bulk of the dust grains will have much lower temperatures, peaking at even longer wavelengths. Thus the thermal emission by dust grains will predominantly be at infrared wavelengths.

1.2.2 Scattering

When a parallel beam of light meets an obstacle the light is spread out in all directions. This phenomenon is called scattering. An object that does not itself emit radiation in a certain wavelength regime can still be observed in this wavelength regime because it can scatter light from a source, such as the Sun, into a detector, like for example our eyes. The color of the object is determined by the wavelength dependence of the incident radiation and its scattering efficiency. For example, when we look at the sky we observe sunlight scattered by the molecules in the Earth's atmosphere. As shown already by Lord Rayleigh in 1871 these molecules are much more efficient in scattering blue light, i.e. light at relatively short wavelengths, than they are in scattering light at longer wavelengths. Therefore, the sky appears blue.

Scattering of radiation by an object will, quite often, not alter the wavelength of radiation. In the environments we consider the dominant source of radiation is stellar. The stars studied in this thesis have their maximum emission at optical wavelengths. This implies that the best way of observing scattered radiation from dust grains orbiting these stars is by looking in the optical part of the spectrum.

The degree of linear polarization

When unpolarized radiation is incident on a collection of particles with random orientations, the scattered radiation will, in general, be polarized to a certain extent. The degree of polarization depends on the wavelength of incident radiation as well as on the angle between the incident and the scattered light (see e.g. Hovenier et al. 2004). Most ensembles of particles do not produce significant circular polarization. We consider only the degree of linear polarization. The degree of linear polarization as a function of the scattering angle is a very important observable which contains valuable information on,

for example, the size and shape of the scattering particles. It can be measured in the laboratory (see e.g. Hovenier et al. 2003), and is a frequently used observable for cometary dust (see e.g. Kolokolova et al. 2004). For an overview of polarimetry of dust in the solar system see e.g. Levasseur-Regourd (2004). Maybe one of the most striking examples of the diagnostic power of the observed degree of linear polarization is given by Hansen & Hovenier (1974). From observations of the degree of linear polarization of light scattered by Venus at various angles, they were able to derive the size, shape and composition of the particles in its upper atmosphere. They concluded that the droplets in the clouds covering Venus are most likely spherical, have a radius of approximately $1\ \mu\text{m}$, and are composed of a concentrated solution of sulfuric acid (H_2SO_4).

1.2.3 Extinction

The total amount of energy removed from the incident light beam by scattering and absorption is referred to as *extinction*. Extinction occurs when a bright source is located behind a column of dust. The wavelength dependence of the extinction provides information on the characteristics of the grains responsible. For example, the spectral shape of the $10\ \mu\text{m}$ extinction feature towards the galactic center can be used to determine the average size and composition of the interstellar silicate dust population (see Draine & Lee 1984; Li & Draine 2001; Kemper et al. 2004).

1.3 Dust grain characteristics

One of the aims of the study of cosmic dust is to understand the characteristics of the dust grains, i.e. their size, shape, structure and composition, and from this to reconstruct its processing history, and possibly even predict its future. The characteristics of a dust grain determine its optical properties, i.e. the absorption and scattering properties. Therefore, one can try to reconstruct the grain characteristics from astronomical observations. The most important grain characteristics are described below.

1.3.1 Grain composition and lattice structure

The composition of dust in astronomical environments can be analyzed by comparing thermal emission spectra with spectral properties of materials as measured in the laboratory. Also, laboratory measurements of scattered light can provide important clues on the composition of the grains. Another source of information is the study of interplanetary dust particles (IDPs) that pervade the solar system and cause the so-called Zodiacal light. Some of these particles can enter the Earth's atmosphere where they can be picked up, for example, on the wings of special, stratospheric airplanes. The dust grains shown in Fig. 1.1 have been collected in this way. The composition of these particles provides important information on the possible composition of dust in various environments. We will now discuss what we think are the most abundant materials in cosmic dust.

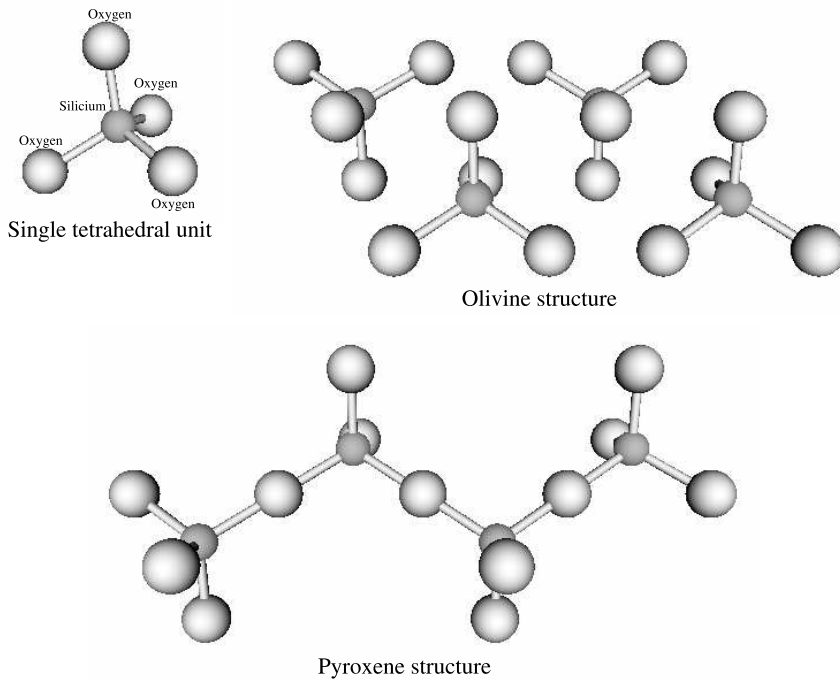


Figure 1.3: A schematic representation of a few silicate species. Shown is the ordering of the SiO_4 tetrahedra. The cations (Fe, Mg) that are in between the tetrahedra in the olivine and pyroxene structures are not shown.

Silicates

Silicates are the most abundant rock forming species. They are composed of silicon (Si), oxygen (O) and in most cases a cation, which is often iron (Fe) or magnesium (Mg). The Si and O atoms are ordered in SiO_4 tetrahedral structures (see the upper left structure in Fig. 1.3). The ordering of the tetrahedra and of the cations in between the tetrahedra determine the material properties of the silicates.

The most abundant silicate in cosmic dust and also in the Earth's mantle is olivine, which owes its name to its olive-green color. Its lattice structure is depicted in the upper right corner of Fig. 1.3. None of the oxygen atoms of the SiO_4 tetrahedra of olivine are shared which results in the chemical formula $\text{Mg}_{2y}\text{Fe}_{2-2y}\text{SiO}_4$, where y can vary between 0 and 1. The second most abundant silicate in the Earth's mantle is pyroxene. The name is derived from the Greek words for fire (pyros) and stranger (xenos). Pyroxene crystals are sometimes found embedded in volcanic glass, hence the name *fire stranger*. In the pyroxene lattice structure every SiO_4 tetrahedron shares a single oxygen atom with another tetrahedron. This results in a chain-like structure shown in the lower part of Fig. 1.3. The chemical formula for pyroxene is $\text{Mg}_y\text{Fe}_{1-y}\text{SiO}_3$. The last silicate that we introduce here is silica. In silica all the oxygen atoms of the tetrahedra are shared which

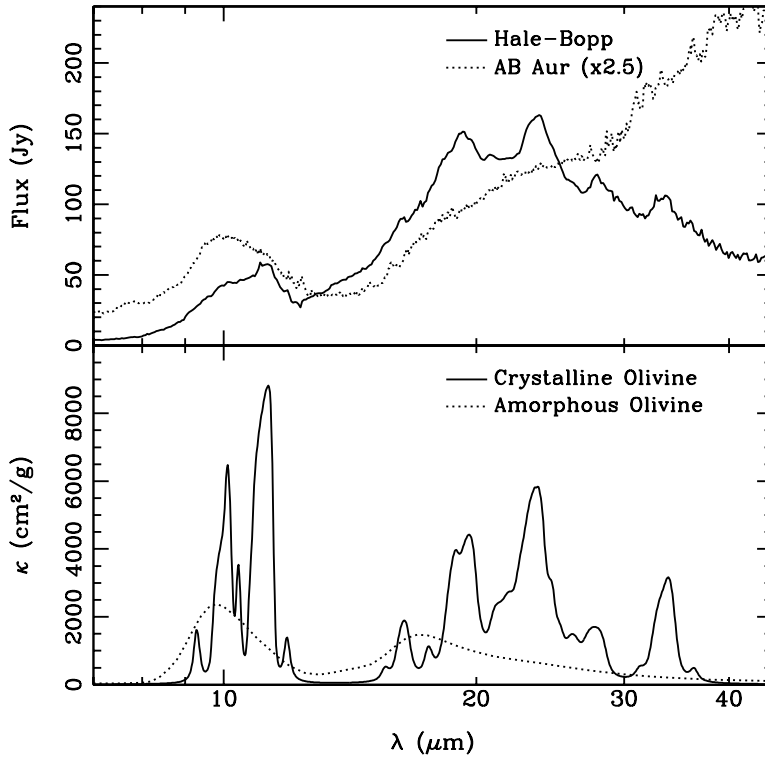


Figure 1.4: The infrared spectra of comet Hale-Bopp (Crovisier et al. 1997) and the circumstellar disk around the young star AB Aur (van den Ancker et al. 2000) as observed by the Infrared Space Observatory (ISO) (upper panel). The spectrum of AB Aur is multiplied by 2.5 for clarity. In the lower panel the mass absorption coefficient as a function of wavelength for small amorphous and crystalline olivine particles is shown. The spectra in the lower panel are computed by using a distribution of hollow spheres to represent irregularly shaped particles as described in chapter 5 using a volume equivalent radius of $0.1 \mu\text{m}$. The data for the complex refractive index of the dust material as a function of wavelength are taken from Servoin & Piriou (1973) and Dorschner et al. (1995). The figure clearly shows the differences in absorption spectra between amorphous and crystalline olivine. As can be seen by comparing the two panels, the spectral signature of both species is detected in astronomical sources.

gives the chemical formula SiO_2 . Silica is the main component of common sand.

The emission spectra of silicates display emission features around $10 \mu\text{m}$ due to the Si-O stretching mode, and around $20 \mu\text{m}$ due to the O-Si-O bending mode. We can roughly distinguish between two types of ordering of the positions of the atoms in the silicates, namely amorphous and crystalline. The crystalline silicates have a long-range ordering of the lattice structure, whereas in the amorphous silicates only a short-range ordering can be found. The crystal structure is the lowest energy state for the atoms to be in. Amorphous silicates can form when the atoms in the material condensate rap-

idly enough so that there is no time to find the lowest energy state. The most common example of amorphous silicate on Earth is plain window glass. When the material is heated above the so-called glass temperature, the atoms can move more freely and find the lowest energy state, thus the material crystallizes. The differences between crystalline and amorphous silicates are visible in their spectral characteristics. Roughly speaking the scattering of phonons inside the irregularly structured amorphous silicate lattice broadens the spectral features, which results in broad spectral features with relatively low contrast. The (near) perfect ordering of the crystalline silicates causes their spectral resonances to be much more pronounced and narrow. The mass absorption coefficient, κ , which is a measure for the absorption efficiency per unit mass, as a function of wavelength, λ , of grains composed of amorphous and crystalline olivine is shown in the lower panel of Fig. 1.4. Here, we plot the magnesium end member of the crystalline olivine family ($y = 1$), which is referred to as crystalline forsterite. For comparison, in the upper panel of Fig. 1.4 the emission spectra of comet Hale-Bopp and the circumstellar disk surrounding the young star AB Aur are shown.

Other components

Other dust components that make up a significant fraction of cosmic dust grains are carbonaceous species, metallic iron and iron sulfide.

Carbon is an abundant element in the Universe and is, as far as we know, the basis for all life on Earth. In astronomical environments we find carbon in the solid and in the gas phase. For the solid phase we can roughly discriminate between the amorphous carbon component, and the component of large molecules called PAHs (Polycyclic Aromatic Hydrocarbons).

Metallic iron is a material that is sometimes found in IDPs or meteorites. Small iron grains have a very high absorption efficiency in the optical and ultraviolet part of the spectrum. Also, due to their magnetic properties, small iron inclusions are believed to be one of the possible causes for the orientation of dust grains in the interstellar medium. The spectral structure of metallic iron grains is very smooth and shows no prominent spectral features.

Iron sulfide (FeS) is the most important sulfur bearing material in IDPs and meteorites that have been studied. Basically, in these particles, all the available sulfur is contained in iron sulfide. When and how the iron sulfide grains form is still not clear. In the interstellar medium most of the available sulfur is in the gas phase, which means that the iron sulfide grains must condense in molecular clouds or in circumstellar disks. The spectral structure of emission by iron sulfide grains shows a broad feature around $23\ \mu\text{m}$. This feature was first detected in young stellar objects by Keller et al. (2002).

1.3.2 Grain size

The sizes of the dust grains are very important for constraining models of grain growth and planet formation. The size of an irregularly shaped dust grain is not trivially defined. In this thesis the size of a dust grain is taken to be the radius of a sphere with the same material volume. For very fluffy or porous particles, the outer radius might be

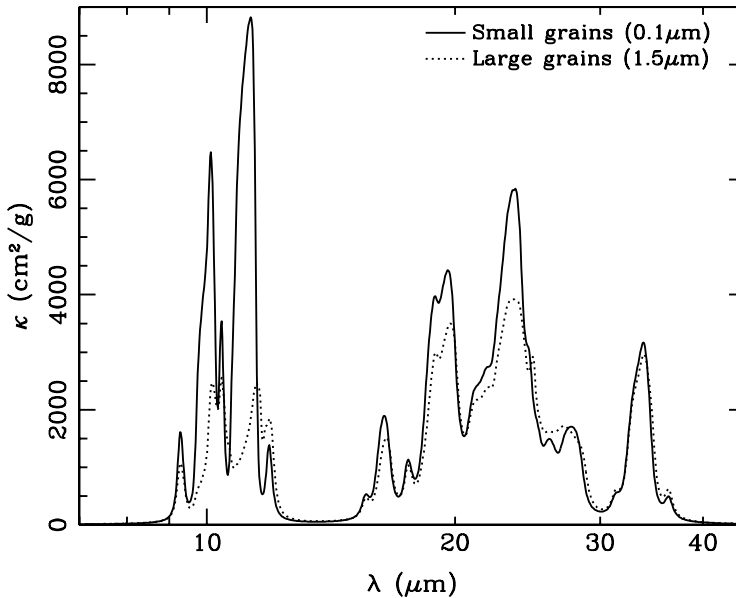


Figure 1.5: The mass absorption coefficient as a function of the wavelength for crystalline forsterite particles for two different grain sizes. The spectra are computed using a distribution of hollow spheres to represent irregularly shaped particles. Measurements of the complex refractive index as a function of wavelength are taken from Servoin & Piriou (1973).

much larger than this volume equivalent radius. The effects of fluffiness on the emission spectra of particles of various sizes is discussed in chapter 6.

An important parameter for the optical properties of a particle is the so-called size parameter, x , which is basically the size of the grain with respect to the wavelength of incoming radiation, $x = 2\pi r/\lambda$ (r the effective radius of the particle, λ the wavelength). In general, when the size parameter is increased beyond a certain value the amplitude of the spectral absorption features tends to decrease. Thus increasing the particle size first affects the strengths of the features at shorter wavelengths. In order for the features at longer wavelengths to be affected, the particle size has to be increased further. A second important parameter is the size of the particle with respect to the wavelength *inside* the particle. The wavelength inside the particle depends on the refractive index of the particle. For large values of the refractive index, the wavelength inside the particle is small. In general the refractive index is high in the spectral features. This causes the amplitude of the strongest features to decrease already at smaller particle sizes than the weaker features do since the particle is already large compared to the wavelength of radiation inside the particle. These effects can be seen in Fig. 1.5 where the mass absorption coefficient of crystalline forsterite particles as a function of wavelength for two particle sizes is plotted. It can be seen from this figure that the features at longer wavelengths are less affected by the increase of particle size than the features at short

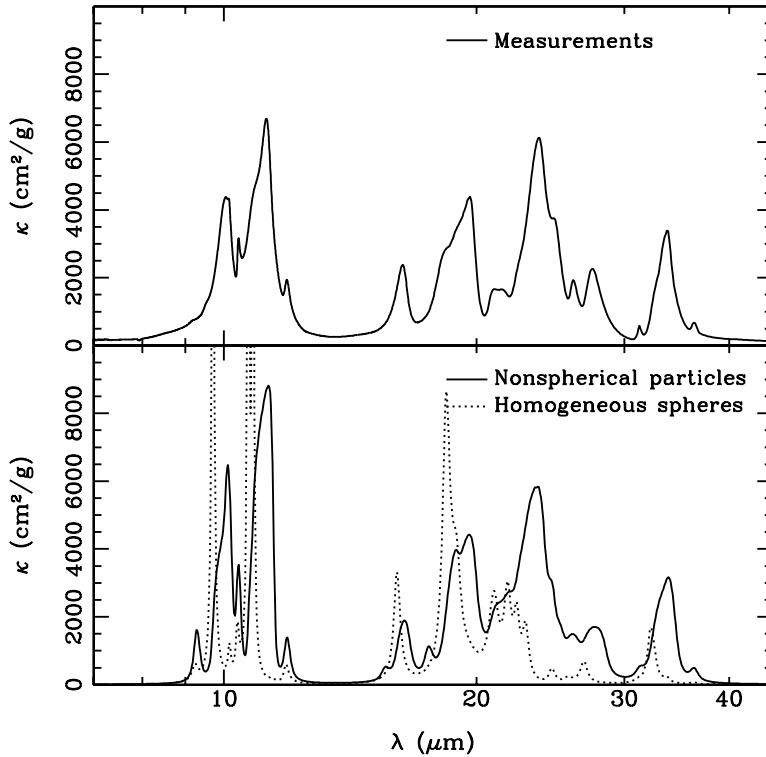


Figure 1.6: The mass absorption coefficient as a function of the wavelength for small crystalline forsterite particles. In the upper panel, laboratory measurements by Chihara et al. (2001) are shown. Shown in the lower panel are computations for two different particle shape distributions, a distribution of hollow spheres representing irregularly shaped, nonspherical particles as described in chapter 5, and homogeneous spheres. The grain size in these computations is taken to be $0.1 \mu\text{m}$. Measurements of the wavelength dependent complex refractive index are taken from Servoin & Piriou (1973). It can be seen that the measured mass absorption coefficients are best reproduced by computations using the distribution of hollow spheres.

wavelengths. A detailed explanation of this is given in chapter 5. These two effects can be used as a diagnostic tool to determine the typical size of the emitting dust grains by comparing the relative strength of the emission features. This will be applied to obtain the size of the crystalline forsterite grains in the coma of comet Hale-Bopp in chapter 8.

1.3.3 Grain shape and structure

The shape of a dust grain is a very important grain characteristic for its scattering and absorption behavior. The positions and strengths of the spectral features seen in, for example, crystalline silicates are sensitive to the shape of the particles (see Fig. 1.6). When considering the absorption spectra of small particles it is shown in chapter 2 that

one can distinguish basically two groups of particle shapes. The first group contains the homogeneous spheres and the second group all other particle shapes. Shape effects within the second group are very small compared to the differences with homogeneous spheres. This can be understood as follows. A small dust grain disturbs the electromagnetic field because its composition, which is reflected in its refractive index, is different from the surrounding medium (which is in most cases vacuum). Roughly speaking, one would expect that the larger the difference in refractive index between the particle and the surrounding medium, the more the electromagnetic field will be influenced. This is generally the case in the absence of resonance effects due to the geometry of the particle. However, symmetries in a particle can cause the perturbation to be large at specific values of the refractive index. Breaking the geometrical symmetries of a particle, and especially the perfect symmetry of a homogeneous sphere, is therefore crucial in providing a meaningful representation of the properties of small irregularly shaped particles.

The effects of non-sphericity on the optical properties of particles is an important element of this thesis. The fact that shape effects within the group of nonspherical particles are small compared to the differences with homogeneous spheres allows one to choose an ensemble of simple shapes to compute the optical properties of irregularly shaped particles. This concept is referred to as the *statistical approach* and will be discussed in more detail in the next section.

1.4 Computing the optical properties of dust grains

To study the absorption or scattering by cosmic dust grains the optical properties have to be computed in an accurate way. All grain characteristics described above influence these properties. The computation of the optical properties of cosmic dust grains requires that the Maxwell equations for the interaction of the incident light with the particle are solved. This is in general not a trivial exercise (see e.g. Mishchenko et al. 2000). For this reason – in most cases – the shape of the dust particle we model has to be simplified.

In 1908 Gustav Mie published an exact solution for the interaction of light with a homogeneous sphere of arbitrary composition and radius. Mie theory is still one of the most commonly used ways to compute the interaction of light with small particles. However, as can already be seen from Fig. 1.1, cosmic dust grains are not homogeneous spheres. This influences the optical properties (see Fig. 1.6).

Roughly speaking there are two extreme ways to approach the problem of light scattering and absorption by small particles. The first approach is to assume that the dust grains can be approximated by homogeneous spheres. In this way the optical properties can be obtained from Mie theory. The second approach is to model the dust grains in the most exact way possible. To obtain the optical properties one then has to employ a robust computer algorithm. Both approaches have their pros and cons. The first approach is fast and easy. In addition, it provides useful insights in the physical processes and general trends that play a role (see e.g. van de Hulst 1957). However, since most dust grains are not homogeneous spheres, the computed optical properties are often much different from those of realistically shaped dust grains. This limits the applicability of

this approach. The second approach provides accurate results for the optical properties of realistically shaped particles. However, the heavy computational demand of robust computer algorithms allowing for complex particle shapes limits the applicability of this approach. Especially in studies where a large part of the parameter space (refractive index, grain size, wavelength) needs to be considered, the second approach is at present too time consuming. Fortunately, a third method is available which tries to combine the best of the two extreme approaches (see e.g. Bohren & Huffman 1983). This method is referred to as the *statistical approach*.

1.4.1 The statistical approach

The idea behind the statistical approach is perhaps best described by the words of Einstein,

Everything should be made as simple as possible, but not simpler.

The statistical approach basically tries to find a way of modeling the optical properties of irregularly shaped dust grains by finding an ensemble of simple shapes with the same optical properties. This has the advantage that by choosing a broad distribution of simple shapes, including extreme cases, we can get rid of non-realistic resonance effects as seen in the optical properties of homogeneous spheres. In addition, choosing the class of simple shapes carefully allows for relatively fast computations of the optical properties.

Bohren & Huffman (1983) proposed to use a distribution of ellipsoidal shapes to model the characteristics of realistically shaped dust grains with sizes much smaller than the wavelength both inside and outside the particle, i.e. in the Rayleigh domain. Their Continuous Distribution of Ellipsoids (CDE) is widely employed in studies of emission and absorption spectra. However, the tri-axial ellipsoids used in the CDE allow only for fast computations of the optical properties of particles in the Rayleigh domain. This excludes the study of particle size effects on the optical properties of particles. Using different classes of particle shapes, the statistical approach has been studied and applied to various observations and measurements (see e.g. Hill et al. 1984; Mishchenko et al. 1997; Kahnert et al. 2002; Kahnert 2004).

In this thesis the basis of the statistical approach is studied. In chapters 2 and 5 it is shown that the exact choice of the class of simple shapes employed is not very important for the obtained results, as long as the perfect symmetry of a homogeneous sphere is broken. An analytical basis for the statistical approach for computing absorption properties of particles in the Rayleigh domain is provided in chapter 3. Two classes of simple shapes that may be used in the statistical approach, spheroids and hollow spheres, with sizes comparable to the wavelength are considered in chapters 4 and 5.

1.5 Applications to astronomical observations

One of the aims of the studies presented in this thesis is to deduce the characteristics of small dust grains from their optical properties. Dust grains are the building blocks of

larger bodies like comets, asteroids and planets. Therefore the study of the properties of these small particles provides a better understanding of the dynamical and evolutionary processes that occur in the phase before a planetary system is formed. Below, we provide a very brief overview of the formation of stars and planetary systems and of the processing of grains in protoplanetary disks.

1.5.1 The formation of planetary systems

We will concentrate on the formation of low mass, isolated stars and the planets that may form around these stars. The current paradigm of how these stars form was put forward by Shu et al. (1987). Stars form in molecular clouds. In these clouds of gas and dust a denser core can form, which will start to contract under its own gravity. From this point on four distinct phases in star formation are identified. The classification of these phases is based on the properties of the spectral energy distribution that can be observed and can be summarized as follows (see also Fig. 1.7).

Class 0 Objects in this phase have just started to contract. In the center of the contracting core, a protostar forms. Because the cloud is contracting and will always have a non-zero angular momentum, the matter will form a rotating accretion disk around the protostar. The protostar and its accretion disk remain deeply embedded in the surrounding molecular cloud and are thus not visible. This phase lasts for about 10^4 years (Andre et al. 2000).

Class I The star continues to accrete matter from the accretion disk, and along the rotational axis of the system a bipolar outflow can be created. This outflow clears the material from the surrounding cloud and the accretion disk becomes visible. The material is still actively accreted onto the protostar and also new material from the surrounding cloud is provided through the disk. In this phase, which lasts for about 10^5 years, the circumstellar disk is mainly actively heated by gravitational energy that is dissipated in the disk due to viscous processes.

Class II In this phase the protostar starts to develop a more or less spherically symmetric outflowing wind, blowing away the remaining low density material from the surrounding cloud. The star becomes optically visible. The accretion rate from the disk onto the star goes down significantly and the disk is only passively heated by stellar radiation. The objects studied in chapters 9 and 10 are in this evolutionary phase. It is believed that in this phase, which lasts for about 10^7 years (Haisch et al. 2001), larger bodies like comets, asteroids and planets may form. These larger bodies form through the aggregation of small dust grains.

Class III The star has reached the main sequence and is completely powered by thermonuclear fusion. Almost all of the gas and most of the dust in the system has been removed. Some of the dust may be incorporated into comets, asteroids and perhaps planets. The small amount of dust that is still left is contained in relatively large particles.

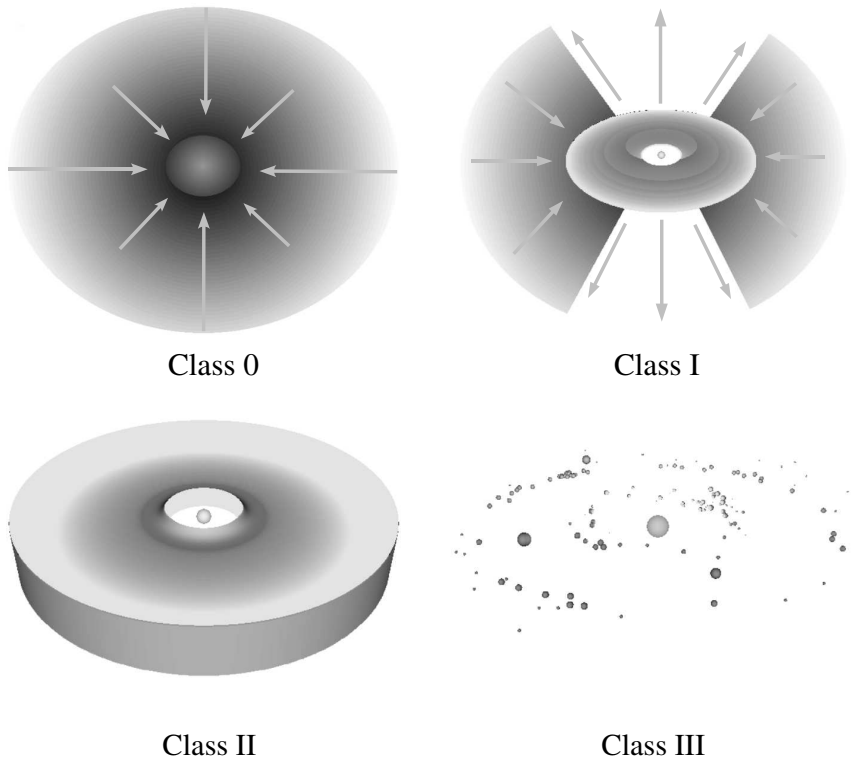


Figure 1.7: *The four stages of star formation as put forward by Shu et al. (1987).*

1.5.2 Circumstellar dust

As described above a forming star is surrounded by a circumstellar disk. In these disks chemical and physical processes occur that alter the composition, size and structure of the grains. Understanding the dynamics of these protoplanetary disks is important for understanding how larger bodies form.

In chapters 9 and 10 we study the dust in a large sample of protoplanetary disks around Class II objects. In chapter 10 the combined light from two 8.2 meter telescopes is analyzed which gives information on the innermost regions of protoplanetary disks. At a later stage terrestrial planets may assemble in these regions. We are thus for the first time able to analyze the building blocks of terrestrial planets. The observations show that in the inner regions of these disks most of the silicates have crystallized, suggesting terrestrial planets form from crystals. In addition, these observations combined with the results from other studies and the findings presented in chapter 9 suggest a scenario in which the crystalline silicates are produced by heating close to the central star and subsequently have been mixed outwards. In the outer regions they can be incorporated into, for example, comets.

When large bodies form from small dust grains that stick together, the material com-

position can be altered by so-called *parent body processing*. This includes, for example, melting of the material and subsequent differentiation, which means that the heavier elements sink to the core of the object. Also, under the influence of water, parent body processing can include the formation of hydro-silicates. For parent body processing to occur, the body in which the dust is incorporated has to be large enough (typically a few hundred kilometers in radius). For example, cometary dust is believed to be practically unaltered since its incorporation into the comet. Dust that has been processed in a larger body can become visible when this body collides with another one and shatters. This secondary dust is believed to be present in the so-called debris disks around Class III sources. In chapter 7 we provide a diagnostic for studying the mineralogy of the dust around Class III objects.

1.5.3 Cometary dust

Another interesting source of information on the material that was available in the early solar system are comets. Comets are kilometer sized, porous bodies composed of ice and dust. Since comets are too small to have ever been molten the material of which they are composed is thought to be unaltered since its incorporation into the comet. Therefore, these objects are a valuable reservoir of unaltered, early solar system material. When a comet comes close to the Sun on its eccentric orbit, the ice melts and releases a large amount of gas and dust. This gas and dust surrounds the comet and forms its *coma*. The radiation pressure and wind from the Sun blows away the gas and the dust. The gas is most affected by this and forms a tail pointing directly away from the Sun. The dust forms a second tail pointing away from the Sun, but also still slightly following the trajectory of the comet. This can result in a spectacular sight. A famous example was the great comet Hale-Bopp in 1997, a picture of which is shown in Fig. 1.8. The dust released by comets can be studied in different ways, for example, by interpretation of astronomical observations as described in this thesis.

The infrared spectrum of comet Hale-Bopp taken by the Infrared Space Observatory (ISO) (Crovisier et al. 1997) provided a unique opportunity to study the composition of cometary dust. We analyze the dust released by Hale-Bopp in chapter 8. One of our findings is that the crystallinity of the dust is quite low. In addition, *in situ* measurements of cometary dust have been done, and more will be conducted in the future. Spacecrafts can do measurements inside the coma of a comet. During the Stardust mission dust particles from the coma of comet Wild 2 have been collected in January 2004. The spacecraft is planned to bring its sample of cometary dust particles to Earth in 2006. In 2014 a small lander will be placed on the surface of comet Churyumov-Gerasimenko by the Rosetta space probe. The mission Deep Impact will involve smashing a small spacecraft into Comet Tempel 1 on the 4th of July 2005 creating a crater on the surface of the comet nucleus. The impact will be monitored by a flyby spacecraft and many telescopes on Earth to try to determine the properties of the cometary nucleus. All these missions will provide crucial information on the composition of cometary material. This information can be used to validate studies of dust based on telescopic observations. This is of great value because it helps to interpret observations from sources where *in situ* measurements are not feasible, such as protoplanetary disks.



Figure 1.8: Comets form large tails of gas and dust when they come close to the Sun. A very bright comet forms a beautiful sight in the night sky. A famous example of this is the great comet Hale-Bopp shown above, which was visible in 1997. Picture credits: A. Dimai and D. Ghirardo (Col Druscie Obs.), AAC

1.6 Summary and conclusions

Detailed study of the optical properties of dust grains as functions of the grain characteristics, like size, shape and composition, can provide valuable knowledge and insights when studying observations of dusty astronomical sources. A good understanding of the dependence of the optical properties on each of these characteristics is crucial in obtaining reliable information on the nature of astronomical environments. In this thesis methods to study the composition and size of cosmic dust grains in a fast and reliable way are presented.

The outline of the thesis is as follows. First the optical properties of various particle shapes and shape distributions in the Rayleigh domain, i.e. particles much smaller than the wavelength of radiation inside and outside the particle, are studied in chapters 2 and 3. In the studies presented in chapters 4, 5, and 6 the grain size of the particles is increased to the so-called *resonance region*, i.e. particles with sizes comparable to the wavelength. In chapter 7 the optical properties of particles much larger than the wavelength are studied. In the last three chapters the results are applied to cometary dust (chapter 8) and dust in circumstellar disks around young stars (chapters 9 and 10).

In chapter 2 various shape distributions of particles in the Rayleigh domain are studied using different classes of simple shapes. It is found that the optical properties of very small particles are, to a certain extent, independent of the distribution of simple shapes employed as long as the perfect symmetry of a homogeneous sphere is broken.

In chapter 3 this idea is developed further and an efficient method to compute the absorption and scattering properties of arbitrarily shaped particles in the Rayleigh domain is provided. This method is then used to show that for any arbitrarily shaped and arbitrarily oriented particle, or ensemble of particles, there exists a unique distribution of spheroidal particles with the same composition and in a fixed orientation with exactly the same absorption properties. This distribution of spheroidal particles only depends on the geometry of the particle, or ensemble of particles, it represents, and is independent of the particle composition. This provides a theoretical basis for the statistical approach. The derived distribution of spheroidal particles provides a well founded choice for computations of larger particles, i.e. outside the Rayleigh domain.

In chapter 4 a combination of exact techniques and approximations are used to develop a scheme to compute the absorption and scattering cross sections of randomly oriented spheroids of arbitrary size. This method can be used to study combined particle size and shape effects.

Since in chapter 2 it is shown that the optical properties of small particles are, to a certain degree, independent of the exact particle shapes employed, the possibility of adopting a distribution of hollow spheres is studied in chapter 5. The distribution of hollow spheres has the advantage that computations for arbitrarily sized particles can be done quite easily and efficiently. The combined effects of particle size and shape are studied. Also the results obtained using a distribution of hollow spheres and the uniform distribution of spheroids, as presented in chapter 4, are compared. It is found that these two shape distributions display the same trends in the wavelength dependence of the absorption properties with particle size. In chapter 5 laboratory measurements of the degree of linear polarization of small quartz particles are fitted successfully using hollow spheres and, from the fit parameters, the size distribution of the particles is also successfully reproduced. From this it is concluded that the distribution of hollow spheres can be employed to model certain optical properties of cosmic dust grains.

When employing the statistical approach for computing the optical properties of irregularly shaped particles, one should be aware that the derived grain parameters do not always have a one-to-one correspondence to the parameters of the actual dust grains. Therefore, in chapter 6 the optical properties of fractal aggregates and compact particles with complex shapes are studied. In this chapter we concentrate on the $10\ \mu\text{m}$ absorption feature of amorphous olivine because this feature is frequently employed to derive the size and composition of cosmic dust grains. It is concluded that the strength and the shape of the $10\ \mu\text{m}$ feature is sensitive to the shapes of the particles causing it. Large, very fluffy aggregates of spheres display a feature that is characteristic for much smaller, homogeneous spheres. To a lesser extent the same is found for large, very irregular compact particles. This implies that by using homogeneous spheres to represent the optical properties of irregularly shaped particles or fluffy aggregates, the size of the particles is underestimated. In chapter 6 a way of correcting for this effect is suggested.

In chapter 7 the spectroscopic characteristics of grains much larger than the wavelength of radiation are studied. The absorption spectrum of very small grains usually displays high contrast spectral structure characteristic for the composition of the grains. When the particle size is increased, the contrast of the spectral structure de-

creases. It is generally assumed that when the grains are sufficiently large, there will be no detectable spectral structure left. However, in chapter 7 it is shown that detectable spectral structure can still be observed in the emission spectra of arbitrarily large particles. It is shown that the strong, sharp emission enhancements visible in the spectrum emitted by very small crystalline silicate particles change into emission dips in the emission spectrum of very large crystalline silicate particles. These emission dips are also seen in measurements of the emission spectra of macroscopic rocks (see e.g. Christensen et al. 2000). An example of how this spectroscopic diagnostic can be used to determine the crystallinity in the circumstellar material surrounding Vega is also provided.

In chapter 8 the statistical approach using the distribution of hollow spheres is applied to obtain the characteristics of the dust in the coma of comet Hale-Bopp. We reproduce for the first time the observed short and long wavelength infrared emission spectrum as well as the observed degree of linear polarization at various angles and wavelengths using a single dust model. We employ an objective least squares fitting routine to derive the size distribution and composition of the dust particles. From the ratios of the observed emission features of crystalline forsterite it is derived that the crystalline silicates must be submicron sized, contrary to the amorphous silicate grains which must have a size distribution including grains with sizes up to $\sim 40 \mu\text{m}$. In contrast with previous analyses of the dust in Hale-Bopp, that were not able to account correctly for this effect, it is found that the fraction of crystalline silicates is relatively low. The resulting particle composition and size distribution can be accounted for by models of dust in the early solar system. It is also consistent with the typical abundance and size of crystalline inclusions found in IDPs.

In chapter 9 observations and analysis of a large sample of dusty protoplanetary disks around young stars are presented. The characteristics of the dust around these stars is derived and a detailed statistical analysis of the dust properties is presented. An important result of this analysis is that all sources with a high fraction of crystalline silicates also have a high fraction of large grains, i.e. efficient grain growth has occurred. This implies that grain growth is in general easier than producing crystalline silicates in a significant part of the disk. The results from the analysis indicate that the final crystallinity of the disks is reached during the so-called *active disk phase*, when the star was still a Class I object, or early in the Class II phase. The combination of the findings presented in this chapter with results from other studies seems to favor a scenario in which the crystalline silicates are produced in the inner parts of the disk, i.e. close to the central star, by thermal annealing and transported outwards to the regions where they can be detected.

The above result is strengthened by the results from the analysis as presented in chapter 10. In this chapter the first view of the innermost regions of three protoplanetary disks using spectral infrared interferometry is presented. The part of the disk that is probed is where in our own solar system the terrestrial planets have assembled from small dust grains. This thus provides a unique view of the building blocks of terrestrial planets. It is found that the dust grains in these inner regions of the disk are much more crystalline than the dust grains further out in the disk. Also in one of the sources we

derive a difference between the inner and outer disk regions in the composition of the crystalline silicates in terms of crystalline olivine and pyroxene in the sense that there is more crystalline pyroxene in the outer disk regions. These results are again consistent with the crystalline silicates being produced close to the central star and being moved outwards to the regions where objects like comets, planetesimals and planets form.

The main results of the work presented in this thesis may be summarized as follows.

- The statistical approach is given a firm foundation. It is shown that applying the statistical approach to astronomical observations makes sense.
- In most previous studies of infrared spectra the optical properties of dust grains were computed by either applying a particle model that cannot account for non-spherical particle shapes (Mie theory) or a particle model that cannot account for the real particle size (CDE). The distribution of hollow spheres proposed in this thesis accounts for both effects and provides an efficient and accurate way for computing certain optical properties of irregularly shaped particles with arbitrary size.
- An efficient method is presented to compute scattering and absorption by arbitrarily shaped particles in the Rayleigh domain. This method is especially useful for calculations of absorption spectra.
- The diagnostic power contained in the optical properties of cosmic dust grains is studied in detail. A new diagnostic for the size of dust grains from infrared spectroscopy based on the peak ratios of the crystalline silicate resonances is presented. In addition, the distribution of hollow spheres allows to combine observations of the thermal infrared emission of dust grains and the degree of linear polarization of scattered light in the visible part of the spectrum to better constrain dust properties derived from observations.
- The dust in the coma of comet Hale-Bopp contains less crystalline silicates than previously thought. The size of these crystals is much smaller than the typical size of the other dust components. The composition, crystallinity and size distribution of the dust is in agreement with that found for IDPs and with predictions from the composition of cometary dust from models of the early solar system.
- The crystalline silicates in protoplanetary disks are, most likely, mainly produced by heating close to the central star after which they are mixed outwards to the regions where they can be incorporated into, for example, comets. The results suggest that this process happens predominantly in the early stages of the evolution of the disk. In the inner regions of these disks, a large reservoir of highly crystalline material is present.

1.7 A look into the future

Although the study of scattering and absorption by small particles originated in the 17th century, the field of infrared astromineralogy is much younger. A great step forward in

our understanding of cosmic dust was made possible by the Infrared Space Observatory (ISO). Currently a rich variety of new instruments has been developed which will help us to solve some of the unresolved issues in this field. The high sensitivity of the Spitzer space telescope will provide infrared spectra over a long wavelength range of many sources. This will allow for a statistical analysis of the dust properties. High spatial resolution studies of the dust in circumstellar environments may help us understand the dynamical processes occurring in these environments. These high spatial resolution observations can for instance be done with the MID-Infrared Interferometric Instrument (MIDI) on the Very Large Telescope Interferometer (VLTI). Some of the first results obtained with this instrument on circumstellar disks are presented in chapter 10. This already shows that the dust is far from uniformly distributed in the disk. Interferometry of these protoplanetary disks at different baselines can give us the dependence of the dust mineralogy on the distance from the central star.

The huge observational progress that has been made and will likely be made in the future deserves the best possible effort also on the theoretical and experimental side. There remain many open theoretical issues that need answering. As a first example, the absorption and scattering properties of composite particles, i.e. materially inhomogeneous particles, are not well understood. Modeling of composite particles is now mostly done by treating the optical properties of all materials separately. If, and under which conditions, this is a good approximation needs to be investigated. In order to study the composition of dust from observations, a fast diagnostic tool to study these kinds of particles has to be developed in order to apply objective fitting routines to the data. A second example of an issue to be further explored is the influence of the disk structure on the observed emission from circumstellar disks. The current disk models are not able to reproduce all of the observed characteristics of protoplanetary disks. More realistic representations of these disks have to include information on the mixing of material in the disk, grain growth, thermal processing of the dust, and the chemistry of the solid state as well as the gaseous component.

The study of cometary material provides a different way of studying the history and evolution of dust. The *in situ* measurements done by, for example, the Stardust mission will undoubtedly add a lot of information to our current knowledge on the composition, fluffiness and size of cometary dust particles when it returns its sample of dust from Comet Wild 2 to Earth in 2006. This information can be used to fine-tune and constrain dust models used to study, for example, protoplanetary disks.

The new observational opportunities together with the theoretical and experimental progress will undoubtedly provide us with the answers to many of the open questions. Like any progress in science, however, the answer to one question opens other, new and interesting questions. All in all, the future looks bright.

2

Shape effects in scattering and absorption by randomly oriented particles small compared to the wavelength

*M. Min, J. W. Hovenier, and A. de Koter
Astronomy & Astrophysics, v.404, p.35-46 (2003)*

Abstract

We study the effects of particle shape on the absorption and scattering cross sections of randomly oriented particles in the Rayleigh domain, i.e. particles that are very small compared to the wavelength of radiation both inside and outside the particle. In particular, we investigate the validity of the so-called statistical approach. In this approach it is assumed that the scattering and absorption properties of irregularly shaped particles can be simulated by the average properties of a distribution of simple shapes. We depart from the assumption of homogeneous spherical particles in two ways: 1) by using various distributions of elongated and flattened homogeneous ellipsoids and spheroids, 2) by using a distribution of hollow spherical particles. We derive explicit formulas for the shape averaged scattering and absorption cross sections as functions of the refractive index for various distributions of particle shapes in the Rayleigh limit. We compare the absorption cross sections as functions of the refractive index of the various distributions with each other and with those of homogeneous spheres. We also study the effects of the distributions on the shapes of absorption spectra. We find that there is a strong similarity between the absorption spectra of distributions of various non-spherical homogeneous particles and a distribution of hollow spheres. We show that the positions of features in the shape averaged mass absorption coefficient as a function of wavelength of small ellipsoidal, spheroidal or hollow spherical crystalline forsterite particles coincide with those deduced from the spectral energy distributions of various astronomical sources and with measurements of the mass absorption coefficients of small particles. This is not the case when we use homogeneous spherical particles.

2.1 Introduction

In many astrophysical environments dust is an important constituent. Radiation interacting with the dust particles can be absorbed, scattered and re-emitted. For the interpret-

ation of infrared spectra of dusty objects it is, therefore, needed to understand the way small particles interact with light. This strongly depends on the size, structure, shape and composition of the dust grains. In this article we consider the limiting case of particles very small compared to the wavelength of radiation inside and outside the particle (the Rayleigh limit) and concentrate on how the absorption and scattering properties depend on the shape of the particles. In this paper all particles are in random orientation.

Calculations of scattering and absorption properties of homogeneous spherical particles can be done very accurately using the so called Mie theory (Mie 1908). For this reason, in most applications of light scattering the particles are considered to be spherical and homogeneous. However, if we look at, for example, pictures of interplanetary dust particles, we see that these particles are not at all spherical and in most cases are inhomogeneous in structure and composition (Warren et al. 1994). Also, when we compare the positions of features in the spectra of the mass absorption coefficients of homogeneous spherical particles with the positions of features derived from the spectral energy distributions of various astronomical dusty environments, we find that there is often no satisfactory agreement (see e.g. Hony et al. 2002; Bouwman et al. 2001). Therefore, it is important to study the absorption and scattering properties of particles that are not homogeneous and not spherical.

Because the solid particles in astrophysical environments are expected to be very irregular in shape, it is very difficult (if not impossible) to characterize the shape of the particles in an appropriate way. Therefore, we employ the idea of a statistical approach as suggested by Bohren & Huffman (1983). In this approach one simulates the scattering and absorption characteristics of irregularly shaped particles by those of a shape distribution of particles with various simple shapes, such as ellipsoids or spheroids. Important tests of this idea have been done by for example Mishchenko et al. (1997), Kahnert et al. (2002) and Kahnert & Stamnes (2002). The statistical approach has been extensively applied for ellipsoids in the Rayleigh limit (see Bohren & Huffman 1983; Fabian et al. 2001). However, it is difficult to calculate scattering by randomly oriented ellipsoids outside the Rayleigh limit. However, for ellipsoids of revolution (spheroids) with moderate aspect ratios calculations of scattering by shape distributions of randomly oriented spheroids of arbitrary size can be performed very well and with sufficient accuracy using the so-called T-matrix method in combination with appropriate approximate methods (see Min et al. 2003a).

One of the main assumptions in the statistical approach is that when we average over a wide range of shapes, the typical characteristics of the separate shapes blend together into something which is independent of the choice of the separate shapes we used for the averaging. If this is true we can indeed simulate a shape distribution of irregular particles by using a distribution of simple shapes. We test this assumption by comparing the absorption characteristics of shape distributions of ellipsoids, spheroids and a distribution of hollow spheres.

Already, some studies of the effects of porosity on the absorption and extinction spectra of dust particles have been performed (see e.g. Iatì et al. 2001; Hage & Greenberg 1990; Jones 1988). As a result of the frequently employed dust model suggested by Mathis (1996), which uses composite and fluffy particles with approximately 45%

vacuum, Dwek (1997) studied whether porous particles could solve the so-called "carbon crisis". Vaidya & Gupta (1999) used the Discrete Dipole Approximation (Purcell & Pennypacker 1973) to calculate scattering by porous grains to fit the interstellar extinction curve. All these models use a fixed fraction of porosity. However, in line with the statistical approach, in this paper we study the effects of averaging over the porosity fraction, i.e. the fraction of the total volume of the sphere occupied by the vacuum inclusions.

We will first derive expressions for the scattering and absorption cross sections and the single scattering albedo of several shape distributions of randomly oriented ellipsoids and spheroids in the Rayleigh limit. All ellipsoids and spheroids in this paper are homogeneous, but we discuss homogeneous as well as hollow spheres. We will then generate formulas for a shape distribution of spheroids to be used outside the Rayleigh limit. Next we consider hollow spheres with a uniform distribution of porosity which can be used for calculations for arbitrary particle sizes using Mie theory in combination with effective medium approximations, by using hollow spherical shells or by using the exact method as discussed in Iatì et al. (2001).

We will calculate absorption cross sections as functions of the wavelength for the various shape distributions to study the similarities and differences between the spectra. Also we will compare the positions of absorption maxima in the spectrum with those derived from the spectral energy distributions of various astronomical sources.

2.2 Light scattering by ellipsoids small compared to the wavelength

If we want to calculate scattering by a particle that is small compared to the wavelength of the radiation inside and outside the particle, we can ignore the time variation of the incident radiation field and use the electrostatic or Rayleigh approximation. This approximation is valid when the size parameter $x = 2\pi r/\lambda \ll 1$ and $|mx| \ll 1$. Here r is a typical size of the particle (we take r to be the radius of a volume equivalent sphere), λ is the wavelength of incident radiation and m is the complex refractive index. The cross sections for scattering and absorption by an arbitrary particle in this approximation, averaged over all orientations, can be shown to be (Bohren & Huffman 1983)

$$C_{\text{abs}} = kV \text{Im}(\alpha_1 + \alpha_2 + \alpha_3), \quad (2.1)$$

$$C_{\text{sca}} = \frac{k^4 V^2}{2\pi} [|\alpha_1|^2 + |\alpha_2|^2 + |\alpha_3|^2]. \quad (2.2)$$

Here $k = 2\pi/\lambda$, V is the volume of the particle and the α_i with $i = 1, 2, 3$ are the polarizabilities per unit volume.

For an ellipsoid we have,

$$\alpha_i = \frac{m^2 - 1}{3 + 3L_i(m^2 - 1)}, \quad (2.3)$$

where L_i are geometrical factors defined by the shape of the ellipsoid. For a homogeneous sphere $L_1 = L_2 = L_3 = 1/3$ so

$$\alpha_i = \frac{m^2 - 1}{m^2 + 2}. \quad (2.4)$$

For an ellipsoid with semi-axes, a, b and c (van de Hulst 1957),

$$L_1 = \int_0^\infty \frac{abc \, ds}{2\sqrt{(s+a^2)^3(s+b^2)(s+c^2)}}, \quad (2.5)$$

while L_2 and L_3 can be found similarly by cyclic permutation of a, b and c . For all a, b and c we have $L_1 + L_2 + L_3 = 1$, so there are only two independent geometrical factors. From now on we shall use only L_1 as well as L_2 and take $L_3 = 1 - L_1 - L_2$.

When we consider shape distributions of ellipsoidal particles with the same volume, we want to average the cross sections for absorption and scattering over the particle shapes. For C_{abs} this can be done by averaging the polarizabilities. However, C_{sca} is not linearly dependent on the polarizabilities and thus, the averaging is, in general, not that easy. However, we can derive a very useful relation between the cross sections for scattering and absorption of ellipsoidal particles. For that purpose we first show the following general theorem. For every complex number z we have

$$\text{Im}(z) = -|z|^2 \text{Im}(z^{-1}). \quad (2.6)$$

The proof is very straightforward. We can write every complex number as $z = |z|e^{i\phi}$ so that $z^{-1} = |z|^{-1}e^{-i\phi}$. Therefore, $\text{Im}(z) = |z| \sin \phi = -|z|^2 \text{Im}(z^{-1})$ which completes the proof.

We now get the relation between the scattering and absorption cross sections as follows. We start by rewriting Eq. (2.3) in the form

$$\alpha_i = \frac{1}{3} \frac{1}{\beta + L_i}, \quad (2.7)$$

where

$$\beta = \frac{1}{m^2 - 1}. \quad (2.8)$$

Because each L_i is a real number, we can use Eq. (2.6) to show that

$$\text{Im}(\alpha_i) = -|\alpha_i|^2 \text{Im}(3\beta). \quad (2.9)$$

Again using Eq. (2.6) yields

$$\text{Im}(\beta) = -|\beta|^2 \text{Im}(m^2) = -\frac{\text{Im}(m^2)}{|m^2 - 1|^2}. \quad (2.10)$$

Combining Eqs. (2.9) and (2.10) we find

$$\text{Im}(\alpha_i) = \frac{3 \text{Im}(m^2)}{|m^2 - 1|^2} |\alpha_i|^2. \quad (2.11)$$

If we combine this result with Eqs. (2.1)-(2.2) we come to our final relation between the scattering and absorption cross sections

$$C_{\text{sca}} = \frac{C_{\text{abs}}}{\sigma}, \quad (2.12)$$

where

$$\sigma = \frac{6\pi}{k^3 V} \frac{\text{Im}(m^2)}{|m^2 - 1|^2}. \quad (2.13)$$

Eq. (2.12) enables us to compute C_{sca} directly from C_{abs} . Since σ is independent of the shape of the particle it can be easily verified that Eq. (2.12) still holds for a shape distribution of ellipsoids with the same volume. When $\text{Im}(m) = 0$ and $m^2 \neq 1$ both C_{abs} and σ are equal to 0. In this case we have to carefully determine the limit $\text{Im}(m) \rightarrow 0$ in Eq. (2.12) to compute C_{sca} .

It follows from Eq. (2.12) that in the Rayleigh approximation the single scattering albedo for a collection of randomly oriented homogeneous ellipsoids

$$\varpi = \frac{C_{\text{sca}}}{C_{\text{sca}} + C_{\text{abs}}} = \frac{1}{1 + \sigma}, \quad (2.14)$$

which is independent of the shape of the ellipsoids as long as their volume is the same.

2.3 Distributions of shapes, the statistical approach

The main idea behind the statistical approach is that the light scattering properties of a collection of irregularly shaped particles can be represented on average by those of a distribution of many simple shapes. The most widely used shapes for this purpose are ellipsoids. Following Bohren & Huffman (1983) we use a shape probability function, $\mathcal{P}(L_1, L_2)$, resulting in an average absorption cross section for randomly oriented ellipsoids with the same volume V

$$\langle C_{\text{abs}} \rangle = kV \int_0^1 dL_1 \int_0^{1-L_1} dL_2 \text{Im}(\alpha_1 + \alpha_2 + \alpha_3) \mathcal{P}(L_1, L_2) = kV \text{Im}(\bar{\alpha}). \quad (2.15)$$

In this equation $\bar{\alpha}$ is the average polarizability per unit volume of the shape distribution $\mathcal{P}(L_1, L_2)$, which is normalized to unity.

As already mentioned in the previous section, the scattering cross section is not linearly dependent on the α_i so the average scattering cross section, $\langle C_{\text{sca}} \rangle$, is in principle not as easy to calculate as $\langle C_{\text{abs}} \rangle$. Goncharenko et al. (1999) found an analytic solution for the averaged scattering cross section for a shape distribution quite similar to the so-called continuous distribution of ellipsoids (see next section). Although correct, the expression found by him is only applicable to his specific shape distribution. However, we can use Eq. (2.12) immediately to obtain for the averaged scattering cross section

$$\langle C_{\text{sca}} \rangle = \frac{\langle C_{\text{abs}} \rangle}{\sigma} = \frac{kV}{\sigma} \text{Im}(\bar{\alpha}). \quad (2.16)$$

Thus, when for a certain shape distribution of ellipsoids $\bar{\alpha}$ has been found, we can readily compute $\langle C_{\text{abs}} \rangle$ and $\langle C_{\text{sca}} \rangle$.

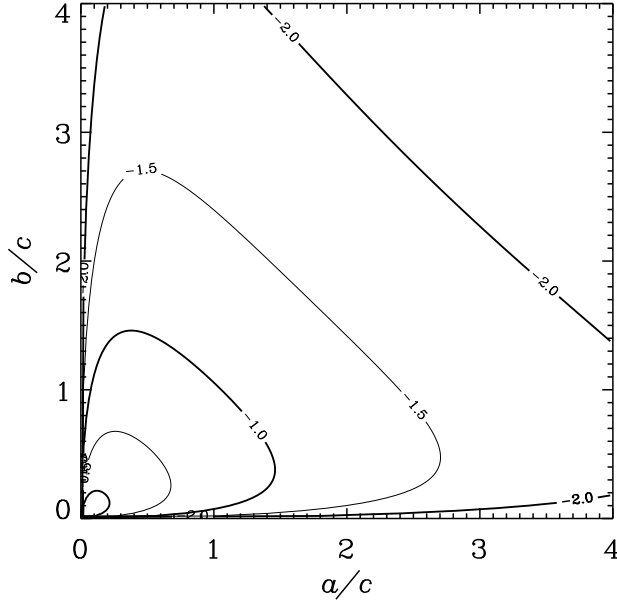


Figure 2.1: Contour plot of the logarithm of the CDE shape distribution expressed in a/c and b/c , i.e. $\log \{\mathcal{P}(a/c, b/c)\}$, in steps of 0.5

2.3.1 Continuous Distribution of Ellipsoids (CDE)

As the most simple example of a distribution $\mathcal{P}(L_1, L_2)$, Bohren & Huffman (1983) describe the so called Continuous Distribution of Ellipsoids (CDE) which is just $\mathcal{P}(L_1, L_2) = 2$. Using this distribution the average polarizability per unit volume is given by

$$\bar{\alpha} = \int_0^1 dL_1 \int_0^{1-L_1} dL_2 (\alpha_1 + \alpha_2 + \alpha_3) \mathcal{P}(L_1, L_2) = 2 \frac{m^2}{m^2 - 1} \ln m^2 - 2. \quad (2.17)$$

Here, and elsewhere in this paper, $\ln(z)$ denotes the principal value of the logarithm of z . Using this and Eqs. (2.15)-(2.16) we have for the average scattering and absorption cross sections

$$\langle C_{\text{abs}} \rangle = 2kV \operatorname{Im} \left(\frac{m^2}{m^2 - 1} \ln m^2 \right), \quad (2.18)$$

and

$$\langle C_{\text{sca}} \rangle = \frac{k^4 V^2 |m^2 - 1|^2}{3\pi \operatorname{Im}(m^2)} \operatorname{Im} \left(\frac{m^2}{m^2 - 1} \ln m^2 \right). \quad (2.19)$$

In the non-absorbing case we have to be careful when calculating the averaged scattering cross section directly from the averaged absorption cross section. By carefully taking

the limit $\text{Im}(m) \rightarrow 0$ we can show that for real values of m we have

$$\langle C_{\text{sca}} \rangle = \lim_{\text{Im}(m) \rightarrow 0} \frac{\langle C_{\text{abs}} \rangle}{\sigma} = \frac{k^4 V^2}{3\pi} (m^2 - 1 - \ln m^2). \quad (2.20)$$

Because the geometrical factors have no direct physical meaning, we would like to express the shape distribution in terms of the semi-axes of the ellipsoid a , b and c . This would also give a clearer picture of what the particle shapes in the distribution look like. Since we are only interested in the shape of the particles, we can express the distribution in terms of (a/c) and (b/c) and by considering the Jacobian of the transformation $dL_1 dL_2 \rightarrow d(a/c) d(b/c)$ we find for the CDE distribution expressed in (a/c) and (b/c)

$$\mathcal{P}(a/c, b/c) = \left| \frac{dL_1}{d(a/c)} \frac{dL_2}{d(b/c)} - \frac{dL_1}{d(b/c)} \frac{dL_2}{d(a/c)} \right|. \quad (2.21)$$

The derivatives with respect to (a/c) and (b/c) can be taken inside the integrals in Eq. (2.5), so we are left with four integrals which can be calculated numerically. Fig. 2.1 shows the logarithm of $\mathcal{P}(a/c, b/c)$. It can be shown that the distribution goes to infinity for (a/c) and $(b/c) \rightarrow 0$, so for extremely elongated needles. It has been checked that by inverting the coordinate transformation back to a distribution in the L_i 's, we get $\mathcal{P}(L_1, L_2) = 2$.

2.3.2 Continuous Distribution of Spheroids (CDS)

Outside the Rayleigh limit it is more difficult to calculate light scattering properties of tri-axial ellipsoids than of spheroids. Therefore we would like to use spheroids in the statistical approach. The cross sections of shape distributions of randomly oriented spheroids with moderate aspect ratios can be calculated outside the Rayleigh limit quite well and with sufficient accuracy for most purposes (see Min et al. 2003a).

Spheroids are ellipsoids with two equal semi-axes. We take $L = L_2$ and $L_1 = L_3 = (1 - L)/2$ (this means $a = c$). For spheroids Eq. (2.5) gives (see van de Hulst 1957)

$$L = \begin{cases} \frac{1 - e^2}{e^2} \left(-1 + \frac{1}{2e} \ln \left(\frac{1 + e}{1 - e} \right) \right), & e^2 = 1 - \frac{a^2}{b^2}, \quad \text{Prolates,} \\ \frac{1}{e^2} \left(1 - \frac{\sqrt{1 - e^2}}{e} \arcsin(e) \right), & e^2 = 1 - \frac{b^2}{a^2}, \quad \text{Oblates.} \end{cases} \quad (2.22)$$

Here a/b is the aspect ratio. For prolate spheroids $a/b < 1$, while for oblate spheroids $a/b > 1$. So the b -axis coincides with the axis of rotation and we have for prolate spheroids $0 < L < 1/3$, for oblate spheroids $1/3 < L < 1$ and for spheres $L = 1/3$.

In line with the basic idea of the CDE, the CDS averages over all possible shapes by integrating C_{sca} and C_{abs} over L with $0 < L < 1$ and with equal probability for all L ($\mathcal{P}(L) = 1$). We will refer to this distribution as the *unlimited CDS*, because in the next sections we will also use limited versions of the CDS where we limit the domain

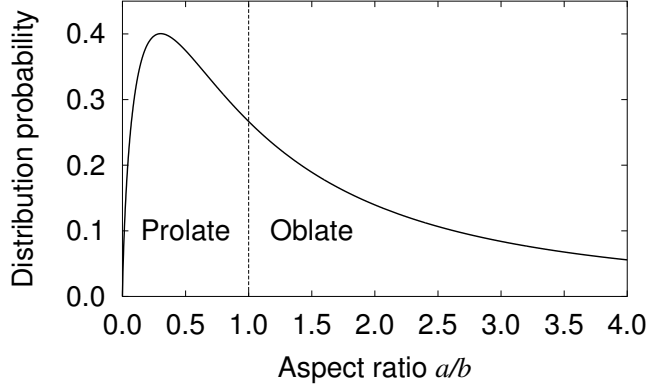


Figure 2.2: The shape distribution in a/b of the unlimited CDS as defined by Eq. (2.25).

of aspect ratios used. We now find for the average polarizability per unit volume of randomly oriented spheroids with the same volume in the unlimited CDS

$$\bar{\alpha} = \int_0^1 (2\alpha_1 + \alpha_2) \mathcal{P}(L) dL = \frac{1}{3} \ln m^2 + \frac{4}{3} \ln \left(\frac{m^2 + 1}{2} \right). \quad (2.23)$$

This yields the average scattering and absorption cross sections employing Eqs. (2.15)-(2.16). For the non-absorbing case we can again take the limit for $\text{Im}(m) \rightarrow 0$. This results for real values of m in the average scattering cross section

$$\langle C_{\text{sca}} \rangle = \lim_{\text{Im}(m) \rightarrow 0} \frac{\langle C_{\text{abs}} \rangle}{\sigma} = \frac{k^4 V^2}{18\pi} \frac{(m^2 - 1)^2 (5m^2 + 1)}{m^2 (m^2 + 1)}. \quad (2.24)$$

To do calculations for spheroids outside the Rayleigh limit we need the unlimited CDS expressed in a/b . Using Eq. (2.22), we can again calculate the Jacobian of this transition. The result is that the probability for a particle shape with a certain aspect ratio a/b in the unlimited CDS, $\mathcal{P}(a/b) = dL/d(a/b)$, is given by

$$\frac{dL}{d(a/b)} = \begin{cases} \frac{\sqrt{1-e^2}}{2e^5} \left((3-e^2) \ln \left(\frac{1+e}{1-e} \right) - 6e \right), & \text{Prolates} \\ \frac{1-e^2}{e^5} \left((3-2e^2) \arcsin(e) - 3e \sqrt{1-e^2} \right), & \text{Oblates} \end{cases} \quad (2.25)$$

This distribution is shown in Fig. 2.2 and can be used to apply the statistical approach outside the Rayleigh limit. It has been verified that this distribution has the same shape as the CDE along the line $a/c = 1$ in Fig. 2.1.

2.3.3 Uniform Distribution of Spheroids (UDS)

Another shape distribution we can consider is the Uniform Distribution of Spheroids. This distribution actually consists of a uniform distribution of oblate spheroids with

$1 \leq a/b < \xi$ and a uniform distribution of prolate spheroids with $1 \leq b/a < \xi$, where all particles have the same volume, $\xi > 1$ is the maximum aspect ratio for the oblate part of the distribution and $1/\xi$ is the minimum aspect ratio of the prolate part. Thus we give equal weights to all prolate and oblate spheroidal shapes with aspect ratios between $1/\xi$ and ξ . Because the geometrical factor L is a complicated function of the aspect ratio (Eq. (2.22)), it is not possible to find an analytic expression for the average polarizability per unit volume for this distribution. However, for a given ξ it is straightforward to perform the shape averaging of the cross sections numerically.

2.3.4 Distribution of Hollow Spheres

In most applications of light scattering the particles are assumed to be homogeneous. This can be a good approximation in some cases but in a lot of applications the particles are inhomogeneous in composition or porous. We will study here porous particles. This means that we consider particles with a material having a refractive index m with vacuum inclusions having a refractive index equal to 1.

The simplest porous particle is a hollow spherical shell. Since for a sphere (homogeneous or hollow) the polarizability per unit material volume is isotropic we have $\alpha_1 = \alpha_2 = \alpha_3 = \alpha$. The polarizability per unit *material* volume is (van de Hulst 1957, chap. 6)

$$\alpha = \frac{(m^2 - 1)(2m^2 + 1)}{(m^2 + 2)(2m^2 + 1) - 2(m^2 - 1)^2 f}. \quad (2.26)$$

In this equation f is the fraction of the total volume of the sphere occupied by the inclusion. The total material volume of a hollow spherical shell with outer radius r is $V = \frac{4}{3}\pi r^3(1 - f)$. Using Eq. (2.1) we find

$$C_{\text{abs}} = kV \text{Im}(3\alpha) = 4\pi r^3 k \text{Im} \left(\frac{(1 - f)(m^2 - 1)(2m^2 + 1)}{(m^2 + 2)(2m^2 + 1) - 2(m^2 - 1)^2 f} \right). \quad (2.27)$$

The next step we want to take is applying the statistical approach to hollow spheres. We can do this by averaging over the volume fraction occupied by the inclusion. If we average 3α over the entire range of volume fractions $f = [0, 1]$, we get

$$\bar{\alpha} = \int_0^1 (3\alpha) df = \frac{6m^2 + 3}{2m^2 - 2} \ln \left(\frac{(2m^2 + 1)(m^2 + 2)}{9m^2} \right). \quad (2.28)$$

We will refer to this distribution as the *Distribution of Hollow Spheres*. The average absorption cross section is given by

$$\langle C_{\text{abs}} \rangle = kV \text{Im}(\bar{\alpha}), \quad (2.29)$$

where V is the material volume. Since all particles used for the averaging have the same material volume, the particles with higher values of f must have a larger outer radius than the particles with smaller values of f . Consequently, the average surface area for the distribution of hollow spheres will be significantly larger than that of a homogeneous sphere with the same material volume. The outer radius of a hollow sphere with material

volume V is a factor $(1 - f)^{-1/3}$ larger than that of a homogeneous sphere with the same material volume. The surface area of such a hollow sphere is, therefore, a factor $(1 - f)^{-2/3}$ larger. Thus the average surface area of a particle in the distribution of hollow spheres divided by that of a homogeneous sphere with the same material volume is

$$\frac{\langle A_{\text{Hollow Spheres}} \rangle}{A_{\text{Hom. Sphere}}} = \int_0^1 (1 - f)^{-\frac{2}{3}} df = 3. \quad (2.30)$$

To calculate the scattering cross section we cannot use Eq. (2.12) since it is not valid for hollow spheres. Instead we would have to average $|\alpha|^2$ over the range $f = [0, 1]$ numerically.

A hollow spherical shell might seem quite an artificial choice for a porous particle. However, we will show that there is a strong similarity between porous spheres with multiple, randomly located vacuum inclusions and hollow spherical shells. The usual way of dealing with inhomogeneities is through an effective medium theory. The main idea behind all these theories is that, when the inclusions are isotropically distributed in the particle, the electromagnetic wave effectively encounters an average medium. We use the Maxwell-Garnett approximation (see e.g. Bohren & Huffman 1983). The main assumptions in this approximation are: 1) that the sizes of the inclusions are much smaller than the wavelength in the host material and in the inclusions and 2) that the inclusions are isolated, i.e. they scatter independently. Although these assumptions are made in the derivation of the approximation, many people found that the results can also be quite accurate when the requirements are not fulfilled (see e.g. Chýlek et al. 2000). For a study of the validity of different effective medium approximations see Kolokolova & Gustafson (2001). In our case we automatically fulfill requirement 1), since the particles containing the inclusions are in the Rayleigh limit ($x \ll 1$, $|m.x| \ll 1$). In order for the inclusions to scatter independently, they must be far enough apart. However, when there is only one inclusion, both requirements are immediately fulfilled. Therefore, we can show that the polarizability per unit volume of a porous sphere, derived using the Maxwell-Garnett approximation, is exactly the same as the polarizability of a hollow spherical shell. For this purpose we first note that the effective refractive index, m_{eff} , given by the Maxwell-Garnett approximation for spherical inclusions in a material is

$$m_{\text{eff}}^2 = m^2 \left(1 + \frac{3f}{\frac{1 + 2m^2}{1 - m^2} - f} \right). \quad (2.31)$$

Here the refractive index of the inclusions is 1. If we now use this refractive index in the calculation for the polarizability per unit volume of a sphere, we have to keep in mind that because we placed a volume fraction f of inclusions inside the particle, we decreased the particle material volume by a factor $(1 - f)$. Therefore, applying Eq. (2.31) to Eq. (2.4) results in

$$\alpha = \frac{(1 - f)(m^2 - 1)(2m^2 + 1)}{(m^2 + 2)(2m^2 + 1) - 2(m^2 - 1)^2 f}, \quad (2.32)$$

but because we want α to be the polarizability per unit material volume, we have to divide this polarizability by $(1 - f)$ to account for the missing volume fraction of inclusions. In this way the correct polarizability per unit material volume of a porous sphere becomes

$$\alpha = \frac{(m^2 - 1)(2m^2 + 1)}{(m^2 + 2)(2m^2 + 1) - 2(m^2 - 1)^2 f}. \quad (2.33)$$

This is indeed the same equation for the polarizability per unit material volume as Eq. (2.26). This means that in the Rayleigh domain a hollow spherical shell is a good approximation to a porous sphere for the absorption and scattering cross sections as long as f is sufficiently small to ensure independent scattering of the separate inclusions. Thus in our averaging over f over the entire range $[0, 1]$ we have hollow or porous spheres for small values of f and hollow spheres for large values of f . Nevertheless, we will still refer to this distribution as the distribution of hollow spheres.

2.4 Spectral features

To analyze the wavelength dependence of the cross sections we need the wavelength dependent refractive index of the material. Fortunately, the wavelength dependence of the refractive index can be modeled in such a way that we can study the general features. We use the Lorentz oscillator model to obtain the refractive index as a function of wavelength (see e.g. Bohren & Huffman 1983). This model considers the refractive index due to harmonic lattice vibrations. The eigenfrequency of the harmonic oscillator is ω_0 . If there is only one eigenfrequency (resonance) this gives a refractive index

$$m^2 = m_0^2 + \frac{f\omega_p^2}{\omega_0^2 - \omega^2 - i\gamma\omega}. \quad (2.34)$$

In this equation m_0 is the real valued refractive index for $\omega \rightarrow \infty$, f is the oscillator strength of the feature, ω_p is the plasma frequency, ω is the frequency of incident radiation and γ is a damping factor. If ω is expressed in wavenumbers, we can express Eq. (2.34) in wavelengths by using $\omega = \lambda^{-1}$. If there are multiple eigenfrequencies, m^2 is a sum over different values of f , ω_0 and γ . This model is used quite successfully, for example, for obtaining the refractive index from reflectance data.

2.4.1 Shape dependence of spectral features

To analyze the dependence of the shape of the absorption spectrum on the shape of the particles, we first analyze in more detail the dependence of $\text{Im}(\bar{\alpha})$ on the refractive index. Because the refractive index is a complex number, we can represent each shape distribution uniquely by a contour plot with $\text{Re}(m)$ and $\text{Im}(m)$ on the x and y axes, respectively, and values of $\text{Im}(\bar{\alpha}) = \langle C_{\text{abs}} \rangle / (kV)$ in the contours. The contour plots in Fig. 2.3 show this for the different shape distributions of section 2.3. For homogeneous spherical particles we notice that $\text{Im}(\bar{\alpha})$ shows a rapid increase as m approaches $i\sqrt{2}$, as was expected from Eq. (2.4). For all other distributions considered in Fig. 2.3 we do not

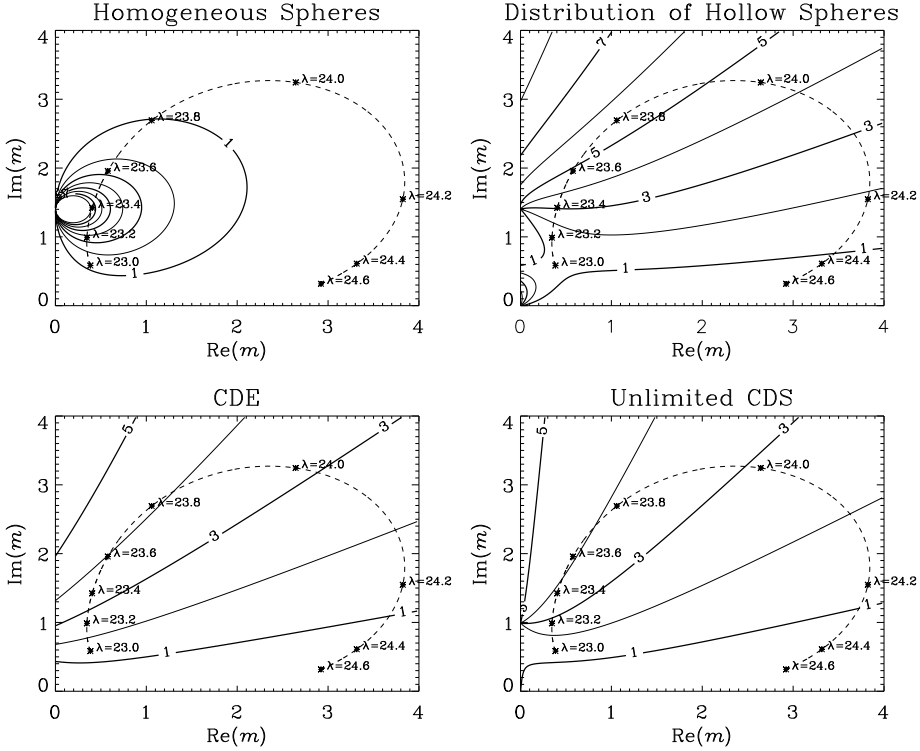


Figure 2.3: The imaginary part of the average polarizability per unit material volume of four distributions of particle shapes (solid contours) as functions of the real and imaginary part of the refractive index. The increment between two contours is unity. CDE stands for Continuous Distribution of Ellipsoids, CDS denotes a Continuous Distribution of Spheroids. The dashed curves represent the values of the refractive index given by the single oscillator model for various values of the wavelength in μm (indicated by the crosses). Here $m_0 = 1.63$, $f = 1$, $\omega_p = 218.3 \text{ cm}^{-1}$, $\omega_0 = 415.6 \text{ cm}^{-1}$ ($\lambda_0 = 24.1 \mu\text{m}$) and $\gamma = 5.9 \text{ cm}^{-1}$. These parameters correspond to the best fit that can be obtained by applying a Lorentz oscillator model to a particular feature in the reflectivity spectrum of forsterite (Servoin & Piriou 1973)

see this behavior. These distributions all show a somewhat similar behavior, namely, in general, increasing $\text{Im}(\bar{\alpha})$ for increasing $\text{Im}(m)$ and decreasing $\text{Re}(m)$. For the unlimited CDS $\text{Im}(\bar{\alpha})$ is undefined at $m = i$ since in Eq. (2.23) $\text{Im}(\ln z)$ is undefined for $z \rightarrow 0$. In particular we can see by using Eq. (2.23) for $\text{Re}(m) = 0$ that we have

$$\text{Im}(\bar{\alpha}) = \begin{cases} \frac{1}{3}\pi, & \text{Im}(m) < 1, \\ \text{undefined}, & \text{Im}(m) = 1. \\ \frac{5}{3}\pi, & \text{Im}(m) > 1. \end{cases} \quad (2.35)$$

Similarly, Eq. (2.28) shows that the imaginary part of the average polarizability per unit material volume for the distribution of hollow spheres is undefined at $m = i\sqrt{2}$ and

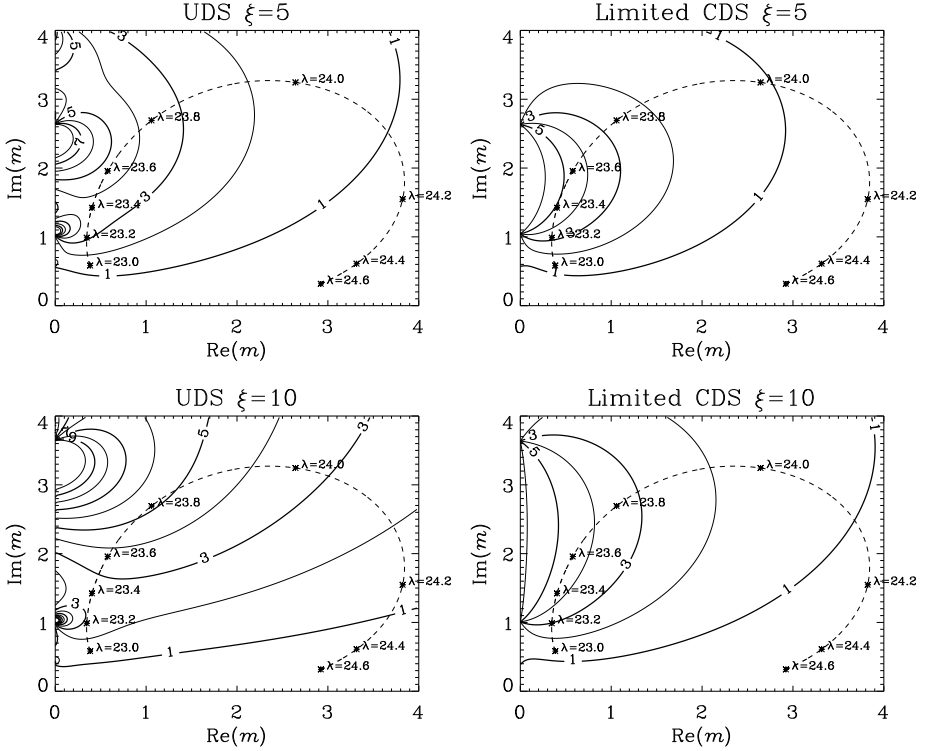


Figure 2.4: Similar to Fig. 2.3 but with the UDS, denoting a Uniform Distribution of Spheroids, and limited CDS distributions integrated between $1/5 < a/b < 5$ (upper panels) and $1/10 < a/b < 10$ (lower panels).

$m = i\sqrt{1/2}$ in accordance with Fig. 2.3.

Overplotted in Fig. 2.3 (the dashed curve) is the refractive index for various values of the wavelength for a certain choice of the parameters in Eq. (2.34). We see that for this choice of parameters a shift of the maximum value of $\text{Im}(\alpha)$ from $\lambda \approx 23.4 \mu\text{m}$ for homogeneous spherical particles towards $\lambda \approx 23.8 \mu\text{m}$ for the distribution of hollow spheres occurs.

We now try to find out if the shift of the maximum of $\text{Im}(\bar{\alpha})$ when going from homogeneous spheres towards non-spherical or hollow particles is generally towards longer wavelengths. To do this we first derive from Eq. (2.34) that

$$\lim_{\omega \rightarrow 0} m = \sqrt{m_0^2 + f\omega_p^2/\omega_0^2}, \quad (2.36)$$

and

$$\lim_{\omega \rightarrow \infty} m = m_0. \quad (2.37)$$

Since m_0, f, ω_p and ω_0 are all real and positive, we first notice that both limits are real

and the refractive index for $\omega = 0$ is always larger than the refractive index for $\omega = \infty$. Secondly we notice that the curve for m as function of ω never crosses itself. We can see this by solving $m(\omega) = m(\omega')$ using Eq. (2.34). This equation has two solutions; $\omega = \omega'$ and $\omega = -i\gamma - \omega'$. Since γ is real and positive, the second solution is unphysical because it would require ω to be complex or negative. Thirdly, from the quadratic nature of Eq. (2.34) it is quite easy to show that for every value of $\text{Re}(m)$ there are at maximum two solutions for ω that are real and positive. Combining these three facts, we see that we always run along the dashed curve in Fig. 2.3 counterclockwise with increasing ω , so clockwise with increasing λ , when we look into the paper. When we now study the contours in Fig. 2.3 closely, we see that this means that, going from homogeneous spheres towards non-spherical or hollow particles, the maximum of $\text{Im}(\bar{\alpha})$ (and therefore of $\langle C_{\text{abs}} \rangle$) shifts towards longer wavelengths. This is confirmed by results of calculations for various other values of the parameters in Eq. (2.34). A shift towards longer wavelengths compared to spherical particles was found in the infrared absorption cross sections of ammonia ice crystals with tetrahedral shapes (West et al. 1989) and with spheroidal shapes (Mishchenko 1991).

Outside the Rayleigh limit numerical calculations of light scattering properties of spheroids are limited to certain ranges of sizes and aspect ratios. Therefore, it is interesting to study the effects of limiting the aspect ratios in the distributions. The UDS was already limited by the maximum and minimum aspect ratios, ξ and $1/\xi$. For the CDS we can do something similar by using Eq. (2.25). When we limit the aspect ratio in the CDS this leads to

$$\begin{aligned} \bar{\alpha} &= \int_{L_{\min}}^{L_{\max}} \frac{2\alpha_1 + \alpha_2}{L_{\max} - L_{\min}} dL \\ &= \frac{1}{3(L_{\max} - L_{\min})} \left[\ln \left(\frac{1 + L_{\max}(m^2 - 1)}{1 + L_{\min}(m^2 - 1)} \right) \right. \\ &\quad \left. + 4 \ln \left(\frac{1 + m^2 + L_{\min}(1 - m^2)}{1 + m^2 + L_{\max}(1 - m^2)} \right) \right]. \end{aligned} \quad (2.38)$$

where L_{\min} is the geometrical factor with $a/b = \xi^{-1}$ and L_{\max} is the geometrical factor with $a/b = \xi$ (see Eq. (2.22)). We will refer to this distribution as a *limited CDS*. This distribution can be used outside the Rayleigh limit by numerically integrating and using the distribution as defined by Eq. (2.25). The results for a UDS with $\xi = 5$, a UDS with $\xi = 10$, a limited CDS with $\xi = 5$ and a limited CDS with $\xi = 10$ are plotted in Fig. 2.4. We see that there are differences between the contours for the unlimited CDS and the two cases of limited CDS. We also notice that the contours for the UDS with $\xi = 5$ and with $\xi = 10$ do not look as simple as the contours in Fig. 2.3. Nevertheless, for a large area in the plots, the general behavior of $\text{Im}(\bar{\alpha})$ is similar to that of the contours in Fig. 2.3. We also see that the shift of the maximum of $\text{Im}(\alpha)$ towards longer wavelengths is stronger for the two cases of UDS than for the two cases of limited CDS. This is due to the fact that the limited CDS gives less weight to the more extreme shapes (see Fig. 2.2).

As an example of the shape of the spectral features of $\langle C_{\text{abs}} \rangle$ we used the theoretical frequency dependence of the refractive index given by Eq. (2.34) with the same values of the parameters as in Fig. 2.3. We calculated the position of the maximum of $\langle C_{\text{abs}} \rangle$

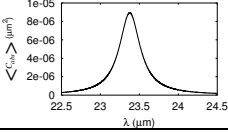
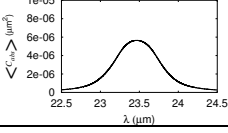
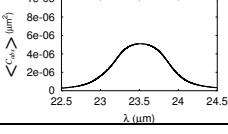
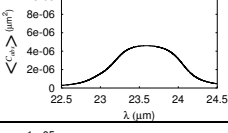
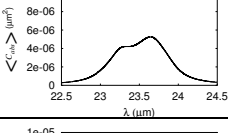
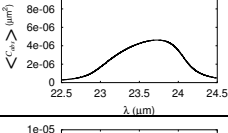
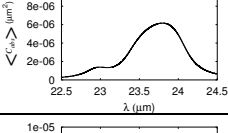
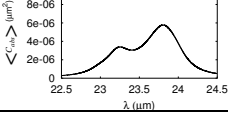
Name	Typical feature shape	Characteristics
Homogeneous Spheres		$\lambda_{\max} = 23.38 \mu\text{m}$ FWHM= 0.32 μm
Limited CDS $\xi = 5$		$\lambda_{\max} = 23.47 \mu\text{m}$ FWHM= 0.67 μm
Limited CDS $\xi = 10$		$\lambda_{\max} = 23.52 \mu\text{m}$ FWHM= 0.80 μm
Unlimited CDS		$\lambda_{\max} = 23.59 \mu\text{m}$ FWHM= 0.97 μm
UDS $\xi = 5$		$\lambda_{\max} = 23.65 \mu\text{m}$ FWHM= 0.81 μm
CDE		$\lambda_{\max} = 23.73 \mu\text{m}$ FWHM= 1.01 μm
Distribution of Hollow Spheres		$\lambda_{\max} = 23.80 \mu\text{m}$ FWHM= 0.74 μm
UDS $\xi = 10$		$\lambda_{\max} = 23.81 \mu\text{m}$ FWHM= 0.90 μm

Table 2.1: The average absorption cross section (in μm^2) for different shape distributions of particles with the same material volume. The radius of the material volume equivalent sphere is $r = 0.01\mu\text{m}$. The refractive index as a function of the wavelength is determined by the Lorentz oscillator model with parameter values as in Fig. 2.3. The distributions are ordered according to the position of the maximum. Also given is the Full Width at Half Maximum (FWHM).

and the Full Width at Half Maximum (FWHM) of $\langle C_{\text{abs}} \rangle$ as a function of wavelength. The results are summarized in Table 2.1. We see that the most extreme shifts with respect to homogeneous spherical particles are produced by a UDS with $\xi = 10$ and the distribution of hollow spheres. The broadest features are produced by the CDE and the unlimited CDS, because they cover the broadest range of possible shapes. The wavelength shifts and FWHM's presented in Table 2.1 are fairly general. Notice in Table 2.1 that for the UDS with $\xi = 5$ and with $\xi = 10$ as well as for the distribution of hollow spheres, we have two local maxima. This can be understood when we look at the contours for the distribution of hollow spheres in Fig. 2.3 and the contours for the UDS with $\xi = 5$ and with $\xi = 10$ in Fig. 2.4. We see that local maxima of the imaginary parts of the polarizabilities per unit volume as functions of the refractive index occur for these distributions, resulting in local maxima of the average absorption cross sections as functions of the wavelength.

For calculations of $\langle C_{\text{abs}} \rangle$ of shape distributions outside the Rayleigh limit we are restricted to the use of UDS, limited CDS or hollow spheres. However, calculations for spheroids with aspect ratios of 10 are very time consuming and not possible for all size parameters. Absorption cross sections for a shape distribution of hollow spheres can always be calculated quite fast using an effective medium approximation in combination with Mie theory or exact calculations for a shape distribution of hollow spherical shells. We should note here that the similarity of the absorption spectra in the Rayleigh domain for various shape distributions does not guarantee a similar behavior outside the Rayleigh limit.

2.4.2 An example: Forsterite (20-40 μm)

As an example we use the various shape distributions of the previous sections to calculate the wavelength dependence of the average absorption cross section of small crystalline forsterite particles in the region 20-40 μm . The pure magnesium silicate forsterite (Mg_2SiO_4) is end member of the olivine family ($\text{Mg}_{2-x}\text{Fe}_{2-2x}\text{SiO}_4$, with x between 0 and 1), and is e.g. observed in (i) the disks surrounding binary red-giant stars (Molster et al. 1999b), (ii) in the circumstellar dust disks around young intermediate mass pre-main-sequence Herbig Ae/Be stars, which are believed to be sites of on-going planet formation (see e.g. Waters & Waelkens 1998; Bouwman et al. 2001), (iii) in comet Hale-Bopp (Crovisier et al. 1997; Bouwman et al. 2003), and (iv) in interplanetary dust particles (Bradley et al. 1999). The mass absorption coefficient of small forsterite particles has many narrow resonances in between about 10 and 40 μm , due to stretching and bending modes within the SiO_4 tetrahedron, but it also exhibits relatively strong features at longer wavelength. For the objects mentioned above, the characteristic dust temperatures are often such that the dust emits most effectively in the wavelength interval between ~ 20 to 40 μm , which is why we focus our attention on this spectral range.

We use the refractive index values for the three crystallographic axes as provided by Servoin & Piriou (1973). We then calculate the shape averaged mass absorption

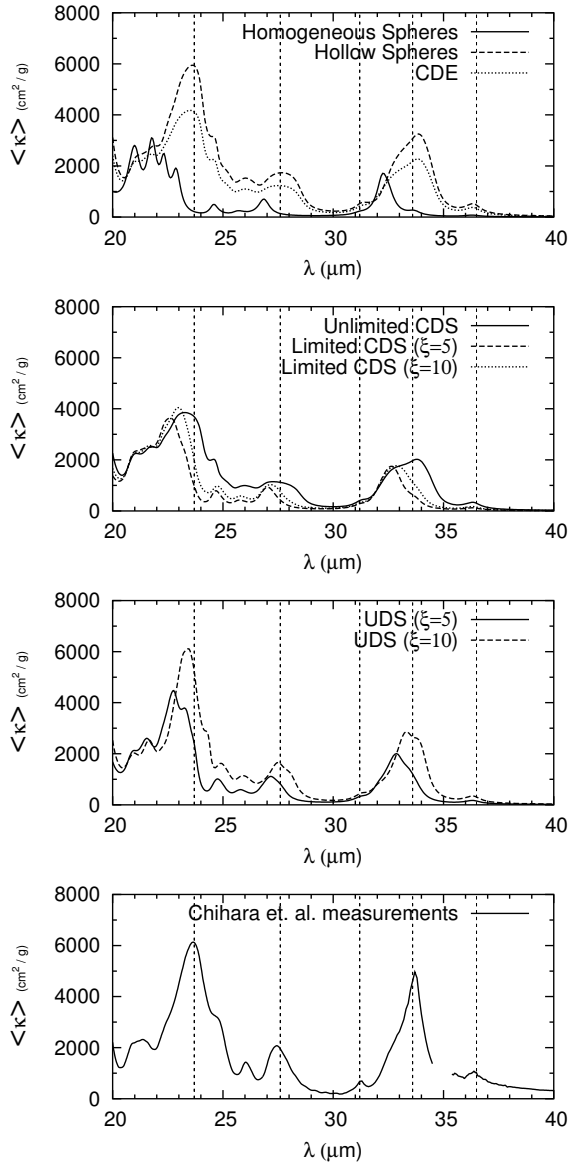


Figure 2.5: The upper three panels show the average mass absorption coefficients of small crystalline forsterite particles for different shape distributions. The lower panel shows the average mass absorption coefficients of small forsterite grains as measured in the laboratory by Chihara et al. (2001). The dashed vertical lines show the positions of features attributed to forsterite as derived from spectral energy distributions of many astronomical objects. These measured peak locations are at 23.7, 27.6, 31.2, 33.6 and 36.5 μm (Molster et al. 2002a).

coefficient $\langle \kappa \rangle$ for particles with material volume V from,

$$\langle \kappa \rangle = \frac{\langle C_{\text{abs}} \rangle}{\rho V} = \frac{k}{\rho} \text{Im}(\bar{\alpha}), \quad (2.39)$$

where ρ is the material density of the particle. For forsterite $\rho = 3.33 \text{ g cm}^{-3}$. In Eq. (2.39) we used Eqs. (2.15) and (2.29) to show that in the Rayleigh limit $\langle \kappa \rangle$ does not depend on the sizes of the individual grains. Since $\langle \kappa \rangle$ and $\langle C_{\text{abs}} \rangle$ as functions of λ differ by a constant factor only, we will call their graphical representations as curves the absorption spectrum in both cases. We average the shape averaged mass absorption coefficients over the three different crystallographic axes and call the result the average mass absorption coefficient $\langle \kappa \rangle$. The resulting absorption spectrum is shown in Fig. 2.5 together with measurements of the mass absorption coefficient of small forsterite grains by Chihara et al. (2001). We see that the CDE, unlimited CDS and distribution of hollow spheres all show more or less the same shape of the absorption spectrum. The average mass absorption coefficients of the distribution of hollow spheres are significantly higher than that of CDE and unlimited CDS for almost all values of the wavelength. This is a result of the larger total surface area of this distribution. We notice that the number of peaks in Fig. 2.5 is significantly different for non-spherical and homogeneous spherical particles. For the UDS with $\xi = 10$ the positions of the peaks are more or less the same as for the CDE, unlimited CDS and the distribution of hollow spheres but the shape of the features is slightly sharper. For the UDS with $\xi = 5$ the peak positions are in-between those for CDE and homogeneous spheres. For the limited CDS we see that even with aspect ratios up to 10 we cannot get a good approximation for the results obtained for the unlimited CDS. When we compare the shapes, heights and positions of the features with the experimental data from Chihara et al. (2001), we see that of the shape distributions considered here, the UDS with $\xi = 10$ and the distribution of hollow spheres best reproduce the data.

Also plotted in Fig. 2.5 (the dashed vertical lines) are positions of the features that were found in the spectral energy distributions of a large sample of stars with surrounding dust, after subtracting a continuum, and that were assigned to forsterite (Molster et al. 2002a). We see that the maxima found in the average mass absorption coefficient for homogeneous spheres do not correspond to the positions of features derived from the spectral energy distributions. However for the CDE, unlimited CDS, the hollow spheres and for the UDS with $\xi = 10$, the positions of the maxima do match the observed positions. This means that for the interpretation of infrared spectra of these stars the use of these distributions provide a better fit than homogeneous spheres. From this we can conclude that both the forsterite particles in the measurements of Chihara et al. (2001) and the particles in circumstellar dust found by Molster et al. (2002a) cannot be considered to be homogeneous spheres.

From the strong similarity between the absorption spectra in Fig. 2.5 for CDE, unlimited CDS, UDS ($\xi = 10$) and the distribution of hollow spheres we can conclude that it can be very difficult, if not impossible, to distinguish between particles with non-spherical shapes and hollow spheres on the basis of infrared spectra. Although the first three distributions are significantly different, they all consist of ellipsoids, so the similarity of the average absorption cross sections might not be very surprising. However, the

similarity for the distribution of hollow spheres is a surprising result which is a strong encouragement for the use of the statistical approach since it seems that quite different shape departures from homogeneous spheres result in most cases in more or less the same shape of the wavelength dependence of $\langle\kappa\rangle$. This suggests that an ensemble of irregularly shaped particles will also result in this shape of the absorption spectrum. This is in agreement with the similarity of the positions of the maxima in $\langle\kappa\rangle$ with the positions of features derived from observations. For calculations of scattering and absorption characteristics of small particles it is much easier to do calculations for hollow spheres than for non-spherical particles with an extreme shape distribution. Therefore we recommend to use the distribution of hollow spheres to get a quick impression of non-sphericity effects in infrared spectra. Notice that the average mass absorption coefficient of volume equivalent homogeneous non-spherical particles is roughly 50 percent higher than that of homogeneous spheres, and that the $\langle\kappa\rangle$ of hollow spheres is even about a factor of two more than that of homogeneous spheres. The latter is essentially the result of the increase in average surface area of hollow grains relative to homogeneous spheres (see Eq. (2.30)). This implies that mass determinations of (in this case) forsterite material in e.g. Herbig Ae/Be objects using classical Mie calculations likely overestimate the observed mass of this material by about a factor of two.

2.5 Conclusions

In this article we have investigated shape effects in scattering and absorption by randomly oriented particles small compared to the wavelength. We first derived a relation between the average absorption cross section and the average scattering cross section of an arbitrary shape distribution of randomly oriented ellipsoidal particles with the same volume. With this relation it is possible to calculate the average scattering cross section from the average absorption cross section of this shape distribution. We have derived explicit expressions for the average polarizability per unit material volume of a continuous distribution of spheroids as well as for a distribution of hollow spheres as functions of the refractive index of the particles. With these expressions it is possible to calculate the average absorption cross sections of these distributions.

We have shown that there is a strong similarity between the polarizability per unit material volume as a function of refractive index for shape distributions with elongated and flattened ellipsoids and spheroids and a distribution of hollow spherical shells. This similarity in polarizability as a function of refractive index means that there is also a strong similarity in the average absorption cross sections as functions of the wavelength. These results are a strong encouragement for the use of the statistical approach in the interpretation of infrared spectra since it suggests that the shape of the absorption spectrum is, to a certain degree, independent of the exact shapes of the individual particles as long as we average over a wide range of shape parameters. However, this also means that it can be very difficult, if not impossible, to distinguish between different non-spherical shapes of the particles by just using infrared spectroscopy.

Using theoretical and experimental data of the wavelength dependence of the refractive index we have studied absorption spectra of homogeneous spherical particles,

several shape distributions of ellipsoidal and spheroidal particles and of a distribution of hollow spheres. Using the Lorentz oscillator model for the refractive index as a function of wavelength we showed that, for all shape distributions considered, the positions of spectral features in the average absorption cross sections shift towards longer wavelengths (by about $1\text{--}2\ \mu\text{m}$) when we go from homogeneous spherical particles to a shape distribution of non-spherical particles or hollow spheres. This should be kept in mind when identifying mineral species in astronomical objects. Also, the distributions of non-spherical and hollow spherical particles have a larger average mass absorption coefficient, implying that mass determinations assuming homogeneous spheres overestimate the mass of the species investigated. For the crystalline forsterite material investigated in this paper this may amount to about a factor of two.

A great advantage of the distribution of hollow spheres is that it can be used fairly easily outside the Rayleigh domain. However, we should note here that the similarity between the absorption spectra of spheroids and hollow spheres in the Rayleigh limit does not guarantee a similar behavior for particles large compared to the wavelength.

Acknowledgments

We are indebted to C. V. M. van der Mee for accurate checks and simplifications of the theory. Comments on an earlier version of this paper by M. I. Mishchenko are gratefully acknowledged.

3

Absorption and scattering properties of arbitrarily shaped particles in the Rayleigh domain

A rapid computational method and a theoretical foundation for the statistical approach

*M. Min, J. W. Hovenier, C. Dominik, A. de Koter, and M. A. Yurkin
to be submitted*

Abstract

We provide a theoretical foundation for the statistical approach for computing the absorption properties of particles in the Rayleigh domain. We present a general method based on the Discrete Dipole Approximation (DDA) to compute the absorption and scattering properties of particles in the Rayleigh domain. The method allows to separate the geometrical aspects of a particle from its material properties. Doing the computation of the optical properties of a particle once, provides them for any set of refractive indices, wavelengths and orientations. This allows for fast computations of e.g. absorption spectra of arbitrarily shaped particles. Other practical applications of the method are in the interpretation of atmospheric and radar measurements as well as computations of the scattering matrix of small particles as a function of the scattering angle. In the statistical approach, the optical properties of irregularly shaped particles are represented by the average properties of an ensemble of particles with simple shapes. We show that the absorption cross section of an ensemble of arbitrarily shaped particles with arbitrary orientations can always be uniquely represented by the average absorption cross section of an ensemble of spheroidal particles with the same composition and fixed orientation. This proves for the first time that the statistical approach is generally viable in the Rayleigh domain.

3.1 Introduction

The absorption and scattering properties of small particles are very important in both astronomical and atmospheric remote sensing applications. The interaction of light with particles much smaller than the wavelength of radiation has been studied first by Lord Rayleigh (1871) who explained from basic physical principles the color and polarization of the light from the sky. When studying the detailed spectral properties of the interaction of particles with light, we have to consider the effects of particle size, shape and

composition. In this paper we discuss the effects of shape and composition of homogeneous particles, while taking the particle sizes to be in the Rayleigh domain, i.e. much smaller than the wavelength both inside and outside the particle.

When considering the possibilities for computing the optical (i.e. the absorption and scattering) properties of small particles there are two extreme approaches one can take. The first approach is to assume the particles are homogeneous in composition and spherical in shape, which allows us to perform fast and simple computations of its interaction with light using Mie theory (Mie 1908). The second extreme is to make a model of the particle in an exact way, and perform numerical calculations to obtain its optical properties. This can be done using, for example, the so-called DDA (Discrete Dipole Approximation; see e.g. Draine 1988) or the T-matrix method (see e.g. Mishchenko et al. 1996; Wriedt 2002). The first approach is fast, and provides insight into the physics and effects that play a role in the interaction of light with small particles (see e.g. van de Hulst 1957). However, due to the perfect symmetry of homogeneous spheres, resonance effects may occur, for example, at particular values of the refractive index, that are not seen in realistically shaped natural particles. This limits the applicability of this approach. The second approach allows us to reproduce details in the observed properties of irregular particles. The main drawback is, however, that the computational demand of most numerical techniques available to compute the optical properties of realistically shaped particles, is high. If we wish to consider a large collection of various particle compositions, sizes or wavelengths, one can resort to a third method, the statistical approach. In the statistical approach one simulates the average optical properties of an ensemble of irregularly shaped particles by the average properties of an ensemble of particles with simple shapes. These simple shapes guarantee computations of the optical properties to be relatively fast. In addition, by choosing a broad distribution of simple shapes, we can get rid of the resonance effects which can occur when using homogeneous spheres. The statistical approach is proven useful for, for example, computing absorption spectra of small forsterite grains (Min et al. 2003b), and for calculating the degree of linear polarization for small quartz particles (Min et al. 2005). Some of the successes and limitations of the statistical approach are discussed in Hill et al. (1984); Mishchenko et al. (1997); Kahnert et al. (2002); Min et al. (2003b); Kahnert (2004).

In this paper we employ an analytical method based on the DDA to compute the optical properties of particles in the Rayleigh domain in an efficient way. This method is then used to show that the average absorption cross section of an ensemble of particles with arbitrary shapes and orientations is identical to that of an ensemble of particles with spheroidal shapes in a fixed orientation and with the same composition. We thus provide an analytical basis for the use of the statistical approach in computing the absorption cross sections of particles in the Rayleigh domain.

In Sect. 3.2 we outline the method which is summarized for practical purposes in Sect. 3.2.4. In Sect. 3.3 a few examples of applications to complex particles shapes are provided. A discussion of the implications for the applicability of the statistical approach is given in Sect. 3.4. In this section we will also provide suggestions on how to use the derived shape distribution of spheroids to calculate the optical properties of particles with sizes outside the Rayleigh domain.

3.2 The absorption properties of very small particles

In this section we will outline the method to obtain the optical properties of arbitrarily shaped and arbitrarily oriented particles small compared to the wavelength. We do this using a solution of the DDA. The general equations for the optical properties of particles in the Rayleigh domain are given in Sect. 3.2.1. The method to compute the optical properties for arbitrarily shaped particles is outlined in Sect. 3.2.2 and summarized in Sect. 3.2.4. In Sect. 3.2.3 we introduce the *distribution of form-factors*. Using this distribution we prove the following fundamental theorem:

Theorem 3.1. *The absorption cross section of an arbitrarily shaped and arbitrarily oriented, homogeneous particle in the Rayleigh domain, or an ensemble of such particles with various shapes and orientations, equals the average cross section of an ensemble of spheroidal particles in a fixed orientation with the same composition and a shape distribution that is independent of the composition of the particle.*

This theorem proves the validity of the statistical approach for calculations of the absorption cross sections for particles in the Rayleigh domain. It is also an encouraging result for applications of the statistical approach for other purposes.

3.2.1 General equations in the Rayleigh domain

In the Rayleigh domain a particle in a given orientation interacts with incident light as a single dipole with dipole moment \mathbf{p} given by

$$\mathbf{p} = \alpha \mathbf{E}_{\text{inc}} . \quad (3.1)$$

In this equation α is the 3×3 polarizability tensor, and \mathbf{E}_{inc} is the incoming electric field. From the polarizability tensor it is possible to obtain all scattering and absorption properties of the particle (see e.g. Bohren & Huffman 1983). The absorption cross section of such a particle when the incident field is applied along the x, y or z axis of a Cartesian coordinate system (indicated by the symbol $\mu = 1, 2, 3$) is given by (Mackowski 1995)

$$C_{\text{abs}}^{(\mu)} = k \operatorname{Im} \left(\alpha^{(\mu\mu)} \right), \quad (3.2)$$

and the scattering cross section by

$$C_{\text{sca}}^{(\mu)} = \frac{k^4}{6\pi} \sum_{\nu=1}^3 \left| \alpha^{(\mu\nu)} \right|^2, \quad (3.3)$$

where $\alpha^{(\mu\nu)}$ is the μ, ν -th component of the polarizability tensor ($\mu, \nu = 1, 2, 3$), and $k = 2\pi/\lambda$, with λ the wavelength of incident radiation. Note that when a particle is in the Rayleigh domain the electric field can be taken constant over the particle volume. This implies that the direction of wave propagation of the incident light is not important for the interaction of the light with the particle, but only the direction of the electric field.

The cross sections averaged over all particle orientations (denoted by $\langle \dots \rangle$) are simply given by the average over the three axes which results in

$$\langle C_{\text{abs}} \rangle = \frac{k}{3} \text{Im} \left(\sum_{\mu=1}^3 \alpha^{(\mu\mu)} \right), \quad (3.4)$$

and

$$\langle C_{\text{sca}} \rangle = \frac{k^4}{18\pi} \sum_{\mu,\nu=1}^3 |\alpha^{(\mu\nu)}|^2. \quad (3.5)$$

For only a few particle shapes simple analytical equations are available to compute the polarizability tensor. These are the shapes of homogeneous, layered and hollow spheres, and homogeneous, layered and hollow ellipsoids. For a homogeneous sphere α is given by (Bohren & Huffman 1983)

$$\alpha = 3V \frac{m^2 - 1}{m^2 + 2} \mathbf{I}_3, \quad (3.6)$$

with m the complex refractive index of the particle material, V the material volume of the particle, and \mathbf{I}_3 the 3×3 identity matrix. The polarizability tensor of a homogeneous ellipsoidal particle is given by (Bohren & Huffman 1983)

$$\alpha = V \begin{bmatrix} \frac{m^2-1}{1+L_1(m^2-1)} & 0 & 0 \\ 0 & \frac{m^2-1}{1+L_2(m^2-1)} & 0 \\ 0 & 0 & \frac{m^2-1}{1+L_3(m^2-1)} \end{bmatrix}, \quad (3.7)$$

where the L_i are geometrical form-factors with values between 0 and 1 depending on the shape of the ellipsoid.

For an ellipsoid of revolution (a spheroid) with axes a and b we have

$$L_1 = \begin{cases} \frac{1-e^2}{e^2} \left(-1 + \frac{1}{2e} \ln \left(\frac{1+e}{1-e} \right) \right), & e^2 = 1 - \frac{a^2}{b^2}, & \text{Prolates,} \\ \frac{1}{e^2} \left(1 - \frac{\sqrt{1-e^2}}{e} \arcsin(e) \right), & e^2 = 1 - \frac{b^2}{a^2}, & \text{Oblates,} \end{cases} \quad (3.8)$$

and $L_2 = L_3 = (1 - L_1)/2$. Here b is the rotation axis, and a/b is the aspect ratio. For prolate spheroids $a/b < 1$ and $0 < L_1 < 1/3$, while for oblate spheroids $a/b > 1$ and $1/3 < L_1 < 1$. For homogeneous spheres $L_1 = L_2 = L_3 = 1/3$.

The equations for the polarizability of hollow spheres or ellipsoids can be found in Van de Hulst 1957. For a hollow sphere having a volume fraction f occupied by a central vacuum inclusion, the polarizability tensor is given by

$$\alpha = 3V \frac{(m^2 - 1)(2m^2 + 1)}{(m^2 + 2)(2m^2 + 1) - 2(m^2 - 1)^2 f} \mathbf{I}_3, \quad (3.9)$$

where $V = \frac{4}{3}\pi r^3(1 - f)$ is the material volume of a hollow sphere with outer radius r .

For convenience we introduce the dimensionless polarizability per unit material volume of a particle $\bar{\alpha} = \alpha/V$.

3.2.2 The Discrete Dipole Approximation (DDA)

In the Discrete Dipole Approximation (DDA) a particle is represented by a collection of interacting dipoles. This idea was proposed by Purcell & Pennypacker (1973), who derived the general equations for the interaction of the dipoles with the incident light and with each other. The approach is equivalent to a discretization of the particle volume and the assumption that each volume element interacts with the radiation field as a single dipole j with polarizability β_j . For a theoretical derivation of this approach from the Maxwell equations see e.g. Lakhtakia (1992); Lakhtakia & Mulholland (1993). For inhomogeneous particles the polarizability can vary throughout the particle depending on the material properties of the local volume element. Also the polarizability tensor can be anisotropic. In this paper we consider only homogeneous particles, i.e. $\beta_j = \beta$ for all j . In addition we consider only the case when the polarizability is isotropic in which case the polarizability tensor can be written as $\beta \mathbf{I}_3$, with β the scalar polarizability. For the DDA to be valid, the volume elements represented by the dipoles have to be in the Rayleigh domain.

To compute the interaction of N dipoles with the incident field and with each other we have to solve a set of N inhomogeneous linear vector equations, namely

$$\sum_{j=1}^N (\mathbf{A}_{ij} + \beta^{-1} \mathbf{I}_3) \mathbf{P}_j = \mathbf{E}_{\text{inc},i} \quad (i = 1, \dots, N). \quad (3.10)$$

Here the polarization vector at the position of dipole j , \mathbf{P}_j , is a column vector with 3 elements. $\mathbf{E}_{\text{inc},i}$ is a column vector representing the incoming electric field at the position of dipole i . The \mathbf{A}_{ij} are 3×3 matrices determined by the positions of the dipoles in the particle and thus by the particle geometry. The general equations for the \mathbf{A}_{ij} are given by Draine (1988). We assume in this paper that the entire particle is in the Rayleigh domain. This implies that the electric field is constant, so we are in the limit of $k \rightarrow 0$. Then

$$\mathbf{A}_{ij} = \begin{cases} \frac{\mathbf{I}_3 - 3\hat{\mathbf{r}}_{ij}\hat{\mathbf{r}}_{ij}}{4\pi r_{ij}^3}, & i \neq j, \\ 0, & i = j. \end{cases} \quad (3.11)$$

Here $\hat{\mathbf{r}}_{ij}$ is the unit vector pointing from dipole i to dipole j , and r_{ij} is the distance between these two dipoles. The 3×3 matrix $\hat{\mathbf{r}}_{ij} \hat{\mathbf{r}}_{ij}$ is defined as the product of $\hat{\mathbf{r}}_{ij}$ as a column vector and $\hat{\mathbf{r}}_{ij}$ as a row vector, i.e.

$$\hat{\mathbf{r}}_{ij} \hat{\mathbf{r}}_{ij} = \begin{bmatrix} \hat{r}_{ij,x}^2 & \hat{r}_{ij,x} \hat{r}_{ij,y} & \hat{r}_{ij,x} \hat{r}_{ij,z} \\ \hat{r}_{ij,x} \hat{r}_{ij,y} & \hat{r}_{ij,y}^2 & \hat{r}_{ij,y} \hat{r}_{ij,z} \\ \hat{r}_{ij,x} \hat{r}_{ij,z} & \hat{r}_{ij,y} \hat{r}_{ij,z} & \hat{r}_{ij,z}^2 \end{bmatrix}, \quad (3.12)$$

where $\hat{r}_{ij,x}$, $\hat{r}_{ij,y}$ and $\hat{r}_{ij,z}$ are the x , y and z components of the unit vector $\hat{\mathbf{r}}_{ij}$, respectively.

Following Draine (1988) we define the $3N$ dimensional column vectors $\tilde{\mathbf{E}}_{\text{inc}} = (\mathbf{E}_{\text{inc},1}, \mathbf{E}_{\text{inc},2}, \dots, \mathbf{E}_{\text{inc},N})$ and $\tilde{\mathbf{P}} = (\mathbf{P}_1, \mathbf{P}_2, \dots, \mathbf{P}_N)$ and the $3N \times 3N$ matrix $\tilde{\mathbf{A}}$ such that

$\tilde{\mathbf{A}}_{3(i-1)+\mu,3(j-1)+\nu} = (\mathbf{A}_{ij})_{\mu\nu}$, $\{i, j = 1 \dots N; \mu, \nu = 1, 2, 3\}$. In this way Eq. (3.10) can be written as a single matrix equation

$$(\tilde{\mathbf{A}} + \beta^{-1} \mathbf{I}_{3N}) \tilde{\mathbf{P}} = \tilde{\mathbf{E}}_{\text{inc}} . \quad (3.13)$$

Note that in this equation the matrix $\tilde{\mathbf{A}}$ only depends on the particle geometry, while the matrix $\beta^{-1} \mathbf{I}_{3N}$ only depends on the dielectric properties of the particle.

Eq. (3.13) can be solved for $\tilde{\mathbf{P}}$ using, for example, a conjugate gradient method. In the literature considerable effort has been reported to increase the efficiency of solution methods for Eq. (3.13) (see e.g. Goodman et al. 1991; Hoekstra et al. 1998). In contrast to the general equations for $\tilde{\mathbf{A}}$, in the Rayleigh domain this matrix is real and symmetric. This implies that the eigenvalues of $\tilde{\mathbf{A}}$ are real, and that the eigenvectors form an orthonormal basis. As we will detail below, once the eigenvalues and eigenvectors of $\tilde{\mathbf{A}}$ have been determined, the solution of Eq. (3.13) can be obtained for arbitrary values of β , and thus for any particle material. This method is similar to that presented by Markel et al. (1991).

Using the eigenvalues and eigenvectors, the matrix $\tilde{\mathbf{A}}$ can be diagonalized by writing

$$\tilde{\mathbf{A}} = \mathbf{U} \mathbf{D} \mathbf{U}^T , \quad (3.14)$$

where a superscript T is used to denote the transpose of a matrix. The columns of \mathbf{U} are the $3N$ real valued eigenvectors of $\tilde{\mathbf{A}}$, and the elements of the diagonal matrix \mathbf{D} are the corresponding eigenvalues of $\tilde{\mathbf{A}}$. Since the eigenvectors of $\tilde{\mathbf{A}}$ are orthonormal the transpose of \mathbf{U} equals its inverse, i.e. $\mathbf{U}^T = \mathbf{U}^{-1}$. The eigenvalues and eigenvectors of a real symmetric matrix can be found relatively easy using numerical techniques.

The matrix on the left hand side of Eq. (3.13) can be rewritten after diagonalization since

$$(\tilde{\mathbf{A}} + \beta^{-1} \mathbf{I}_{3N}) = (\mathbf{U} \mathbf{D} \mathbf{U}^T + \beta^{-1} \mathbf{I}_{3N}) = \mathbf{U} (\mathbf{D} + \beta^{-1} \mathbf{I}_{3N}) \mathbf{U}^T . \quad (3.15)$$

Using this, the solution of Eq. (3.13) can be written as

$$\tilde{\mathbf{P}} = \mathbf{U} (\mathbf{D} + \beta^{-1} \mathbf{I}_{3N})^{-1} \mathbf{U}^T \tilde{\mathbf{E}}_{\text{inc}} . \quad (3.16)$$

Since $(\mathbf{D} + \beta^{-1} \mathbf{I}_{3N})$ is a diagonal matrix, its inverse is readily computed. Once \mathbf{U} and \mathbf{D} have been calculated, the solution can be easily computed for every value of β . Since \mathbf{U} and \mathbf{D} only depend on the geometry of the particle, we only have to calculate them once in order to find the solution for arbitrary values of β , and thus for any particle material.

In the Rayleigh domain, the incident electric field constant throughout the particle. This means that, at each dipole j , $\mathbf{E}_{\text{inc},j} = \mathbf{E}_{\text{inc}}$. The total dipole moment of the particle then is

$$\mathbf{p} = \sum_{j=1}^N \mathbf{P}_j = \alpha \mathbf{E}_{\text{inc}} . \quad (3.17)$$

Combining this equation with Eq. (3.16) gives us the polarizability tensor α with elements

$$\alpha^{(\mu\nu)} = \sum_{j=1}^{3N} \frac{w_j^{(\mu\nu)}}{\lambda_j + \beta^{-1}} , \quad (3.18)$$

where the λ_j are the $3N$ eigenvalues of $\tilde{\mathbf{A}}$, and the $w_j^{(\mu\nu)}$ are given by

$$w_j^{(\mu\nu)} = \sum_{i,k=1}^N \mathbf{U}_{j,3(i-1)+\mu} \mathbf{U}_{j,3(k-1)+\nu} . \quad (3.19)$$

Note that since the matrix \mathbf{U} is real valued, the $w_j^{(\mu\mu)}$ are real valued and positive since

$$w_j^{(\mu\mu)} = \left(\sum_{i=1}^N \mathbf{U}_{j,3(i-1)+\mu} \right)^2 . \quad (3.20)$$

Using Eqs. (3.2) and (3.18), the absorption cross section when the field is applied along the μ axis becomes

$$C_{\text{abs}}^{(\mu)} = k \operatorname{Im} \left(\sum_{j=1}^{3N} \frac{w_j^{(\mu\mu)}}{\lambda_j + \beta^{-1}} \right) . \quad (3.21)$$

Also all the scattering properties, i.e. the scattering cross section, matrix, and depolarization factors, of the particle can be obtained from the polarizability tensor. The scattering cross section when the field is applied along the μ axis can be computed using Eqs. (3.3) and (3.18) and becomes

$$C_{\text{sca}}^{(\mu)} = \frac{k^4}{6\pi} \sum_{\nu=1}^3 \left| \sum_{j=1}^{3N} \frac{w_j^{(\mu\nu)}}{\lambda_j + \beta^{-1}} \right|^2 . \quad (3.22)$$

The orientation averaged cross sections can also be obtained from Eq. 3.18 using Eqs. (3.4) and (3.5). In the following we focus on the absorption cross section.

3.2.3 The distribution of form-factors

In the previous sections we have shown how to separate the geometrical and dielectrical properties when computing the absorption properties of arbitrarily shaped particles in the Rayleigh domain. In this section we show how the particle geometry can be uniquely described by a distribution of *form-factors*. Also, we will show how this distribution can be used to construct a shape distribution of spheroidal particles in a fixed orientation and with the same composition which has identical absorption properties.

We take the polarizability of a single volume element to be the Clausius-Mossotti polarizability of a cubic volume element with size d (Purcell & Pennypacker 1973), i.e.

$$\beta = 3d^3 \frac{m^2 - 1}{m^2 + 2} . \quad (3.23)$$

When the size of the volume elements is sufficiently small, this is the polarizability that follows directly from the Maxwell equations (see e.g. Lakhtakia 1992; Lakhtakia & Mulholland 1993).

The equation for the absorption cross section (Eq. 3.21) then reduces to

$$C_{\text{abs}}^{(\mu)} = \sum_{j=1}^{3N} \frac{w_j^{(\mu\mu)}}{N} \left[kV \operatorname{Im} \left(\frac{m^2 - 1}{1 + L_j (m^2 - 1)} \right) \right], \quad (3.24)$$

with $V = Nd^3$ the total material volume of the particle and the form-factor L_j defined by

$$L_j = \frac{1}{3} + \lambda_j d^3. \quad (3.25)$$

Comparing Eq. (3.24) with Eq. (3.7) we see that Eq. (3.24) is equal to the equation for the average absorption cross section of an ensemble of oriented ellipsoids with various shapes. We have thus proven theorem 3.1.

The result given above implies that we can represent the absorption properties of an arbitrarily shaped and arbitrarily oriented particle uniquely by a distribution of the form-factors, $\mathcal{P}(L)$. But in order to represent an ellipsoid with a given aspect ratio, the L_j have to be between 0 and 1. This implies that the eigenvalues, λ_j , have to be between $-1/(3d^3)$ and $2/(3d^3)$ for arbitrary shapes. For all particle shapes that we considered this was the case. From the $w_j^{(\mu\mu)}$ (given by Eq. 3.20) and the L_j (given by Eq. 3.25) it is straightforward to construct the distribution of form-factors.

In practice we often meet ensembles of particles with different shapes and orientations. In the Rayleigh domain, averaging over particle orientations can be done by averaging over three perpendicular orientations. In view of Eq. (3.24) it is clear that the shape and orientation averaged polarizability (and thus the average absorption cross section) of such ensembles can be obtained from the ensemble averaged form-factor distribution. This allows us to construct average form-factor distributions of different classes of particle shapes, resulting in a unique distribution of spheroidal particles to represent the absorption properties of each class.

3.2.4 Summary of the procedure

The method described above provides a practical way of computing the optical properties of arbitrarily shaped and arbitrarily oriented particles in the Rayleigh domain. It separates the geometrical and material properties of the particle. This implies that for a given particle geometry the computation has to be done only once to obtain the absorption and scattering properties for arbitrary values of the refractive index and wavelength.

The procedure to obtain the optical properties of an arbitrarily shaped and arbitrarily oriented particle in the Rayleigh domain is outlined as follows.

1. Construct the matrix $\tilde{\mathbf{A}}$ using Eq. (3.11) and $\tilde{\mathbf{A}}_{3(i-1)+\mu, 3(j-1)+\nu} = (\mathbf{A}_{ij})_{\mu\nu}$.
2. Compute the eigenvalues, λ_j , and the matrix of eigenvectors, \mathbf{U} , of the real symmetric matrix $\tilde{\mathbf{A}}$.
3. Compute the $w_j^{(\mu\nu)}$ using Eq. (3.19).
4. Compute the polarizability tensor α from Eq. (3.18).

5. From the polarizability tensor the absorption and scattering cross sections for the particle in a single orientation are obtained from Eqs. (3.2) and (3.3). Also, the scattering matrix can be obtained from the polarizability tensor (see Bohren & Huffman 1983)
6. The absorption and scattering cross sections for an ensemble of particles with random orientations can be obtained from Eqs. (3.4) and (3.5). The scattering matrix for an ensemble of randomly oriented particles is given in Bohren & Huffman (1983).

The computationally demanding steps (1), (2) and (3) have to be done only once for a given particle geometry and structure. Steps (4), (5) and (6) then provide the optical properties for arbitrary orientation, wavelength, and particle material.

The distribution of form-factors is computed from the λ_j and the $w_j^{(\mu\mu)}$ by using Eq. (3.25). The corresponding distribution of spheroids is obtained from the form-factor distribution using Eq. (3.8). In Sect. 3.4.4 we outline how the distribution of spheroidal particles that is obtained might be used to compute the optical properties of particles outside the Rayleigh domain.

3.3 Application to various shapes

3.3.1 Homogeneous spheres and spheroids

Since the average polarizability of an ensemble of homogeneous spheroids in random orientation consists of the sum of two polarizabilities with different values of L (see Eqs. 3.7 and 3.8), the ensemble averaged form-factor distribution displays two distinct peaks, one at the value of L determined by Eq. (3.8) and one at $(1 - L)/2$ (with double intensity).

By way of example we computed the form-factor distributions of a homogeneous sphere, a prolate spheroid with aspect ratio $a/b = 0.5$ and an oblate spheroid with $a/b = 2.0$, averaged over all particle orientations using the DDA method (see Fig. 3.1). The material volume of each particle is discretized by using 3000 dipoles. We also indicate in this figure the positions of the peaks as determined by Eq. (3.8). We see that, in general, the positions of the peaks in the calculated distributions match the expected values fairly well. The differences are mainly caused by the fact that by using a discrete array of cubic dipoles it is not possible to represent the shape of a spheroid exactly.

The refractive index of natural materials is a function of wavelength. The refractive index of most materials exhibits resonances in the infrared part of the spectrum. These resonances lead to corresponding resonances in the absorption cross section which can be detected, for example, in thermal emission spectra. The wavelength positions of the features are sensitive to the particle shape and can be used to determine the shape and composition of the emitting grains. Therefore, it is important to study the absorption cross section as a function of the refractive index and wavelength.

In the left panel of Fig. 3.2 we show $C_{\text{abs}}/(kV)$ or, in other words, the imaginary part of the polarizability per unit volume, of a single homogeneous sphere as a function of

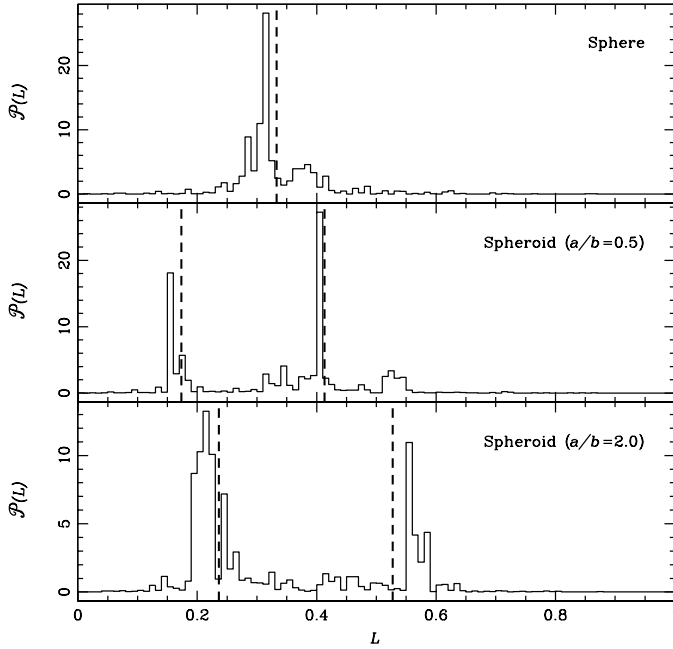


Figure 3.1: The form-factor distributions as calculated for an array of 3000 dipoles representing a sphere, a prolate spheroid with $a/b = 0.5$ and an oblate spheroid with $a/b = 2.0$ averaged over all particle orientations. The expected positions of the peaks in the distribution are indicated by the dashed lines.

the real and imaginary part of the refractive index as computed from Eq. (3.6). Note the sharp increase of the imaginary part of the polarizability when $m \rightarrow i\sqrt{2}$ typical for homogeneous spherical particles (cf. Eq. 3.6). When considering the absorption cross section as a function of wavelength near a resonance, this leads to a sharp peak in the absorption spectrum. The imaginary part of the polarizability per unit volume of an ensemble of randomly oriented prolate spheroids with aspect ratio $a/b = 0.5$ is shown in the right panel of Fig. 3.2. In this contour plot we see two sharp maxima, caused by the two values of L determining the polarizability. In general, we expect particles with a few isolated form-factors to show strong resonances for each form-factor. As will be shown below, a full distribution leads to a smoother absorption spectrum.

3.3.2 Gaussian random sphere

In order to model the optical properties of irregularly shaped particles we have to employ a model for the shape of the particles. A successful model that is frequently used in light scattering theory is that of a Gaussian random sphere (Muinonen et al. 1996). The basis of this shape model is a homogeneous sphere of which the surface is distorted according to a Gaussian random distribution. The distortion of the surface is paramet-

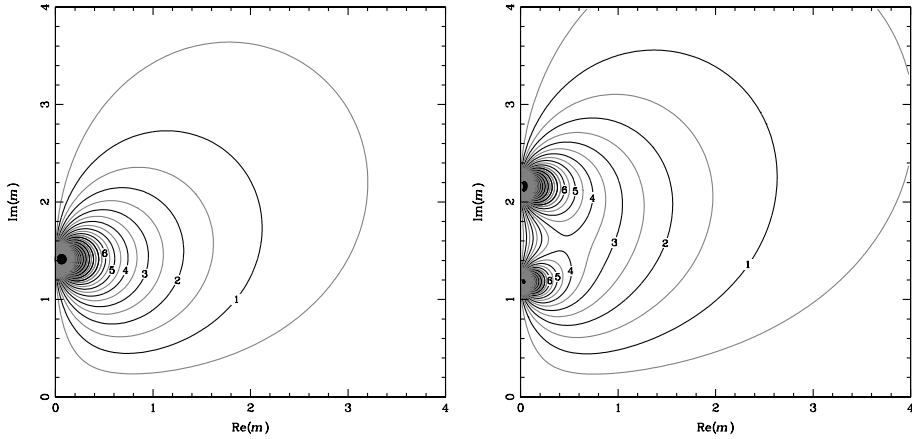


Figure 3.2: Contour plots of the imaginary part of the polarizability per unit volume as functions of the real and imaginary part of the refractive index. The left panel is for a single homogeneous sphere and the right panel for an ensemble of randomly oriented prolate homogeneous spheroids with aspect ratios $a/b = 0.5$.

erized by two shape variables, the standard deviation, σ , of the distance to the center, and the average correlation angle, Γ . The value of Γ determines the number of hills and valleys on the surface within a solid angle, while σ determines the height of these hills and valleys. For details see Muinonen et al. (1996). Using different shape parameters we can create particles with varying degrees of irregularity. Volten et al. (2001) successfully used Gaussian random spheres to compute the scattering matrices of mineral particles as functions of the scattering angle. They found that in order to reproduce the experimentally determined scattering behavior they had to employ very large values of σ .

In the top panel of Fig. 3.3 we show the form-factor distribution of various ensembles of randomly oriented Gaussian random spheres with different values of σ . In all cases we fix the value of Γ to 10° . For each value of σ we construct an ensemble of 10 different Gaussian random spheres, each with the same value for the shape parameter but different seeds of the random number generator. Above the two panels of Fig. 3.3 we show some typical examples from the ensembles. The volume of each particle is discretized using 3000 dipoles in order to construct the orientation and ensemble averaged form-factor distribution. The form-factor distribution of each ensemble is used to compute its average polarizability per unit volume as a function of the refractive index from Eq. (3.24). The imaginary part of the average polarizability per unit volume is shown by contours in the bottom panel of Fig. 3.3.

Fig. 3.3 shows that for small deformations of the surface of the sphere (most left panel), the form-factor distribution is dominated by one peak at $L \approx 1/3$ and the absorption properties are rather similar to those of spherical particles (see the left panel of Fig. 3.2). For larger values of σ the distribution of form-factors gets broader. If $\sigma = 0.5$

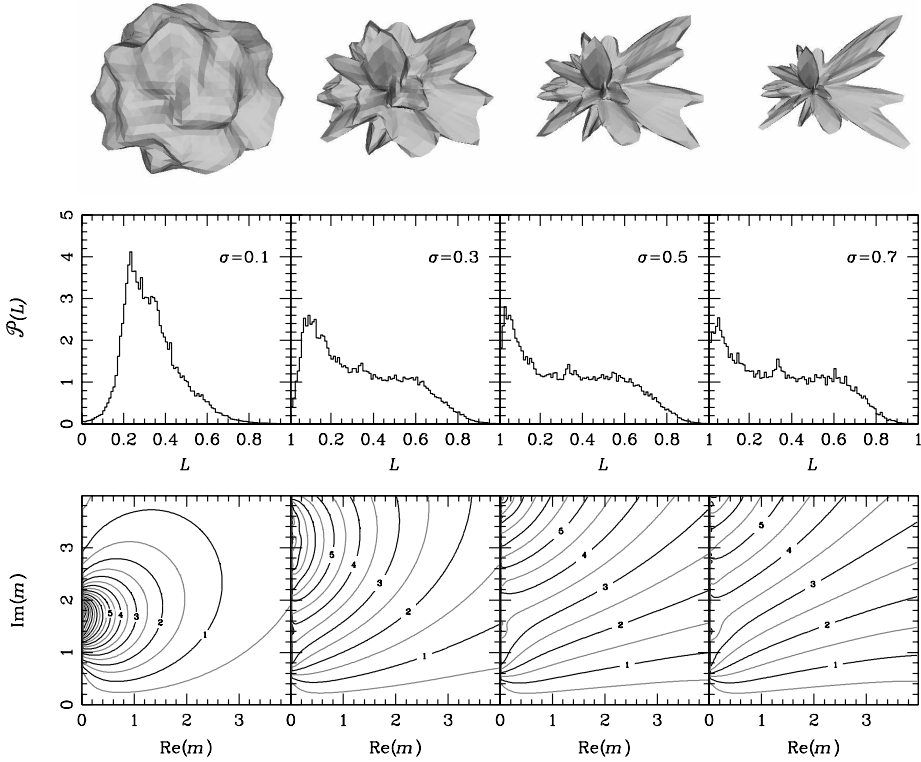


Figure 3.3: The orientation and ensemble averaged form-factor distribution (top panels) and the imaginary part of the average polarizability per unit volume as a function of the real and imaginary part of the refractive index (bottom panels) of the ensembles of randomly oriented Gaussian random spheres. Above the figures we show typical examples of particles from the various ensembles. From left to right the relative standard deviation of the distance to the center is 0.1, 0.3, 0.5 and 0.7, respectively. The correlation angle $\Gamma = 10^\circ$, and is the same for all four shapes. For each shape we considered an ensemble of 10 different particles with the same parameters but different seeds of the random number generator. We average over these different particles in order to reduce the effects of random variations of the particle shapes on the final results.

or 0.7 we see that for a fixed value of $\text{Re}(m)$ the polarizability is a smooth, continuously increasing function of $\text{Im}(m)$, as expected in the absence of resonance effects caused by the geometry of the particle.

In Battaglia et al. (1999) a method is proposed to compute the scattering and absorption properties of Gaussian random spheres in the Rayleigh domain. However, the method used in that paper is an approximation using only a single ellipsoid as a best fit to the particle shape. From the discussion given above it is clear that this can provide only a very rough approximation to the real absorption properties of Gaussian random spheres.

3.3.3 Aggregates with various fractal dimensions

In environments where dust particles grow by aggregation of smaller constituents, the resulting grains might be modeled as fractal aggregates. The fractal dimensions of these aggregates are a measure for the compactness or fluffiness of the particle and depend on the conditions in the environment. A large part of the interplanetary dust particles collected in the Earth's atmosphere are aggregates of small particles. Therefore, the optical properties of particle aggregates are very important in astrophysics and planetary physics. Fogel & Leung (1998) computed emission and extinction spectra of fractal aggregates with various fractal dimensions. They found that the mass absorption and extinction coefficients of fractal aggregates are on average higher than those of volume equivalent spheres. Mackowski (1995) developed a method to obtain the optical properties of sphere clusters in the Rayleigh domain. For computations of various values of the refractive index, which are needed, for example, for computing absorption spectra, the method we employ is much faster and, in addition, it is easier to implement.

We construct aggregates with various fractal dimensions using a sequential tunable particle-cluster aggregation method developed by Filippov et al. (2000). A fractal aggregate composed of homogeneous spheres obeys the so-called scaling law (Filippov et al. 2000)

$$N = k_f \left(\frac{R_g}{a} \right)^{D_f}. \quad (3.26)$$

Here N is the number of constituents, each with radius a ; k_f is the fractal prefactor; D_f is the fractal dimension, and R_g is the radius of gyration defined by

$$R_g^2 = \frac{1}{N} \sum_{i=1}^N |\mathbf{r}_i - \mathbf{r}_0|^2, \quad (3.27)$$

$$\mathbf{r}_0 = \frac{1}{N} \sum_{i=1}^N \mathbf{r}_i, \quad (3.28)$$

where \mathbf{r}_i is the position of the i th constituent. The value of the fractal dimension can in theory vary between the two extremes $D_f = 1$ (a thin, straight chain of particles) and $D_f = 3$ (a homogeneous sphere). The aggregation method we employ ensures that with every particle that is added to the aggregate the scaling law (Eq. 3.26) is fulfilled exactly (Filippov et al. 2000). For all aggregates we choose the fractal prefactor $k_f = 2$. Different values of k_f result in slightly different fractal aggregate shapes. By comparing the results obtained for various aggregates using different values of the fractal prefactor we find that the results are not very sensitive to the exact value chosen.

The structure of aggregates depends strongly on the precise mechanism by and environment in which these aggregates form. The shape of aggregates formed in high density environments, for example small gold particles in aqueous suspension, is determined by the random-walk nature of the different particles upon approach. This process can lead to aggregates with a fractal dimension of about 1.7 (Weitz et al. 1985). In low density environments like protoplanetary disks and molecular clouds in astrophysics, particles approach each other on straight lines before collisions. If such clusters grow by addition

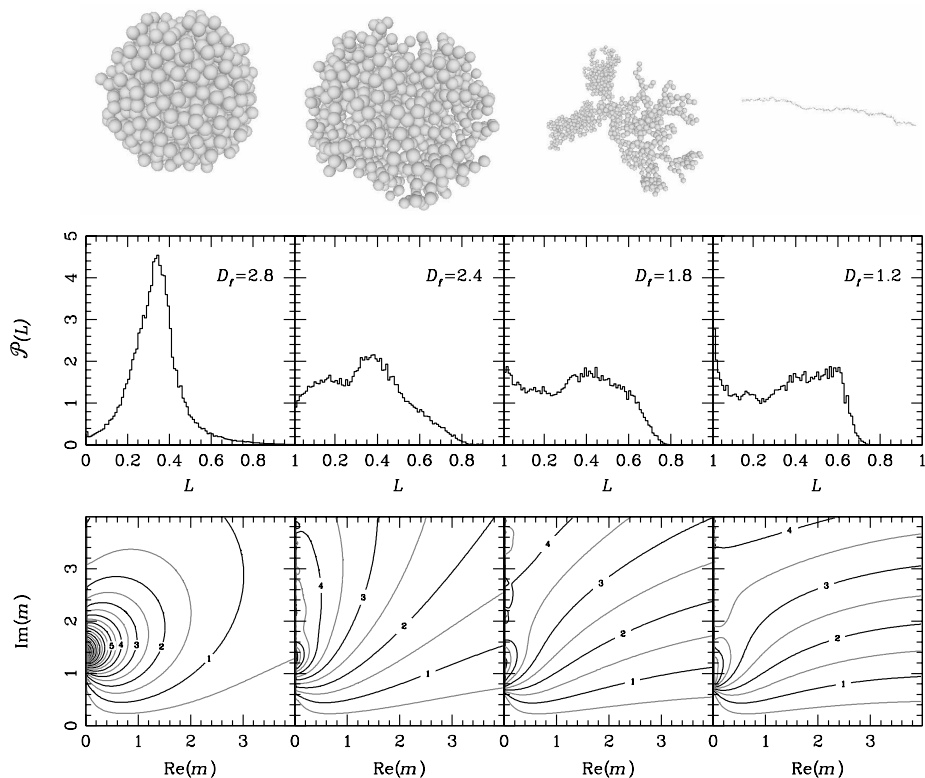


Figure 3.4: Same as Fig. 3.3 but for fractal aggregates. From left to right the fractal dimension $D_f = 2.8, 2.4, 1.8$ and 1.2 , respectively. For all four fractal dimensions we considered an ensemble of 10 particles with the same shape parameters but different seeds of the random number generator. This results in 10 fractal aggregates with the same fractal dimension but different locations of the constituents. By averaging over these aggregates we reduce the effects of random variations of the particle shapes on the final results.

of single grains to an aggregate (“Ballistic particle cluster aggregation”, BPCA), this process leads to aggregates with a fractal dimension of exactly 3 in the limit of large aggregates (Ball & Witten 1984), and slightly less than three for smaller aggregates. If on the other hand, the growth is approximately mono-disperse, i.e. each aggregate grows by collisions with aggregates of similar size (“Ballistic cluster cluster aggregation”, BCCA), the expected fractal dimension is between 1.8 and 2.1 (Kempf et al. 1999). Almost linear aggregates ($D_f \approx 1$) may be formed from particles with electric or magnetic dipoles in external fields (Dominik & Nübold 2002; Nübold et al. 2003)

Some typical examples of fractal aggregates are shown above the two panels of Fig. 3.4. The top panel of Fig. 3.4 shows the ensemble and orientation averaged form-factor distributions of ensembles of fractal aggregates with different fractal dimensions. Each ensemble consists of fractal aggregates with the same fractal dimension and fractal

prefactor, but with different values of the seed of the random number generator. Also shown in Fig. 3.4 (bottom panel) is the average polarizability per unit volume as a function of the real and imaginary part of the refractive index of the particles.

It is apparent from Fig. 3.4 that the imaginary part of the polarizability per unit volume of compact aggregates ($D_f = 2.8$) resembles that of compact homogeneous spheres (see the left panel of Fig. 3.2). When the fractal dimension is decreased, the resonance at $m = i\sqrt{2}$ disappears. Note the strong similarity between the bottom panels of Figs. 3.3 and 3.4. Although the Gaussian random spheres are very different from the fractal aggregates, the absorption properties for both classes of particles are quite similar.

3.4 Discussion

3.4.1 Comparison with distributions of simple shapes

In order to model irregularly shaped particles, several distributions of simple shapes are presented in the literature. We consider here the widely used Continuous Distribution of Ellipsoids (CDE, Bohren & Huffman 1983) and the Distribution of Hollow Spheres (DHS, Min et al. 2003b). For these distributions we compute the corresponding form-factor distributions and compare these to the form-factor distributions of irregularly shaped particles.

The CDE averages over all possible tri-axial ellipsoids with a specific weighting function (see Min et al. 2003b). The sum of the form-factors of a tri-axial ellipsoid averaged over all orientations has to be unity. Therefore, there are only two independent form-factors, L_1 and L_2 and one form-factor $1 - L_1 - L_2$. Since all form-factors have to be positive, another constraint is that $L_2 < 1 - L_1$. The CDE averages over all possible ellipsoidal shapes by taking the distribution function $\mathcal{P}(L_1, L_2) = 2$. The average polarizability then becomes

$$\begin{aligned}\alpha &= \frac{2}{3} \int_0^1 dL_1 \int_0^{1-L_1} dL_2 (\alpha(L_1) + \alpha(L_2) + \alpha(1 - L_1 - L_2)) \\ &= 2 \int_0^1 dL (1 - L) \alpha(L).\end{aligned}\tag{3.29}$$

Thus, the form-factor distribution according to the CDE is

$$\mathcal{P}(L) = 2(1 - L).\tag{3.30}$$

In the DHS we average over the volume fraction, f , occupied by the central vacuum inclusion of a hollow sphere, while keeping the material volume of the particle constant. This implies that the outer radius of such a particle increases when f increases. We consider the shape of a homogeneous hollow sphere to be different from that of a homogeneous sphere. As can be verified from Eq. (3.9) by substitution, the form-factor

distribution of a single hollow sphere displays two features located at

$$L_1 = \frac{1}{2} - \frac{1}{6} \sqrt{8f+1}, \quad (3.31)$$

$$L_2 = \frac{1}{2} + \frac{1}{6} \sqrt{8f+1}, \quad (3.32)$$

which have respective strengths

$$w_1 = \frac{1}{2} + \frac{1}{2\sqrt{8f+1}}, \quad (3.33)$$

$$w_2 = \frac{1}{2} - \frac{1}{2\sqrt{8f+1}}. \quad (3.34)$$

From these equations it is already clear that the part $1/3 < L < 2/3$ in the form-factor distribution is not covered when using hollow spheres. From the above equations, the form-factor distribution for the DHS can be obtained and yields

$$\mathcal{P}(L) = \begin{cases} \frac{3}{2}|2-3L|, & 0 \leq L \leq \frac{1}{3} \quad \text{and} \quad \frac{2}{3} \leq L \leq 1, \\ 0, & \frac{1}{3} < L < \frac{2}{3}. \end{cases} \quad (3.35)$$

Fig. 3.5 shows the form-factor distributions of CDE (Eq. 3.30) and DHS (Eq. 3.35) together with those of an ensemble of Gaussian random spheres with $\sigma = 0.7$ in random orientation and an ensemble of fractal aggregates with fractal dimension 1.8 in random orientation. We can see that the form-factor distribution for the CDE and the Gaussian random spheres are in many respects very similar. This might explain the success of the CDE as a statistical representation of the absorption properties of irregularly shaped particles. We can also see from Fig. 3.5 that by using hollow spheres we do not cover the range of form-factors $1/3 < L < 2/3$ (cf. Eq. 3.35). Furthermore, the DHS shows a strong contribution of $L \gtrsim 0.8$ which is absent in the form-factor distributions of realistically shaped particles.

3.4.2 Absorption spectra

If we consider the wavelength dependence of the refractive index of the particle material, we can construct the absorption spectrum of the particle, i.e. its absorption cross section as a function of wavelength, using the form-factor distribution. In general, this absorption spectrum will display resonances, the exact positions and strengths of which are sensitive to the shape of the particles. As an example we consider the resonance of a single Lorentz oscillator. Its refractive index is given by (see e.g. Bohren & Huffman 1983)

$$m^2 = m_0^2 + \frac{f\omega_p^2}{\omega_0^2 - \omega^2 - i\gamma\omega}. \quad (3.36)$$

In this equation $m_0 > 1$ is the real valued refractive index for $\omega \rightarrow \infty$, f is the oscillator strength of the feature, ω_p is the plasma frequency, ω is the frequency of incident radiation and γ is a damping factor. If ω is given in wavenumbers, we can express Eq. (3.36)

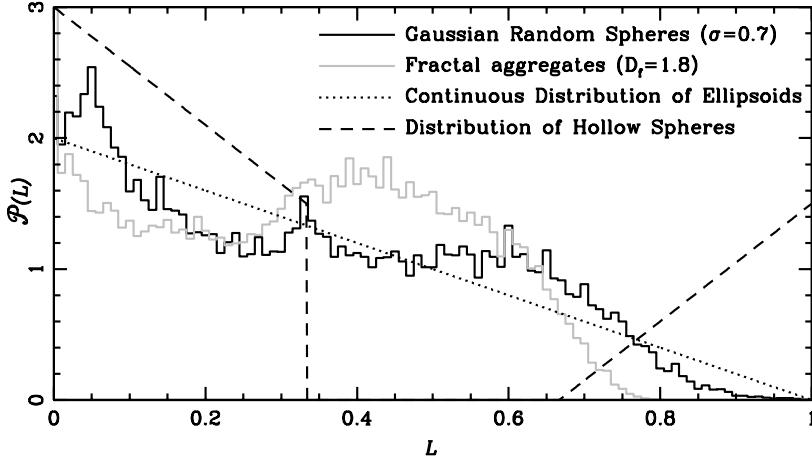


Figure 3.5: The form-factor distribution of various particle shape distributions. The solid black line represents the distribution for an ensemble of randomly oriented Gaussian Random Spheres with $\sigma = 0.7$, the solid gray line represents an ensemble of randomly oriented fractal aggregates with fractal dimension $D_f = 1.8$, the dotted line represents the Continuous Distribution of Ellipsoids (CDE, Bohren & Huffman 1983) and the dashed line refers to the Distribution of Hollow Spheres (DHS, Min et al. 2003b). We chose $\sigma = 0.7$ for the Gaussian random spheres since more modest random spheres ($\sigma = 0.1$ or 0.3) still show too much resonance behavior (see Fig. 3.3). The value of the fractal dimension $D_f = 1.8$ is chosen because this is approximately expected from cluster-cluster aggregation (Kempf et al. 1999) and it represents a reasonably fluffy aggregate. Note the remarkable similarity between the Gaussian Random Spheres with $\sigma = 0.7$ and the CDE form-factor distribution.

in wavelengths by using $\omega = \lambda^{-1}$. It can be shown that for a single form-factor, L , the absorption spectrum due to a single resonance given by Eq. (3.36) displays a single feature at position ω_{\max} given by (Bohren & Huffman 1983)

$$\omega_{\max}^2 = \omega_0^2 + \frac{Lf\omega_p^2}{1 + L(m_0^2 - 1)}, \quad (3.37)$$

with a typical width γ . From this equation we can see that ω_{\max} is an increasing function of L . This means that low values of L give a red feature (shifted towards long wavelengths, low frequencies), while high values of L result in a blue feature (shifted towards short wavelengths, high frequencies). Eq. (3.37) shows that the position of a resonance, ω_{\max} , caused by a dust grain in the Rayleigh domain must obey the inequality

$$\omega_0^2 \leq \omega_{\max}^2 \leq \omega_0^2 + \frac{f\omega_p^2}{1 + (m_0^2 - 1)}. \quad (3.38)$$

The maximum value of the imaginary part of the polarizability for a given Lorentz

oscillator is also determined by the form-factor L . Furthermore,

$$\max [\operatorname{Im}(\alpha)] \propto \left(\frac{1}{1 + L(m_0^2 - 1)} \right)^2. \quad (3.39)$$

Thus, a low value of L will result in a high value of the imaginary part of the polarizability. Combining this with the fact that low values of L give a red feature, and that all of the form-factor distributions we computed give more weight to the lower values of L than to the higher values, we conclude that, in general, particle shape effects tend to a broadening and a red-shift of the spectral features. This is in agreement with the findings of Min et al. (2003b).

3.4.3 The statistical approach

The method described in this paper provides a strong argument in favor of the main assumption of the statistical approach, namely that the optical properties of an ensemble of irregularly shaped particles can be represented in a statistical sense by the average properties of an ensemble of particles with the same composition, but with simple shapes. We have proved that for the absorption properties of particles in the Rayleigh domain, the statistical approach has an analytical basis given by the form-factor distribution. This implies that the average absorption cross section of an ensemble of arbitrarily shaped and arbitrarily oriented particles can be represented by a shape distribution of spheroidal particles with the same composition and in a fixed orientation.

We note that the form-factor distribution only provides the absorption cross sections, and not the scattering properties of small particles. It is in general not possible to find a distribution of spheroidal particles that gives both the absorption and the scattering cross section of an ensemble of arbitrarily shaped particles for every value of the refractive index. For an ensemble of ellipsoidal particles there is a relation between the scattering and the absorption cross section which is independent of the shape of the ellipsoids and is given by (Min et al. 2003b)

$$C_{\text{sca}} = \frac{k^3 V |m^2 - 1|^2}{6\pi \operatorname{Im}(m^2)} C_{\text{abs}}. \quad (3.40)$$

From Eqs. (3.21) and (3.22) it is clear that for arbitrarily shaped particles such a simple relation which is independent of the particle shape can only be found in very specific cases. This implies that in general there is no shape distribution of spheroids that can provide both the absorption and the scattering cross sections of an arbitrarily shaped particle for every value of the refractive index.

3.4.4 Extrapolation to larger particles

The form factor distribution can be used to construct for a given ensemble of irregularly shaped particles a shape distribution of simply shaped particles that has the same absorption properties in the Rayleigh domain. This distribution of simply shaped particles can

be used for computations outside the Rayleigh domain. Combining the form-factor distribution of an irregularly shaped particle, $\mathcal{P}(L)$, with the equations for the form-factor of a spheroid with the field applied along the rotation axis, $L(a/b)$ (see Eq. 3.8), the shape distribution of spheroids corresponding to this irregular particle shape is given by

$$\mathcal{P}(a/b) = \mathcal{P}(L(a/b)) \left| \frac{dL(a/b)}{d(a/b)} \right|. \quad (3.41)$$

Computations for spheroids in a fixed orientation can be computed relatively fast for large particles using for example the Separation of Variables Method (SVM, Voshchinnikov & Farafonov 1993) or the T-matrix method (Mishchenko et al. 1996). Thus, Eq. (3.41) provides a well founded choice for a distribution of spheroidal particles that can be employed for the computation of absorption properties of arbitrarily shaped particles with sizes outside the Rayleigh domain. However, it needs to be proven that this approach provides the correct optical properties in all cases.

3.5 Conclusions

We have presented an easy to use method to compute the absorption and scattering properties of small particles with arbitrary shape, structure, orientation and composition. The method is based on a solution of the DDA equations in the Rayleigh domain. For a given geometrical shape of the particles, the solution has to be computed only once to obtain the absorption and scattering properties for arbitrary values of the refractive index. This provides a significant speedup of the computations in cases where calculations for many values of the refractive index have to be done. For example, it allows for fast computations of absorption spectra of arbitrarily shaped and arbitrarily oriented particles in the Rayleigh domain. Other practical applications are, for example, interpretation of atmospheric and radar measurements as well as calculations of the scattering matrix of small particles as a function of the scattering angle.

The method we use can be employed for calculating a form-factor distribution. This distribution uniquely determines the absorption properties of a particle or an ensemble of particles. Using the form-factor distribution, we have studied the basis of the statistical approach in the Rayleigh domain. Various shape distributions of particles can then exhibit the same absorption properties. Two ensembles of dust grains with the same composition and the same average form-factor distribution, but with different shape distributions have exactly the same absorption properties. Therefore, it is not possible to distinguish between these two ensembles from their absorption properties alone. Furthermore, for a given form-factor distribution it is trivial to obtain a distribution of spheroidal shapes with exactly the same average form-factor distribution. This provides a strong argument in favor of the fundamental assumption of the statistical approach, i.e. that the average absorption and scattering properties of an ensemble of irregularly shaped particles can be represented by an ensemble of simple shapes.

The form-factor distribution uniquely determines the absorption properties of arbitrarily shaped particles allowing for the construction of a shape distribution of spheroids with the same composition and a fixed orientation with the same average absorption

cross section. It is, however, in general not possible to obtain a shape distribution of spheroidal particles with both the same average absorption and the same average scattering cross section. It needs to be investigated what the error on the computed scattering properties is when using the shape distribution of spheroids.

The conclusions presented in this paper are valid for particles in the Rayleigh domain. The form-factor distribution of an ensemble of irregularly shaped particles can be used to construct a shape distribution of spheroidal particles in a fixed orientation with exactly the same absorption properties in the Rayleigh domain. Since the absorption properties of spheroidal particles in a fixed orientation can be obtained relatively easy also for larger particles (i.e. outside the Rayleigh domain), this shape distribution provides a well founded choice for studying combined particle size and shape effects.

Acknowledgments

We are grateful to M. I. Mishchenko for valuable comments on an earlier version of this manuscript.

4

Scattering and absorption cross sections for randomly oriented spheroids of arbitrary size

M. Min, J. W. Hovenier, and A. de Koter

Journal of Quantitative Spectroscopy & Radiative Transfer, v.79-80, p.939-951 (2003)

Abstract

We present a useful practical approach for calculating extinction, absorption and (single) scattering cross sections for scattering by size-shape distributions of randomly oriented spheroids using a combination of various techniques and approximations. Wide ranges of refractive indices and size parameters are considered. We compare the optical cross sections of randomly oriented spheroids to those of volume equivalent spheres. Using the T-matrix method in combination with Geometrical Optics and Anomalous Diffraction theory, the optical cross sections of size-shape distributions of prolate and oblate spheroids with aspect ratios up to 5 can be computed within an accuracy of about 8% for all values of the size parameter and a wide range of refractive indices.

4.1 Introduction

The astrophysical interpretation of images and spectra at optical and infrared wavelengths of circumstellar material often requires knowledge of the scattering and absorption cross sections of ensembles of particles over wide ranges of size parameters and refractive indices (see e.g. Waters et al. 1997/1998). The large range of size parameters is needed in order to cover a large wavelength range from the ultraviolet to the infrared, such that, for example, grain temperatures may be determined. The wide range of refractive indices is necessary in order to model, for example, the resonances in crystalline silicates. To compute such cross sections it is usually assumed (i) that the particles are spherical, so that Mie theory can be used, or (ii) that the particles are nonspherical, but small compared to the wavelength and, in addition, that a so-called continuous distribution of randomly oriented ellipsoids (CDE) can be used to compute the optical cross sections (Bohren & Huffman 1983, Ch. 12).

Since it is very likely that the particles in circumstellar material are nonspherical and not always smaller than the wavelength, it is important to seek ways to compute

optical cross sections beyond these assumptions. In this context the so-called statistical approach (Bohren & Huffman 1983; Kahnert et al. 2002) is important. According to this approach one may try to represent the average scattering and absorption properties of a collection of particles having different shapes by using shape distributions of fairly regular particles like spheroids. Indeed, Mishchenko et al. (1997) found very good agreement between a phase function computed with this approach and one measured for micrometer sized irregularly shaped soil particles. Thus, studies of light scattering by spheroids are not only important in themselves but of much wider importance in the framework of the statistical approach.

In this paper we present a methodology to compute optical cross sections for uniform shape distributions of polydisperse randomly oriented oblate and prolate spheroids, relative to those of volume equivalent spheres. We use volume equivalent spheres, and not surface equivalent spheres, to keep the total mass in the collection of particles under consideration the same, so that we can concentrate on the shape effects. In addition to approximations for very small and very large spheroids we use the T-matrix method for computing the optical cross sections for the size-shape distributions of randomly oriented spheroids. We consider particles in random orientation since this is quite common in planetary atmospheres and astrophysical environments due to turbulence. Comparisons of scattering by nonspherical particles with volume or surface equivalent spheres can also be found in Mishchenko & Travis (1994); Mishchenko et al. (1996); Mishchenko et al. (1996); Krotkov et al. (1999). Here we focus on wide ranges of refractive indices and size parameters.

Some general theoretical aspects and limiting cases for very small and very large particles are discussed in section 4.2. Computational results are presented and discussed in section 4.3. Conclusions and a practical scheme for calculating cross sections for scattering and absorption by size-shape distributions of randomly oriented spheroids are presented in section 4.4.

4.2 Theoretical aspects

4.2.1 General

In this study the scattering and absorption cross sections of spheroids are first averaged over all orientations. After that, following Van de Hulst (van de Hulst 1957, Ch. 21), we average over sizes by using a narrow uniform size distribution to eliminate most interference effects (tiny ripples), namely

$$n(r) = \begin{cases} 2/r_m, & 0.75 r_m \leq r \leq 1.25 r_m, \\ 0, & \text{elsewhere,} \end{cases} \quad (4.1)$$

where $n(r)dr$ is the fraction of volume-equivalent spheres with radii between r and $r + dr$ per unit volume. The size distribution is centered around a radius r_m , which we will refer to as the average radius, and is normalized to unity (see Fig. 4.1). The size parameter $x = 2\pi r/\lambda$, where λ is the wavelength of the incident radiation. The cross sections averaged over the size distribution will be denoted by $\langle C \rangle$. Finally, we average

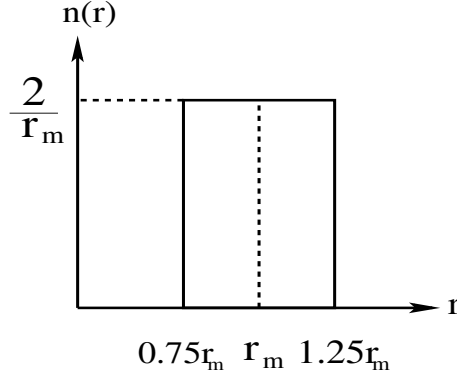


Figure 4.1: Uniform size distribution for volume equivalent spheres with radii near r_m .

over a mixture of prolate and oblate shapes of the spheroids. In our notation $2b$ is the length of the axis of rotation of the spheroid and $2a$ is the length of the other axis. So the aspect ratio a/b is smaller than one for prolate spheroids and larger than one for oblate spheroids. For the oblate spheroids we use a uniform shape distribution in a/b and for the prolate spheroids a uniform shape distribution in b/a . The size and shape averaged cross sections will be denoted by $\langle\langle C \rangle\rangle$.

In order to investigate the effects of non-sphericity, we calculate the ratios $\langle\langle C \rangle\rangle/\langle C^V \rangle$, where $\langle C^V \rangle$ is the average cross section pertaining to the size distribution (Eq. (4.1)) of volume equivalent spheres. An additional advantage of considering these ratios is that they can be easily calculated in the limiting case of large spheroids. Naturally, knowledge of each such ratio readily provides $\langle\langle C \rangle\rangle$ since $\langle C^V \rangle$ can always be accurately computed using Mie theory. We study the ratios $\langle\langle C \rangle\rangle/\langle C^V \rangle$ as functions of the so called phase-shift parameter $\rho = 2x_m|\text{Re}(m) - 1|$ (see van de Hulst 1957, Ch. 11), where the average size parameter $x_m = 2\pi r_m/\lambda$ and m is the complex refractive index. In this paper $\text{Im}(m)$ is non-negative. Although the phase-shift parameter only denotes an actual phase-shift in the case of spherical particles and is mainly useful for optically soft particles ($|m - 1| \ll 1$), it is in fact a useful parameter for all particles, whether they are optically soft or not.

For modeling circumstellar matter it is important to know the scattering properties of particles for a wide range of refractive indices. Especially in crystalline silicates the refractive index can vary enormously with wavelength, sometimes up to about $m = 9 + 9i$, but mostly below $\text{Re}(m) \approx 6$. An example is shown in Fig. 4.2. We can see from this figure that refractive indices with $\text{Re}(m) < 1$ also occur. This is also true for other silicates, both amorphous and crystalline. The results presented in this paper cover $\text{Re}(m) \leq 6$ and arbitrary $\text{Im}(m)$.

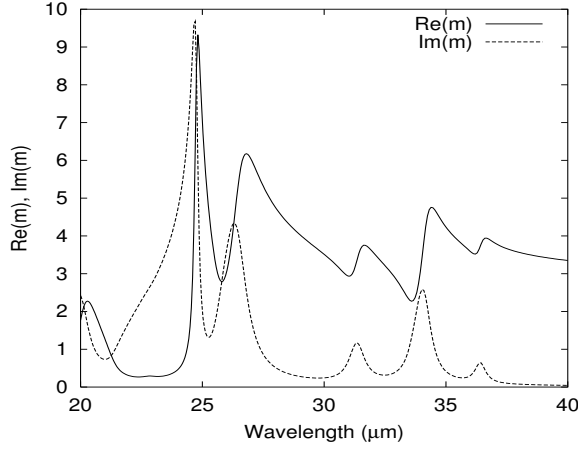


Figure 4.2: The real and imaginary part of the refractive index of one of the crystallographic axes of forsterite as functions of wavelength. The data were taken from Servoin & Piriou (1973)

4.2.2 Particles small compared to the wavelength

In the limit for particles small compared to the wavelength inside and outside the particle ($x \ll 1$ and $|mx| \ll 1$), the Rayleigh or electrostatic limit, we can calculate the cross sections for absorption and scattering of a spheroid with volume V averaged over all orientations from

$$\begin{aligned} C_{\text{abs}} &= kV \operatorname{Im}(\alpha_1 + 2\alpha_2), \\ C_{\text{sca}} &= \frac{k^4 V^2}{2\pi} [|\alpha_1|^2 + 2|\alpha_2|^2]. \end{aligned} \quad (4.2)$$

Here $k = 2\pi/\lambda$ and α_i is the polarizability per unit volume given by,

$$\begin{aligned} \alpha_1 &= \frac{m^2 - 1}{3 + 3L(m^2 - 1)}, \\ \alpha_2 &= \frac{m^2 - 1}{3 + 3\frac{1-L}{2}(m^2 - 1)}, \end{aligned} \quad (4.3)$$

where the so-called form factor L is defined by the shape of the spheroid (see (see Bohren & Huffman 1983).

Using Eqs. (4.2)-(4.3) we can derive a simple relation between the cross sections for scattering and absorption of a spheroid, averaged over all orientations. It can be shown that (Min et al. 2003b)

$$C_{\text{abs}} = \sigma C_{\text{sca}}, \quad (4.4)$$

with

$$\sigma = \frac{6\pi}{k^3 V} \frac{\operatorname{Im}(m^2)}{|m^2 - 1|^2}. \quad (4.5)$$

It should be emphasized that σ does not depend on the shape of the spheroid. Consequently, the single scattering albedo, ϖ , that follows from Eq. (4.4), is also independent of the shape of the spheroid and given by

$$\varpi = \frac{C_{\text{sca}}}{C_{\text{sca}} + C_{\text{abs}}} = \frac{1}{1 + \sigma}. \quad (4.6)$$

Clearly, Eq. (4.4) is also valid for a shape distribution of spheroids with equal volume. Using this it can be easily verified that in the Rayleigh limit the ratios we want to calculate are the same for scattering, absorption and extinction and are given by

$$\frac{\langle\langle C_{\text{ext}} \rangle\rangle}{\langle C_{\text{ext}}^V \rangle} = \frac{\langle\langle C_{\text{sca}} \rangle\rangle}{\langle C_{\text{sca}}^V \rangle} = \frac{\langle\langle C_{\text{abs}} \rangle\rangle}{\langle C_{\text{abs}}^V \rangle} = \frac{\text{Im}[\langle\langle \alpha_1 + 2\alpha_2 \rangle\rangle]}{\text{Im}[\alpha^V]}, \quad (4.7)$$

where $\langle\langle \alpha_1 + 2\alpha_2 \rangle\rangle$ is the shape and orientation averaged polarizability per unit volume of the spheroids and α^V is the polarizability per unit volume of a volume equivalent sphere ($L = 1/3$). It should be noted that the ratios given in Eq. (4.7) depend on the refractive index but are independent of the average radius r_m .

4.2.3 Particles large compared to the wavelength

In the limit for particles large compared to the wavelength ($x \gg 1$ and $2x|\text{Re}(m) - 1| \gg 1$) we can treat the electromagnetic waves as single geometrical rays and we can apply the laws of Geometrical Optics. In this limit it can be shown that the extinction cross section of a convex particle averaged over all orientations, is simply (van de Hulst 1957),

$$C_{\text{ext}} = 2G, \quad (4.8)$$

where G is the area of the geometrical shadow of the particle averaged over all orientations. If the particle is large enough and there is at least a little absorption, so that every ray that enters the particle is completely absorbed inside the particle, the scattering cross section consists of a term due to reflection at the boundary of the particle and a term due to diffraction which is equal to G . So, for any convex particle the scattering and absorption cross sections averaged over all orientations can be written as (Bohren & Huffman 1983, Ch. 7),

$$\begin{aligned} C_{\text{sca}} &= G + G\mathcal{R}, \\ C_{\text{abs}} &= G - G\mathcal{R}, \end{aligned} \quad (4.9)$$

where \mathcal{R} is a reflection factor which does not depend on the size and shape of the particle.

Because Eqs. (4.8)-(4.9) are valid for all randomly oriented convex particles, it is clear that for all these particles in the Geometrical Optics limit the albedo of single scattering,

$$\varpi = \frac{1 + \mathcal{R}}{2}. \quad (4.10)$$

It follows from Eqs. (4.8)-(4.9) that the ratios we are interested in are again the same for scattering, absorption and extinction and are equal to

$$\frac{\langle\langle C_{\text{ext}} \rangle\rangle}{\langle C_{\text{ext}}^V \rangle} = \frac{\langle\langle C_{\text{sca}} \rangle\rangle}{\langle C_{\text{sca}}^V \rangle} = \frac{\langle\langle C_{\text{abs}} \rangle\rangle}{\langle C_{\text{abs}}^V \rangle} = \frac{\langle\langle G_{\text{Spheroid}} \rangle\rangle}{\langle G_{\text{Sphere}} \rangle}, \quad (4.11)$$

where $\langle\langle G_{\text{Spheroid}} \rangle\rangle$ is the average geometrical shadow area of an ensemble of spheroids averaged over size, shape and orientation and $\langle G_{\text{Sphere}} \rangle$ is the average geometrical shadow area of a size distribution of volume equivalent spheres. If there is no absorption at all Eq. (4.11) reduces to the ratios at the far left and far right hand sides. The shadow areas of both the spheroids and the spheres are proportional to $V^{2/3}$. Because we use the same size distribution for the spheroids and the volume equivalent spheres, the ratios in Eq. (4.11) do not depend on the size of the particles. This means that these ratios are the same for all values of the refractive index and the phase-shift parameter in the Geometrical Optics limit.

We can calculate the ratio of the shadow areas in Eq. (4.11) using analytical formulas. For an oblate spheroid with aspect ratio a/b averaged over all orientations and a volume equivalent sphere the ratio of the shadow areas is (Krotkov et al. 1999)

$$\frac{G_{\text{Spheroid}}}{G_{\text{Sphere}}} = \frac{1}{2}(1 - \gamma^2)^{-1/3} + \frac{1}{4\gamma}(1 - \gamma^2)^{2/3} \ln\left(\frac{1 + \gamma}{1 - \gamma}\right) \quad [\gamma^2 = 1 - b^2/a^2], \quad (4.12)$$

and similarly for a prolate spheroid

$$\frac{G_{\text{Spheroid}}}{G_{\text{Sphere}}} = \frac{1}{2}(1 - \gamma^2)^{1/3} + \frac{1}{2\gamma}(1 - \gamma^2)^{-1/6} \arcsin \gamma \quad [\gamma^2 = 1 - a^2/b^2]. \quad (4.13)$$

These values still have to be averaged over the shape distribution.

4.3 Computational results

Numerical computations are necessary when the particles are neither small nor large compared to the wavelength. For this purpose we used the T-matrix method to calculate the cross sections. But this method cannot be used for arbitrary values of the input parameters. Due to numerical instability, large values of the size parameter or the phase shift parameter cannot be accommodated using this method. For the same reason it is not possible to calculate cross sections for very elongated or flattened shapes. In our case, where we want to average over shapes and sizes in a lot of different domains in parameter space, we also have to take into account the computational speed. For large values of the size parameter, the phase-shift parameter or the aspect ratio, the convergence of the method is too slow for our purpose. We will say the method *breaks down* when the computer code is not stable anymore or when it is stable but too slow for our purpose. For a detailed evaluation of the capabilities and limitations of the code we refer to Mishchenko & Travis (1998).

By way of example the ratios $\langle\langle C \rangle\rangle/\langle C^V \rangle$ are plotted in Fig. 4.3 for uniform shape distributions of spheroids with $\frac{1}{2} \leq a/b \leq 2$ for several values of the refractive index,

m . The horizontal lines in the figures show the values of the ratios of the geometrical shadows according to Eqs. (4.12)-(4.13) after averaging over the shape distributions. We will call this ratio the geometrical limit (GL). Fig. 4.3 shows that large differences from Mie theory may occur and that rather smooth transitions to the GL are quite normal, albeit within a certain accuracy. We notice that there is some similarity between the graphs for different values of m . This similarity is due to the fact that we used the phase-shift parameter instead of the size parameter. We also notice that the limits for $\rho \rightarrow 0$ and $\rho \rightarrow \infty$ are the same for extinction, scattering and absorption, while the limit for $\rho \rightarrow \infty$ is refractive index independent. This is in agreement with Eqs. (4.7) and (4.11). To check our numerical computations we verified that indeed the values found with the T-matrix method in these limits are in complete agreement with Eqs. (4.7) and (4.11).

We define $\rho_0(\epsilon)$ to be the smallest value of the phase-shift parameter for which the differences with the GL values for all three types of cross sections are within ϵ for all $\rho > \rho_0(\epsilon)$. Fig. 4.3 illustrates that for the aspect ratios and refractive indices considered we reach $\rho_0(3\%)$ before the T-matrix method breaks down. For values of m close to unity the calculations are more time consuming. This can be understood by inspection of Fig. 4.3 which shows that the GL is always reached at approximately the same value of ρ , the phase-shift parameter. Therefore, when $|\text{Re}(m) - 1|$ decreases we have to increase the size parameter in order to reach the same value of the phase-shift parameter. Although the T-matrix calculations for these values of the refractive index can be performed for larger values of the size parameter, this often takes a lot of computational time. However it is possible to do so for uniform shape distributions of spheroids with $\frac{1}{2} \leq a/b \leq 2$ when an accuracy of 3% is sufficient.

It may seem that $\rho_0(3\%)$ is not reached for $m = 1.5 + 0.0i$ in Fig. 4.3. However, from the strong similarity between the graphs for $m = 1.5$ and $m > 1.5$, we can determine that for values of ρ larger than where the curve stops in Fig. 4.3 the oscillations in the graph for $m = 1.5$ will not deviate more than 3% from the GL. This means that we can calculate all cross sections for uniform distributions of spheroids with $\frac{1}{2} \leq a/b \leq 2$ within an error of 3% for all values of the phase-shift parameter, using the T-matrix for $\rho \leq \rho_0(3\%)$ and Mie calculations for volume equivalent spheres for $\rho > \rho_0(3\%)$ in conjunction with Eq. (4.11). We have checked that this is true for all values of the refractive index with real parts up to 6 and arbitrary imaginary parts, using $\rho_0(3\%) = 20$.

In the statistical approach it is desirable to have as many shapes in the distribution as possible. For example, it seems likely that very spiked or edgy particles are best represented by very elongated or flattened spheroidal shapes. This means that we would like to broaden the shape distribution to more extreme values of the aspect ratio. Therefore we also considered uniform shape distributions of spheroids with $\frac{1}{5} \leq a/b \leq 5$. Some results are shown in Fig. 4.4. Here the T-matrix method breaks down before $\rho_0(3\%)$ is reached and this problem becomes more severe when $\text{Re}(m)$ approaches unity. However, for all values of the refractive index with real parts up to 6 and arbitrary imaginary parts we can reach $\rho_0(16\%)$ for all cross sections. So for these refractive indices and this distribution of aspect ratios we can calculate the cross sections for all values of the size parameter within an error of 16% using $\rho_0(16\%) = 9$.

It should be mentioned that in both Fig. 4.3 and Fig. 4.4 the geometrical *optics* limit

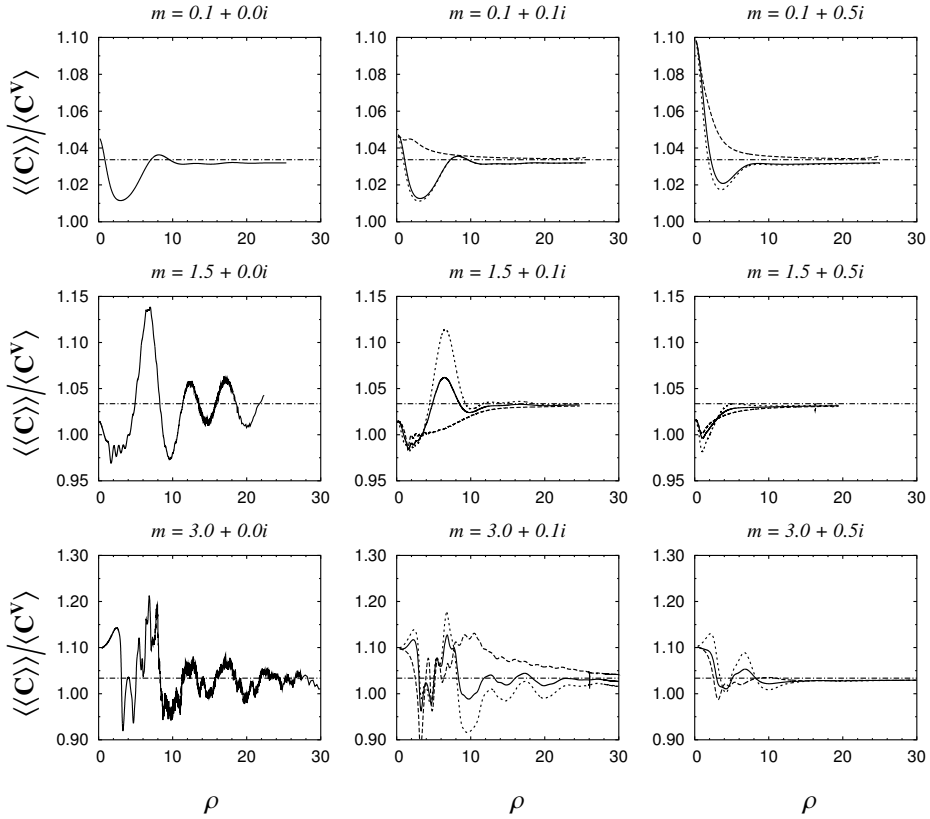


Figure 4.3: Optical cross sections of a size-shape distribution of randomly oriented spheroids divided by the corresponding cross sections of a size distribution of volume equivalent spheres as functions of the average phase-shift parameter, $\rho = 2x_m |\operatorname{Re}(m) - 1| = 4\pi r_m \lambda^{-1} |\operatorname{Re}(m) - 1|$, for different values of the refractive index, m . The cross sections for extinction (solid curves), scattering (dotted curves) and absorption (dashed curves) are shown. The shape distribution of spheroids covers the range $\frac{1}{2} \leq a/b \leq 2$. Not all minor wiggles are shown. The horizontal straight lines indicate the geometrical limits, i.e. the ratios for $\rho \rightarrow \infty$.

is not yet reached within the mentioned accuracy. The limit reached here is the GL for $\langle\langle C \rangle\rangle / \langle\langle C^V \rangle\rangle$ (see Eqs. (4.12)-(4.13)). This means that to calculate the cross sections for $\rho > \rho_0(\epsilon)$, it is better not to use geometrical optics but to perform Mie calculations for volume equivalent spheres and to multiply the resulting cross sections by the geometrical limit. This is illustrated by the example shown in Fig. 4.5. Here the average extinction efficiency, $\langle\langle Q_{\text{ext}} \rangle\rangle \equiv \langle\langle C_{\text{ext}} \rangle\rangle / \langle\langle G \rangle\rangle$, is plotted versus the phase-shift parameter for uniform distributions of spheroids and volume equivalent spheres with the same value of the refractive index. We see that the extinction efficiencies of the spheres and the spheroids converge towards each other before converging towards the Geometrical Optics limit of $\langle\langle Q_{\text{ext}} \rangle\rangle = 2$ (see Eq. (4.8)). Consequently, it is advantageous to

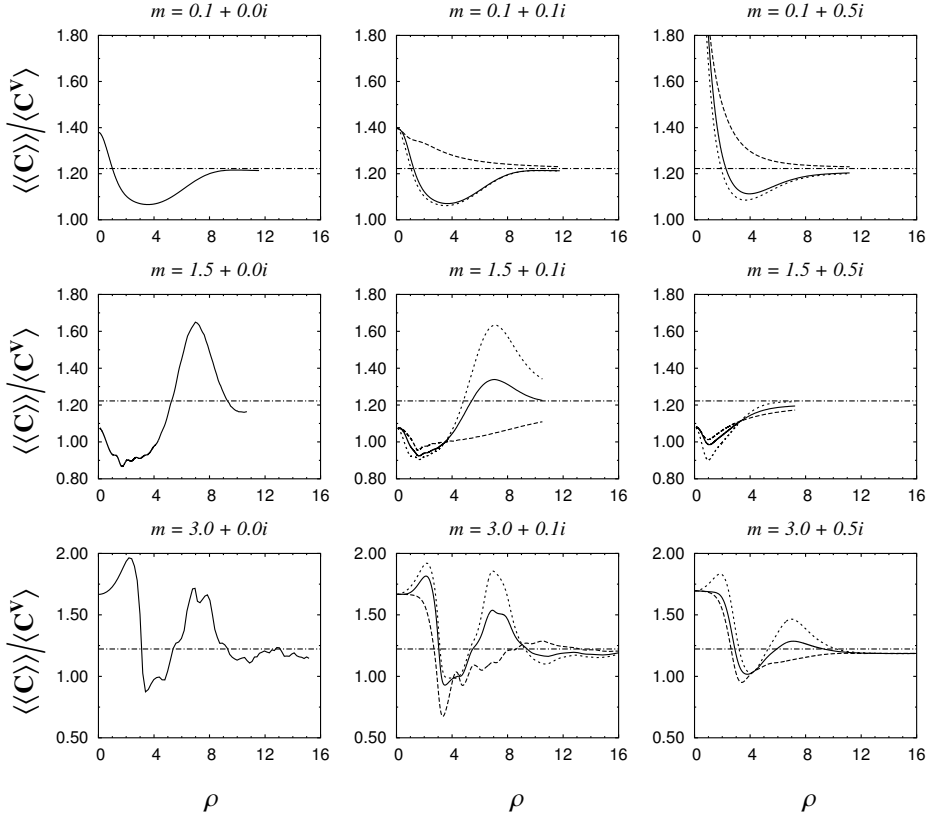


Figure 4.4: Same as Fig. 4.3 but for a size-shape distribution of randomly oriented spheroids with $\frac{1}{5} \leq a/b \leq 5$. The limiting value for $m = 0.1 + 0.5i$ if $\rho \rightarrow 0$ equals 2.57.

conduct not only T-matrix calculations for the cross sections of the spheroids, but also Mie calculations for their volume equivalent spheres.

The accuracy of 16% reached for the shape distribution with $\frac{1}{5} \leq a/b \leq 5$ is not really satisfactory. We can improve on this result when we realize that the values of the refractive index where the worst accuracy was achieved, were close to unity. This suggests that we may use the theory of Anomalous Diffraction (van de Hulst 1957, see Appendix A) to get a better accuracy. For this purpose we calculated both the average cross sections of the size-shape distribution of randomly oriented spheroids and those of the size distribution of volume equivalent spheres with Anomalous Diffraction. By using the T-matrix method and Mie theory, we then calculated the ratio,

$$\delta = \frac{\langle\langle C \rangle\rangle \langle C_{AD}^V \rangle}{\langle C^V \rangle \langle\langle C_{AD} \rangle\rangle}, \quad (4.14)$$

for extinction, absorption and scattering and for various values of ρ . Here the subscript AD denotes Anomalous Diffraction. This ratio converges to unity for $x_m \rightarrow \infty$ and

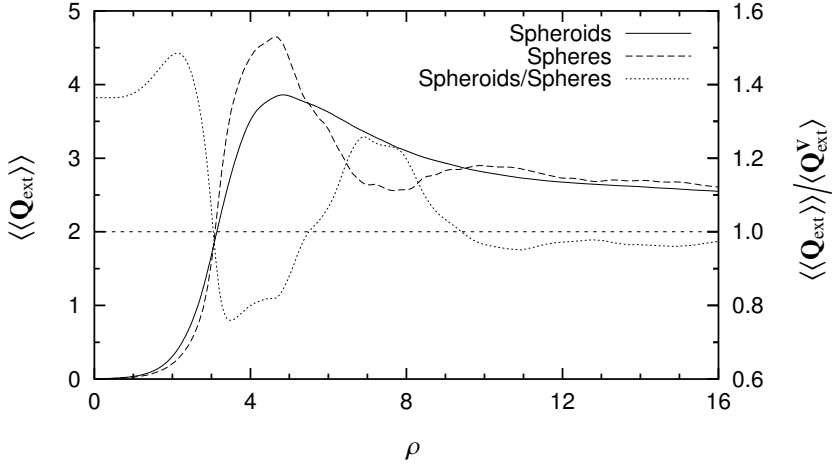


Figure 4.5: The size and shape averaged extinction efficiencies versus the phase-shift parameter of spheroids and spheres (scale on the left vertical axis). The refractive index is $m = 3.0 + 0.1i$. The uniform shape distributions of spheroids cover the range $\frac{1}{5} \leq a/b \leq 5$. The dotted curve (scale on the right vertical axis) is the ratio of the two other curves and is close to unity for small values of ρ (≈ 12) relative to when the Geometrical Optics limit is reached ($\rho \approx 60$).

$|m - 1| \rightarrow 0$, where Anomalous Diffraction theory is valid. When we know for what values of ρ this ratio equals unity within the desired accuracy, we can calculate the cross-sections of the size-shape distribution of randomly oriented spheroids, $\langle\langle C \rangle\rangle$, in these regions very easily from Eq. (4.14) by taking $\delta = 1$.

The approach is illustrated in Fig. 4.6 for 4 different values of m . In this figure we plotted as an example the extinction, scattering and absorption efficiencies of the uniform distributions of spheroids as computed using T-matrix calculations (thick lines) and the the same efficiencies computed by putting $\delta = 1$ (thin lines). For these values of the refractive index, the geometrical limit is reached only within an accuracy of 16% [cf. Fig. 4.4]. Fig. 4.6 shows that a smooth transition between the curves computed by the two methods occurs at $\rho \approx 11$ for extinction scattering and absorption. By closer inspection it has been established that the error we make when using the ($\delta = 1$)-method is smaller than 8% for $\rho > 11$. Further computations showed that this holds for $0.5 < \text{Re}(m) < 2$. For values of m with $\text{Re}(m) < 1.5$, Anomalous Diffraction is a better approximation, and it turns out that indeed the error is smaller than 8%. For values of m with $2 \leq \text{Re}(m) \leq 6$ or $\text{Re}(m) \leq 0.5$, T-matrix calculations in conjunction with calculations from volume equivalent spheres (see Fig. 4.4) already provide us an accuracy of about 8%. Summarizing, this means that the combination of the T-matrix method, Mie calculations and Anomalous Diffraction theory give us the cross-sections of the size-shape distribution of randomly oriented spheroids with $\frac{1}{5} \leq a/b \leq 5$ for all values of the average size parameter, within an accuracy of about 8% for all values of the refractive index with real part up to 6 and arbitrary imaginary part.

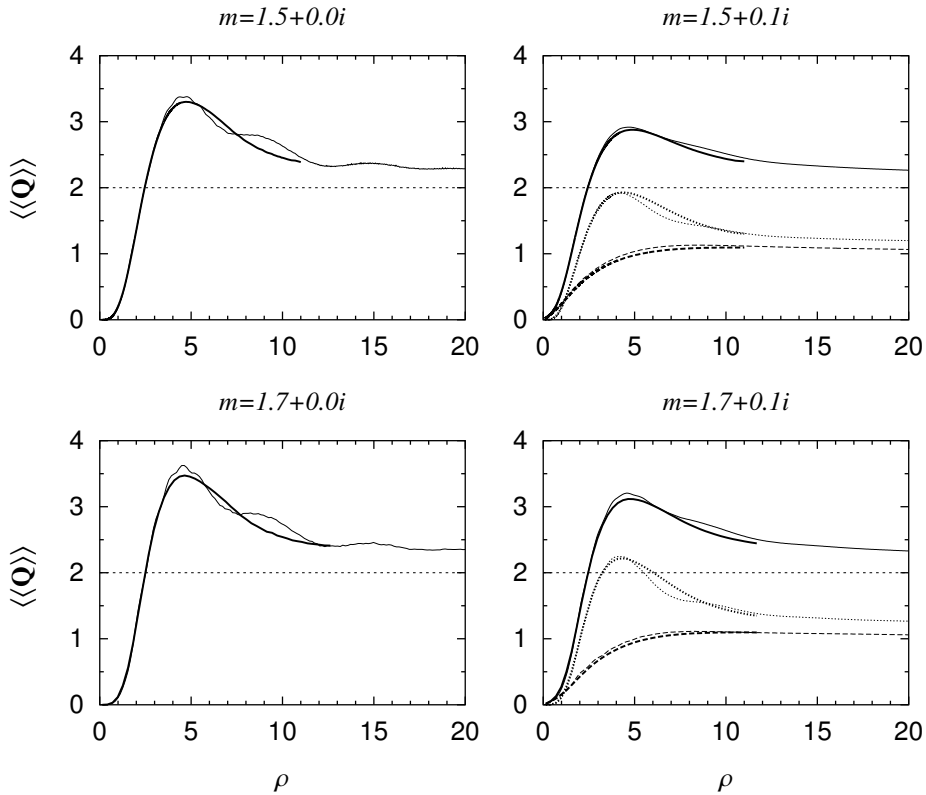


Figure 4.6: The size and shape averaged efficiencies for extinction (solid curves), scattering (dotted curves) and absorption (dashed curves) versus phase-shift parameter for uniform shape distributions of spheroids with $\frac{1}{5} \leq a/b \leq 5$ and various values of the refractive index. The thin curves are calculated by putting $\delta = 1$ and the thick curves are computed using T-matrix calculations. There is a smooth transition between the curves computed by the two methods at $\rho \approx 11$.

Besides the cross sections, the albedo of single scattering is also very interesting and important for many applications. We found in sections 4.2.2 and 4.2.3 that the albedos of small and large particles are the same for spheroids and volume equivalent spheres. Fig. 4.7 illustrates this and also shows that this is not the case in the intermediate region. Apparently, quite large deviations from Mie-theory can occur. However, in most cases the expected limits are reached early when ρ increases (within a certain accuracy) compared to the ratios of the cross sections (Figs. 4.3 and 4.4). It also seems that the relative deviations from Mie theory are for all values of the refractive index and for both shape distributions generally much smaller than in the case of the cross sections.

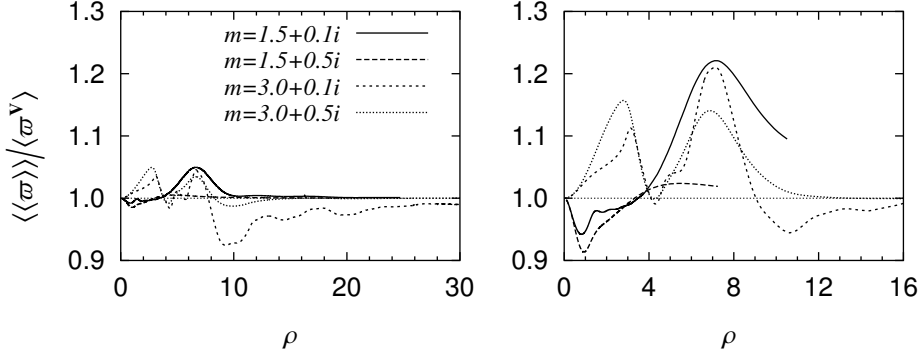


Figure 4.7: The average albedos for a size-shape distribution of randomly oriented spheroids divided by the average albedos of a size distribution of volume equivalent spheres as a function of the phase-shift parameter, $\rho = 2x_m|\text{Re}(m) - 1|$, for various values of the refractive index. The shape distribution covers the range $\frac{1}{2} \leq a/b \leq 2$ (left figure) and $\frac{1}{3} \leq a/b \leq 5$ (right figure). In the limits for $\rho \rightarrow 0$ and $\rho \rightarrow \infty$ these ratios converge to unity.

$\frac{1}{2} \leq a/b \leq 2$	
$\rho \leq 20$	T-matrix calculations
$\rho > 20$	$\langle\langle C \rangle\rangle = \frac{\langle\langle G_{\text{Spheroid}} \rangle\rangle}{G_{\text{Sphere}}} \langle C^V \rangle$

Table 4.1: Scheme for calculating the extinction, absorption and scattering cross sections of a size-shape distribution of randomly oriented spheroids with aspect ratios between $\frac{1}{2} \leq a/b \leq 2$. The accuracy of the cross sections is within 3% if $\text{Re}(m) \leq 6$ and $\text{Im}(m)$ is arbitrary.

4.4 Conclusions

The behavior of the (optical) cross sections of a size-shape distribution of spheroids divided by those of volume equivalent spheres is best described in terms of the phase-shift parameter $\rho = 2x_m|\text{Re}(m) - 1|$. For different values of the refractive index, convergence towards the geometrical limit is reached at comparable values of the phase-shift parameter.

It is possible to obtain extinction, absorption and scattering cross sections for a size-shape distribution of randomly oriented spheroids with aspect ratios between $\frac{1}{2} \leq a/b \leq 2$ for all values of the size parameter within an accuracy of 3% using only T-matrix calculations for spheroids with small and moderate values of the phase-shift parameter and Mie calculations combined with Eq. (4.11) for particles with large values of the phase-shift parameter. This can be done for values of the refractive index with real part up to 6 and arbitrary imaginary part. We showed that we do not need Geometrical Optics for calculating the cross sections.

We can calculate the cross sections for a size shape distribution of randomly oriented spheroids with aspect ratios between $\frac{1}{3} \leq a/b \leq 5$ within an accuracy of about 8% for all

$\frac{1}{5} \leq a/b \leq 5$		
$\text{Re}(m) \leq 0.5$	$\rho \leq 11$	T-matrix calculations
or $\text{Re}(m) \geq 2$	$\rho > 11$	$\langle\langle C \rangle\rangle = \frac{\langle\langle G_{\text{Spheroid}} \rangle\rangle}{G_{\text{Sphere}}} \langle C^V \rangle$
$0.5 < \text{Re}(m) < 2$	$\rho \leq 11$	T-matrix calculations
	$\rho > 11$	$\langle\langle C \rangle\rangle = \frac{\langle\langle C_{\text{AD}} \rangle\rangle}{\langle C_{\text{AD}}^V \rangle} \langle C^V \rangle$

Table 4.2: Scheme for calculating the extinction, absorption and scattering cross sections of a size-shape distribution of randomly oriented spheroids with aspect ratios between $\frac{1}{5} \leq a/b \leq 5$. The accuracy of the cross sections is within 8% if $\text{Re}(m) \leq 6$ and $\text{Im}(m)$ is arbitrary.

values of the size parameter using the same method but in combination with Anomalous Diffraction theory for values of the refractive index close to unity. This accuracy can be attained for values of the refractive index with real part up to 6 and arbitrary imaginary part.

To summarize the results of our numerical computations we present a practical scheme for calculating the cross sections with an accuracy sufficient for many practical applications. For the size-shape distributions with aspect ratios $\frac{1}{2} \leq a/b \leq 2$ and $\frac{1}{5} \leq a/b \leq 5$, respectively, the best ways to calculate the cross sections are summarized in Tables 4.1 and 4.2. It should be noted that in both cases calculations for spheres, using Mie-theory, and numerical implementation of Anomalous Diffraction theory can be done very easily and with high accuracy.

In conclusion, we have presented a methodology to apply the statistical approach for cross sections and albedos of single scattering, by employing shape distributions of spheroids with arbitrary sizes.

Acknowledgments

It is a pleasure to express our gratitude to M. I. Mishchenko for fruitful discussions and for providing us with his T-matrix code. We are indebted to L. B. F. M. Waters for enlightening conversations. AdK also kindly acknowledges support from NWO Pionier grant 600-78-333 to L. B. F. M. Waters and from NWO Spinoza grant 08-0 to E. P. J. van den Heuvel.

Appendix A: Anomalous Diffraction

In this Appendix we will show how $\langle C_{AD}^V \rangle$ and $\langle\langle C_{AD} \rangle\rangle$ occurring in Eq. (4.14) can be calculated. The theory of Anomalous Diffraction, first developed by Van de Hulst (van de Hulst 1957, Ch. 11), is based on the assumptions $x \gg 1$ and $|m - 1| \ll 1$ and can be applied for any value of $2x|\text{Re}(m) - 1|$. The extinction, absorption and scattering efficiencies (cross sections divided by geometrical shadow areas) of a sphere with refractive index $m = n + in'$ then become

$$Q_{\text{ext}} = 4\text{Re}(K(ip^*)), \quad (4.15)$$

$$Q_{\text{abs}} = 2K(4xn'), \quad (4.16)$$

$$Q_{\text{sca}} = Q_{\text{ext}} - Q_{\text{abs}}, \quad (4.17)$$

with

$$\rho^* = 2x|n - 1| - i2xn', \quad (4.18)$$

$$K(z) = \frac{1}{2} + \frac{e^{-z}}{z} + \frac{e^{-z} - 1}{z^2}. \quad (4.19)$$

The cross sections $\langle C_{AD}^V \rangle$ can now be calculated by multiplying the efficiencies of Eqs. (4.15)-(4.17) with the geometrical shadow area of a sphere ($G_{\text{Sphere}} = \pi r^2$) and averaging over the size distribution.

For a spheroid with aspect ratio a/b and $2b$ as the length of the axis of rotation, the only quantity that changes is the length of the path traveled through the particle. We can calculate the efficiencies for a spheroid in fixed orientation in the Anomalous Diffraction limit by using Eqs. (4.15)-(4.17) but with the size parameter, x , replaced by (Kokhanovsky 2001)

$$h = \frac{x_V(a/b)^{1/3}}{\sqrt{1 + ((a/b)^2 - 1)\cos^2\theta}}, \quad (4.20)$$

where a/b is the aspect ratio of the spheroid, x_V is the size parameter of a volume equivalent sphere and θ is the angle between the axis of rotation of the spheroid and the incoming light beam. The area of the geometrical shadow of an oblate or prolate spheroid oriented in this way is (Kokhanovsky 2001)

$$G_{\text{Spheroid}}(\theta) = \pi r_V^2 \frac{\sqrt{1 + ((a/b)^2 - 1)\cos^2\theta}}{(a/b)^{1/3}} \quad (4.21)$$

where r_V is the radius of the volume equivalent sphere. We can now calculate $\langle\langle C_{AD} \rangle\rangle$ by first multiplying the efficiencies calculated from Eqs. (4.15)-(4.20) by the geometrical shadow area given by Eq. (4.21) and then averaging over all orientations and the size-shape distributions.

5

Modeling optical properties of cosmic dust grains using a distribution of hollow spheres

*M. Min, J. W. Hovenier, and A. de Koter
Astronomy & Astrophysics, v.432, p.909-920 (2005)*

Abstract

In this paper we study the combined effects of size and shape of small solid state particles on the absorption, emission and scattering characteristics. We use the statistical approach to calculate these optical properties. In this approach the average optical properties of an ensemble of particles in random orientation are represented by the average optical properties of an ensemble of simple shapes. The validity of this approach is studied in detail for a uniform distribution of hollow spheres where the fractional volume of the central inclusion is varied. We apply the results to two different areas of interest, i) infrared spectroscopy and ii) polarization of scattered light. The effects of particle size and shape on the optical characteristics are discussed. We compare the results using the distribution of hollow spheres with those obtained by using randomly oriented spheroids. Also we compare the results with observations and laboratory measurements. The distribution of hollow spheres is very successful in reproducing laboratory measurements of the scattering angle distribution of the degree of linear polarization for incident unpolarized light of randomly oriented irregular quartz particles. Furthermore, we show that we are able to derive the size distribution of dust grains by fitting the measured degree of linear polarization using computational result for hollow spheres. It is shown that the distribution of hollow spheres is a powerful tool for studying light scattering, absorption and emission by cosmic dust grains and in particular when large numbers of particle parameters need to be considered since the computational demand of the distribution of hollow spheres is small.

5.1 Introduction

Dust is an important constituent of many astrophysical as well as atmospheric environments. The interpretation of observed infrared spectra, images and polarization requires knowledge of the scattering, absorption and emission properties of dust particles of various compositions, shapes and sizes. Optical properties calculated with the widely used Mie theory, which is valid for homogeneous spherical particles, often do not give

satisfactory agreement with measurements and observations. Therefore, complicated methods have been developed to calculate the optical properties of irregularly shaped particles such as the Discrete Dipole Approximation (DDA) and the T-matrix method (see e.g. Purcell & Pennypacker 1973; Draine 1988; Mishchenko et al. 2000, 2002; Wriedt 2002; Kahnert 2003). For realistically shaped particles these methods are all very computationally expensive. Another approach to obtain optical properties of ensembles of irregularly shaped particles is the so-called statistical approach. In this approach the average optical properties of an ensemble of irregularly shaped particles are represented by the average properties of a distribution of simply shaped particles with a given shape distribution. Examples of simple shapes used in this way are spheroids and circular and hexagonal cylinders (Mishchenko & Travis 1994; Mishchenko et al. 1996; Kahnert et al. 2002; Kahnert 2004). In Min et al. (2003b) it was shown that the statistical approach is very successful in calculating the absorption cross sections of an ensemble of randomly oriented very small particles, i.e. in the Rayleigh regime, as a function of wavelength. In that paper also results of calculations were presented for a uniform distribution of hollow spherical particles, varying the volume fraction occupied by the central inclusion. This shape distribution reproduces the measured absorption cross sections of small crystalline forsterite particles remarkably well. Because of their spherical symmetry the optical properties of hollow spheres can be obtained easily by using an extension of Mie theory. This makes this grain model an ideal candidate for studies where a large number of calculations for various grain sizes and/or compositions is required.

Jones (1988) used hollow spherical grains to model grain porosity in the ultraviolet to near infrared. The computational results using hollow spheres were compared with those obtained by using effective medium theories. The main motivation of that study was to find out if porous grains could enhance the interstellar extinction per unit mass. This turned out to be of much astrophysical significance in view of the so-called 'carbon crisis' which was brought up 7 years later by Snow & Witt (1995). It was found that, although by using porous particles the extinction is enhanced at some wavelengths, it is decreased at other wavelengths, consistent with the expectation from the Kramers-Kronig relations (Purcell 1969). However, Jones (1988) argues that this problem might be solved by changing the size distribution of interstellar grains. We will discuss the effect of grain shape and porosity on the interstellar silicate extinction feature in the mid infrared by applying the hollow sphere model.

In this paper we will use a distribution of hollow spheres to calculate absorption, extinction and scattering properties for various particle sizes beyond the Rayleigh regime. We compare our results to those obtained by using a shape distribution of spheroidal particles and to laboratory measurements of the scattering properties of irregular particles.

In Sect. 5.2 we introduce the dust shape models employed in this paper. Then we will concentrate on two main areas; i) absorption and extinction spectra (Sect. 5.3) and ii) the degree of linear polarization (Sect. 5.4). Some examples of applications in both areas are provided. In Sect. 5.5 we discuss the physical interpretation of the results.

5.2 Dust shape models

In order to understand the effects of particle shape and internal structure on the emissivities of dust grains we consider two simple dust models. As a first approximation we change the internal structure of homogeneous spherical dust grains in the most simple way by using a distribution of hollow spherical particles, varying the volume fraction occupied by the central inclusion. In the second distribution we change the external shape of the homogeneous spherical particles by using a distribution of spheroidal particles, varying the aspect ratio. In these shape distributions the material volume of the particles is kept constant. Both shape distributions have been studied in the Rayleigh limit, i.e. when the particles are very small compared to the wavelength inside and outside the particle. In Min et al. (2003b) it was found that in this limit the absorption properties for the distribution of spheroidal particles and for the distribution of hollow spherical particles are very similar and that both shape distributions provide good agreement with laboratory measurements of the absorption cross sections as a function of wavelength in the infrared part of the spectrum. This suggests that the exact shape of the particles is to a certain degree not important as long as we break the perfect symmetry of a homogeneous sphere. When applying the statistical approach one needs to realize that the particle shapes used contain only very limited information on the real shapes of the dust grains and that additional research has to be done in order to decode this information into physical characteristics of the dust grains (see also e.g. Kahnert et al. 2002).

5.2.1 Distribution of Hollow Spheres (DHS)

The simplest internal deviation from a homogeneous sphere is a hollow spherical shell with the same material volume. In Min et al. (2003b) a Distribution of Hollow Spheres (DHS) is used to calculate the absorption cross sections for very small particles. In this shape distribution we simply average over the fraction f occupied by the central vacuum inclusion in the particle from zero to some value $f_{\max} \leq 1$, giving equal weights to all values of f while the material volume of the particle is kept the same. This means that the particles with higher values of f have a larger outer radius. Thus, the distribution is given by

$$n(f) = \begin{cases} 1/f_{\max}, & 0 \leq f < f_{\max}, \\ 0, & f \geq f_{\max}, \end{cases} \quad (5.1)$$

where $n(f)df$ is the fraction of the number of particles in the distribution between f and $f + df$. Unless stated otherwise, in this paper we will take $f_{\max} = 1$, the most extreme shape distribution. We have to note here that particles with $f = 1$ and a finite volume have an infinitely large outer radius. For particles much smaller than the wavelength, integrating the optical properties up to $f = 1$ can be done analytically (Min et al. 2003b). For larger particles numerical computations are necessary, but these are not possible for $f = 1$. However, we then chose f_{\max} large enough to reach convergence to the values for $f_{\max} = 1$. For most cases we considered, it suffices to integrate up to $f = 0.98$. The choice of the shape distribution we take is motivated by the fact that for many

applications one of the parameters of interest is the dust mass. Therefore, it is convenient to choose a shape distribution in which the total mass of the particles is conserved. Other choices of the shape distribution, e.g. conserving the surface area of the particles, might be convenient in other cases. The equations for the optical cross sections in the Rayleigh limit are provided by van de Hulst (1957). In Aden & Kerker (1951) the general equations for light scattering and absorption by layered spheres of arbitrary size are derived as a simple extension of Mie theory (Mie 1908). By taking the refractive index of the core of a layered particle to be that of vacuum these general equations can be used to calculate the optical properties of hollow spherical particles for almost all particle sizes.

The calculations were done using the layered sphere code for which the basic ideas are explained in Toon & Ackerman (1981). We successfully performed the Cloude test (see Hovenier & van der Mee 2000) on the 4×4 scattering matrix obtained with this code. Also we checked that the computed values of the scattering matrix obtained for forward and backward scattering are in agreement with theoretical values derived from symmetry arguments. In addition, we considered the limiting case $f \rightarrow 0$ and compared this with calculations for homogeneous spheres, all with satisfying results.

5.2.2 Uniform Distribution of Spheroids (UDS)

The simplest external deviation from a homogeneous sphere is a homogeneous spheroid with the same material volume. In Min et al. (2003a) a method was developed to calculate the optical cross sections of a Uniform Distribution of Spheroids (UDS) for every particle size using a combination of the T-matrix method (Mishchenko et al. 1996) and some approximate methods. In the UDS we average over the aspect ratios (i.e. the ratio between the major and minor axis) of the spheroids giving equal weights to all oblate and prolate spheroidal shapes. The material volume of all particles in the shape distribution is the same. For details we refer to Min et al. (2003b,a). Although the average absorption cross sections for this distribution can be calculated, the computations become very slow for intermediate sized particles (with sizes comparable to the wavelength of radiation) where we still have to apply the T-matrix method.

In this paper we will average the spheroidal shapes over all prolate and oblate shapes up to an aspect ratio of 10. This is at the moment the most extreme shape distribution for which calculations can be done in a reasonable time. For the T-matrix calculations we used the well tested code developed by Mishchenko & Travis (1998).

5.3 The absorption, extinction and emission spectra

Absorption, extinction and emission spectra of dust provide crucial information on the size and composition of the dust grains. The thermal emission spectrum of a dust grain in thermal equilibrium averaged over all orientations is proportional to the orientation averaged emission cross section times a Planck function. From Kirchhoff's law we know that this emission cross section is equal to the orientation averaged absorption cross section. The size of a particle, r_V , is defined to be the radius of a sphere with the

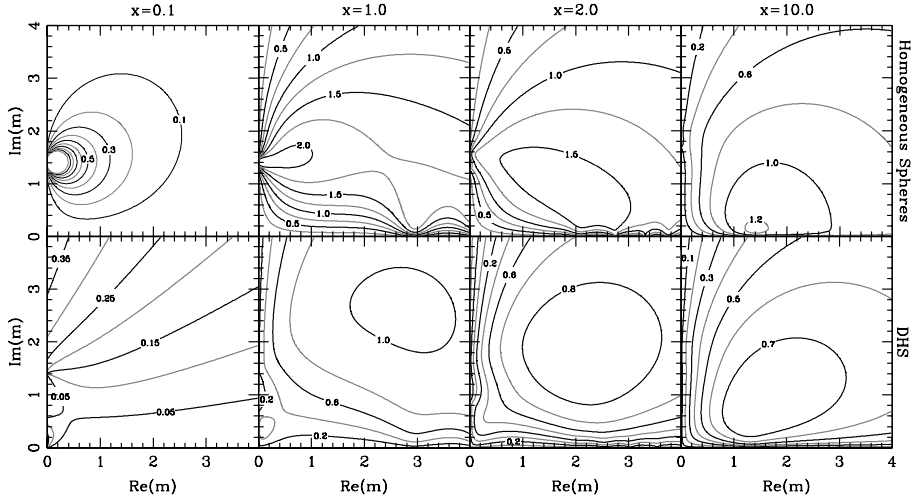


Figure 5.1: The shape averaged absorption efficiency as a function of the real and imaginary part of the refractive index for various values of the dimensionless size parameter $x = 2\pi r_V/\lambda$, where r_V is the radius of a volume equivalent sphere and λ is the wavelength of incident radiation. The upper panels are for homogeneous spheres, the lower panels for the distribution of hollow spheres (DHS).

same material volume as the particle. We define the average absorption cross section, $\langle C_{\text{abs}} \rangle$, to be the shape- and orientation-averaged absorption cross section of a collection of particles with a shape distribution and a fixed value of the material volume equivalent radius. In this paper we will always first average over all particle orientations. After this we will average over particle shape, which is denoted by one bracket $\langle \dots \rangle$. For calculations of the optical characteristics of a particle it is useful to define the dimensionless size parameter

$$x = \frac{2\pi r_V}{\lambda}, \quad (5.2)$$

where λ is the wavelength of incident radiation. The mass absorption coefficient κ is the average absorption cross section per unit mass

$$\kappa = \frac{\langle C_{\text{abs}} \rangle}{M}. \quad (5.3)$$

Here M is the mass of the particles in the collection with the same r_V .

The orientation averaged absorption efficiency of a particle defined as $Q_{\text{abs}} = C_{\text{abs}}/G$, with G the orientation averaged geometrical shadow, only depends on the shape, size parameter and complex refractive index m of the particle. Because the distribution of normals to the surface of all convex particles is uniform (van de Hulst 1957), the absorption efficiency of very large convex solid particles averaged over all

orientations is the same as for spheres and can be written as (Bohren & Huffman 1983)

$$Q_{\text{abs}} = 1 - \mathcal{R}, \quad (5.4)$$

where \mathcal{R} is a reflection factor which does not depend on the size and shape of the particle but only on the complex refractive index m . Eq. (5.4) also holds for particles with one or more inclusions when the outer surface of the particle is convex (e.g. hollow spheres). Therefore, for very large particles the absorption efficiency and cross section averaged over all orientations as a function of wavelength will have the same behavior for all particles with a convex outer surface.

In Fig. 5.1 the shape averaged absorption efficiency, $\langle Q_{\text{abs}} \rangle$, is plotted as a function of the real and imaginary part of the refractive index for various values of the size parameter for homogeneous spheres (upper panels) and for the distribution of hollow spheres (DHS, lower panels). We clearly see that there is a large difference between the contours for homogeneous spheres and those for the DHS when x is small and that this difference slightly disappears when we go to larger values of x , which is to be expected from Eq. (5.4). The difference between the two types of contours is already small for $x = 10$, which is much too small to expect Eq. (5.4) to be valid. Based on the assumptions used to derive Eq. (5.4), it is expected to be valid only when $x \gtrsim 60$. This suggests that for particles with a size parameter larger than about 10 with a convex outer surface the behavior of the absorption cross section as a function of wavelength is to a certain degree independent of particle shape, which allows us to use homogeneous spheres to calculate the absorption cross sections for $x \gtrsim 10$.

5.3.1 Example: amorphous silicates

As a first example we consider the infrared mass absorption coefficient of amorphous olivine ($\text{Mg}_{2y}\text{Fe}_{2-2y}\text{SiO}_4$ with $0 \leq y \leq 1$) which is one of the most abundant species found in astronomical environments. This silicate is observed by looking at the thermal emission from, for example, comets (see e.g. Crovisier et al. 1997; Hanner et al. 1994), proto-planetary disks (see e.g. Bouwman et al. 2001; van Boekel et al. 2003), asymptotic giant branch stars (see e.g. Molster et al. 1999a; Hoogzaad et al. 2002) as well as by looking at the extinction by interstellar dust grains (see e.g. Draine & Lee 1984; Li & Draine 2001; Kemper et al. 2004). The exact behavior of the mass absorption and extinction coefficients as functions of the wavelength for various grain sizes is therefore crucial in understanding the formation and processing of grains in these environments. The observed spectrum is dominated by two broad features, one at $9.8 \mu\text{m}$ and one at $17.5 \mu\text{m}$. The $9.8 \mu\text{m}$ feature has been studied very extensively because the atmospheric window around $10 \mu\text{m}$ allows ground based observations.

Fig 5.2 shows the mass absorption coefficient, κ , as a function of wavelength for amorphous olivine grains with various sizes and $y = 0.5$. The refractive indices as a function of wavelength are taken from Dorschner et al. (1995); Jäger et al. (2003). We see that for the smaller grain sizes, the $17.5 \mu\text{m}$ feature broadens significantly when going from homogeneous spheres towards the distribution of hollow or spheroidal particles. This becomes important when identifying features in the region $20 - 30 \mu\text{m}$.

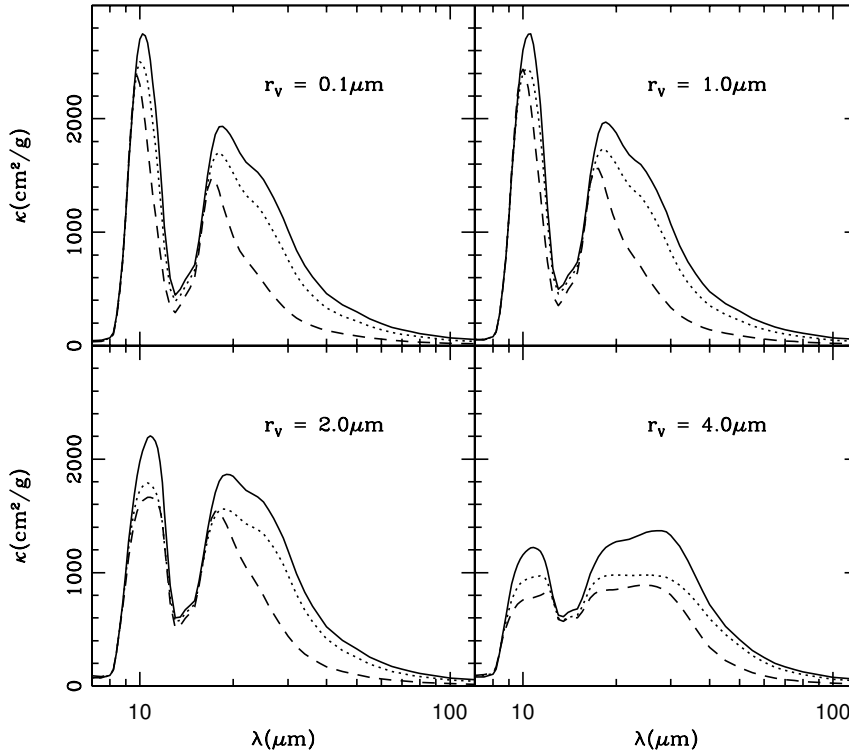


Figure 5.2: Absorption cross section per unit mass for amorphous olivine for different shape distributions and grain sizes. The solid line is for the distribution of hollow spheres (DHS), the dotted line for the uniform distribution of spheroids (UDS) and the dashed line for homogeneous spheres.

It should be noted that all spectroscopic features that we considered are broadened with respect to those calculated using homogeneous spherical particles. Actually, it might be argued that the correct way to put it is that the features as calculated using homogeneous spheres are sharpened with respect to those of all other particle shapes. The reason for this is that small homogeneous spherical particles exhibit a rather artificial sharp resonance close to when the refractive index $m = \sqrt{-2}$. For irregular particles the mass absorption coefficient is a smoother function of the refractive index which has its maximum approximately when the bulk refractive index is at its maximum. This causes the difference in feature shape observed in, for example, the 18 micron feature in Fig. 5.2.

Many sources show a $9.8 \mu\text{m}$ extinction or emission feature that is remarkably compatible with amorphous olivine grains that are very small ($r_v \lesssim 0.1 \mu\text{m}$), homogeneous in composition, spherical in shape and have a magnesium/iron content with $y = 0.5$.

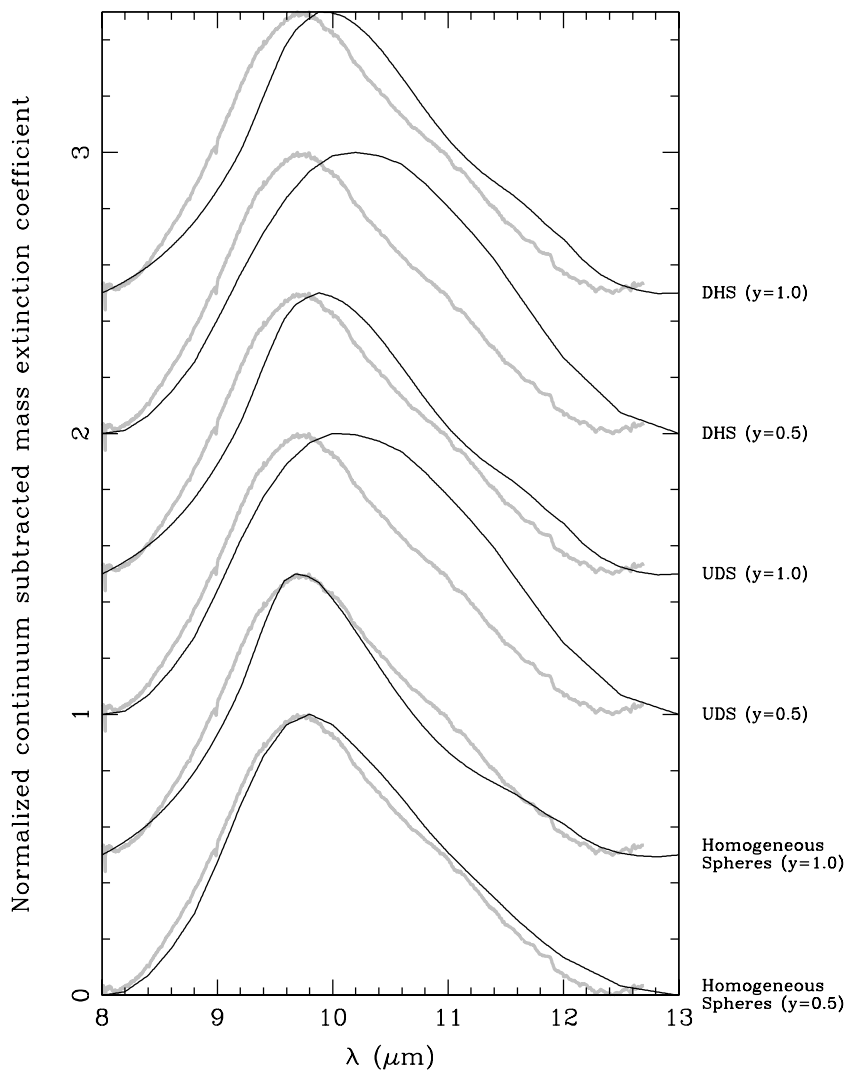


Figure 5.3: The normalized, continuum-subtracted mass extinction coefficients for various grain shape distributions and chemical compositions (black curves). The grain size $r_V = 0.1 \mu\text{m}$. Also plotted is the normalized, continuum subtracted extinction of interstellar dust grains as observed towards the Galactic center taken from Kemper et al. (2004) (gray curves). The refractive indices as functions of wavelength are taken from Jäger et al. (2003) for the $y = 1.0$ data and from Dorschner et al. (1995) for the $y = 0.5$ data. The continuum that was subtracted from all spectra is taken to be a straight line from 8 to $13 \mu\text{m}$. The normalization is done such that the maximum value of all curves equals unity. The curves are shifted with respect to each other with intervals of 0.5.

When we change the shape of the particles, the $9.8\ \mu\text{m}$ feature shifts towards longer wavelengths and broadens (see Fig. 5.2) which is not compatible with observations. This is puzzling since for example images of interplanetary dust particles show that these grains have a very irregular shape (Warren et al. 1994). In addition grains in interstellar space produce observable linear polarization in the forward scattering direction which can only be explained using non-spherical dust grains that are aligned to a certain degree (see e.g. Hildebrand & Dragoon 1995). Fig. 5.3 shows the normalized continuum subtracted mass extinction coefficient in the $10\ \mu\text{m}$ region of amorphous olivine grains with $y = 0.5$ and $y = 1.0$. Note that here we plot the mass *extinction* coefficient, which is just the average extinction cross section per unit mass. For very small particles the scattering is negligible, in which case the mass extinction coefficient is equal to the mass absorption coefficient, κ . The figure shows the normalized continuum subtracted mass extinction coefficient for small homogeneous spherical particles, for the uniform distribution of spheroids (UDS) and for the distribution of hollow spheres (DHS) all with $r_V = 0.1\ \mu\text{m}$. The continuum that was subtracted is taken to be a straight line between 8 and $13\ \mu\text{m}$. The normalization of all curves in Fig. 5.3 is such that the maximum value equals unity. Also plotted in this figure is the normalized continuum subtracted extinction towards the Galactic center (Kemper et al. 2004). We see that the extinction spectrum towards the galactic center is fairly well reproduced by both curves with homogeneous spherical particles. The feature obtained by using the spheroids or hollow spheres with $y = 0.5$ is much broader than the galactic extinction feature. Also the maximum for these grains is shifted towards longer wavelengths than observed. For the magnesium silicates ($y = 1.0$), the agreement with the interstellar extinction feature for the DHS and UDS shape distributions is better. Because of the observed degree of linear polarization the interstellar grains are most likely non-spherical (see e.g. Greenberg & Li 1996). A possible explanation for the shape of the observed interstellar extinction feature might be that the grains in the interstellar medium have a very high magnesium over iron ratio. Note that the particle ensembles considered here are in random orientation and would therefore not produce any linear polarization in the forward scattering direction. However, aligned, non-spherical dust grains produce an extinction spectrum which is more similar to that of randomly oriented non-spherical or non-homogeneous grains than to that of homogeneous spheres.

5.3.2 Example: crystalline silicates

Another example of the importance of grain shape for the absorption and extinction spectra are the spectra of crystalline silicate particles. Small crystalline silicate grains have a very clear spectral signature in the infrared part of the spectrum which makes them easy to detect in for example thermal emission spectra (e.g. Bouwman et al. 2003, and references at the start of Sect. 5.3.1). Crystalline silicates can form only under certain conditions from gas phase condensation or by annealing of amorphous silicates. The abundance of crystalline silicates is therefore a good probe for the processing history of the dust grains.

The mass absorption coefficient as a function of wavelength for small crystalline silicate grains shows many very narrow and strong resonances in the infrared part of the

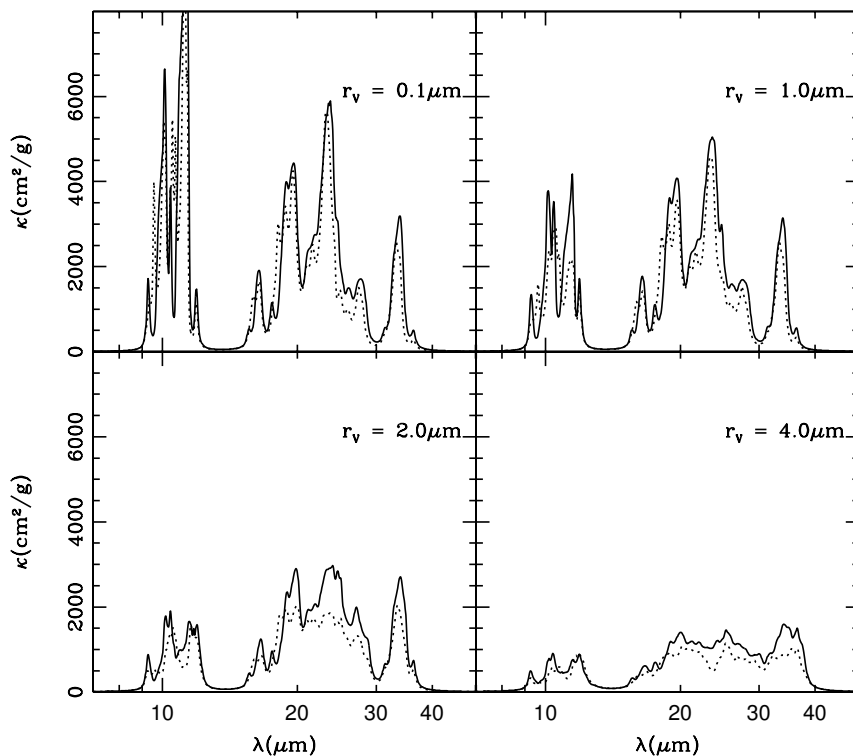


Figure 5.4: Mass absorption coefficient, κ , for various sizes of crystalline forsterite particles. The solid line is for the distribution of hollow spheres (DHS), the dotted line is for the uniform distribution of spheroids (UDS). The refractive index as a function of wavelength is taken from Servoin & Piriou (1973).

spectrum. Because of the strength of the resonances, their shape and wavelength positions are very sensitive to the particle shape. For example, calculations of the mass absorption coefficient as a function of wavelength using homogeneous spherical particles completely fail to reproduce laboratory measurements on small crystalline forsterite grains (Fabian et al. 2001; Min et al. 2003b). A very successful shape model which is frequently used to calculate the absorption spectra of these grains is the so-called Continuous Distribution of Ellipsoids (CDE) (Bohren & Huffman 1983). This distribution takes all possible ellipsoidal shapes into account. Although the measured absorption spectrum is very well reproduced using this shape distribution, a major disadvantage is that calculations for this distribution are restricted to the Rayleigh domain since it uses ellipsoidal shapes, and it is thus not suitable for studying combined size/shape effects. We performed calculations using the shape distribution suggested by Li et al. (2002). However, the results for, for example, the wavelength positions of the crystalline silicate

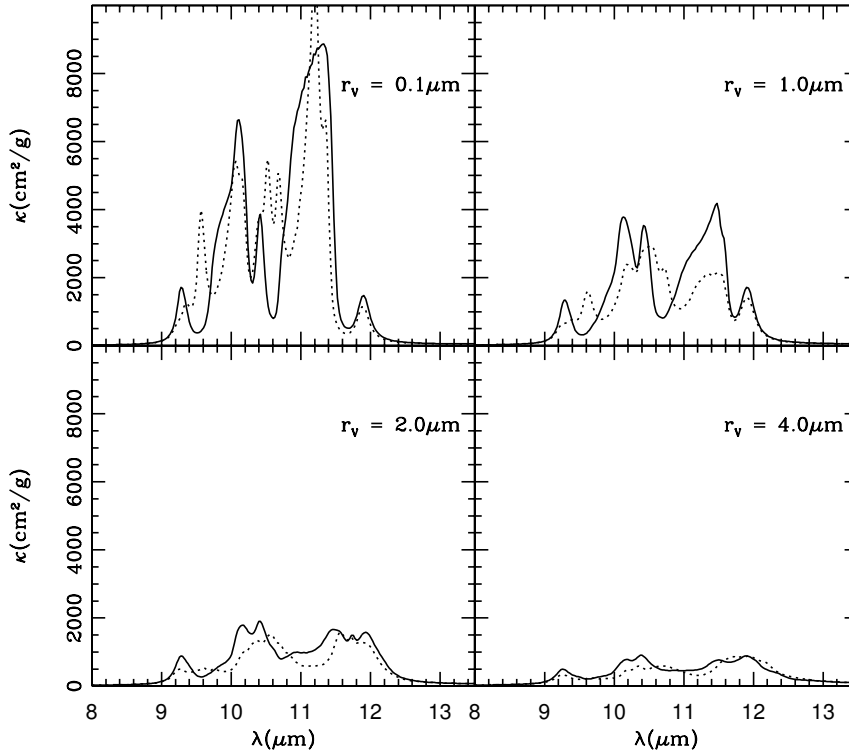


Figure 5.5: Same as Fig. 5.4 but only for $\lambda = 8 - 13.5 \mu\text{m}$.

resonances were poorly reproduced, in contrast with using CDE. The shape distributions we use here also reproduce the measurements on small forsterite grains (Min et al. 2003b) and can be used outside the Rayleigh domain.

Fig. 5.4 shows the mass absorption coefficient as a function of wavelength for various grain sizes. The refractive index as a function of wavelength is taken from Servoin & Piriou (1973). The solid curve is for the distribution of hollow spherical particles (DHS), the dotted curve is for the uniform distribution of spheroids (UDS). We see that the strong resonances visible for very small particles disappear when we increase the particle size. We notice that the resonances at shorter wavelengths disappear first. Also, the stronger resonances disappear before the weaker resonances do. These effects are due to the fact that the important parameter which determines the absorption properties is $|2\pi m r_v/\lambda|$. So the strength of the resonances is influenced by the wavelength, the refractive index and the size of the particle. This effect causes the ratios between the various resonances to change when we increase the particle size. In the interpretation of observations this ratio can be used as an indicator of the typical particle size.

We now compare the curves calculated for the uniform distribution of spheroids with

those calculated for the distribution of hollow spheres in Fig. 5.4. First we note that for very small particles ($r_V = 0.1 \mu\text{m}$) the differences are very small. When the grain size is increased the trends seen in the two curves are the same, as is described above. However, we see that the resonances for a given grain size obtained from the distribution of hollow spheres are generally stronger. Since in the DHS we average over all possible inclusion fractions from 0 to 1, we always include spheres with extremely thin shells. These thin shells will, to a certain degree, simulate the optical properties of very small homogeneous particles, resulting in stronger spectral features. This can be understood by considering the particle as a combination of small volume elements, each interacting with the electromagnetic field like dipoles (the Discrete Dipole Approximation; Purcell & Pennypacker 1973). If these volume elements are close together, the interaction between the volume elements is important. However, if the volume elements are distributed over a larger area, as in a thin shell, the interactions between the volume elements are less important and the total interaction will be closer to the sum of the separate dipoles. In a thin shell the volume elements are distributed over a larger volume area than in a homogeneous spheroid with the same material volume, so the interaction of the light with the separate dipoles becomes more important.

As already mentioned, the 10 micron region is very important in astrophysics because of the possibility of ground based observations. Fig. 5.5 is a blowup of the 10 micron region. It shows that for the detailed shape of the spectrum, there are differences between the UDS and DHS results. In both sets of curves the trends as discussed above are still clear. Besides a change in the feature strengths and ratios, we also observe a shift in the wavelength positions of the resonances. For example the $11.3 \mu\text{m}$ feature shifts towards $11.45 - 11.5 \mu\text{m}$ (depending on the shape distribution used) when the grain size is increased from $r_V = 0.1 \mu\text{m}$ to $r_V = 1.0 \mu\text{m}$. A similar shift from 11.3 to $11.44 \mu\text{m}$ is observed when the chemical composition is changed from magnesium rich (forsterite, $y = 1$) to iron rich (fayalite, $y = 0$) (Fabian et al. 2001; Honda et al. 2004). Therefore, it is necessary to consider multiple resonances, at a large range of wavelengths, to disentangle the effects of particle size and chemical composition. Because we are looking at relatively short wavelengths, the spectral diagnostics of the emission resonances of forsterite are already reduced significantly when the volume equivalent radius of the particles is $\sim 2 \mu\text{m}$. Therefore, the mineralogy that can be deduced from $10 \mu\text{m}$ spectroscopy is limited to particles smaller than a few micron. This has to be kept in mind when analyzing these spectra (cf. Honda et al. 2004).

5.4 The degree of linear polarization

Another area we wish to consider is the degree of linear polarization of the light scattered by dust grains in the visible part of the spectrum, which is a frequently used observable. For comets it is possible to obtain measurements for various angles of scattering by doing measurements at different orbital phases of the comet. For discussions on the polarization of light scattered by cometary dust and the possible implications for the grain properties see e.g. Levasseur-Regourd (1999) and Kolokolova et al. (2001). The degree of linear polarization as a function of scattering angle can also be measured dir-

actly in the laboratory for collections of randomly oriented particles (see e.g. Hovenier et al. 2003; Volten et al. 2001). In most cases the shape of the linear polarization curve cannot be reproduced by using homogeneous spherical particles. Therefore it is very interesting to calculate the polarization properties of inhomogeneous or non-spherical particles. Many studies concerned the linear polarization of collections of spheroids or cylinders (Mishchenko et al. 2002; Kahnert et al. 2002; Kahnert 2004). Here, we will focus on calculations using the distribution of hollow spheres and compare our results with homogeneous spheres and laboratory measurements on irregular quartz particles.

Figs. 5.6 and 5.7 show the degree of linear polarization of light scattered by collections of particles for incident unpolarized light as a function of scattering angle, θ , and effective size parameter. Fig. 5.6 is for a refractive index typical for olivine with $y = 0.5$, Fig. 5.7 is for a magnesium rich olivine with $y = 1.0$. In order to reduce the effects of resonances a narrow gamma size distribution given by

$$n(x) = c \cdot x^{(1-3v_{\text{eff}})/v_{\text{eff}}} \exp\left(-\frac{x}{v_{\text{eff}}x_{\text{eff}}}\right), \quad (5.5)$$

was employed. In this equation $n(x)dx$ is the number of particles with size parameter $2\pi r_V/\lambda$ between x and $x + dx$, x_{eff} is the effective size parameter, v_{eff} is the effective variance, which we take to be 0.1, and c is a normalization constant. For values of the effective size parameter smaller than approximately unity we see in Figs. 5.6 and 5.7 the well known Rayleigh pattern with a maximum degree of linear polarization of 100% at 90° . For the homogeneous spheres and for the distribution of hollow spheres with $f_{\text{max}} = 0.2$ large areas in parameter space produce negative polarization. There are even values of the effective size parameter for which the linear polarization is negative over the entire range of scattering angles. For the most extreme distribution of hollow spheres (with $f_{\text{max}} = 1$) we see that the regions of negative polarization shift towards the very small and large scattering angles. This is consistent with a frequently observed negative polarization branch at large scattering angles ($\theta \approx 160 - 180^\circ$) (Volten et al. 2001; Muñoz et al. 2000; Lévassieur-Regourd 1999; Kolokolova et al. 2001). Also we note that the difference between the values obtained for olivine particles with $y = 0.7$ and olivine particles with $y = 1.0$ decreases when we increase f_{max} . This suggests that for very irregular particles the refractive index of the material is of lesser importance. This agrees well with the observed similarity of the degree of linear polarization as a function of scattering angle for various mineral types (Volten et al. 2001).

The contours in Figs. 5.6 and 5.7 for $f_{\text{max}} = 1.0$ show that the degree of linear polarization for this shape distribution is very high (up to 90% at intermediate scattering angles) even for very large particles. The high degree of linear polarization seen here might be due to the fact that although the outer radius of the particles is large, the thickness of the shell is still very small compared to the wavelength, which causes a high degree of linear polarization (see also Sect. 5.3.2).

5.4.1 Example: the polarization of small quartz particles

Quartz, SiO_2 , is one of the most abundant minerals in the Earth's crust. It is believed to be formed when amorphous silicates are annealed to form forsterite (Fabian et al. 2000).

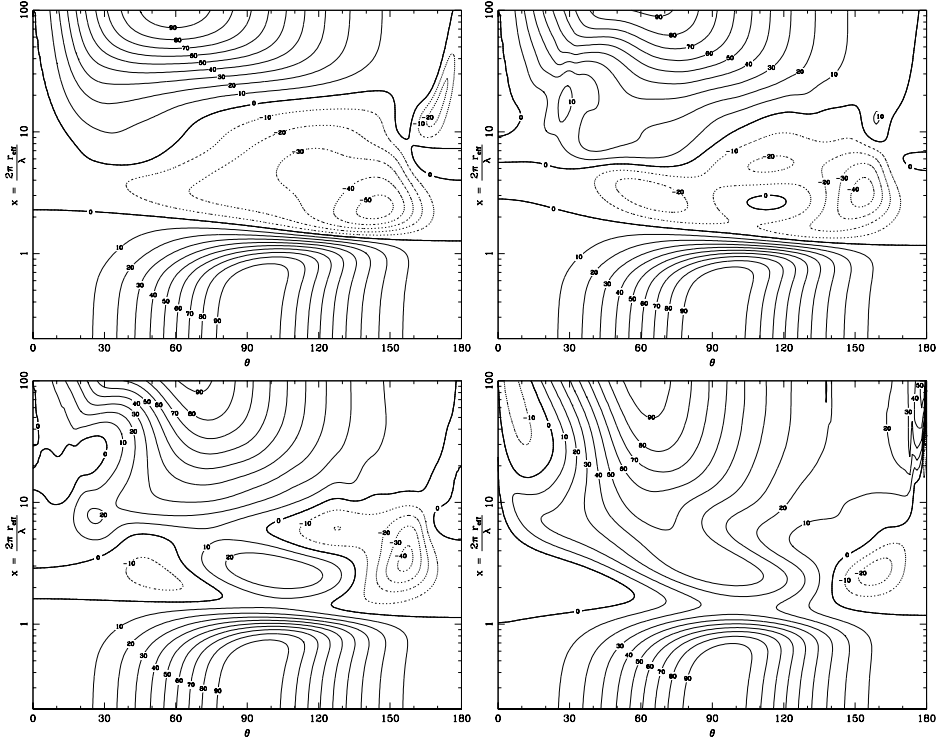


Figure 5.6: The degree of linear polarization of solid and hollow spheres as a function of the scattering angle and the effective size parameter for different values of f_{\max} . The refractive index of the material $m = 1.76 + 0.024i$ which is typical for amorphous silicate with 30% iron at $\lambda = 0.65 \mu\text{m}$ (Henning & Stognienko 1996). Upper left $f_{\max} = 0$ (homogeneous spheres), upper right $f_{\max} = 0.2$, lower left $f_{\max} = 0.5$ and lower right $f_{\max} = 1.0$. A gamma size distribution with $v_{\text{eff}} = 0.1$ was used (see Eq. (5.5)). Solid and dotted curves represent the areas with positive and negative polarization respectively.

The refractive index of quartz in the visible part of the spectrum is very well known, which makes it an ideal test case for comparison between measurements and theory. Volten et al. (2001) measured the complete scattering matrix as a function of scattering angle in the range $5 - 173^\circ$ of an ensemble of small irregular quartz particles in random orientation at two wavelengths, 442 nm and 633 nm. The data of these measurements are available online together with the particle size distribution obtained from laser diffraction (Volten et al. 2005). From these scattering matrices we can obtain the degree of linear polarization for incident unpolarized light

$$P(\theta) = -\frac{F_{21}(\theta)}{F_{11}(\theta)}, \quad (5.6)$$

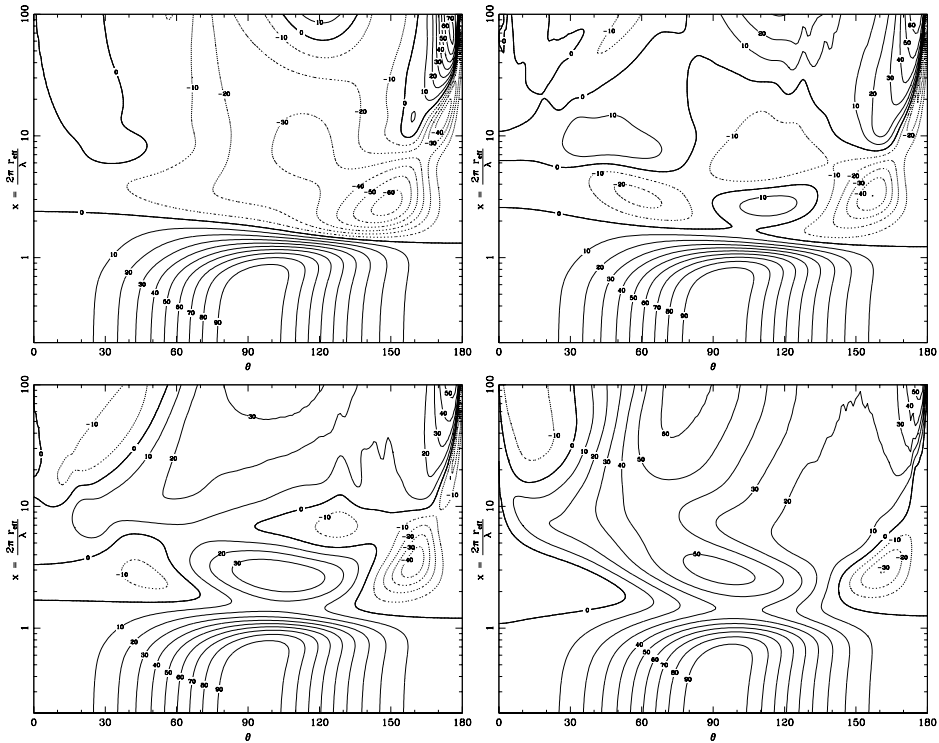


Figure 5.7: As Fig. 5.6 but for a refractive index of the material $m = 1.67 + 0.0001i$ which is typical for iron poor amorphous olivine at $\lambda = 0.65 \mu\text{m}$ (Henning & Stognienko 1996).

where θ is the scattering angle and F_{nk} is the n, k th element of the 4×4 scattering matrix (for details see Volten et al. 2005). The laboratory data provide the element F_{12} . However, the symmetry of the system yields $F_{12} = F_{21}$. For comparison we also compute the degree of linear polarization using the distribution of hollow spheres together with the measured particle size distribution. For consistency with calculations elsewhere in the paper, we use volume equivalent radii to represent the size of the particles, although the measured size distribution is obtained for projected-surface-area equivalent spheres.

Fig. 5.8 shows calculated polarization curves for distributions of hollow spheres with $f_{\text{max}} = 0.3, 0.4$ and 0.5 together with the laboratory measurements. The results for $f_{\text{max}} = 0.4$ agree best with the measurements. This shape distribution reproduces the measured shape of the degree of linear polarization as a function of scattering angle reasonably well. The calculations show a feature at $\sim 170^\circ$ which may be caused by the fact that the particles in the hollow sphere distribution are still spherical in shape.

In most applications the real size distribution of the dust grains is not known. In these cases one would like to extract the size distribution from the measured polarization curve. To do this we try to minimize the difference between the measurements and the

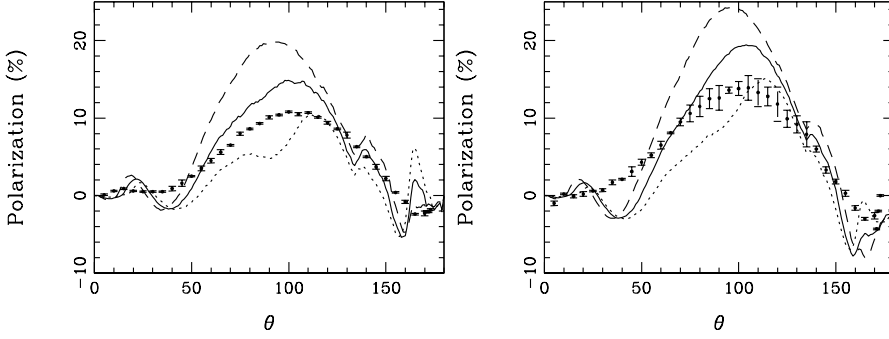


Figure 5.8: The degree of linear polarization of small quartz particles versus scattering angle, θ . Shown are the measurements (points) and calculations (curves) using the measured size distribution and the distribution of hollow spheres with $f_{\max} = 0.3$ (dotted curve), $f_{\max} = 0.4$ (solid curve) and $f_{\max} = 0.5$ (dashed curve). The left figure is for a wavelength $\lambda = 422$ nm and the right figure for $\lambda = 633$ nm. The refractive index is $m = 1.559 + i \cdot 10^{-8}$ and $m = 1.542 + i \cdot 10^{-8}$ for $\lambda = 442$ nm and $\lambda = 633$ nm, respectively (Gray 1963).

calculations by fitting the size distribution. To find the least squares solution we have to minimize χ^2 with respect to the size distribution. The χ^2 for this problem is defined by

$$\chi^2 = \sum_j \left| \frac{\frac{\sum_i w(r_i) \langle F_{12}(\theta_j, r_i) \rangle}{\sum_i w(r_i) \langle F_{11}(\theta_j, r_i) \rangle} - P_{\text{obs}}(\theta_j)}{\sigma_j} \right|^2. \quad (5.7)$$

In this equation $\langle F_{nk}(\theta_j, r_i) \rangle$ is the n, k th element of the scattering matrix of an ensemble of randomly oriented particles with a certain shape distribution and a volume equivalent radius r_i at scattering angle θ_j , $w(r_i)$ is the value of the relative number size distribution at radius r_i (these are the fitting parameters), $P_{\text{obs}}(\theta_j)$ is the observed degree of linear polarization at scattering angle θ_j and σ_j is the error in $P_{\text{obs}}(\theta_j)$. The r_i represent different values in the size distribution, and the θ_j represent the scattering angles at which measurements have been done. Unfortunately, Eq. (5.7) is not linear in the $w(r_i)$, which makes minimization of χ^2 very difficult, especially in the case when we want to sample the size distribution with high resolution, which means we would have a large number of fitting parameters. However, we can linearize the equation by minimizing

$$\chi^2 = \sum_j \left| \frac{-\sum_i w(r_i) (\langle F_{12}(\theta_j, r_i) \rangle - P_{\text{obs}}(\theta_j) \langle F_{11}(\theta_j, r_i) \rangle)}{\gamma_j \sigma_j} \right|^2, \quad (5.8)$$

where the γ_j are scaling factors which can be different for each θ_j . The right hand side of Eq. (5.8) reduces to that of Eq. (5.7) when

$$\gamma_j = \sum_i w(r_i) \langle F_{11}(\theta_j, r_i) \rangle. \quad (5.9)$$

We can now iteratively solve Eq. (5.7) and (5.8) in the following way.

1. As a first estimate take $\gamma_j = 1$ for all j .
2. Solve Eq (5.8) for the $w(r_i)$.
3. The resulting values of $w(r_i)$ are used to generate new γ_j from Eq. (5.9).
4. Repeat steps 2 and 3 until convergence is reached, i.e. the γ_j do not change during one iteration.

In all cases that we considered convergence is reached within 15 iterations. This method is much faster than a nonlinear minimization algorithm and has the advantage that it is less sensitive to local minima.

If one would use the above scheme without further considerations, the solution for the $w(r_i)$ that is found will in general not be a smooth function of the r_i . Therefore, we add a regularization term to Eq. (5.8) which is defined as

$$\chi_R^2 = \sum_i |w(r_i) - w(r_{i+1})|^2, \quad (5.10)$$

and minimize $\chi^2 + b \chi_R^2$ using the iterative scheme described above. The value of b is chosen in such a way that the contributions from the two terms are balanced. For details on this regularization we refer to Press et al. (1992).

We have to avoid finding solutions with $w(r_i) < 0$ or the solution with $w(r_i) = 0$ for all i . To do this we use a linear least squares fitting procedure with linear equality and inequality constraints. The constraints we use are $\sum_i w(r_i) = 1$ and $w(r_i) > 0$ for all i .

From the derived $w(r_i)$ we can construct the relative projected-surface-area distribution $S(\log r)$. This size distribution is defined in such a way that $S(\log r) d \log r$ gives the relative contribution to the total projected surface area of grains in the size range $\log r$ to $\log r + d \log r$ (see the appendix of Volten et al. 2005). We have to note here that we use volume equivalent radii of the particles while the measured size distribution is based on a projected-surface-area equivalent radius. This might introduce a small difference in the size distributions when the particles deviate strongly from homogeneous spheres. The differences here will be minimal.

The best fit results are obtained when we take $f_{\max} = 0.4$. The resulting polarization curves are shown in the upper panels of Fig. 5.9. Plotted in the lower panels of this figure are the phase functions F_{11} for the two different wavelengths. We see that the polarization curves are reproduced very well for both wavelengths. We have to note that for the other elements of the scattering matrix the agreement with the laboratory measurements is less convincing. For example depolarization and circular polarization effects cannot be explained using hollow spheres, because of the spherical symmetry of the particles. Also, as can be seen from Fig. 5.9, the calculated phase functions display an increase at large scattering angles which is absent in the measurements. The size distribution obtained by fitting the degree of linear polarization is plotted in Fig. 5.10 together with the measured size distribution using laser diffraction. We see that the grain sizes contributing most to the total projected-surface-area of all three size distributions

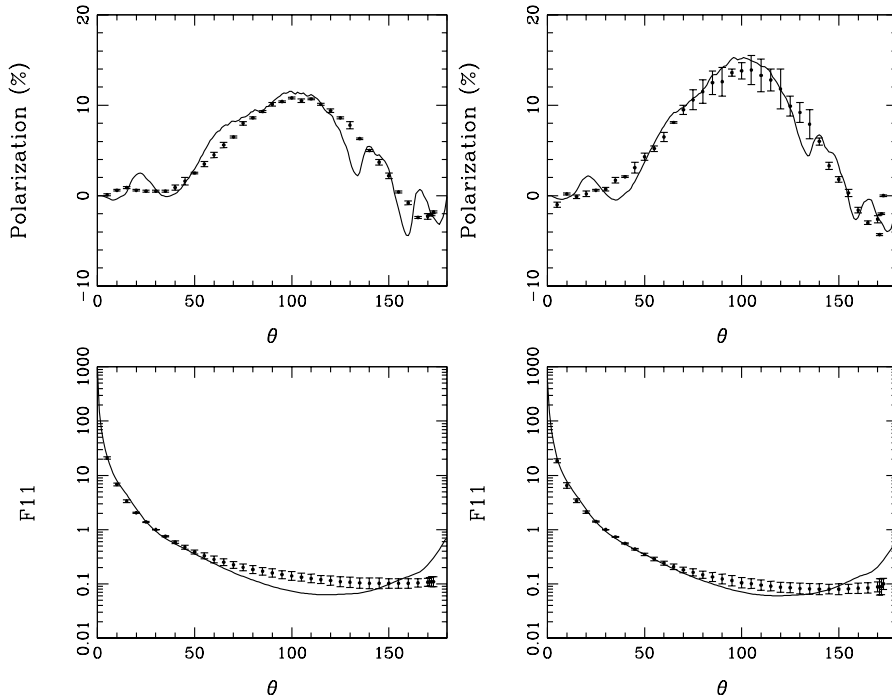


Figure 5.9: The degree of linear polarization (upper panels) and the phase function F_{11} (lower panels) of small quartz particles versus scattering angle, θ . All phase functions are normalized so that their values at $\theta = 30^\circ$ equals unity. Shown are the measurements (points) and the best fit to the polarization measurements using the distribution of hollow spheres with $f_{\max} = 0.4$ (solid curve). The left figures are for a wavelength $\lambda = 422$ nm and the right figures for $\lambda = 633$ nm. The refractive indices are as in Fig. 5.8. The curves for the two different wavelengths have been fitted independently and the resulting size distributions are plotted in Fig. 5.10. The phase functions have not been fitted but are calculated using the size distribution derived from the fit to the polarization measurements.

match very well. In general, we find that an extra contribution of very small grains is required with respect to the measured size distribution in order to reproduce the measured polarization curve. The laser diffraction method used to measure the size distribution of the quartz particles in the laboratory is inaccurate for very small grains, which could be the reason why this small grain component is not found when this method is used. Another reason could be that the small grain component is used by the fitting procedure to simulate scattering by small scale structures in the particles itself. Considering the limited information used in the fitting procedure and the relatively simple grain shape distribution used, the similarity is remarkable. This is an encouraging result for the use of the distribution of hollow spheres in inverse problems to obtain the size distribution from the degree of linear polarization. We have to stress here that having a reasonable

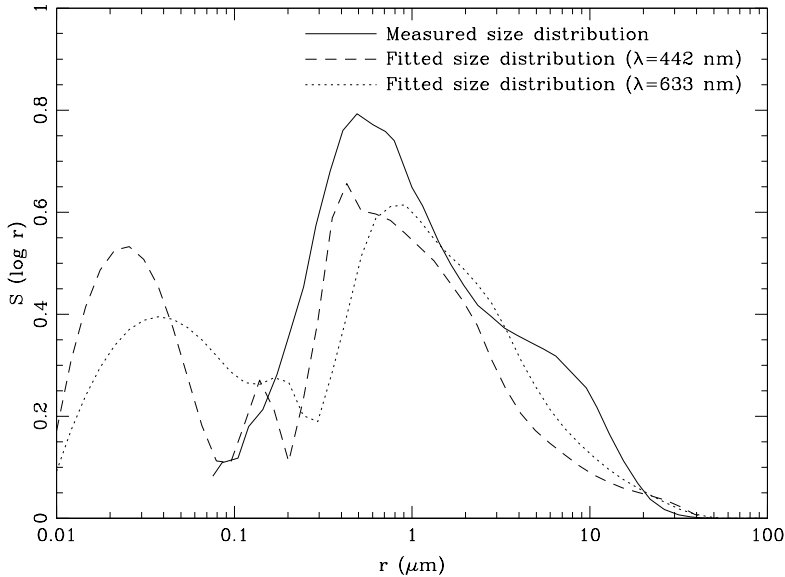


Figure 5.10: The size distribution, $S(\log r)$, of small quartz particles as measured by laser diffraction (solid curve) and as fitted from the linear polarization curve at $\lambda = 442$ nm (dashed curve) and at $\lambda = 663$ nm (dotted curve).

estimate of the value of the refractive index is important for obtaining reliable results.

5.5 Discussion

In the previous sections it has been shown that the distribution of hollow spheres is a useful tool for calculating the optical properties of irregularly shaped particles. The question remains *why* this is the case. It is clear that the particles in astrophysical environments or in the laboratory are not hollow spheres. Therefore, there must be a fundamental characteristic of the particles that determines their optical properties. This characteristic on the one hand has to be important for the scattering and absorption properties and on the other hand it has to be clearly different for homogeneous spheres and hollow or non-spherical particles. One of the main things that discriminates a homogeneous sphere from other types of particles is its perfect symmetry. This perfect symmetry makes the interaction of an electromagnetic wave with this particle very sensitive to interference effects. This will determine to a large extent the optical properties. Only small deviations from a homogeneous sphere are required to disturb these interference effects. This suggests that the first disturbance in the perfect homogeneous sphere is very important and is not very shape-dependent.

5.6 Conclusions

In this paper we examine the applicability of the statistical approach for computations of optical properties of ensembles of irregularly shaped particles in random orientation when a distribution of hollow spherical particles is used.

The range of particle sizes for which we did numerical computations covers a critical region if we wish to study the combined size and shape effects on the absorption, extinction and scattering cross sections as functions of the wavelength. For smaller particles we are in the Rayleigh regime, where the shapes of the spectra are independent of particle size. For particles larger than in the critical regime the effects of particle shape become negligible. We may thus conclude that, for all particle sizes, the emission and extinction spectra in the infrared computed by using the distribution of hollow spheres display the same trends and overall spectral shape as a uniform distribution of spheroids. These spectra are significantly different from those obtained using homogeneous spheres. This suggests that the shape of these spectra is, to a certain degree, not sensitive to the exact particle shape as long as the deviations from homogeneous spherical particles are large enough. This result is in agreement with the conclusion of Min et al. (2003b) for very small particles and is extended here to particles of arbitrary size.

The exact wavelength positions of observed spectral features are frequently used to identify the chemical composition of solid state particles. These wavelength positions also depend on particle size and shape. A reliable identification of solid state components can therefore only be made if the effects of both particle size and shape are taken into account. Calculations using the distribution of hollow spheres allow such a detailed analysis.

The degree of linear polarization for incident unpolarized light of hollow spheres with various volume fractions of the central vacuum inclusion was studied and compared to that of laboratory measurements at wavelengths of 442 and 633 nm. Good agreement was found with laboratory measurements for small, irregular quartz particles for scattering angles between 5° and 173° . It was also shown that the particle size distribution can be derived by fitting the calculated degree of polarization to the laboratory data. With this procedure we found an overabundance of small grains with respect to the measured size distribution. This can be due to the fact that the laser diffraction method used to measure the size distribution is inaccurate for small grains, or that the fitting procedure tries to simulate small scale structures that are present in the 'real' particles but absent in the hollow spheres. If the cause of the overabundance of small grains is the inaccuracy of laser diffraction when the particles are small, fitting the degree of linear polarization might be a good alternative for obtaining information on the particle size distribution.

Although our results imply that the optical properties of dust grains only contain limited information on the exact particle shape, by using the distribution of hollow spheres we have a more reliable diagnostic to derive the mineralogy, size and total mass of these dust grains than when only homogeneous grains and CDE are used. We conclude that, because of its simplicity, low computational demand and success in reproducing the optical properties of irregular particles, the distribution of hollow spheres can be a powerful tool in studies of light scattering, absorption and emission by particles, and in particular

in cases where large numbers of particle parameters need to be considered.

Acknowledgments

We are grateful to L. B. F. M. Waters and H. Volten for enlightening conversations. We would like to thank M. I. Mishchenko and O. Muñoz for valuable comments on an earlier version of this paper.

6

The $10\mu\text{m}$ amorphous olivine feature of fractal aggregates and compact particles with complex shapes

*M. Min, C. Dominik, J. W. Hovenier, A. de Koter, and L. B. F. M. Waters
to be submitted*

Abstract

We model the $10\mu\text{m}$ absorption spectra of nonspherical particles composed of amorphous olivine. We consider two classes of particles, compact ones and fractal aggregates composed of homogeneous spheres. For the compact particles we consider various degrees of non-sphericity. For the fractal aggregates we compute the absorption spectra for various fractal dimensions. The resulting $10\mu\text{m}$ spectra are compared to those of homogeneous spheres. We conclude that, in general, nonspherical particles show a spectral signature that is similar to that of homogeneous spheres with a smaller particle size. For aggregates with fractal dimensions typically predicted for cosmic dust, we show that the spectral signature characteristic of very small homogeneous spheres can be detected even in particles with a volume equivalent radius of at least $6\mu\text{m}$ and a linear extent of approximately $36\mu\text{m}$. We conclude that when using homogeneous spheres to model the emission spectra of astronomical sources, the masses can be estimated with relative accuracy, but the volume equivalent radii are severely underestimated.

6.1 Introduction

The interpretation of absorption and emission spectra observed from astronomical objects requires knowledge of the absorption cross section as a function of the dust grain characteristics, such as size, shape and composition. Usually the absorption spectra are modeled using homogeneous spherical particles for which calculations can easily be done using Mie theory (Mie 1908). Although cosmic dust grains are in general not homogeneous spheres, in some cases Mie theory calculations can reproduce the observations quite accurately (see e.g. Hansen & Hovenier 1974; Kemper et al. 2004). However, in other cases one has to find a way of modeling the effects of particle shape in order to reproduce observations or laboratory measurements (see e.g. Mishchenko et al. 2000).

It is therefore important to know the effects of the adopted particle shape model on the derived dust parameters, such as the particle size and structure.

From different formation mechanisms different types of particles may form. For example, when dust grains form from direct gas phase condensation, compact particles may be created. Alternatively, when dust grains stick together to form larger particles, complex aggregated structures may be formed. We study particles in both classes using irregularly shaped compact particles and fractal aggregates. For the compact particle shapes we use so-called Gaussian random spheres (Muinonen et al. 1996) which allows for a varying degree of irregularity. The fractal aggregates are composed of homogeneous spheres and are constructed using a sequential tunable particle cluster aggregation method, that allows us to construct particles with arbitrary values of the fractal dimension.

We concentrate on the effects of particle non-sphericity on the so-called 10 μm amorphous olivine feature. Amorphous olivine is one of the most abundant dust components in various astronomical environments. The absorption spectrum of small amorphous olivine grains displays a characteristic feature peaking around 9.7 μm . The wavelength position of this feature is ideal for ground based observations because of the 10 μm atmospheric window. For the interpretation of astronomical observations it is therefore of great importance to know how the shape and strength of the 10 μm amorphous olivine feature depends on the size, shape and structure of the grains causing it.

The 10 μm absorption spectra are computed using the Discrete Dipole Approximation (DDA). We analyze the error that is made when employing homogeneous spheres to fit observations of the emission spectra of nonspherical particles.

The method is briefly outlined in Sect. 6.2. The particle shapes are described in Sect. 6.3. In Sect. 6.4 we present the resulting 10 μm amorphous olivine spectra. An analysis of our results and a discussion of the implications on the modeling of 10 μm spectra in astronomical observations is given in Sect. 6.5.

6.2 Absorption and emission spectra

The shape of the absorption spectrum of a dust grain, i.e. its absorption cross section as a function of wavelength, contains important information about the dust characteristics. This spectrum can be observed as absorption against a strong infrared background, or as thermal emission.

In this paper we consider two measures for the size of a particle, the volume equivalent radius and the circumscribed sphere radius. The volume equivalent radius, r_V , is defined as the radius of a sphere with the same material volume as the particle. For very fluffy particles, i.e. particles with a small space filling fraction, the volume equivalent radius does not provide an accurate measure for the actual linear extent of the particle. For this we define the circumscribed sphere radius, r_c , to be the radius of the smallest sphere centered on the center of mass of the particle and containing the entire particle. As an important parameter we consider the ratio of the circumscribed sphere radius and

the volume equivalent radius

$$\gamma = \frac{r_c}{r_V}. \quad (6.1)$$

This parameter determines how dense the material is packed in space. A very fluffy aggregate will have a high value of γ while a very dense particle will have a value of γ close to unity. For a homogeneous sphere $\gamma = 1$.

The mass absorption coefficient, κ , of a dust grain is defined as its absorption cross section per unit mass

$$\kappa = \frac{C_{\text{abs}}}{M}. \quad (6.2)$$

Here C_{abs} is the absorption cross section, and M is the mass of the particle. For grains that are much smaller than the wavelength of radiation both inside and outside the particle, i.e. in the Rayleigh domain, the absorption cross section is proportional to the particle material volume. This means that the mass absorption coefficient of very small particles, which is generally relatively high, is independent of the particle size. For compact particles much larger than the wavelength we are in the geometrical optics domain and the absorption cross section is proportional to the surface area of the particle. For a compact particle this implies that the mass absorption coefficient scales as r_V^{-1} for large values of r_V .

In general the optical properties of nonspherical particles depend on the orientation of the particle with respect to the incoming electromagnetic field. In the astronomical environments we are interested in, we are dealing with an ensemble of dust grains with random orientations. Therefore, in this paper we will always average the absorption cross section over all particle orientations.

6.2.1 The Discrete Dipole Approximation

The discrete Dipole Approximation (DDA) proposed by Purcell & Pennypacker (1973) allows for the computation of the optical properties of arbitrarily shaped particles. In the DDA the particle material volume may be divided into small volume elements. Each of these volume elements is assumed to interact with the radiation as a single dipole. The interaction of all dipoles with the incoming field and with the field of all other dipoles is then obtained by solving a $3N \times 3N$ matrix equation, where N is the number of dipoles used to represent the particle volume. For a theoretical foundation of the method in terms of the Maxwell equations see Lakhtakia (1992); Lakhtakia & Mulholland (1993). For applications of the DDA in the Rayleigh limit, i.e. for sizes of the particles as a whole small compared to the wavelength, see Henning & Stognienko (1993); Stognienko et al. (1995).

In order for the DDA to be valid, the size of the volume elements has to be much smaller than the wavelength of radiation both inside and outside the particle, i.e. (see e.g. Draine & Goodman 1993; Draine & Flatau 1994; Draine 2000),

$$ka|m| < 1, \quad (6.3)$$

where $k = 2\pi/\lambda$ is the wavenumber of radiation in vacuum, λ the wavelength in vacuum, a the size of the volume element, and m the complex refractive index of the material.

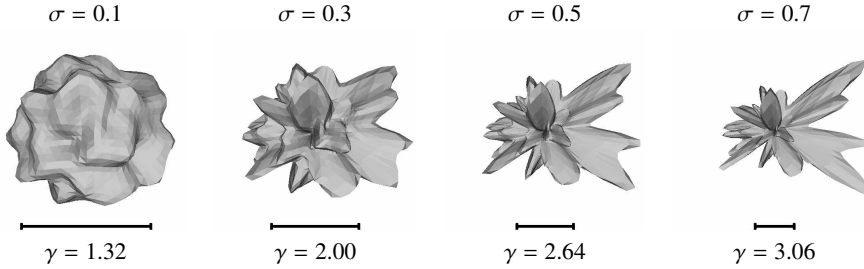


Figure 6.1: Pictures of the Gaussian random spheres employed in our calculations. The diameters of the corresponding volume equivalent spheres are indicated by bars below the particles.

DDA computations for large particles require a large number of dipoles. Several methods have been suggested to speed up the computations. The most important one makes use of the Fast Fourier Transform (FFT) together with a conjugate gradient solution method (see e.g. Goodman et al. 1991; Hoekstra et al. 1998). A disadvantage of this method is that all dipoles have to be located on a rectangular grid, and also the empty, vacuum places on the grid are taken into account in the computation. This slows down the method for fluffy particles with a low volume filling fraction. For example, for particles with a volume filling fraction of 1%, N is increased by a factor 100. Therefore, we chose for a direct solution method of the DDA equations. For moderate values of N this allows for relatively fast computations, not only for compact but also for very fluffy grains. An additional advantage is that we only have to do the computation for a particle in a fixed orientation once in order to obtain the optical properties of the particle for any other orientation, whereas the FFT method requires the computation to be repeated for every orientation. Since the computing time required for the direct solution method scales as N^3 , and the method using FFT scales as $N \log N$, the FFT method becomes faster when large values of N are needed. Typically, both methods are equally fast for $N \sim 10^3$ for a particle with a volume filling fraction of 1%.

6.3 Particle shapes

The shape of a dust grain is an important parameter determining its spectroscopic characteristics. In this paper we distinguish between two classes of shapes, aggregates and compact particles. For the compact particles we use Gaussian random spheres, while for the aggregates we use fractal aggregates with varying fractal dimensions.

6.3.1 Gaussian Random Spheres

A Gaussian random sphere (Muinonen et al. 1996) is a homogeneous sphere the surface of which is distorted according to a Gaussian random distribution. The distortion of the surface is parameterized by two shape variables, the standard deviation of the distance to the center, σ , and the average correlation angle, Γ . Using various values for these

two parameters allows us to construct particles with varying degrees of irregularity. The number of ‘hills and valleys’ on the surface in a solid angle is determined by the value of Γ , while σ determines the height of these hills and valleys. For details see Muinonen et al. (1996).

In Fig. 6.1 we show pictures of the Gaussian random spheres used in our computations. We vary the value of σ from 0.1 to 0.7 and fix the value of Γ to 10° .

6.3.2 Fractal aggregates

In astronomical environments large grains form by aggregation of small particles (see e.g. Kempf et al. 1999). Studies on interplanetary dust particles from likely cometary origin show that cometary dust grains are likely to be aggregates. A special class of aggregates are the so-called fractal aggregates.

A fractal aggregate composed of homogeneous spheres obeys the scaling law (Filipov et al. 2000)

$$N = k_f \left(\frac{R_g}{a} \right)^{D_f}. \quad (6.4)$$

Here N is the number of constituents each with radius a ; k_f is the fractal prefactor; D_f is the fractal dimension, and R_g is the radius of gyration defined by

$$R_g^2 = \frac{1}{N} \sum_{i=1}^N |\mathbf{r}_i - \mathbf{r}_0|^2, \quad (6.5)$$

$$\mathbf{r}_0 = \frac{1}{N} \sum_{i=1}^N \mathbf{r}_i, \quad (6.6)$$

where \mathbf{r}_i is the position of the i th constituent, and \mathbf{r}_0 is the center of mass. The value of the fractal dimension can in theory vary between the two extremes $D_f = 1$ (a thin, straight chain of particles) and $D_f = 3$ (a homogeneous sphere).

We use a sequential tunable particle-cluster aggregation method developed by Filipov et al. (2000) to construct the fractal aggregates. This method allows us to construct aggregates with arbitrary fractal dimension.

Note that for a fractal aggregate the circumscribed sphere radius and the volume equivalent radius cannot be the same. The reason is that the constituents are homogeneous spheres, therefore they do not allow for a full packing of the volume of the circumscribed sphere. The maximum packing density of a collection of spheres with the same radius is $\pi/\sqrt{18}$ (Hales 1992). This implies that for an aggregate composed of homogeneous spheres the minimum value of $\gamma = (\sqrt{18}/\pi)^{1/3} \approx 1.105$. The maximum value of γ depends on the number of spheres that make up the aggregate. The least dense packing is a straight line of spheres and results in $\gamma = N^{2/3}$.

In nature fractal aggregates can grow with a wide range of fractal dimensions depending on the formation mechanism and the environment in which they form. In astronomical environments the fractal dimension can vary between approximately 1 up to almost 3. Almost linear aggregates ($D_f \approx 1$) might form when the particles have

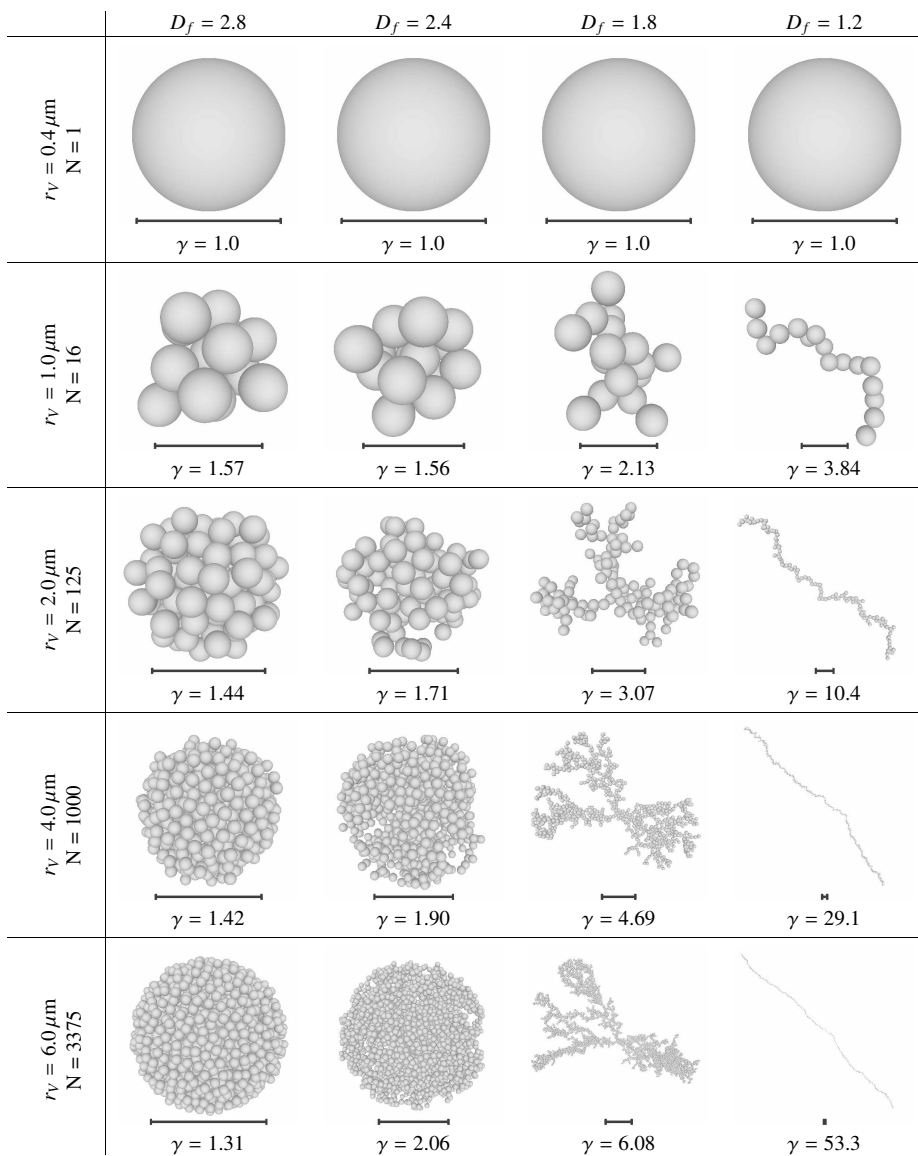


Figure 6.2: Pictures of the fractal aggregates we used in our calculations. Indicated by the bar below the aggregates is the diameter of the corresponding volume equivalent sphere.

an electric or magnetic dipole and are in an external field (Dominik & Nübold 2002; Nübold et al. 2003). In the case that grain growth occurs by coagulation of aggregates with approximately equal size the resulting aggregates will have a fractal dimension of approximately 1.8 to 2.1 (Kempf et al. 1999). On the other hand, when the growth occurs

by adding single monomers to a larger aggregate, aggregates with a fractal dimension of 3 might form (Ball & Witten 1984).

In this paper we consider aggregates composed of homogeneous spheres with fractal dimensions ranging from 1.2 up to 2.8. The radius of the monomers, a , is chosen to be $0.4\ \mu\text{m}$. For particles composed of amorphous olivine, the absolute value of the refractive index in the $10\ \mu\text{m}$ region reaches values up to $|m| \approx 2.2$ with a corresponding maximum value of $ka|m| = 0.5$. Thus, when applying DDA in this spectral region for the material we consider, each monomer can be represented by a single dipole (see Eq. 6.3). By using several values of k_f we find that the results are not very sensitive to the fractal prefactor chosen. For all aggregates we use $k_f = 2.0$. Pictures of the fractal aggregates we constructed for various numbers of monomers, and thus for various volume equivalent radii, are shown in Fig. 6.2. The bar below the pictures shows the diameter of a volume equivalent sphere. Also denoted are the corresponding values of γ . Thus we find that for a fractal aggregate with $D_f = 1.2$ and a volume equivalent radius $r_V = 6\ \mu\text{m}$, we have $r_c = \gamma r_V \approx 320\ \mu\text{m}$.

When we consider growth, we do not scale the aggregate but add more grains to it. This is an important difference with the Gaussian random spheres, since it implies that aggregates with different sizes have different shapes. For Gaussian random spheres the size is changed by scaling the entire grain, which implies that the shape of the particle is independent of its size.

6.4 Results

6.4.1 The $10\ \mu\text{m}$ amorphous silicate feature

The absorption spectrum of silicate particles display a feature around $10\ \mu\text{m}$ due to the stretching mode of the Si-O bond in the SiO_4 tetrahedra of which silicates are made. This feature has been observed in many astronomical sources. Fortunately, the wavelength range of this feature almost exactly fits in the $10\ \mu\text{m}$ atmospheric window. Therefore, the $10\ \mu\text{m}$ silicate feature can be observed using ground based infrared telescopes. Here we will concentrate on the $10\ \mu\text{m}$ feature of amorphous olivine, which is the most important dust constituent in many astronomical environments.

The spectral shape and amplitude of the mass absorption coefficient of particles composed of amorphous olivine as a function of wavelength in the $10\ \mu\text{m}$ region is sensitive to the size and shape of the grains causing it. Computations using homogeneous spheres show that an increase in particle size tends to broaden and flatten the $10\ \mu\text{m}$ feature. When Mie theory is employed to compute the emission spectrum, the feature strength diminishes rapidly when the grain size is increased.

6.4.2 Fractal aggregates versus Gaussian random spheres

The solid curves in Fig. 6.3 display the mass absorption coefficients as a function of wavelength for the various Gaussian random spheres (Fig. 6.1), and different particle sizes. Also shown in this figure, by the dotted lines, is the mass absorption coefficient

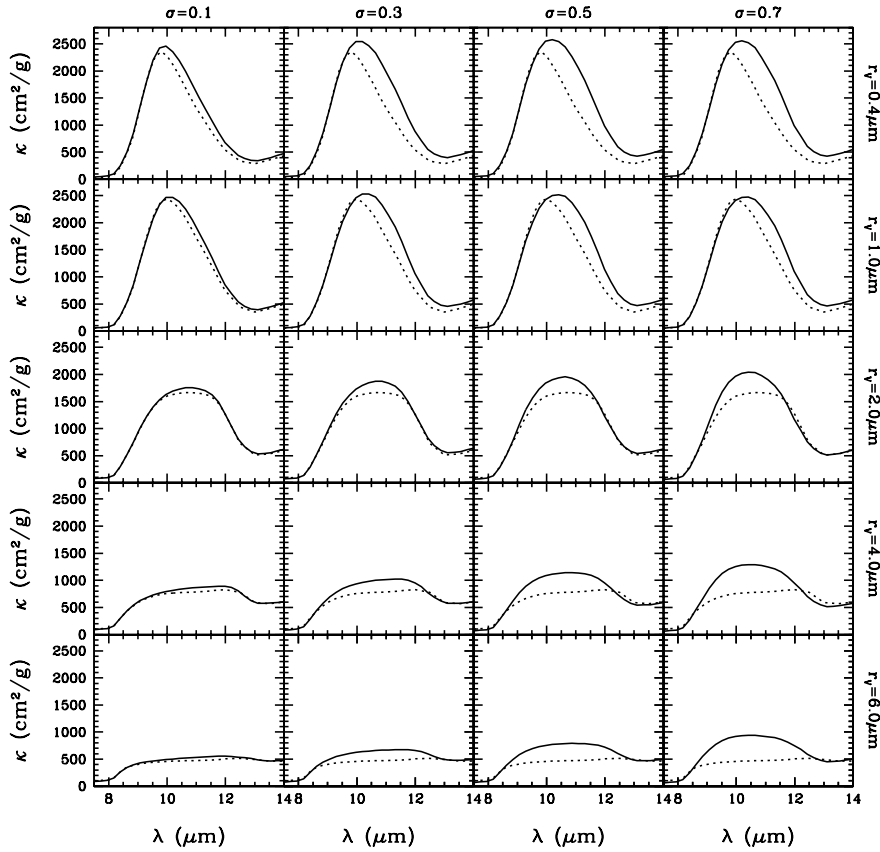


Figure 6.3: The mass absorption coefficient, κ , averaged over all particle orientations as a function of wavelength for Gaussian Random Spheres composed of amorphous olivine (solid lines) with various values of the shape parameter σ and grain sizes r_v . Also shown are the spectra for volume equivalent homogeneous spheres (dotted lines). Particle size is increased from top to bottom, while the particle non-sphericity is increased from left to right. The refractive index of amorphous olivine as a function of wavelength used in the calculations was taken from Dorschner et al. (1995).

of volume equivalent homogeneous spherical particles. It is clear that in all cases by increasing the particle size beyond 1 μm , the strength of the 10 μm feature is decreased. Also, for the grains with a volume equivalent radius larger than 1 μm , increasing the value of σ increases the peak value. The reason is probably that the bumps and spikes sticking out of the particle for high values of σ (see Fig. 6.1) roughly interact with the radiation like small separate particles. In general, the feature as computed using volume equivalent homogeneous spheres is narrower and weaker. When for homogeneous spheres the grain size is increased, the feature weakens and flattens, i.e. it becomes more flat-topped. For the Gaussian random spheres the feature also weakens when the grain size is increased, however, the shape of the feature still shows a more rounded top.

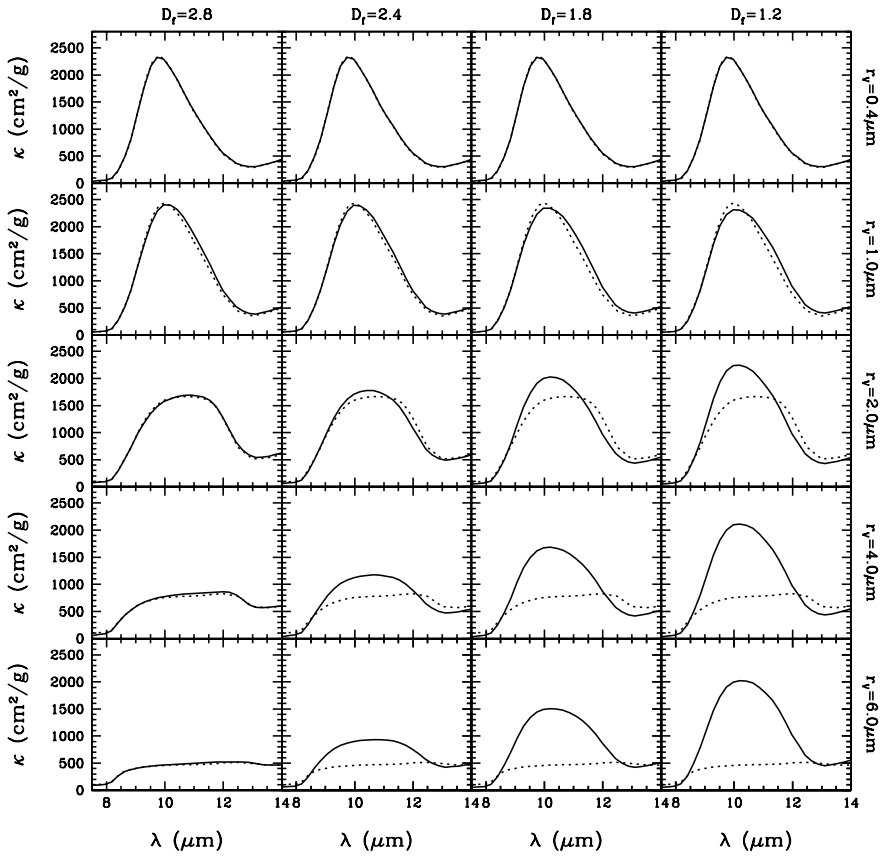


Figure 6.4: Same as Fig. 6.3 but for fractal aggregates with various values of the fractal dimension (solid lines). The increase in particle size for aggregates implies an increase of the number of constituents (see Fig. 6.2).

By considering the spectra of different realizations of the Gaussian random spheres with the same shape parameters σ and Γ but different seeds for the random number generator we find that the differences in the absorption spectra are small and that all trends are conserved (not shown in the figure).

Plotted by the solid curves in Fig. 6.4 is the mass absorption coefficient as a function of wavelength for the fractal aggregates with different fractal dimensions and aggregate sizes as shown in Fig. 6.2. It is clear from this figure that the $10\mu\text{m}$ feature of fractal aggregates with a low value of the fractal dimension in general has a much weaker dependence on the particle size than that of aggregates with a higher value of the fractal dimension. For a fractal aggregate with $D_f = 1.2$ the feature strength is only very slightly decreased even if the volume equivalent radius is increased from $0.4\mu\text{m}$ to $r_V = 6\mu\text{m}$, in which case $r_c = 320\mu\text{m}$. This is probably caused by the fact that the constituents in

fractal aggregates with low fractal dimensions are separated by large distances. This reduces the interaction between the different volume elements within the aggregate. Thus, the monomers interact, to a certain extent, as if they were separate small particles, displaying a feature typical for small dust grains. We have to note here that there is a difference between the spectra for the separate constituent (upper panels) and the fully grown aggregates (shown in the lower panels) even for the most fluffy aggregates. This means that even in the most extreme case $D_f = 1.2$ there has to be interaction between the constituents of the aggregate. Thus, the effects of aggregation on the spectral signature will always be visible, even in the case that the aggregates form almost linear chains. In general, when increasing the fractal dimension, the spectral signature of the monomers becomes more apparent in the spectrum of the aggregate. Comparing the resulting spectra for the fractal aggregates with homogeneous spheres we see that, as with the Gaussian random spheres, the features for the larger fractal aggregates also have a generally more rounded shape. The spectra of very compact aggregates ($D_f = 2.8$) show virtually no differences with those of homogeneous spheres.

Also for the fractal aggregates we considered different realizations of the particles with the same shape parameters but different seeds of the random number generator and found that the differences in the spectra obtained are negligible.

6.5 Implications for grain growth and dust modeling

In this section we will quantify the effects of the assumption of particle shape on the derived grain size and dust mass when fitting observed infrared $10\mu\text{m}$ spectra. We do this by taking the $10\mu\text{m}$ spectra presented in the previous section and fitting these with the $10\mu\text{m}$ spectrum of an ensemble of homogeneous spheres with radius r_f and total mass M_f . This showed that, in general, the spectral shapes shown in Figs. 6.4 and 6.3 are very well reproduced using homogeneous spheres. In almost all cases the fitted curves deviate less than the linewidth from the curves shown in Figs. 6.3 and 6.4. Only for the large (4 and $6\mu\text{m}$) Gaussian random spheres with high values of σ and the large fractal aggregates with intermediate values of D_f the fits are of a slightly lesser quality. In these cases, the nonspherical particles display a feature with low contrast combined with a relatively rounded top. This cannot be reproduced accurately by using homogeneous spherical particles. The fact that most spectra are fitted very well implies that it is difficult to determine particles shapes from the shape of the $10\mu\text{m}$ feature alone. Thus, one has to resort to other observables, like for example the degree of linear polarization in the visible part of the spectrum, to obtain information on the particle shape. The resulting values of the best fitting r_f for the different values of σ , D_f , and r_V are presented in Table 6.1 and the corresponding values of M_f in Table 6.2. In Fig. 6.5 we plot r_f as a function of r_V for all particle shapes we considered. It is clear that in almost all cases the size of the particles is underestimated when fitting the $10\mu\text{m}$ absorption spectrum using homogeneous spheres. For the fractal aggregates with very low fractal dimension this is most extreme. Extrapolation of the curves in Fig. 6.5 beyond $6\mu\text{m}$ for fractal aggregates with low fractal dimension suggests that even for very large aggregates the $10\mu\text{m}$ feature will display a signature typical for relatively small homogeneous spheres.

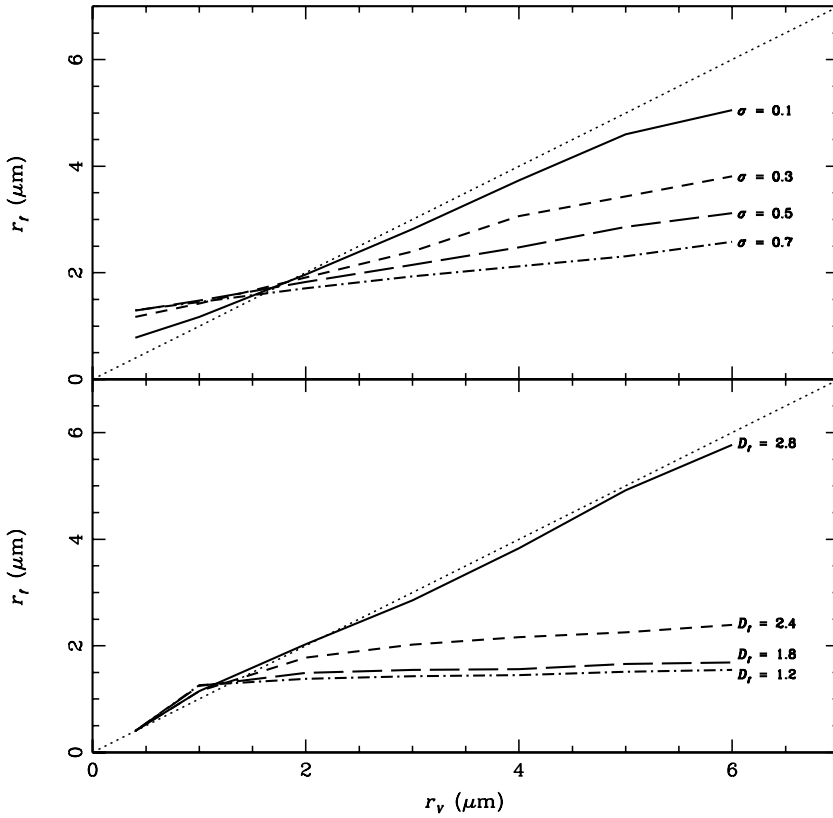


Figure 6.5: The best fit size of a homogeneous sphere to the $10\mu\text{m}$ amorphous olivine spectra, r_f , of particles with different shapes as a function of the volume equivalent radius of the particles, r_v . The top panel is for the Gaussian random spheres with different values of σ , while the lower panel is for the fractal aggregates with different fractal dimensions, D_f . The values of σ and D_f are indicated at the right side of the curves. The dotted lines represent the case in which the fitted size and the real size are equal, i.e. $r_v = r_f$.

The mass estimate we get from the fit using homogeneous spheres is in most cases close to the real mass (M_f is relatively close to unity). This is a result of the fact that the particles we consider are not extremely large. For very large particles, $r_v \gtrsim 20\mu\text{m}$, the error in the mass estimate will be much larger. For the intermediate fractal dimensions and for the irregularly shaped compact particles we make an error in the mass estimate of 30% for the largest values of r_v .

In several studies of the $10\mu\text{m}$ spectra of circumstellar disks (see e.g. Bouwman et al. 2001; Honda et al. 2004; van Boekel et al. 2004a, ; chapter 9 of this thesis) particle size effects have been modeled by using a typical size for the large particles of $r_v = 1.5$ or $2.0\mu\text{m}$. The spectral signature of particles with these sizes is reported in these spectra.

	Gaussian random spheres				Fractal aggregates			
	σ	σ	σ	σ	D_f	D_f	D_f	D_f
	0.1	0.3	0.5	0.7	2.8	2.4	1.8	1.2
$r_V = 0.4 \mu\text{m}$	0.8	1.2	1.3	1.3	0.4	0.4	0.4	0.4
$r_V = 1.0 \mu\text{m}$	1.2	1.4	1.5	1.5	1.2	1.1	1.3	1.3
$r_V = 2.0 \mu\text{m}$	2.0	1.9	1.8	1.7	2.0	1.8	1.5	1.4
$r_V = 4.0 \mu\text{m}$	3.7	3.1	2.5	2.1	3.8	2.2	1.6	1.4
$r_V = 6.0 \mu\text{m}$	5.1	3.8	3.1	2.6	5.8	2.4	1.7	1.5

Table 6.1: The radius of the best fit homogeneous sphere, r_f , in μm for the absorption spectra of the Gaussian random spheres and the fractal aggregates.

Since this grain size is significantly larger than that derived for the dust in the interstellar medium (Kemper et al. 2004) this provides clear evidence of grain growth in these disks. In these studies the particles are considered to be compact, and in most cases homogeneous spheres. However, models of grain growth in astronomical environments show that aggregates with a wide range of fractal dimensions can be formed. As we showed, in general, fractal aggregates and irregularly shaped compact particles display the spectral signature of smaller homogeneous spheres. Thus, when interpreting emission spectra of astronomical objects using compact particles, the size of the emitting grains is generally underestimated. A good estimate of the real particle shape or fractal dimension may be available from, for example, theoretical arguments. In that case the r_f derived from fitting 10 μm spectra of astronomical sources using homogeneous spheres can be used, in combination with Table 6.1, to estimate the volume equivalent radius of the particles, r_V .

For example, say that we derive from the shape of an observed 10 μm feature using homogeneous spheres that the typical particle size $r_f = 1.7 \mu\text{m}$. Furthermore, we expect that the grains present in the environment we are observing are fractal aggregates with $D_f \approx 1.8$. We can then estimate from Table 6.1 that the true volume equivalent radius of the grains is $r_V \approx 6 \mu\text{m}$. The linear extent of the aggregates can be estimated using γ to be $r_c \approx 36 \mu\text{m}$ (see Fig. 6.2). In addition, from Table 6.2 it can be found that the derived dust mass is a likely underestimate of the real dust mass by roughly 20%.

Since the curves for the low fractal dimension are very flat for $r_V \gtrsim 1 \mu\text{m}$, the estimate of r_V strongly depends on the accuracy of r_f . Furthermore, the fractal dimension that is employed can change the estimated value of r_V from a given value of r_f significantly. Coagulation calculations and experiments play a crucial role in determining the possible shapes and fractal dimensions that can be formed under different conditions. Therefore, these calculations and experiments are very important for a correct analysis of 10 μm spectra.

Models of grain growth predict that, for example, in protoplanetary disks, grain growth rapidly removes small grains (Dullemond & Dominik 2005). When homogeneous spheres are used to compute the 10 μm spectra of amorphous olivine particles, already for a grain with a 4 μm radius the feature is flattened so much that it becomes

	Gaussian random spheres				Fractal aggregates			
	σ	σ	σ	σ	D_f	D_f	D_f	D_f
	0.1	0.3	0.5	0.7	2.8	2.4	1.8	1.2
$r_V = 0.4 \mu\text{m}$	1.0	1.1	1.1	1.1	1.0	1.0	1.0	1.0
$r_V = 1.0 \mu\text{m}$	1.0	1.1	1.2	1.2	1.0	1.0	1.0	1.0
$r_V = 2.0 \mu\text{m}$	1.0	1.0	1.1	1.1	1.0	1.0	1.0	1.0
$r_V = 4.0 \mu\text{m}$	1.0	0.9	0.8	0.8	1.0	0.8	0.8	1.0
$r_V = 6.0 \mu\text{m}$	0.9	0.8	0.7	0.7	1.0	0.7	0.8	1.0

Table 6.2: The mass scaling factor of the best fit homogeneous sphere, M_f , for the absorption spectra of the Gaussian random spheres and the fractal aggregates.

very hard to detect. This contradicts observations of protoplanetary disks where prominent $10 \mu\text{m}$ features are found (see e.g. Bouwman et al. 2001). Dullemond & Dominik (2005) propose a possible explanation for this discrepancy by considering destructive particle collisions. This causes an equilibrium situation with a significant amount of small grains. In addition to this, we have shown that when the particles grow as fluffy aggregates, the $10 \mu\text{m}$ feature will be visible for much larger particle sizes.

A flattened, square $10 \mu\text{m}$ feature as seen in the absorption spectra of homogeneous spheres is observed in the $10 \mu\text{m}$ emission spectra of some protoplanetary disks (see e.g. Bouwman et al. 2001). Since the features of very irregularly shaped particles or fluffy aggregates as presented in Figs. 6.3 and 6.4 show a somewhat more rounded top, one could argue that this suggests that the particles in these protoplanetary disks may be relatively compact. However, a firmer analysis of the observations is needed in order to confirm this.

6.6 Conclusions

We have presented calculations of the $10 \mu\text{m}$ absorption spectra of complex shaped compact particles and fractal aggregates with various fractal dimensions. We have compared the resulting spectra and studied the dependence of the spectral signature on the size of the particles. It is clear that the size dependence of the spectral signature of fractal aggregates depends strongly on the fractal dimension of the aggregate. For very fluffy aggregates, i.e. low fractal dimensions, the spectral signature of very large aggregates still looks like that of very small compact particles.

For the complex shaped compact particles the size dependence of the spectral signature also depends on the actual shape of the emitting grains. In general we find that the strength of the $10 \mu\text{m}$ absorption spectrum of a nonspherical particle is equal to that of a smaller homogeneous spherical particle.

Observed $10 \mu\text{m}$ emission and absorption spectra are often interpreted using compact, and in most cases homogeneous spherical, particles. We show that this leads to an underestimate of the actual grain size when the emitting grains are either nonspherical compact particles or fractal aggregates. We present a way of estimating the true particle

size and mass, when an estimate of the shape or fractal dimension of the particles can be provided.

Analysis of the $10\mu\text{m}$ emission spectra of circumstellar disks show that the spectral signature of homogeneous spherical particles with radii of approximately $2\mu\text{m}$ is present in these disks. When the emitting grains are actually fractal aggregates with a fractal dimension of approximately 1.8 this implies a volume equivalent radius of these aggregates of at least $r_V = 6\mu\text{m}$. The radius of the circumscribed sphere is then even of the order of $r_c \approx 36\mu\text{m}$. In environments where aggregates with even lower fractal dimensions can grow, grain sizes will be even more severely underestimated when using compact particles.

7

Spectroscopic diagnostic for the mineralogy of large dust grains

*M. Min, C. Dominik, and L. B. F. M. Waters
Astronomy and Astrophysics, v.413, p.L35-L38 (2004)*

Abstract

We examine the thermal infrared spectra of large dust grains composed of amorphous and crystalline olivine. Strong resonances in the refractive indices result in detectable spectral structure even when the grain is much larger than the wavelength at which it radiates. We apply this to the thermal infrared spectra of compact amorphous and crystalline silicates. The weak resonances of amorphous silicates at 9.7 and 18 μm virtually disappear for grains larger than about 10 μm . In contrast, the strong resonances of crystalline silicates produce *emission dips* in the infrared spectra of large grains; these emission dips are shifted in wavelength compared to the *emission peaks* commonly seen in small crystalline silicate grains. We discuss the effect of a fluffy or compact grain structure on the infrared emission spectra of large grains, and apply our results to the dust shell surrounding Vega.

7.1 Introduction

Infrared spectroscopy is an invaluable tool for the study of the structure and composition of interstellar and circumstellar dust. In the infrared, functional groups in a dust grain lead to spectral features in the absorption cross section of a grain. These features can be detected in absorption against a strong infrared background source, or as emission features if the grains are warm enough to emit thermally in this wavelength region. The precise shapes and positions of such features contain information about grain size, shape and detailed chemical composition (Bohren & Huffman 1983).

It is generally assumed that dust grains need to be small in order to produce spectral structure. When grains are large, each individual grain becomes optically thick at infrared wavelength, and the features in the absorption cross section are expected to weaken with increasing grain size and eventually to disappear completely. In most environments in interstellar space, small dust grains dominate the overall grain surface available and therefore also dominate the total absorption cross section. There are, however, environments where small grains are heavily depleted. In particular in gas-poor circumstellar disks, small dust grains are removed by radiation pressure and larger

grains start to dominate the interaction with radiation. For example, the zodiacal dust in the solar system is dominated by large grains since grains smaller than about 1 micron are quickly lost (Burns et al. 1979). This effect becomes even stronger in debris disks around A-type main sequence stars like Vega, where the increased luminosity shifts the typical blowout size to about 10 micron (Artymowicz 1988). Even stronger effects may exist in disks around (post)-AGB stars, where already grains of mm size will be lost unless the disk is optically thick and gas-rich (Dominik et al. 2003).

We therefore examine in this paper the optical properties of large dust grains. In section 7.2 we show that the strong resonances observed in crystalline materials lead to observable structure in the infrared spectra of large dust grains. In section 7.3 we apply these results to the dust shell around Vega. In sections 7.4 and 7.5 we discuss and summarize our results.

7.2 Infrared emission spectra

In order to calculate the thermal emission spectrum of a dust shell we need to know the emission cross sections of the dust grains. With grain size, shape and chemical composition known, the emission cross section per unit mass as a function of wavelength can be calculated from the wavelength dependent bulk refractive index. In grains much smaller than the wavelength of radiation, a resonance in the bulk refractive index causes a so-called surface mode (Bohren & Huffman 1983). These surface modes are strong enhancements of the absorption cross section and are detected as emission features in the thermal emission spectra of these grains. For larger grains, the contrast in the absorption features is diminished and it is generally assumed that the thermal emission from large particles will be a smooth blackbody without a characteristic signature of the mineralogy. However, this assumption only holds if the refractive index is close to unity over the entire wavelength range. For the resonances in crystalline silicates, both the real and imaginary part of the refractive index can reach values up to ~ 9 . For large particles with these values of the refractive index, most radiation will be reflected off the surface of the particle and will not penetrate the grain. This leads to a significant reduction of the grain absorption efficiency at these wavelengths. Therefore, we also expect to find a corresponding decrease of the emission efficiency, at wavelengths where there is a resonance in the bulk refractive index (Bohren & Huffman 1983). This is illustrated in Fig. 7.1 where the emission cross sections per unit mass are plotted for grains composed of amorphous olivine and crystalline forsterite for different grain sizes. Moving from small to large grains, the structure in the spectrum of amorphous olivine virtually disappears, to a level which makes detection in astrophysical environments extremely hard. However, as pointed out earlier by Lynch & Mazuk (2000), the spectral structure never disappears completely. This effect becomes much more prominent for the crystalline forsterite: the features in this spectrum change from emission peaks to emission dips. The remaining contrast even for very large grains is strong enough to be detected in astrophysical sources. Generally the features at shorter wavelengths and the strongest features are the first to disappear and change into emission dips. Most dips in the spectra of the large grains are slightly red-shifted compared to the corresponding emission

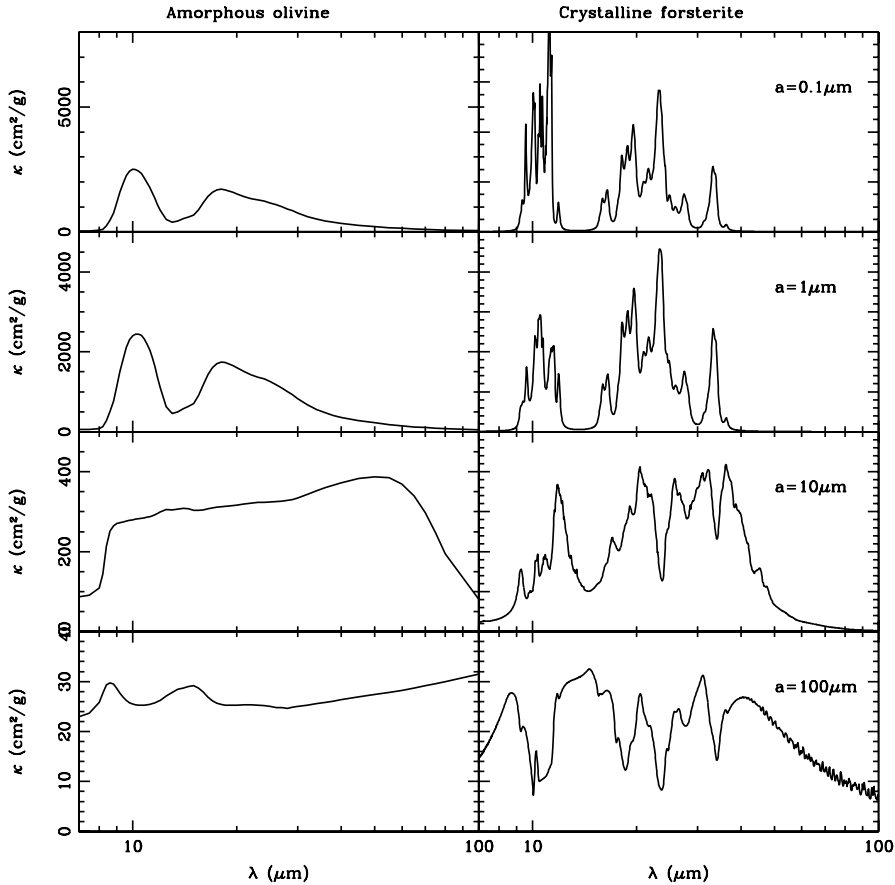


Figure 7.1: The emission cross sections per unit mass, κ , for various sizes of amorphous olivine grains (left panels) and crystalline forsterite grains (right panels) as functions of the wavelength. The emissivities were calculated using a uniform distribution of spheroids (UDS). The refractive index data for the crystalline forsterite are taken from Servoin & Piriou (1973), for the amorphous olivine the data are taken from Dorschner et al. (1995). Note the different y-scales for the different grain sizes.

enhancements in the small grain spectra. When the grain size is increased even more, the overall shape of the spectrum will flatten but the spectral structure remains visible at about the same contrast level.

In order to calculate the emission cross sections, a particle shape has to be assumed. We used a uniform distribution of spheroids which is in very good agreement with laboratory measurements of the mass absorption coefficients of small crystalline silicate grains (Min et al. 2003b). The cross sections were calculated using the method described in Min et al. (2003a). For the large particles, the emission efficiencies are the same for

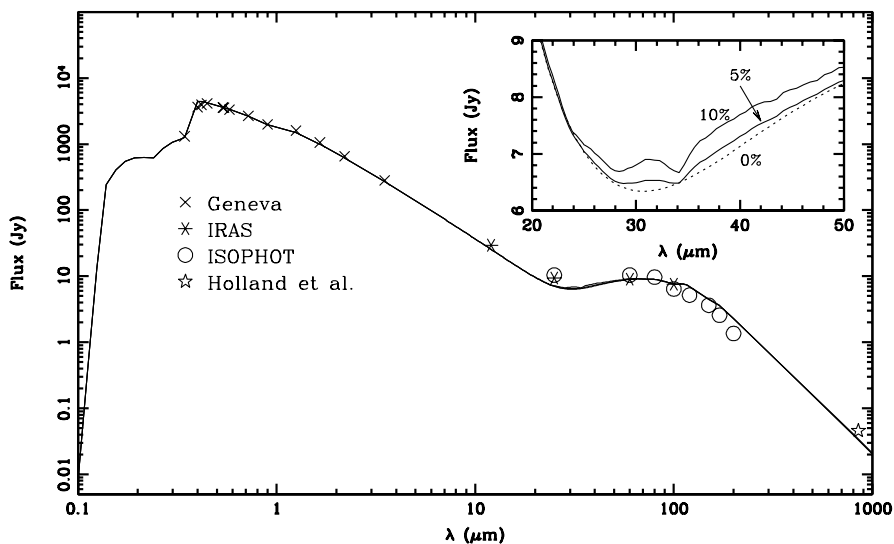


Figure 7.2: Model infrared spectra for Vega. The parameters for the model are given in the text. The IRAS data are taken from Walker & Wolstencroft (1988), the ISOPHOT data are from Heinrichsen et al. (1998) and the submm flux is taken from Holland et al. (1998). The labels with the curves in the inset are the abundances of forsterite for the different models.

all convex shaped particles. Calculations for homogeneous spheres using Mie theory (Mie 1908) will therefore give the same emission spectrum in the large particle limit.

It is important to note that for large compact grains the emission cross section per unit mass is very low compared to small grains - this can be seen from the different scales used in Fig. 7.1. Also, the contrast of the emission dips created in large grains is weaker than the emission peaks due to small grains. In most spectra, the emission by small grains, which is much more efficient, will be dominating. The spectral signature of the large compact dust grains should therefore be observable only in environments where small grains are heavily depleted.

7.3 The spectrum of Vega

An efficient mechanism to remove small grains from a population of grains is radiation pressure on grains in orbit around a star. Due to the efficient absorption, the radiative acceleration on small grains will easily exceed the gravitational force exerted by the stars. If the grains are orbiting in a gas-poor, optically thin circumstellar shell, they will be removed on a Kepler timescale. Such conditions are given in the debris disks around main-sequence stars.

To demonstrate the effects of large compact crystalline grains, we calculated the spectrum of Vega using a dust shell in a distance range of 80-120 AU from the star. The

stellar spectrum is represented by a Kurucz model (Kurucz 1993) with $T_{\text{eff}} = 9500$ K and $\log g = 4$. For the size distribution of the dust grains we used a powerlaw with sizes between 15 and $100 \mu\text{m}$ and a powerlaw index of -3.5 , typical for a collisional cascade (Tanaka et al. 1996). From the collisional model of Dominik & Decin (2003) and the calculated radiation pressure we estimated the fraction of small particles to be $\lesssim 0.1\%$ of the total mass. Calculations show that this mass fraction does not produce significant emission to be visible in the spectrum. The dust is assumed to be a mixture of 20% amorphous carbon and 80% olivine by mass. We calculated various models with different mass fraction of crystalline and amorphous olivine. The dust grains are assumed to be compact particles. Since shape effects are negligible for dust grains of these sizes, the optical properties are calculated using homogeneous spheres. The refractive index data for the amorphous carbon are taken from Preibisch et al. (1993). The dust temperatures are computed self-consistently from the local radiation field. Typical values for the dust temperatures found in this way are ~ 80 K. The total dust mass used in order to fit the photometry points is $\sim 1/10$ of a lunar mass which is in agreement with the estimate by Dent et al. (2000).

The model spectrum is shown in Fig. 7.2, which runs reasonably well through the observed photometry points. It should be stressed here that the presented spectrum is an example to demonstrate the effect of large grains. We do not claim to present the best fit to the available data points. The inset in Fig. 7.2 shows an enlargement of the 20 to $50 \mu\text{m}$ region. A prominent dip in the spectrum at $34 \mu\text{m}$ is caused by large compact forsterite grains. Even with only 5% of the mass present as compact forsterite grains, the dip would most likely be detectable by SIRTF.

7.4 Discussion

7.4.1 Grain composition

In section 7.3 we have shown that a fraction of about 5% in compact forsterite grains would produce a detectable feature in the spectrum of Vega. It is important to note that this mass fraction should be present as separate homogeneous grains. If the forsterite material is present as small inclusions inside an amorphous matrix, a significantly larger fraction of forsterite would be required to produce a spectral signature.

7.4.2 Grain structure

The structure of the dust grains is an important parameter that contains information about its formation and processing history. As a first rough classification we can distinguish between fluffy and compact particles. The structure of a grain can be traced back to its formation process. Dust grains that are grown by coagulation of small (submicron sized) grains will show a very fluffy open structure (Blum et al. 2000), similar to the structure observed in interplanetary dust particles (IDP). Such grains are also expected to result from the destruction of primitive planetary bodies such as small cometary nuclei. Compact (non-fluffy) large grains will result from the destruction of larger parent bodies

which have been molten and possibly differentiated during the formation process, like large asteroids.

Measurements of the infrared transmission spectrum of a large ($a \approx 20 \mu\text{m}$) fluffy IDP by Molster et al. (2003) still shows the resonances characteristic for submicron grains. This indicates that the infrared spectrum of fluffy particles will still be dominated by the spectral signature of the constituents of the aggregate. In other words, we expect to see the small particle crystalline silicate emission features in the emission spectra of these dust grains. For large compact particles we expect to see a spectral signature as shown for $100 \mu\text{m}$ sized particles in Fig. 7.1.

7.5 Conclusions

We have developed a new diagnostic tool for determining the mineralogy of large compact dust grains. The thermal emission spectra of large compact crystalline silicate dust grains exhibit characteristic features that can be detected with high signal to noise spectroscopy. These features are *emission dips* at positions that can be *slightly red shifted* from the corresponding emission peaks observed for small grains. As an example, a model calculation of the infrared emission from the dust shell around Vega shows that these features should be detectable if the dust grains are compact and contain at least 5% crystalline forsterite in a separate grain component. Since there is a clear spectroscopic difference between fluffy and compact dust grains, the spectral signature of crystalline silicates can be used to obtain information on the structure, mineralogy and formation history of the dust grains. Another application of this diagnostic can be the zodiacal dust.

Our model calculations show that if large compact crystalline silicates are present even with modest abundances, this should be detectable as a depression near $34 \mu\text{m}$. If the grains are fluffy, an emission band should be present at a slightly shorter wavelength. Such spectral structure may be measured using the IRS spectrograph on board of SIRTf.

Acknowledgments

We would like to thank J. W. Hovenier for valuable discussions. Comments on an earlier version of this manuscript by F. J. Molster are gratefully acknowledged.

The composition and size distribution of the dust in the coma of comet Hale-Bopp

*M. Min, J. W. Hovenier, A. de Koter, L. B. F. M. Waters, and C. Dominik
Submitted to Icarus*

Abstract

We discuss the composition and size distribution of the dust in the coma of comet Hale-Bopp. We do this using a model fit for the infrared emission measured by the infrared space observatory (ISO) and the measured degree of linear polarization of scattered light at various phase angles and wavelengths. The effects of particle shape on the modeled optical properties of the dust grains are taken into account. Both the short wavelength (7-44 μm) and the long wavelength (44-120 μm) infrared spectrum are fitted using the same dust parameters, as well as the degree of linear polarization at 9 different wavelengths in the optical to near infrared domains. We constrain our fit by forcing the abundances of the major rock forming chemical elements to be equal to those observed in meteorites. The infrared spectrum at long wavelengths reveals that large grains are needed in order to fit the spectral slope. The size and shape distribution we employ allows us to estimate the sizes of the crystalline silicates. The ratios of the strength of various forsterite features show that the crystalline silicate grains in Hale-Bopp must be submicron sized. On the basis of our analysis the presence of large crystalline silicate grains in the coma can be excluded. Because of this lack of large crystalline grains combined with the fact that we do need large amorphous grains to fit the emission spectrum at long wavelengths, we need only approximately 3.5% of crystalline silicates by mass (forsterite and enstatite) to reproduce the observed spectral features. After correcting for possible hidden crystalline material included in large amorphous grains, our best estimate of the total mass fraction of crystalline material is $\sim 7.5\%$, which is significantly lower than deduced in previous studies in which the typical derived crystallinity is $\sim 20 - 30\%$. The implications of this low abundance of crystalline material on the possible origin and evolution of the comet are discussed. We conclude that the crystallinity we observe in Hale-Bopp is consistent with the production of crystalline silicates in the inner solar system by thermal annealing and subsequent radial mixing to the comet forming region (~ 30 AU).

8.1 Introduction

Comet Hale-Bopp is undoubtedly the best studied long period comet in the solar system. The unusual brightness of this comet allowed for its discovery when it was still at 7 AU distance from the Earth, and a long term monitoring of the dust activity after perihelion up to almost 13 AU (Weiler et al. 2003). The infrared spectrum taken by the Infrared Space Observatory (ISO) provided a unique opportunity to study the composition of cometary dust (Crovisier et al. 1997; Lellouch et al. 1998). The strong resonances visible in this spectrum were attributed to the presence of crystalline silicates.

The relatively sharp $9.8\ \mu\text{m}$ feature in the ISO spectrum together with observations of an extremely high degree of linear polarization lead to the conclusion that the dust in the coma of Hale-Bopp has an overabundance of submicron sized grains (see e.g. Hanner et al. 1999; Mason et al. 2001, and references therein).

The composition of the dust in Hale-Bopp has been modeled frequently in the literature applying various approaches (see e.g. Lellouch et al. 1998; Li & Greenberg 1998; Brucato et al. 1999; Wooden et al. 1999; Harker et al. 2002; Bouwman et al. 2003; Moreno et al. 2003). The interpretation of the results obtained from the observations lead to discussions in the literature on the origin and evolution of cometary dust (for a review see Wooden 2002). Cometary dust is believed to be the most primitive material present in the solar system. The high crystallinity found by most studies of the infrared emission spectrum presents a problem for this scenario. Since the dust that entered the proto-solar nebula from the interstellar medium is almost completely amorphous (Li & Draine 2001; Kemper et al. 2004), the crystalline silicates in Hale-Bopp have to be products of processing in the early solar system. Crystalline silicates can only be produced in high temperature environments ($\gtrsim 1000\ \text{K}$), so close to the Sun, while comets form in regions where the temperatures are low enough for water ice to exist ($\lesssim 160\ \text{K}$). Thus, the crystalline silicates have to be transported outwards to the regions where the comets form, or the dust temperature must be locally increased due to for example lightning or shock annealing (Harker & Desch 2002; Pilipp et al. 1998; Desch & Cuzzi 2000).

It is clear that in order to constrain the models explaining the crystalline silicates in cometary material, accurate knowledge of the abundances of the various components in the dust is required. However, the large differences in the derived crystalline silicate abundances published in the literature so far make progress in this area difficult. All studies agree that the abundance of sub-micron sized crystalline silicates is very high (although again with considerable spread), but the question remains open what the crystallinity of the larger grain population is, where most of the mass resides. This is because modeling the optical properties of large, irregularly shaped particles composed of material with high refractive index is difficult.

In this study, we combine for the first time both the available observations of the thermal emission as obtained by ISO (Crovisier et al. 1997; Lellouch et al. 1998) and the degree of linear polarization taken from Ganesh et al. (1998); Jockers et al. (1999) and Manset & Bastien (2000), with a single dust model. In contrast with previous studies we calculate the optical properties of the dust grains using a method where we can take into account both size and shape effects. With this method, we obtain *information on*

the composition and mass of the large grain component. Also we constrain the chemical abundances as known from studies of meteorites. Thus, we are able to better constrain the dust composition and size distribution in the model than previous studies. As we will show, the size distributions of crystalline and amorphous silicates are very different, and we are able to rule out the presence of substantial amounts of large (1-10 μm) crystalline silicates. This results in a much lower overall crystallinity than most other studies found.

In section 8.2 we explain the fitting procedure and the dust model we employ. The results of the best fit model are presented in section 8.3. The implications of these results are discussed in section 8.4.

8.2 Method

In this section we will outline the method used to interpret the observations of the thermal infrared emission and the degree of linear polarization of comet Hale-Bopp in terms of the properties of the particles in the coma. The method we use has a few important characteristics:

- Both size and shape effects of the dust grains are taken into account when calculating the optical properties, i.e. the absorption (emission) cross sections and the degree of linear polarization of scattered light. In contrast with previous studies, our shape distribution enables us to use the same particle shapes for all dust components and grain sizes. This implies that we can, for the first time, include the effects of grain size on the optical properties of crystalline silicate grains.
- The parameters of the size distributions and the abundances of the various components are determined using an 'objective' least squares fitting routine.
- We require the best fit model to fulfill the constraint that the dust in comet Hale-Bopp has the same abundances of the chemical elements of the major solid state materials as observed in interplanetary dust particles and meteorites.

8.2.1 Size and shape of the dust grains

The optical properties at a particular wavelength, i.e. the absorption and scattering cross sections as well as the scattering matrix, of a dust grain are determined by its size, shape, orientation, structure and chemical composition. Throughout this paper the size of a dust grain is defined as the radius of a volume equivalent sphere, r . We use for the size distribution a powerlaw given by

$$n(r) = \begin{cases} C \cdot r^\beta, & r_{\min} \leq r \leq r_{\max}, \\ 0, & \text{elsewhere.} \end{cases} \quad (8.1)$$

Here $n(r)dr$ is the number of dust particles of an ensemble with sizes between r and $r + dr$; r_{\min} and r_{\max} are the minimum and maximum grain size, respectively, in the

size distribution; β is the index of the powerlaw, and C is a normalization constant. We choose C so that

$$\int_{r_{\min}}^{r_{\max}} \frac{4}{3} \pi \rho r^3 n(r) dr = 1, \quad (8.2)$$

where ρ is the density of the material considered. Hence, $n(r)dr$ is the number of dust particles with sizes between r and $r + dr$ per unit mass. The effective radius, r_{eff} , and the effective variance, v_{eff} , are often used to characterize a size distribution. They are defined by (Mishchenko et al. 2002)

$$r_{\text{eff}} = \frac{1}{\langle G \rangle} \int_{r_{\min}}^{r_{\max}} \pi r^3 n(r) dr, \quad (8.3)$$

$$v_{\text{eff}} = \frac{1}{\langle G \rangle r_{\text{eff}}^2} \int_{r_{\min}}^{r_{\max}} \pi r^2 (r - r_{\text{eff}})^2 n(r) dr, \quad (8.4)$$

where

$$\langle G \rangle = \int_{r_{\min}}^{r_{\max}} \pi r^2 n(r) dr, \quad (8.5)$$

is the average geometrical shadow of the dust grains. The r_{eff} is simply the surface-area weighted mean whereas v_{eff} is the surface-area weighted variance of the distribution.

The shape of the dust grains is an important parameter determining their optical properties. Pictures of interplanetary dust particles (IDPs) show very complex shapes and structures (Warren et al. 1994). To model these complex shapes in detail requires much computing time, which limits the number of other particle parameters that can be studied. In Min et al. (2003b) it is shown that when the absorption cross sections of small particles are considered their shapes can be roughly divided into two categories. The first category contains homogeneous spherical particles, whereas the second category contains all other particle shapes. Effects of the specific particle shape distribution on the absorption properties in the second category are present, but small compared to the differences with homogeneous spheres. This implies that the exact shape of the particles is, in a first approximation, not important as long as we brake the homogeneity or perfect spherical symmetry of a homogeneous sphere. This approach is an example of the statistical approach (see e.g. Kahnert et al. 2002; Kahnert 2004). In this approach the absorption properties of an ensemble of irregular particles are simulated by the average absorption properties of an ensemble of particles with simple shapes.

In this paper we use a distribution of hollow spherical particles (DHS). In this distribution a uniform average is taken over the fraction, f , of the total volume occupied by the central vacuum inclusion in the range $0 \leq f < f_{\max}$, where $f_{\max} \leq 1$. All particles in this distribution have the same material volume, so that the particles with higher values of f have larger outer radii. For details regarding this distribution we refer to Min et al. (2003b). In order to reproduce the wavelength positions of the spectral features of crystalline silicate grains, we have to choose $f_{\max} = 1$ (Min et al. 2003b). Numerical computations for particles with $f = 1$ are not possible since these would have an infinitely large outer radius. For particles much smaller than the wavelength, integrating the optical properties up to $f = 1$ can be done analytically (Min et al. 2003b). For larger

particles numerical computations are necessary. We then choose f_{\max} large enough to reach convergence to the values for $f_{\max} = 1$. For most cases we considered, it suffices to integrate up to $f = 0.98$. The optical properties of hollow spherical particles are calculated using a simple extension of Mie theory (Aden & Kerker 1951). The calculations were done using the layered sphere code for which the basic ideas are explained in Toon & Ackerman (1981). We would like to stress that we do not allege that hollow spheres are a good approximation for the real shape of cometary dust grains. Rather, the properties of the particles in the DHS determining the absorption and polarization behavior of the entire ensemble represent in a statistical way those of an ensemble of realistically shaped dust grains.

One of the advantages of the DHS is that the scattering and absorption properties can be calculated easily for almost all grain sizes and wavelengths. This means that we can calculate the absorption cross sections as well as the degree of linear polarization for incident unpolarized light as a function of scattering angle, which enables us to fit simultaneously the observed infrared emission spectrum and the degree of linear polarization using the same dust parameters. In Min et al. (2003b) it is shown that good agreement between calculations for the distribution of hollow spheres and measurements of the mass absorption coefficients of small forsterite grains as a function of wavelength can be obtained. Also, as is shown by Min et al. (2005), the degree of linear polarization as calculated using the DHS is in good agreement with laboratory measurements of irregularly shaped quartz particles.

A cometary dust grain consists most likely of a mixture of various components such as, for example, olivine, carbon and iron sulfide. In using the model described above we assume that the optical properties of such a mixed particle can be represented by the average properties of homogeneous particles for each of the separate components. The validity of this approach for core-mantle grains is studied by Li et al. (2002) and shown to be dependent on the shape of the dust grains. In general, whether it is a valid assumption depends on the compactness of the composite particle. When the grains are very 'fluffy' aggregates composed of homogeneous monomers, the grain components will approximately interact with the incoming light as if they were separate. However, in a more compact structure, the effects of interaction between the separate components can become visible.

Throughout the paper we will first average over particle shape (f) which will be denoted by $\langle \dots \rangle$. The averaging over particle shape and size will be denoted by $\langle\langle \dots \rangle\rangle$.

8.2.2 Thermal emission

To compute the radiation emitted by an ensemble of monodisperse dust grains in random orientation as a function of wavelength we need two ingredients, *i*) the orientation averaged absorption cross section as a function of wavelength, and *ii*) the temperature of the dust grains. When both are known we can calculate the observed thermal radiation of a dust grain averaged over all orientations as follows

$$\mathcal{F}(\lambda) = \frac{C_{\text{abs}}(\lambda)B_{\lambda}(T)}{D^2}. \quad (8.6)$$

Here $\mathcal{F}(\lambda)$ is the flux density at distance D , λ is the wavelength of radiation, T is the temperature of the dust grain, $B_\lambda(T)$ is the Planck function, and $C_{\text{abs}}(\lambda)$ is the orientation averaged absorption cross section of the dust grains at wavelength λ . The thermal radiation of grains with the temperatures we consider is mainly emitted in the infrared part of the spectrum. At these wavelengths the effect of scattering of solar radiation on the total observed flux is negligible.

The temperature of the dust grains is calculated by assuming thermal equilibrium, i.e. the energy absorbed is equal to the energy emitted. Note that dust grains with equal size r and composition but different shapes and/or orientations can have different equilibrium temperatures. However, we assume that all dust grains with the same volume and composition have the same temperature determined by the shape and orientation averaged absorption properties (as is usually done).

The coma of Hale-Bopp is optically thin. Therefore, we only need to consider direct illumination of the coma grains by the Sun and we may ignore the diffuse radiation field caused by, e.g., scattering of solar light by the coma material. We assume the Sun to radiate like a black body with a temperature of $T = 5777$ K.

Since the absorption cross section, and, therefore, the temperature, depends on the size and chemical composition of the particles we determine the temperature for each different dust particle size and material separately. Using the size distribution given by Eq. (8.1) the flux per unit mass from dust component j is given by

$$\langle\langle\mathcal{F}(\lambda)\rangle\rangle_j = \frac{1}{D^2} \int_{r_{\text{min},j}}^{r_{\text{max},j}} n_j(r) \langle C_{\text{abs},j}(\lambda, r) \rangle B_\lambda(T_j(r)) dr. \quad (8.7)$$

In this equation $n_j(r)$ is the size distribution of component j with minimum and maximum radii $r_{\text{min},j}$ and $r_{\text{max},j}$; $\langle C_{\text{abs},j}(\lambda, r) \rangle$ is the orientation and shape averaged absorption cross section of an ensemble of dust grains of material j with size r , and $T_j(r)$ is the temperature of the dust grains in this ensemble. Since the coma of comet Hale-Bopp is optically thin, the total flux averaged over particle size, shape, orientation and composition is simply the sum over the various components

$$\mathcal{F}_{\text{model}}(\lambda) = \sum_j M_j \langle\langle\mathcal{F}(\lambda)\rangle\rangle_j, \quad (8.8)$$

where M_j is the total mass of dust component j .

8.2.3 Degree of linear polarization of scattered light

In the visible part of the spectrum the radiation from the cometary halo is dominated by sunlight scattered once by dust grains. The intensity and polarization of the scattered light depend on the angle of scattering and the wavelength. For a comet it is possible to obtain measurements of the degree of linear polarization for various scattering angles by observing the comet at various moments during its orbit around the Sun. All information on the angular dependence of the scattering behavior of an optically thin ensemble of dust grains is contained in its 4×4 scattering matrix. When the size and shape distributions and the abundances of all dust species are known, we can calculate the average

4×4 scattering matrix of the ensemble if enough data of the refractive index is available. From this matrix we can obtain the degree of linear polarization for incident unpolarized light of dust component j

$$\langle\langle P(\alpha) \rangle\rangle_j = -\frac{\langle\langle F_{21}(\alpha) \rangle\rangle_j}{\langle\langle F_{11}(\alpha) \rangle\rangle_j}, \quad (8.9)$$

where α is the phase angle and $\langle\langle F_{nk} \rangle\rangle_j$ is the n, k th element of the scattering matrix averaged over size and shape of the dust grains (for details see van de Hulst 1957). It should be noted that for calculations and measurements presented in the literature often the scattering angle, θ , is used instead of the phase angle, α . For comets it is more convenient to use the phase angle. Since multiple scattering can be neglected for comets we have $\alpha = 180^\circ - \theta$.

In order to calculate the degree of linear polarization of an ensemble of particles not only averaged over particle size and shape distributions but also over dust materials, we have to average the matrix elements $\langle\langle F_{nk} \rangle\rangle_j$. Thus the average polarization is given by

$$P_{\text{model}}(\alpha) = -\frac{\sum_j M_j \langle\langle F_{21}(\alpha) \rangle\rangle_j}{\sum_j M_j \langle\langle F_{11}(\alpha) \rangle\rangle_j}. \quad (8.10)$$

8.2.4 Least squares fitting procedure

To make a fit to the observations of Hale-Bopp we need to fine-tune the free parameters in the model in such a way that we minimize the differences between the results of the model computations and the observations in a well defined way. The model we constructed has $4N_d$ free parameters, where N_d is the number of dust species we include in the fitting procedure. By choosing the index of the powerlaw, β , the same for all dust species this reduces to $3N_d + 1$ free parameters, namely $(\{r_{\min,j}, r_{\max,j}, M_j, j = 1..N_d\}, \beta)$. The error on the infrared emission spectrum is defined as

$$\chi_{\text{spec}}^2 = \sum_{i=1}^{N_\lambda} \left| \frac{\mathcal{F}_{\text{model}}(\lambda_i) - \mathcal{F}_{\text{obs}}(\lambda_i)}{\sigma_{\mathcal{F}}(\lambda_i)} \right|^2. \quad (8.11)$$

In this equation λ_i ($i = 1..N_\lambda$) is a chosen wavelength grid; $\mathcal{F}_{\text{obs}}(\lambda_i)$ is the observational value of the flux at wavelength λ_i , and $\sigma_{\mathcal{F}}(\lambda_i)$ is the error of the observed flux at wavelength λ_i . In order to estimate $\sigma_{\mathcal{F}}(\lambda_i)$ we assume that the error in the spectral observations is proportional to the square root of the observed flux. The position of the minimum value of χ_{spec}^2 is independent of the absolute value of the error. Note that, since we do not have the values of the absolute errors of the spectral measurements, the χ_{spec}^2 is not equal to the reduced χ_{spec}^2 and cannot be interpreted as the statistical goodness of fit.

The error of the degree of linear polarization is defined as

$$\chi_{\text{pol}}^2 = \sum_j^{N'_\lambda} \sum_i^{N_\alpha} \left| \frac{P_{\text{obs}}(\alpha_i, \lambda_j) - P_{\text{model}}(\alpha_i, \lambda_j)}{\sigma_P(\alpha_i, \lambda_j)} \right|^2. \quad (8.12)$$

In this equation $P_{\text{obs}}(\alpha_i, \lambda_j)$ is the degree of linear polarization observed at phase angle α_i ($i = 1..N_\alpha$) and wavelength λ_j ($j = 1..N'_\lambda$), while $\sigma_P(\alpha_i, \lambda_j)$ is the error in the observed polarization at phase angle α_i and wavelength λ_j . Note that the number of phase angles at which observations are available may vary with wavelength.

The most straightforward way to define the total χ^2 is to take the sum of χ_{spec}^2 and χ_{pol}^2 . However, since we have many more measurements of the infrared flux than we have observations of the degree of linear polarization and we are unable to compute the reduced χ_{spec}^2 , this would lead to a stronger weight of the spectral measurements than the polarization observations. Therefore, we chose to minimize

$$\chi^2 = \chi_{\text{spec}}^2 \cdot \chi_{\text{pol}}^2. \quad (8.13)$$

The minimization of χ^2 as defined by Eq. (8.13) is done using a combination of two methods. Since the total spectrum is a linear combination of the separate spectra for the different components (see Eq. 8.8), we are able to separate the fitting problem into a non-linear and a linear part. The non-linear part consists of minimizing for all $r_{\text{min},j}$, $r_{\text{max},j}$ and β , and the linear part does the minimization for all M_j .

For the non-linear part of the minimization we use a genetic optimization algorithm called PIKAIA (Charbonneau 1995). This algorithm tries to find a global maximum of an arbitrary function in a large parameter space by using concepts from evolution theory. Every set of parameters ($\{r_{\text{min},j}, r_{\text{max},j}, j = 1..N_d\}, \beta$) is called an individual, the parameters are the 'genes'. The procedure starts with a randomly initialized population of N_{pop} individuals and calculates the χ^2 for each individual. The individuals with the highest values of $1/\chi^2$ (lowest values of χ^2) are then given the best chance to 'reproduce' into the next generation of individuals. This reproduction is done by mixing the genes of two individuals into a new individual. When this procedure is repeated through several generations, the individuals with low values of $1/\chi^2$ will die out and only individuals with high values of $1/\chi^2$ will survive. In the end (after N_{gen} generations) the best individual, which represents the best fit parameters, will survive. To ensure convergence also mutations – random variations on the parameters – are included in the algorithm. An extensive description can be found in Charbonneau (1995). Although the algorithm is not very fast – many models need to be calculated – it is very robust in the sense that it will (almost) always find the global maximum, whereas other optimization codes frequently end up with a local maximum.

For every individual in the genetic algorithm we determine the best values for the M_j by minimizing the χ_{spec}^2 using a linear least squares fitting procedure. Linear least squares fitting amounts to solving an overdetermined matrix equation in a least squares sense. To ensure that all M_j are positive we need a robust linear least squares fitting procedure with extra linear equality and inequality constraints. We use the subroutine DLSEI from the SLATEC library¹. The inequality constraints are used to ensure that $M_j > 0$. The equality constraints are used to constrain the chemical abundances as will be explained in section 8.2.6. Using the M_j thus derived, we calculate χ_{pol}^2 and χ^2 . Although in this way we might miss the absolute minimum, we can use this approach

¹The SLATEC library is publicly available for download at: <http://www.netlib.org/slatec/>

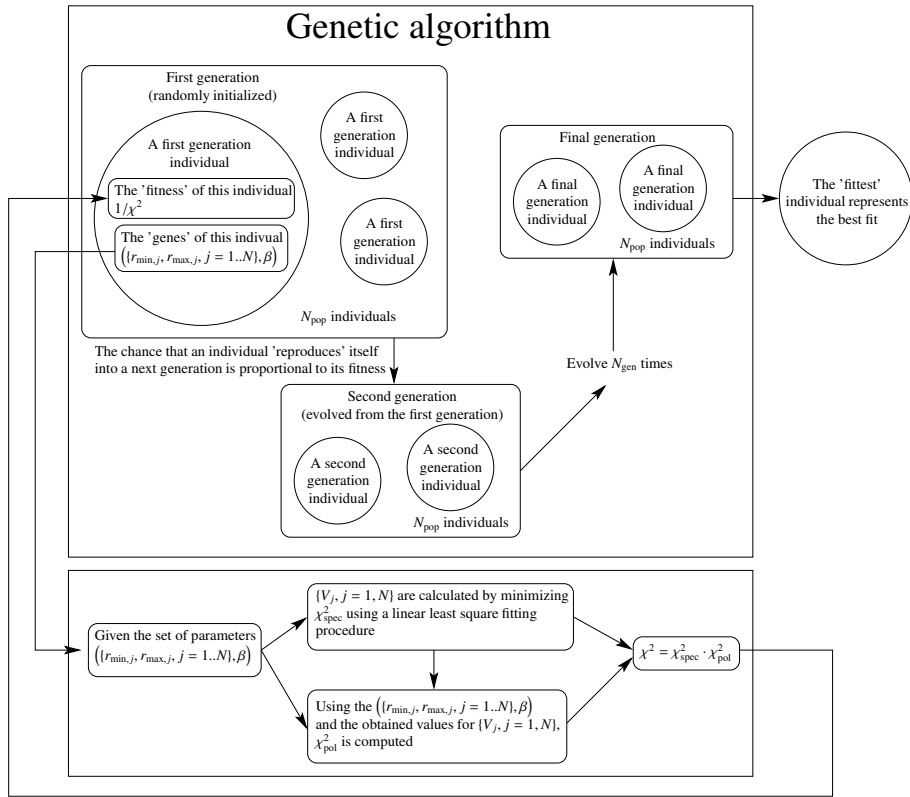


Figure 8.1: A schematic representation of the fitting procedure.

since the infrared spectrum is more sensitive to the exact dust composition than the degree of linear polarization is, which is more sensitive to the size distribution.

In order to estimate the errors on the derived abundances of the dust species we consider all individuals from all generations with a value of χ^2 smaller than 1.1 times the minimum value of χ^2 . The value 1.1 was chosen such that all fits within this range are still in reasonable agreement with the observations.

The entire fit procedure is schematically outlined in Fig. 8.1.

8.2.5 Dust components

In this section we will discuss the dust components we chose for our model computations. Based on previous studies and on the composition of IDPs we make the following selection of components.

- **Amorphous Carbon (C).** We assume that most of the Carbon atoms that are in the solid state phase will be present as amorphous carbon. The emission spectrum

of amorphous carbon gives a smooth continuum contribution without clear spectral structure. From the *in situ* measurements by the Vega spacecraft when it encountered the coma of comet Halley, we know that approximately half of the total available C is present in the solid state phase (Geiss 1987). Carbon probably acts as a matrix in which the other materials are embedded. The refractive index as a function of wavelength is taken from Preibisch et al. (1993).

- **Amorphous Olivine** ($\text{Mg}_{2x}\text{Fe}_{2-2x}\text{SiO}_4$). Amorphous olivine is one of the most abundant dust species in circumstellar and interstellar material (see e.g. Molster et al. 1999a; Bouwman et al. 2001; Li & Draine 2001; Forrest et al. 2004; Kemper et al. 2004). The silicate dust in the diffuse interstellar medium is dominated by amorphous olivine (Kemper et al. 2004). The emission by small amorphous olivine grains shows broad spectral features at 10 and 20 μm . Both are detected in the spectrum of Hale-Bopp. The data for the refractive indices are taken from Dorschner et al. (1995).
- **Amorphous Pyroxene** ($\text{Mg}_x\text{Fe}_{1-x}\text{SiO}_3$). Amorphous pyroxene is spectroscopically hard to distinguish from amorphous olivine. Pyroxene is often found in IDPs. The emission by small amorphous pyroxene grains shows a spectral structure which is similar to that of amorphous olivine grains. However, the maximum of the 10 μm feature is shifted towards slightly shorter wavelengths and the shape of the 20 μm feature is slightly different. The refractive indices for amorphous pyroxene are taken from Dorschner et al. (1995).
- **Crystalline Forsterite** (Mg_2SiO_4). Crystalline forsterite is the magnesium rich end member of the crystalline olivine family. Experiments indicate that when amorphous olivine is annealed under certain conditions, the iron is removed from the lattice structure and crystalline forsterite is formed. The most important resonances in the emission spectrum of small crystalline forsterite grains are located at wavelengths 11.3, 19.5, 23.6 and 33.6 μm . These features are observed in the spectra of, for example, AGB stars and protoplanetary disks (see e.g. Waters et al. 1996; Bouwman et al. 2001) and are clearly visible in the spectrum of Hale-Bopp (Crovisier et al. 1997). For the refractive indices of forsterite we use the data of Servoin & Piriou (1973).
- **Crystalline Enstatite** (MgSiO_3). Crystalline enstatite is the magnesium rich end member of the crystalline pyroxene family. Under the right conditions, enstatite can form from a reaction between forsterite and silica. Also, from IDPs there are indications that some enstatite grains formed directly from gas phase condensation (Bradley et al. 1983). The spectrum of small enstatite grains shows prominent features at 9.3, 10.5, 19.5, 28 and 44.5 μm . Although we have no direct evidence for the presence of most of these features, we include enstatite in the fitting procedure because enstatite features have been reported in the ground based spectrum of Hale-Bopp when it was at 1.2 AU (Wooden et al. 1999). The data for the refractive indices are taken from Jäger et al. (1998).

- **Amorphous Silica** (SiO_2). Laboratory measurements show that when amorphous silicates are annealed to form crystalline silicates, a certain amount of silica is also produced (Fabian et al. 2000). The emission spectrum of small amorphous silica grains shows features at 9, 12.5 and $21 \mu\text{m}$. We take the refractive indices as a function of wavelength measured by Spitzer & Kleinman (1960).
- **Metallic Iron** (Fe). When amorphous silicates are annealed to form magnesium rich crystalline silicates, the iron is removed from the lattice. The spectral signature of metallic iron grains is very smooth but slightly different than that of amorphous carbon. Although it is not crucial in obtaining a reasonable fit, we include the possibility of metallic iron grains in the fitting procedure for completeness. The refractive indices of metallic iron are taken from Henning et al. (1996).
- **Iron Sulfide** (FeS). In IDPs all available sulfur is present as iron sulfide. The spectral structure of emission from iron sulfide grains shows a broad feature around $23 \mu\text{m}$. The fact that this feature is not prominent in the spectrum of Hale-Bopp is probably due to the fact that the iron sulfide grains are relatively large, which reduces the spectral structure significantly. We use the refractive indices measured by Begemann et al. (1994).

To decrease the number of free parameters, we have chosen equal size distributions for both amorphous silicate species (amorphous olivine and amorphous pyroxene) and equal size distributions for both crystalline silicate species (forsterite and enstatite). Furthermore β , the index of the powerlaw, is the same for all materials.

8.2.6 Chemical abundance constraints

The number of free parameters in the method as described above is very large. When we apply no extra constraints we encounter a large set of solutions that all have a more or less equal χ^2 , but with totally different size distributions and material abundances. We also run the risk of obtaining a best fit solution with very implausible values for the fit parameters. To avoid these problems we constrain the solution by requiring that the major elements for solid state materials (Si, Mg, Fe and S) are all in the solid phase and that their chemical abundances are the same as those found in meteorites. Furthermore, we take the abundance of Carbon in the solid phase to be half the solar abundance, consistent with *in situ* measurements of the dust in the coma of comet Halley (Geiss 1987). This gives us four extra constraints on the model. These extra constraints prove to be sufficient to obtain consistent results with the fitting procedure.

We constrain the abundances of C, Mg, Fe and S relative to Si. For the Carbon abundance we take half of the total solar abundance to be in the solid phase, the remaining Carbon is in the the gas phase. Magnesium, iron, sulfur and silicon are assumed to be completely in the solid phase. The abundances we use are taken from Grevesse & Sauval (1998) and are summarized in Table 8.1. All abundance constraints are incorporated as linear equality constraints to the linear least squares fitting part of the minimization procedure.

Chemical element	Meteorites	Solar	Constraints
C/Si	-	9.33	4.67
Mg/Si	1.05	1.07	1.05
Fe/Si	0.87	0.89	0.87
S/Si	0.44	0.60	0.44

Table 8.1: Abundance constraints as applied in the fitting procedure. These values are taken from Grevesse & Sauval (1998). For Carbon we take half of the solar abundance, consistent with in situ measurements of dust in the coma of comet Halley (Geiss 1987).

Dust component	Chemical formula	Abundance (Mass %)
Carbon	C	24.6
Olivine	$\text{Mg}_{2x}\text{Fe}_{2-2x}\text{SiO}_4$	33.4
Pyroxene	$\text{Mg}_x\text{Fe}_{1-x}\text{SiO}_3$	25.0
Iron Sulfide	FeS	17.0

Table 8.2: Abundances as calculated from chemical abundances found in meteorites. In order to satisfy the chemical abundances given in Table 8.1, we have to take $x = 0.7$.

To use the chemical abundance constraints we have to introduce an extra free parameter, x , the magnesium fraction in the amorphous silicates. In section 8.3.2 we will show that the bulk of the material consists of olivine, pyroxene, carbon and iron sulfide. Using this information we can already make a simple but reliable estimate of the value of x by adopting these four species only and applying the abundance constraints discussed above (as this implies that we have four constraints and four unknown parameters the material abundances are uniquely defined). The results of this simple calculation are summarized in Table 8.2, and give $x = 0.7$. Note that here it is not possible to distinguish between amorphous and crystalline material. The results from the fitting procedure will be slightly different due to a different composition of crystalline and amorphous silicates and the fact that in the fitting procedure we also added silica and metallic iron.

8.3 Results

8.3.1 Observations

The spectroscopic observations we use are the infrared spectra obtained by the Short Wavelength Spectrometer (SWS) and the Long Wavelength Spectrometer (LWS) on board the Infrared Space Observatory (ISO) (Crovisier et al. 1997; Lellouch et al. 1998). These spectra were taken when the comet was at 2.9 AU distance from the Sun and 3 AU distance from the Earth. The SWS and LWS spectra have a small overlapping wavelength range ($42\mu\text{m} < \lambda < 45\mu\text{m}$). Since the LWS has a larger beam size, it catches emission from a larger part of the coma, resulting in a higher absolute flux level.

We assume that the properties of the dust causing the emission does not change as a function of distance from the core of the comet, so we can simply scale the LWS spectrum to match the SWS spectrum in the overlapping wavelength region. We have to note here that there are indications that the size distribution or the compactness of the particles varies slightly as a function of position in the coma (see e.g. Kolokolova et al. 2004, and references therein). When the particles move away from the comet nucleus, the particles might fall apart resulting in more fluffy, or smaller structures. Therefore, one might argue that taking into account the extended region covered by the LWS might bias our results towards a slightly higher fraction of small grains. However, we believe that this effect is only minor since these differences are largest when considering the region very close to the coma, which is covered by both the SWS and the LWS (Kolokolova et al. 2004). For the fitting procedure we used the wavelength range from 7 to 120 μm .

For the observational data of the degree of linear polarization we used the combined measurements from various studies in the optical part of the spectrum. The measurements were taken from Ganesh et al. (1998); Jockers et al. (1999) and Manset & Bastien (2000). Polarization observations are also available at some near infrared wavelengths (Hasegawa et al. 1999; Jones & Gehrz 2000). However, in this wavelength region a resonance feature of iron sulfide dominates the scattering behavior. Unfortunately, uncertainties exist about the exact strength of this feature. Therefore, in this paper we focus on the degree of polarization at optical wavelengths. The observations also provide the errors σ_p . Combining the observations in the optical we have polarization data at nine different wavelengths for various phase angles. We note that in order to obtain observations at different phase angles, the comet has to be observed at different phases during its orbit around the Sun. Therefore, in order to model all these observations using a single dust model, we have to assume that the composition and size distribution of the dust is more or less constant at different phases. Since we consider the degree of linear polarization of scattered light, variations in the total dust mass in the coma are not important.

8.3.2 Best fit model

We minimized χ^2 as defined by Eq. (8.13) using the method described in section 8.2.4. The λ_i were chosen on a logarithmic grid. Throughout the fitting procedure we fix the value of f_{max} for each dust species. From the positions of the crystalline silicate resonances we already know that for these materials we have to choose the most extreme shape distribution parameters ($f_{\text{max}} = 1$). The other materials are chosen to have equal values of f_{max} . For these materials, we obtain an optimum value $f_{\text{max}} = 0.2$. The parameters are shown in Table 8.3. The infrared spectrum corresponding to the best fit model is shown in Fig. 8.2 together with the measurements. The resulting curves for the degree of linear polarization as functions of the phase angle, together with the observations, are shown in Fig. 8.3. The emission spectra of the separate dust components are plotted in Fig. 8.4.

Figs. 8.2 and 8.3 show that the observations of both the infrared spectrum and the degree of linear polarization can be reproduced remarkably well using the same dust

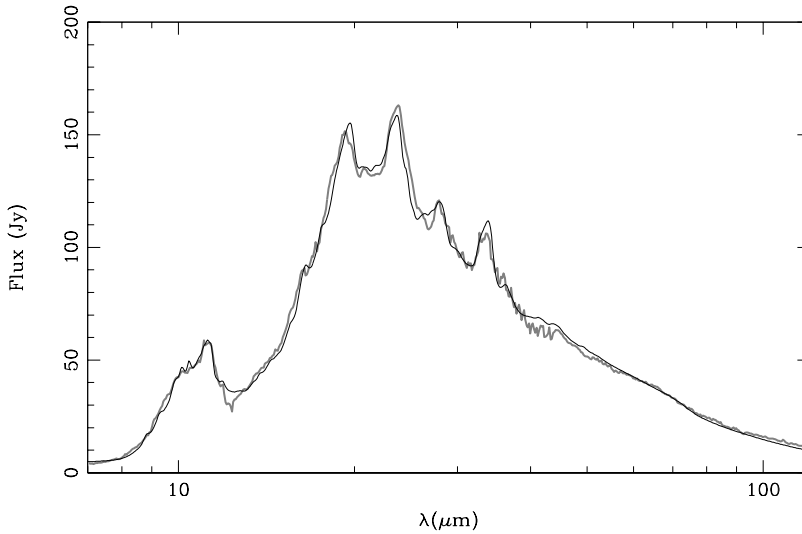


Figure 8.2: Infrared spectral energy distributions of the best fit model (black line) together with the SWS and the LWS observations (gray line).

model. In other words, we do not need quite different models for the infrared and optical parts of the spectrum. The differences between the observed and predicted infrared spectrum are most probably mainly caused by uncertainties in the refractive index data, and the assumptions on which the model is based. For the degree of linear polarization we notice that the negative polarization branch at $\lambda = 684$ nm at small phase angles is not reproduced completely by the model. This is most likely due to the spherical symmetry of the shapes we employed. The scattered light is dominated by the contributions from the silicate (olivine and pyroxene) and iron sulfide grains. The contribution to the scattered light from carbon grains is negligible. Although the abundance of silicates is much higher than that of iron sulfide, the scattering caused by iron sulfide grains is comparable to that of the silicates due to its high scattering efficiency.

The best fit model we present combines for the first time observations of the SWS infrared spectrum ($7 - 44 \mu\text{m}$), the LWS infrared spectrum ($44 - 120 \mu\text{m}$) and the degree of linear polarization at several wavelengths in the optical. This results in a better constrained dust model. The spectral structure of the thermal emission in the SWS part of the spectrum provides crucial information on the composition of the dust. The LWS part of the spectrum combined with the degree of linear polarization provides information on the size of the dust grains. We also constructed fits excluding some of the observations from the model. An attempt to fit only the SWS part of the spectrum resulted in an underestimate of the fraction of large grains, which in turn resulted in a higher fraction of crystalline silicates, more comparable to that found in, for example, Bouwman et al. (2003). Fitting both the SWS and the LWS part of the spectrum without the linear polarization resulted in a dust composition and size distribution not much different from that

Table 8.3: Results for the best fit model. The error estimates are obtained by considering all possible fits with $\chi^2 \leq 1.1\chi_{\min}^2$. The total dust mass in the beam of the SWS as found from the fit is $8.0 \cdot 10^9$ kg.

Material	Chemical Formula	Bulk density (g/cm ³)	f_{\max}	Volume (min / max) (%)	Mass (%)	r_{\min} (μm)	r_{\max} (μm)	β
Amorph. Carbon	C	1.80	0.2	38.9 (38.9 / 39.5)	23.7	9.6	20.1	-3.0
Amorph. Olivine	$\text{Mg}_{2x}\text{Fe}_{2-2x}\text{SiO}_4$	3.71	0.2	25.1 (23.4 / 37.6)	31.6	0.01	38.4	-3.0
Amorph. Pyroxene	$\text{Mg}_x\text{Fe}_{1-x}\text{SiO}_3$	3.20	0.2	22.1 (0.0 / 23.5)	24.0	0.01	38.4	-3.0
Amorph. Silica	SiO_2	2.60	0.2	0.4 (0.0 / 8.5)	0.3	0.06	0.4	-3.0
Cryst. Forsterite	Mg_2SiO_4	3.33	1.0	2.0 (1.5 / 3.2)	2.3	0.03	0.1	-3.0
Cryst. Enstatite	MgSiO_4	2.80	1.0	1.2 (0.8 / 1.7)	1.2	0.03	0.1	-3.0
Metallic Iron	Fe	7.87	0.2	0.2 (0.1 / 0.9)	0.5	0.1	0.15	-3.0
Iron Sulfide	FeS	4.83	0.2	10.0 (10.0 / 10.1)	16.4	0.6	4.2	-3.0

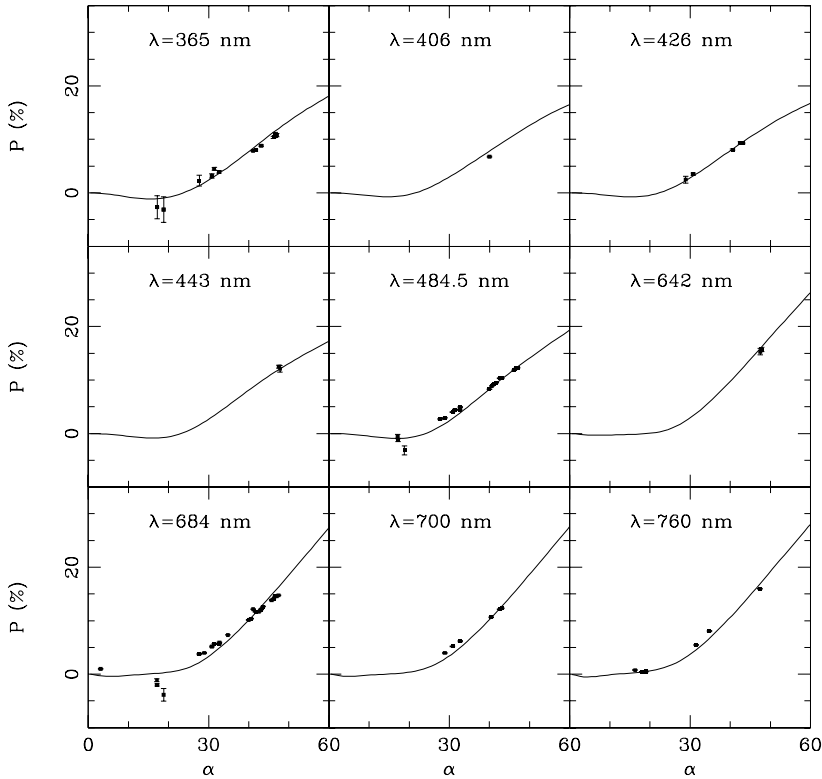


Figure 8.3: The degree of linear polarization from the best fit model as a function of phase angle, α , in degrees (solid curves) based on both the spectral and the polarization measurements. The measurements of the linear polarization are indicated by dots and were taken from Ganesh et al. (1998), Jockers et al. (1999) and Manset & Bastien (2000).

presented in Table 8.3. Including the observations of the degree of linear polarization to the fitting procedure only changed the resulting fit parameters slightly.

The total dust mass in the SWS beam derived from the best fit model is $8.0 \cdot 10^9$ kg. This dust mass is comparable to that derived by Bouwman et al. (2003) which is $4.2 \cdot 10^9$ kg. The difference of roughly a factor of two is a result of the difference in grain sizes between the model by Bouwman et al. (2003) and our model. Note that the dust mass derived in this way is a lower limit on the real mass of the solid state material in the coma of Hale-Bopp since the mass most likely resides predominantly in the very large grains. Using data obtained at submillimeter wavelengths, which provides information on millimeter sized dust grains, Jewitt & Matthews (1999) derive a total dust mass of $\sim 2 \cdot 10^{11}$ kg within a beam size comparable to that of the ISO SWS.

In our model the temperature of all dust species is determined self-consistently. However, from the ratio of the strengths of the forsterite features it can be seen that the temperature of the forsterite grains is higher than would be determined from thermal

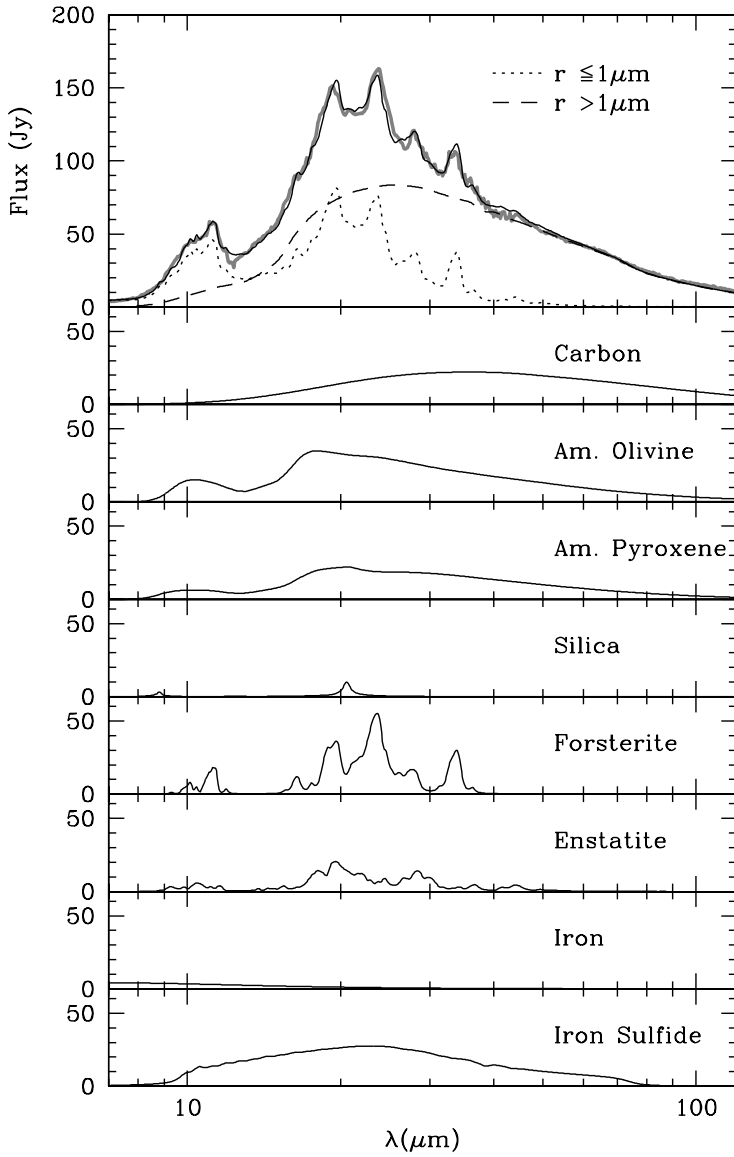


Figure 8.4: The contributions of all small (dots), and large (dashes) grain components to the total spectrum (upper panel). The gray line indicates the observations, the black line indicates the best fit model. Also plotted are the contributions to the emission spectrum of the various dust components (lower panels).

equilibrium calculations using pure forsterite grains (Harker et al. 2002). Pure forsterite grains are not very efficient absorbers in the UV and the optical part of the spectrum where a large part of the solar energy is emitted. They are very efficient emitters in the infrared. Therefore, pure forsterite grains will be cold compared to other dust species. The fact that they are observed to be relatively warm is probably an effect of thermal contact between the various dust species (Bouwman et al. 2003). An aggregated structure where all dust species are in thermal contact is also consistent with pictures of interplanetary dust particles. To calculate the optical properties of an aggregated structure in a completely consistent way is very computationally intensive which makes it extremely difficult to examine the entire parameter space of dust abundances and grains sizes. Some work on this has been done by Moreno et al. (2003) considering fixed values of the material abundances. To simulate thermal contact we polluted the forsterite and enstatite grains with 3% of small metallic iron inclusions. We calculated an effective refractive index using the Maxwell-Garnet effective medium theory (see e.g. Bohren & Huffman 1983). When we pollute the crystalline silicates in this way, the equilibrium temperature is in agreement with the observations.

8.3.3 Dust composition and size distribution

When discussing the size distribution of the dust we have to consider the grain sizes that our analysis is sensitive to. For grains smaller than a few micron ($\lesssim 3 \mu\text{m}$) we have a strong spectroscopic diagnostic. At relatively short wavelengths (around $\sim 10 \mu\text{m}$) we are mainly sensitive to the composition of these small grains. If we go to longer wavelengths, we are also sensitive to the composition of larger grains. Using the SWS and LWS range from $\lambda = 7 - 120 \mu\text{m}$, we have a spectroscopic diagnostic for the composition of grains with a volume equivalent radius up to $\sim 10\text{-}15 \mu\text{m}$. Although larger grains do show spectral structure (Min et al. 2004), their emission efficiency is too low to be detected.

When we compare our best fit parameters with those obtained by others (Brucato et al. 1999; Galdemard et al. 1999; Wooden et al. 1999; Hayward et al. 2000; Harker et al. 2002; Bouwman et al. 2003) there are a few differences. First of all the amount of crystalline silicates is much smaller than that found in most of these studies. This is caused by the fact that previous studies mainly considered the small (submicron sized) grain component. In our model, we find that in order to reproduce the spectral features, the crystalline silicate grains have to be very small and thus they have a high emission efficiency. From, i.e. the LWS spectrum, we find that the amorphous grains are relatively large, and thus emit less efficiently. Thus, if one only considers the small grain component, the crystallinity is increased with respect to our findings. The crystalline grains have to be small in order to reproduce the ratios of the strengths of the different emission features. However, these ratios are also influenced by the temperature of the dust grains. Fortunately, we can distinguish temperature effects from grain size effects in the following way. In determining the absorption cross sections of dust particles the most important parameter is $|mx|$ where m is the complex refractive index and $x = 2\pi r/\lambda$ is the size parameter of the dust grain. When $|mx| \ll 1$ the grains are in the Rayleigh domain and strong spectral emission resonances occur. When $|mx|$ increases, the spec-

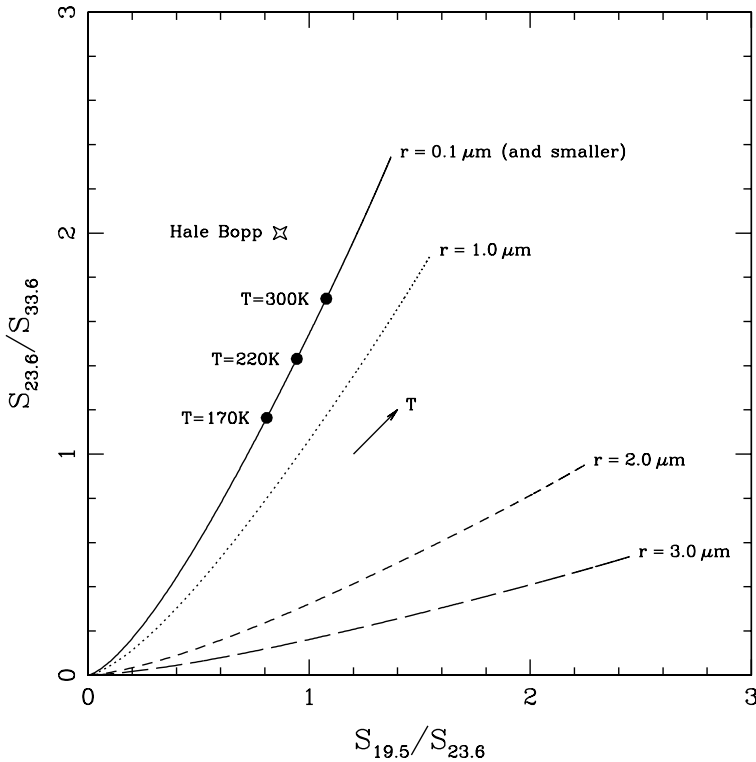


Figure 8.5: The ratios of the peak strengths at 19.5, 23.6 and 33.6 μm of forsterite calculated for various grain sizes and temperatures. The star indicates the measured peak strength ratios of comet Hale-Bopp. Grains smaller than 0.1 μm are in the Rayleigh limit. In this limit, the shape of the spectrum is independent of the particle size.

tral features decrease in strength. For very large grains ($|m|x| \gg 1$) the emission features will change into emission dips (see Min et al. 2004). When the grain size is increased, first the features caused by resonances with high values of $|m/\lambda|$ become weaker and then the features with smaller values of $|m/\lambda|$. This means that this effect depends on the wavelength but also on the refractive index; the strongest features (with the highest values of $|m|$) will go down first. However, when going from high temperatures to low temperatures, the effect on the strength of the features shifts with the maximum of the underlying Planck function, so this effect only depends on the wavelength position of the features. This difference allows us to distinguish between size and temperature effects by carefully looking at the feature strength ratios.

To test if the ratios of the forsterite resonances can be explained using temperature effects instead of a difference in grain size between amorphous and crystalline silicates, we calculated the strengths of the 19.5, 23.6 and 33.6 μm features above the local continuum using the DHS for different grain sizes and temperatures. These strengths are

denoted by $S_{19.5}$, $S_{23.6}$ and $S_{33.6}$ respectively. The strength ratios are plotted in Fig. 8.5 for various grain sizes and temperatures. The temperatures were varied from 10–1500K. Also plotted in Fig. 8.5 is the peak ratio measured in the spectrum of Hale-Bopp. We see that there is no corresponding set of temperature and grain size in Fig. 8.5 that reproduces the ratios measured in Hale-Bopp. To get the best fit we need to go to very small and relatively warm forsterite grains. The fact that the forsterite has to be warm also indicates that the grains must be small and most probably are in thermal contact with (at least) a strong absorbing material like carbon or iron.

The fact that we cannot find a set of temperature and grain size with peak ratios in Fig. 8.5 corresponding to those observed in the infrared spectrum could be caused by the effect that in the spectrum of Hale-Bopp the $33.6\mu\text{m}$ feature is partly blended with an enstatite feature resulting in a weaker feature. If we would take this effect into account, the point would shift downward in Fig. 8.5. Another explanation could be that the forsterite in Hale-Bopp is slightly contaminated with iron, which results in a slightly weaker $33.6\mu\text{m}$ feature (Koike et al. 1993).

As a test we made a fit to the SWS and LWS spectra fixing the upper size of the crystalline silicate grains. We have tried to make a fit to the spectrum using $r_{\text{max,cryst}} = 2, 5$ and $10\mu\text{m}$, respectively, and varying all other parameters. The resulting model spectra did not satisfactorily reproduce the measured ISO spectra. In order to obtain a reasonable fit to the observed forsterite features, we had to employ a power law for the size distribution heavily biased towards small grains, $\beta = -3.6$. However, in all these model fits the strength ratios of the forsterite features were poorly reproduced. In Fig. 8.6 we plot the resulting best fit model for the case when $r_{\text{max,cryst}} = 5\mu\text{m}$. We note that the emission spectrum is not sensitive to the very large forsterite grains. Although these grains still display significant spectral structure (Min et al. 2004), their emission efficiency is small. Therefore, it is possible to have a bimodal size distribution of crystalline silicates, in which only very small and very large crystals are present while the intermediate sized grains are absent, and still reproduce the infrared spectrum of Hale-Bopp. However, such a size distribution is very unlikely.

When comparing our results to those obtained by other studies, we have to be careful with the definition of crystallinity. Here, we mean by crystallinity the mass fraction of crystalline silicates compared to the total dust mass. In previous studies, sometimes the crystallinity is defined as the mass fraction of crystalline silicates compared to the total mass in the silicate component. In our fit, approximately 40% of the dust mass is contained in non silicate materials like carbon and iron sulfide. When comparing with other studies we have to correct for this.

Since previous studies of the mineralogy of the dust in the coma of Hale-Bopp focused on the SWS part of the spectrum, little information was available on the large grain component. As can be seen from Fig. 8.4 the LWS spectrum (longward of $\sim 44\mu\text{m}$) displays a long wavelength slope that can only be explained using large grains at approximately blackbody temperature (see also Lellouch et al. 1998). We have just shown that this large grain component cannot be crystalline. Since the large grains contain most of the mass, the resulting abundance of crystalline silicates is small, 3.5% (Table 8.3). We should note here that part of the crystalline silicates are probably not spectroscopic-

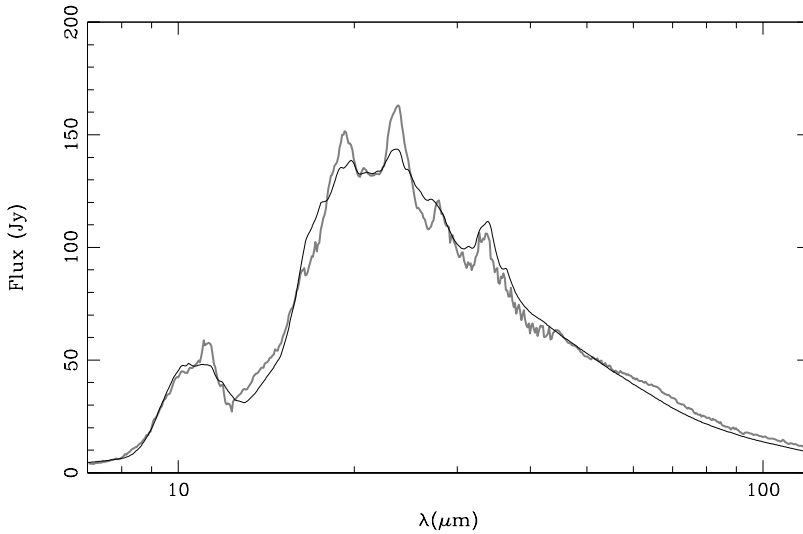


Figure 8.6: Infrared spectral energy distributions of the best possible fit when fixing the maximum volume equivalent radius, $r_{\text{max,cryst}}$, of the crystalline component to $5 \mu\text{m}$ (black line). This fit to the SWS and LWS observations (gray line) therefore does not represent our best fit model (given in Fig. 8.2, which uses $r_{\text{max,cryst}} \sim 0.1 \mu\text{m}$), but is of a much poorer quality. It is clear that large crystalline silicate grains cannot be present as they cannot reproduce the observed peak ratios of the resonances.

ally detectable since these are hidden inside large amorphous silicate or carbon grains. Therefore the 3.5% crystallinity we derive is a lower limit. We can make a quantitative estimate of the true fraction of crystalline grains by only considering grains smaller than a certain size, for which we assume that we observe the properties of the entire grain. In order to assure that the resulting mixture still has solar abundances, we fix the total abundance of silicates (crystalline and amorphous olivine and pyroxene). Considering only the silicate component, we compute the crystalline over amorphous ratio excluding the larger silicate grains. We then use this crystalline over amorphous ratio to compute the fraction of crystalline silicates in the total mixture. We choose a volume equivalent radius of $15 \mu\text{m}$ as the maximum grain size, which represents approximately half of the total dust mass. The crystallinity derived in this way depends on the assumption of this grain size, and detailed calculations are required to obtain a better estimate of the appropriate size. We thus derive a crystallinity of $\sim 7.5\%$ ($\sim 5\%$ of crystalline forsterite and $\sim 2.5\%$ of crystalline enstatite). Note that most previous studies on the SWS spectrum of Hale-Bopp only included forsterite, no enstatite. In contrast with our findings, these studies typically find forsterite fractions of $\sim 20\text{-}30\%$. The fraction of crystalline silicates in our best fit model increases when we consider only smaller grains. The sub-micron grain component contains approximately 25% forsterite and 17% enstatite. This fraction of forsterite is consistent with the results from previous studies that focused on the submicron grain component (see e.g. Brucato et al. 1999).

It can be noted from Table 8.3 that the dust components with a high abundance reside in relatively large grains. Although the large grains contribute much to the total dust mass, they contribute only little to the infrared emission at short wavelengths. Therefore, we conclude that the long wavelength part of the spectrum and the degree of linear polarization contain crucial information on the large dust grains, and, therefore, on a large fraction of the total dust mass.

We can calculate the effective radius and variance, r_{eff} and v_{eff} , of the dust grains in our model using Eqs. (8.3) and (8.4). For our best fit model $r_{\text{eff}} = 1.4 \mu\text{m}$ and $v_{\text{eff}} = 9.7$. Typical values for the effective volume equivalent radii computed from the size distributions found in other studies are $0.5 \mu\text{m}$ (Bouwman et al. 2003) and $0.6 \mu\text{m}$ (Moreno et al. 2003). The larger r_{eff} that we find is most likely due to the additional information contained in the long wavelength slope. Employing a simple model for porous dust grains, Li & Greenberg (1998) argue that the average grain size in Hale-Bopp might be much larger ($\sim 8\text{-}25 \mu\text{m}$) and that the fraction of submicron grains might be negligible. Perhaps cometary dust grains are indeed very fluffy aggregates of small particles. However, it is probably difficult to discriminate between a large fluffy grain and a large number of small separate grains using spectroscopy or observations of the degree of linear polarization.

The fact that the most abundant dust species reside in the largest grains is a natural consequence of the formation mechanism of the larger dust grains. Larger dust grains are believed to form by coagulation of smaller grains. The materials that are more abundant, can form large clusters of this material, whereas the less abundant species may be distributed in the aggregate as separate monomers. If the aggregate is very fluffy, the low abundance of the latter species causes the distance between the inclusions to be on average relatively large. Thus, one could argue that these inclusions will not interact very strongly with each other, and their resulting optical properties will be those of small particles. On the other hand, the larger clusters formed by the more abundant dust species will produce optical properties more like those of large grains. This hypothesis may be tested by simulations of the optical properties of fluffy composite particles with extreme abundance differences.

We conclude that the crystalline silicates in the coma of comet Hale-Bopp are submicron sized. This is much smaller than the typical grain size found for the other dust components. In agreement with these findings, the crystalline silicates found in IDPs are predominantly submicron sized (Bradley et al. 1999). This difference in grain size between the amorphous and crystalline components results in a relatively low overall abundance of crystalline silicates. The abundance of crystalline silicates and the difference in grain size are important constraints when considering models of the processing and dynamical history of dust in the early solar system.

8.4 Discussion: Origin and evolution of cometary dust

Since comets are small bodies that have been frozen all of their lifetime, the comet material is expected to have undergone little processing since the comet's formation. In larger bodies, like planets, the material has experienced severe parent body processing

erasing the information on the original dust grains. Therefore, comets contain a unique diagnostic of the mineralogy of the dust in the protoplanetary disk at times when the planets and comets were formed. The fraction of crystalline silicates in the diffuse interstellar medium (ISM) is very low. Li & Draine (2001) derive an upper limit for the crystallinity of the dust in the ISM of 5%, while Kemper et al. (2004) even derive an upper limit of 0.4%. In addition, the crystallinity of the ISM dust derived in chapter 9 of this thesis is $\sim 1\%$. This implies that the dust in Hale-Bopp has undergone at least some processing in the solar nebula, before it got incorporated into the comet. In order to form crystalline silicates, the amorphous silicates have to be heated above the glass temperature of ~ 1000 K. Comets form in the outer regions of the disk where the temperatures are low enough for water ice to exist $\lesssim 160$ K. There are two possible ways to explain the presence of crystalline silicates in cometary dust grains. The first is that the amorphous silicates are crystallized by thermal annealing in the hot inner regions of the protoplanetary disk. The crystalline silicates are then mixed out to the regions where the comets form. Another possibility is that the crystalline silicates are produced locally. Processes that have been proposed for this are, for example, shock annealing (Harker & Desch 2002) and lightning (Pilipp et al. 1998; Desch & Cuzzi 2000). Recent evidence for radial mixing in protoplanetary disks is presented in van Boekel et al. (2004a) on the basis of interferometric measurements of the dust in the inner disk regions. In that paper it is found that the crystallinity in the inner disk regions is higher than that in the outer disk regions. This difference, along with a varying forsterite over enstatite ratio, is consistent with predictions from radial mixing models (Gail 2004).

Several studies have tried to explain the presence of crystalline silicates in comets by considering radial mixing. In these studies only the evolution of the silicate component is computed. For comparison with our computations, we therefore have to correct for the additional components included in the fit. The fraction of crystalline silicates in the silicate component (amorphous and crystalline olivine and pyroxene) is approximately 12.5%. In Gail (2004) a detailed model for the protosolar disk is presented in which dust chemistry, thermal annealing and radial mixing are incorporated. The computations in this paper are for a stationary model, so an equilibrium situation is calculated. The crystallinity that follows from this detailed model depends strongly on the distance to the star. Close to the star, the crystallinity is very high ($\sim 70\%$ at 3 AU), while in the comet forming region (~ 20 AU) the crystalline fraction equals approximately 24% (8% crystalline olivine and 16% crystalline pyroxene). The author concludes that the results from the stationary model cannot be extrapolated to distances beyond 20 AU, and can only be considered an approximation for the mineral composition of the inner 20 AU at several times 10^5 years. Wehrstedt & Gail (2002) present a time depend model of radial mixing. From the results of this paper, it is apparent that the equilibrium situation as computed in Gail (2004) is already attained after $\sim 10^5$ years. This is slightly shorter than the anticipated typical timescale for comet formation (which is a few times 10^5 years, see Weidenschilling 1997). The crystallinity computed by Wehrstedt & Gail (2002) at a distance of 30 AU is approximately 7% after 10^6 years. Bockelée-Morvan et al. (2002) also present a model describing time-dependent radial mixing in a protoplanetary disk. In this paper, three different solar nebula models are presented, a warm,

a nominal, and a cold model referring to the temperature structure in the solar nebula. This temperature structure is set by the viscosity parameter α ; the higher the values of α the lower the temperature. They derive an extremely well mixed nebula, in which, after $\sim 10^6$ years, the crystallinity at distances > 10 AU is independent of the distance. They arrive at a final crystallinity in the outer solar system (> 10 AU) of approximately 58, 12 and 2% according to the warm, nominal, and cold solar nebula model. Note that the parameters chosen by Wehrstedt & Gail (2002) and Gail (2004) correspond to the warm to nominal solar nebula model of Bockelée-Morvan et al. (2002). The predicted crystallinity in the comet forming region from both Gail (2004) and Bockelée-Morvan et al. (2002) shows that thermal annealing and radial mixing are more than sufficiently efficient mechanisms to explain the crystalline silicates in Hale-Bopp. The most important free parameter in the above models is the viscosity parameter. The crystallinity of cometary dust can be used to constrain this parameter, providing a better insight in the dynamics of protoplanetary disks. While the crystallinity derived for Hale-Bopp in previous studies could only be explained employing a viscosity parameter that is representative for a warm solar nebula model, the crystallinity we derive for Hale-Bopp is consistent with a viscosity parameter that is typical for an approximately nominal solar nebula and a formation distance of some 30 AU from the central star.

The crystalline silicates we find are all submicron sized, consistent with studies of IDPs, in which the crystalline inclusions are predominantly submicron sized (Bradley et al. 1999). There are two possible explanations for this. The first explanation is that the crystalline silicates are formed before efficient grain growth sets in. Due to the low crystallinity this would result in a dust grain that has the crystalline silicates scattered in the aggregate as small separate inclusions. However, this possibility can likely be excluded on the basis of the results presented in chapter 9 of this thesis. From the analysis of a large sample of protoplanetary disks, it is concluded that grain growth occurs before efficient crystallization sets in. Another explanation might be that the mechanism that produces the crystalline silicates in the comet forming region is more efficient for small grains than for large grains. Both local flash heating events (like shock annealing and lightning) as well as radial mixing are more efficient for small grains. For the local production mechanisms this is due to the fact that small grains are more easily heated than large grains. In the radial mixing models this is due to the fact that small grains more easily couple to the gas, and are thus more easily mixed outwards by, for example, turbulent radial mixing. It is, however, unclear if the size dependencies of the various models are strong enough to explain the absence of large crystalline silicate grains in the coma of Hale-Bopp.

8.5 Conclusions

We have successfully modeled the thermal emission and the degree of linear polarization of radiation scattered by grains in the coma of comet Hale-Bopp. Our method has the following important characteristics relative to previous studies.

- Both grain size and grain shape effects are taken into account in the calculations of the optical properties.

- The parameters of the best fit model are determined using an objective least squares fitting routine.
- The best fit solution has abundances of the chemical elements consistent with those observed in interplanetary dust particles and meteorites.
- The resulting model is consistent with the infrared emission spectrum observed in the wavelength range $7 - 120 \mu\text{m}$ and with observations of the degree of linear polarization at various phase angles and nine different wavelengths in the optical part of the spectrum.

To model the effects of grain shape on the optical properties, we employed the distribution of hollow spheres. In this distribution we average over the volume fraction occupied by the central vacuum inclusion while preserving the material volume of the particles. We showed that this shape distribution is successful in reproducing the observed properties of cometary grains.

We deduced from the ratios of the strengths of various forsterite features in the observed spectrum of Hale-Bopp that the crystalline silicate grains have a volume equivalent radius $r \lesssim 1 \mu\text{m}$. This is much smaller than the typical grain size of the other dust components and is in agreement with the sizes of the crystalline silicate inclusions found in fluffy interplanetary dust particles. The crystalline inclusions in these grains are predominantly submicron sized (Bradley et al. 1999).

From the long wavelength observations it can be shown that most of the mass resides in relatively large grains. The lack of large crystalline silicate grains thus implies that the amount of mass in this component is small. Our best fit model has a relative amount of crystalline silicates that is significantly lower than found in previous studies of the infrared spectrum. If we consider only the grains with a volume equivalent radius smaller than $15 \mu\text{m}$, the fraction of the total dust mass contained in crystalline silicates is only $\sim 7.5\%$. The fraction of crystalline silicates in the silicate component (both amorphous and crystalline olivine and pyroxene) is $\sim 12.5\%$. This crystallinity can easily be produced by models in which the crystalline silicates are formed close to the Sun by thermal annealing and then mixed outwards to the comet forming region ($\sim 20\text{-}30 \text{ AU}$). The crystallinity derived by us for comet Hale-Bopp is in agreement with these models assuming an approximately nominal model of the protosolar nebula and a formation of the comet at a distance of $\sim 30 \text{ AU}$ from the Sun. This crystallinity is also in agreement with that found in interplanetary dust particles.

Acknowledgments

It is a pleasure to express our gratitude to M. S. Hanner, C. Dijkstra and L. Kolokolova for enlightening discussions. We are grateful to J. Crovisier for providing us with the reduced data of the LWS spectrum of Hale-Bopp.

A $10\ \mu\text{m}$ spectroscopic survey of Herbig Ae star disks: grain growth and crystallization

*R. van Boekel, M. Min, L. B. F. M. Waters, A. de Koter, C. Dominik,
M. E. van den Ancker, and J. Bouwman*
Accepted for publication in Astronomy & Astrophysics

Abstract

We present spectroscopic observations of a large sample of Herbig Ae stars in the $10\ \mu\text{m}$ spectral region. We perform compositional fits of the spectra based on properties of homogeneous as well as hollow spherical particles, and derive the mineralogy and typical grain sizes of the dust responsible for the $10\ \mu\text{m}$ emission. Several trends are reported that can constrain theoretical models of dust processing in these systems: *i*) none of the sources consists of fully pristine dust comparable to that found in the interstellar medium, *ii*) all sources with a high fraction of crystalline silicates are dominated by large grains, *iii*) the disks around more massive stars ($M \gtrsim 2.5 M_{\odot}$, $L \gtrsim 60 L_{\odot}$) have a higher fraction of crystalline silicates than those around lower mass stars, *iv*) in the subset of lower mass stars ($M \lesssim 2.5 M_{\odot}$) there is no correlation between stellar parameters and the derived crystallinity of the dust. The correlation between the shape and strength of the 10 micron silicate feature reported by van Boekel et al. (2003) is reconfirmed with this larger sample. The evidence presented in this paper is combined with that of other studies to present a likely scenario of dust processing in Herbig Ae systems. We conclude that the present data favor a scenario in which the crystalline silicates are produced in the innermost regions of the disk, close to the star, and transported outward to the regions where they can be detected by means of 10 micron spectroscopy. Additionally, we conclude that the final crystallinity of these disks is reached very soon after active accretion has stopped.

9.1 Introduction

A characteristic shared by many young, low and intermediate mass stars is the presence of a strong infrared excess. This radiation emerges from circumstellar dust grains left over from the star formation process. The material is believed to reside in a disk which is formed as a result of angular momentum conservation in the collapsing molecular cloud.

After an initial strong accretion phase, a much longer pre-main-sequence phase ensues during which the disk slowly dissipates, and possibly planets are formed.

The interstellar dust which finds its way into a proto-planetary disk will undergo large changes in average size and chemical composition. These changes trace the process of disk dissipation and planet formation. Our solar system contains a precious record of the processes that took place during its formation. Comparison of this record to what is observed around young pre-main-sequence stars provides important insight into the history of our own solar system, and helps to constrain planet formation models.

The infrared spectral region is rich in vibrational resonances of abundant dust species. Therefore, infrared spectroscopy can be used to determine the composition of dust in proto-planetary disks, as well as constrain the size and shape of the dust grains. Analysis of the infrared (IR) dust emission features originating from the disk surface layer can be used to establish to what extent the dust composition in the disk has evolved away from that seen in the interstellar medium (ISM). For instance, crystalline silicates appear absent in the ISM (e.g. Demyk et al. 2000; Kemper et al. 2004) but are a substantial component in (some) comets and in interplanetary dust particles (MacKinnon & Rietmeijer 1987; Bradley et al. 1992). Clearly, the refractory material in the proto-solar cloud went through large changes as the solar system was formed. It should be kept in mind that spectroscopy in the 10 micron region is sensitive to a limited grain size range: large grains (with sizes above a few μm , depending on chemical composition and wavelength) show only weak spectral structure and do not contribute significantly to the infrared emission features.

In this work we study the composition of dust in the circumstellar environment of Herbig Ae/Be stars (Herbig 1960), using infrared spectroscopy. We restrict our study to a sub-group of mostly late B and A-F type stars (hereafter HAe stars). These stars show little or no optical extinction and low mass accretion rates, as derived from radio analysis (Skinner et al. 1993), and the lack of significant veiling in optical spectra. For these lower mass members of the Herbig class, evidence for the disk hypothesis is compelling (e.g. Mannings & Sargent 1997; Grady et al. 2001; Augereau et al. 2001; Eisner et al. 2003).

The observed SEDs of these HAe stars can very well be explained with models for gas-rich, passively heated disks in hydrostatic equilibrium and a puffed-up inner rim (Dullemond et al. 2001). These models indicate that the emission observed at near-IR wavelengths is dominated by the inner rim, while the mid-IR spectrum has a large contribution from the dust grains in the warm surface layers of the disk, typically located between a few to several tens of Astronomical Units (AU) from the star. Therefore, mid-IR spectroscopy predominantly relates to the composition of the dust in this surface layer. Van Boekel et al. (2003) argue that due to the turbulent nature of the disks, the small grains observed at the disk surface are well coupled to those in the disk mid-plane, and so the observations of the surface layers likely bear relevance for the overall small grain population.

Observations of the dust composition in HAe disks have revealed a very rich mineralogy, and strong source to source variations of the dust composition (e.g. Bouwman et al. 2001). Some stars show strong 9.7 and $18\ \mu\text{m}$ amorphous silicate emission, with a

band shape and strength very similar to that seen in the interstellar medium. Other objects have only weak silicate emission, with sub-structure at 9.2, 10.6 and 11.3 μm due to crystalline silicates. At longer wavelengths, high-quality observations only exist for a small number of stars, so far all obtained with the Infrared Space Observatory (ISO). This situation is rapidly improving due to ongoing observations with the Infrared Spectrograph on board of the Spitzer Space Telescope. The ISO spectra reveal a mineralogy dominated by the crystalline silicates forsterite and enstatite, i.e. Mg-rich, Fe-poor materials (e.g. Malfait et al. 1998b; Bouwman et al. 2001; Meeus et al. 2001, hereafter ME01). A small group of stars lacks silicate emission, but shows prominent emission from Polycyclic Aromatic Hydrocarbons (PAHs) at 3.3, 6.2, 7.7-7.9, 8.6 and 11.3 μm . Many stars show a combination of silicates and PAHs.

In recent years, several investigators have attempted to find correlations between the properties of the dust in the disk of Herbig stars on the one hand, and global properties of the disk (e.g. disk geometry) and/or the star (e.g. mass, luminosity, age, binarity) on the other hand (ME01; Bouwman et al. 2001; Acke & van den Ancker 2004). Perhaps the most promising results so far are relations between the dust properties and the shape of the SEDs of the disk; for instance, the PAH bands are on average stronger in sources with SEDs that rise at far-IR wavelengths (ME01). This has been interpreted in terms of the disk geometry in the following way. Relatively red SEDs correspond to flaring disks, that have a large surface which is directly irradiated by the star. If PAHs are present in this flaring disk surface layer, they will contribute to the emission in the familiar PAH bands. Van Boekel et al. (2004b) studied the spatial distribution of the PAH emission in HD 97048, which was found to be extended on a scale of 1-2 arcsec (~ 250 AU) but clearly associated with the disk. It is likely that also in the other stars of our sample, the PAH emission originates from the outer disk region. Disks that lack a flaring outer region will have much less prominent PAH emission. Acke & van den Ancker (2004) confirm this relation between PAH band strength and SED shape using a sample of about 50 Herbig Ae/Be stars. Acke et al. (2004) note that stars with flat far-IR SEDs on average have flat millimeter spectral slopes, suggesting that the cold mid-plane grains in these sources have grown to larger size than the corresponding grains of stars with rising far-IR SEDs.

Despite considerable efforts, it has proven difficult so far to determine relations between stellar and dust parameters. This has prompted us to carry out a comprehensive spectral survey at 10 μm of isolated HAe stars. Our goal is to establish relations between star and dust properties that are of relevance for our understanding of the evolution of dusty disks around young stars, by increasing the number of stars for which mid-IR spectra are available. We have used the *Thermal Infrared Multi Mode Instrument 2* (TIMMI2, Reimann et al. 1998), attached to the 3.6 m telescope of the European Southern Observatory for our spectral survey. All known optically bright HAe stars accessible from the La Silla observatory were included in our initial list of targets. In practice, high quality data could be obtained for stars with 10 μm fluxes of about 3 Jy or more.

Here we present the results of our spectroscopic survey at 10 μm . In total, we obtained high quality spectra of a sample of 24 HAe stars, introduced in section 9.2. We report on the observations and data reduction in section 9.3. An overview of the spectra

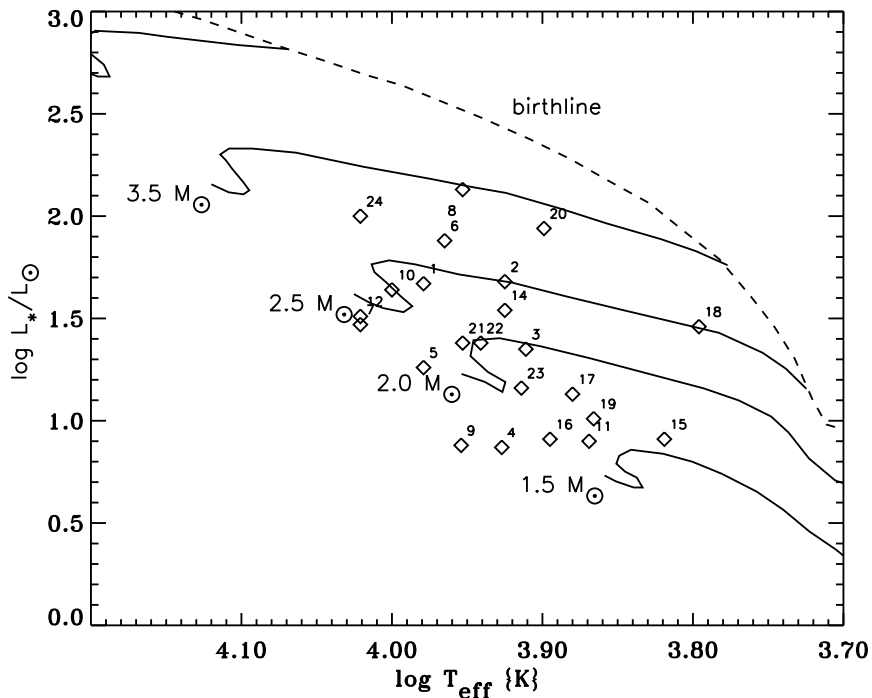


Figure 9.1: The positions of our stars in the HR diagram. The solid curves indicate the pre-main sequence evolutionary tracks of stars of different masses; the dashed curve represents the birthline for an accretion rate of $10^{-5} M_{\odot}\text{yr}^{-1}$ (both are taken from Palla & Stahler 1993).

is given in section 9.4. In section 9.5 we present compositional fits to the silicate feature observed in most of the sources, using the optical properties of minerals commonly found in circumstellar disks. In section 9.6 we discuss the implications of our results for our understanding of dust processing in HAe disks.

9.2 The sample stars

Our sample of stars was selected from a larger list of (candidate) Herbig Ae/Be stars studied by Malfait et al. (1998a). This list was constructed by comparing the positions of stars in the Smithsonian Astrophysical Observatory Star Catalog with positions in the Infrared Astronomical Satellite (IRAS) point source catalogue, and subsequent follow-up studies to find the Herbig star candidates. Clearly, such a way to select stars may introduce biases. Our sample does not contain stars that are heavily obscured due to e.g. on-going accretion or an edge-on dusty disk. Instead, our sample is dominated by stars with a relatively “clean” environment, low optical extinction, and disk orientations

Table 9.1: Basic parameters of the sample stars. In columns 1 and 2 we give the index number by which a star can be identified in tables and figures throughout this work, and the name of the star, respectively. The classification of the sources according to ME01 is listed in the third column. In column 5 the distances, derived from direct (Hipparcos) parallax measurements or by association to a star forming region (SFR, column 4), are given. For the stars where the distance is determined by association with a SFR we assume an error of 30% in the distance. The spectral type according to the MK classification, the effective temperature and the stellar luminosity are given in columns 6, 7 and 8, respectively. Mass and age estimates for most stars, as derived by comparing their positions in the HR diagram to theoretical pre-main-sequence tracks, are given in columns 9 and 10. For HD 101412 we have no reliable distance estimate, and can therefore not determine its luminosity, mass and age.

(1)	(2)	(3)	(4)	(5)	(6)	(7)	(8)	(9)	(10)
#	star	group	SFR	d [pc]	Sp.Type	log T _{eff} [K]	log L [L _⊙]	Mass [M _⊙]	log(Age) [yr]
1	AB Aur	Ia	L519	144 ⁺²² ₋₁₇	A0Ve+sh	3.979	1.67	2.4±0.2	6.3±0.2
2	UX Ori	IIa	Orion OB1a	340 ± 102	A4IVe	3.925	1.68	2.5±0.3	6.3±0.4
3	HD 36112	Ia		204 ⁺⁶³ ₋₃₉	A5IVe	3.911	1.35	2.0±0.3	6.5±0.3
4	HK ORI	IIa	Orion OB1a	340 ± 102	A4pevar	3.927	0.87	1.7±0.3	>6.8
5	HD 245185	Ia	Orion OB1a	340 ± 102	A0Ve	3.979	1.26	2.2±0.3	>6.8
6	V380 Ori	IIa	Orion OB1c	510 ± 153	A1:e	3.965	1.88	2.8±0.5	6.2±0.4
7	HD 37357	IIa		240 ± 72 ¹	A2Ve	4.021	1.47	2.4±0.4	>7.0
8	HD 37806	IIa	Orion OB1b	470 ± 141	A2Vpe	3.953	2.13	3.6±0.8	5.9±0.4
9	HD 95881	IIa	Sco OB2-4?	118 ± 35	A2III/IVe	3.954	0.88	1.7±0.2	>6.5
10	HD 97048	Ib	Ced 111	175 ⁺²⁶ ₋₂₀	B9.5Ve+sh	4.000	1.64	2.5±0.2	>6.3
11	HD 100453	Ib		111 ⁺¹⁰ ₋₈	A9Ve	3.869	0.90	1.7±0.2	7.0±0.1
12	HD 100546	Ia	Sco OB2-4?	103 ⁺⁶ ₋₆	B9Vne	4.021	1.51	2.4±0.1	>7.0
13	HD 101412	IIa			B9.5V				
14	HD 104237	IIa	Cha III	116 ⁺⁷ ₋₆	A4IVe+sh	3.925	1.54	2.3±0.1	6.3±0.1
15	HD 135344	Ib	Sco OB2-3	140 ± 42	F4Ve	3.819	0.91	1.6±0.2	6.9±0.3
16	HD 139614	Ia	Sco OB2-3	140 ± 42	A7Ve	3.895	0.91	1.7±0.3	>7.0
17	HD 142666	IIa	Sco OB2-2	145 ± 43	A8Ve	3.880	1.13	1.8±0.3	6.8±0.4
18	HD 142527	Ia		198 ⁺⁶⁰ ₋₃₇	F7IIIe	3.796	1.46	2.5±0.3	6.0±0.4
19	HD 144432	IIa	Sco OB2-2	145 ± 43	A9IVev	3.866	1.01	1.8±0.2	7.0±0.3
20	HD 144668	IIa	Lupus 3	207 ⁺⁴⁵ ₋₃₁	A5-7III/IVe	3.899	1.94	3.2±0.5	5.7±0.3
21	HD 150193	IIa	Sco OB2-2	150 ⁺³⁰ ₋₃₀	A2IVe	3.953	1.38	2.3±0.2	>6.3
22	HD 163296	IIa		122 ⁺¹⁶ ₋₁₃	A3Ve	3.941	1.38	2.0±0.2	6.7±0.4
23	HD 169142	Ib	Sco OB2-1	145 ± 43	A5Ve	3.914	1.16	2.0±0.3	6.9±0.3
24	HD 179218	Ia	(L693)	243 ⁺⁶⁸ ₋₄₃	B9e	4.021	2.00	2.9±0.5	6.1±0.4

¹ We adopted a distance of 240 pc so that the luminosity of this star matches its spectral type.

that are not close to edge-on. An overview of the stars in the sample and their basic parameters is given in Table 9.1.

In order to select “genuine” HAe stars, we applied the following selection criteria:

1. The position in the HR diagram should be in agreement with that of a pre-main-sequence (PMS) star with a mass between 1.5 and $3.5 M_{\odot}$ (see Fig. 9.1).
2. The color criterion $J-H > 0.25$ mag, assuring that the onset of the near-infrared (NIR) excess is well defined, in agreement with the inner boundary of the gas rich disk being set by the silicate evaporation temperature of ~ 1500 K (see Table 9.2 for an overview of the photometric data used).

9.2.1 Selection effects

In order to identify if other selection effects may have entered our sample, we determined the mass and age (calculated from the birthline, for an accretion rate of $10^{-5} M_{\odot}\text{yr}^{-1}$) of the stars by placing them in the HR diagram (Fig. 9.1) and comparing their positions to PMS evolutionary tracks published by Palla & Stahler (1993). Throughout this work “(PMS) age” τ is defined as the time that past since the star was on the birthline, which is when the star becomes optically visible for the first time. The luminosity is calculated from the observed photometry and the measured distance to each star. The uncertainties in the derived stellar masses and ages listed in Table 9.1 and shown in Fig. 9.2 mainly reflect the uncertainty in the distances (see also van den Ancker et al. 1998). A comparison of the stellar parameters derived using the Palla & Stahler (1993) evolutionary tracks to those obtained using more recent calculations (Palla & Stahler 1999; Siess et al. 2000), shows that the particular choice of PMS tracks introduces an additional uncertainty in the stellar ages that is of the same order as those implied by observational uncertainties in the position of the protostar in the HR diagram. This additional uncertainty is not taken into account. In Fig. 9.2 we show the derived stellar masses versus the PMS ages of the stars. It is evident from this figure that our sample lacks “old” ($\tau \gtrsim 10^{6.3}\text{yr}$) disks around $3\text{--}4 M_{\odot}$ stars, and “young” ($\tau \lesssim 10^6\text{yr}$) disks around stars less massive than about $2.5 M_{\odot}$. The lack of “old” disks around $3\text{--}4 M_{\odot}$ stars is likely caused by the shorter timescale on which the disks around more massive stars are dispersed. It is therefore not a selection effect. The lack of “young” disks around the lower mass stars is most likely caused by the fact that these stars do not clear their environment as rapidly as the more massive (more luminous) stars, and consequently become optically bright later in their evolution. Also, at a given age, lower mass PMS stars are less luminous than more massive ones, and so more easily escape optical detection. This selection effect must be taken into account in any discussion about the evolution of the dust in proto-planetary disks based on optically selected samples.

9.2.2 Classification of the sources

ME01 empirically decomposed the infrared spectra of Herbig Ae/Be stars into three components: a power law component, a cold black-body component, and solid state emission bands (mainly at 10 and $20\mu\text{m}$). They found that some sources exhibit both

Table 9.2: Literature infrared photometry used in this work. Columns 3-7 list the magnitudes in the J (1.25 μ m), H (1.65 μ m), K (2.2 μ m), L (3.6 μ m), and M (4.8 μ m) photometric bands, with references in column 8. The listed reference codes are: BO: Bouchet et al. 1991; CA: Carter 1990; CO: Cohen 1973; CU: Cutri et al. 2003; DW: de Winter et al. 2001; DW2: de Winter et al. 1996; EI: Eiroa et al. 2001; FO: Fouque et al. 1992; GL: Glass & Penston 1974; HI: Hillenbrand et al. 1992; LA: Lawrence et al. 1990; MA: Malfait et al. 1998a; ME: Mendoza 1967; ST: Strom et al. 1990; SY: Sylverster et al. 1996; VR: Vrba et al. 1976; WA: Waters et al. 1988. Columns 9-12 contain the infrared fluxes in Jy from the IRAS Point Source Catalogue (Joint IRAS Science Working Group 1988).

(1)	(2)	(3)	(4)	(5)	(6)	(7)	(8)	(9)	(10)	(11)	(12)
#	star	J	H	K	L	M	references	12 μ m	25 μ m	60 μ m	100 μ m
1	AB Aur	6.10	5.10	4.40	3.30	2.90	HI	27.16	48.10	105.60	114.10
2	UX Ori	8.03	7.43	6.71	5.61	5.32	DW,26.2.1986	2.68	3.69	2.85	~3.76
3	HD 36112	7.44	6.70	5.90	4.75	4.47	MA	5.59	12.59	27.98	18.95
4	HK Ori	9.52	8.38	7.29	5.87	5.10	HI	3.80	4.08	<1.64	<70.37
5	HD 245185	9.34	8.87	8.26	7.46	6.23	HI	4.00	5.96	4.97	3.61
6	V380 Ori	8.25	7.10	6.03	4.44	3.61	J-L ST; M ME	8.61	8.85	<75.90	<38.59
7	HD 37357	8.31	7.88	7.24	6.33		MA	2.01	2.79	~2.90	~20.29
8	HD 37806	7.38	6.68	5.77	4.23	3.79	MA	11.02	9.40	<5.18	<33.98
9	HD 95881	7.50	6.79	5.87	4.28	3.71	MA	9.14	6.87	1.45	<1.09
10	HD 97048	7.30	6.75	6.04	4.61	4.56	HI	14.49	40.34	69.91	<250.10
11	HD 100453	6.97	6.32	5.52	4.20	3.79	MA	7.23	33.59	39.36	23.86
12	HD 100546	6.43	5.88	5.20	4.15	3.80	MA	65.78	242.60	165.20	98.56
13	HD 101412	8.70	8.24	7.25	5.81	5.08	DW	3.22	3.09	~1.69	~10.52
14	HD 104237	5.75	5.14	4.42	3.05	2.58	MA	23.65	23.05	14.72	9.58
15	HD 135344	7.44	6.72	5.96	4.76	4.69	MA	1.59	6.71	25.61	25.69
16	HD 139614	7.75	7.34	6.76	5.68	5.49	MA	4.11	18.14	19.30	13.94
17	HD 142666	7.34	6.72	6.04	4.97	4.69	MA	8.57	11.21	7.23	5.46
18	HD 142527	6.65	5.94	5.20	3.89	3.50	MA	10.38	21.23	105.10	84.70
19	HD 144432	7.21	6.69	6.14	5.14	4.90	MA	7.53	9.36	5.76	3.29
20	HD 144668	5.83	5.18	4.38	3.08	2.54	HI	18.05	14.51	~14.36	<63.25
21	HD 150193	7.05	6.37	5.64	4.37	3.93	MA	17.61	18.10	8.13	<16.25
22	HD 163296	6.24	5.52	4.70	3.52	3.14	MA	18.20	20.99	28.24	<40.62
23	HD 169142	7.43	7.01	6.53	5.64	5.57	MA	2.95	18.43	29.57	23.42
24	HD 179218	6.99	6.64	5.91	4.68	4.18	J,H EI; K-M LA	23.44	43.63	29.92	17.35

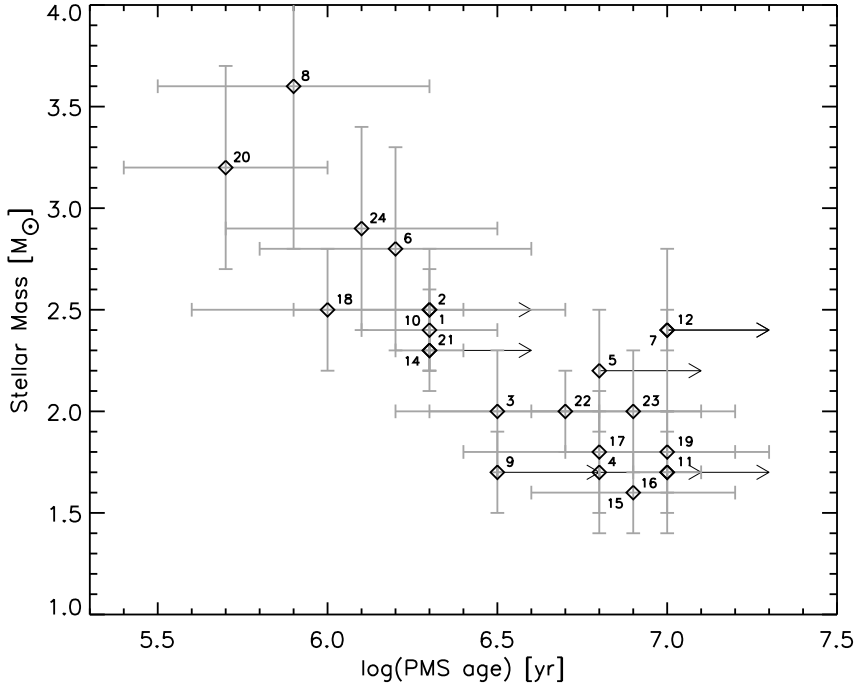


Figure 9.2: The derived stellar mass estimates vs. the pre-main-sequence age estimates derived from a comparison of their position in the HR diagram to PMS evolutionary tracks of Palla & Stahler (1993). Our sample shows a clear lack of disks around relatively old stars of $3\text{--}4M_{\odot}$, and of disks around relatively young stars less massive than about $2.5M_{\odot}$.

the power law and cold black-body component, and classified these sources as “group I”. Sources that lack the cold black-body component were classified as “group II”. A further division into subgroups “a” and “b” serves to indicate the presence or absence, respectively, of silicate emission bands at $10\mu\text{m}$ and $20\mu\text{m}$. It was proposed by ME01 that group I sources have a large (several hundred AU) flared outer disk, whereas the group II sources have a smaller, non-flaring outer disk.

We classify the sources for which we have newly measured N-band ($8\text{--}13.5\mu\text{m}$) spectra following ME01. Whereas ME01 had ISO spectra of their sources at their disposal, our classification is based solely on broad-band photometry. We find that the group I and group II sources are well separated in an IRAS $m_{12}\text{--}m_{60}$ color versus $L_{\text{NIR}}/L_{\text{IR}}$ diagram (Fig. 9.3), where L_{NIR} is the integrated luminosity as derived from the J,H,K,L and M band photometry, and L_{IR} is the corresponding quantity derived from the IRAS 12, 25 and $60\mu\text{m}$ points. For group I sources, $L_{\text{NIR}}/L_{\text{IR}} \leq (m_{12}\text{--}m_{60})+1.5$, group II sources have $L_{\text{NIR}}/L_{\text{IR}} > (m_{12}\text{--}m_{60})+1.5$. The dashed line in Fig. 9.3 indicates the boundary between the two groups. To avoid any pre-assumptions concerning the spectral shapes of our targets, we did not apply color correction to the IRAS data for the classification of the

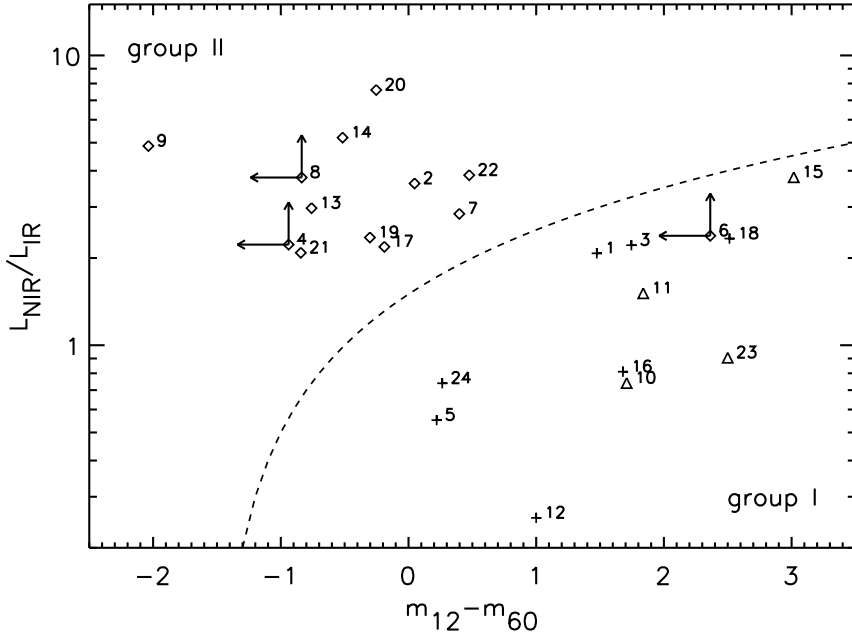


Figure 9.3: Classification of the sources based on global SED properties. We plot the ratio of the near-infrared and infrared luminosity (see section 9.2.2) vs. the IRAS $m_{12}-m_{60}$ color (defined as $m_{12}-m_{60} = -2.5 \log \mathcal{F}_{12}/\mathcal{F}_{60}$, where \mathcal{F}_{12} and \mathcal{F}_{60} are the fluxes at 12 and $60\mu\text{m}$ as listed in the IRAS point source catalogue). Sources classified as group I according to ME01 are in the lower right part of the diagram, group II sources are in the upper left part. Group Ia sources are indicated with crosses, group Ib sources by triangles, and group II sources with diamonds. The dashed curve indicates our division line between the two groups (section 9.2.2).

sources.

By use of the $L_{\text{NIR}}/L_{\text{IR}}$ ratio (van Boekel et al. 2003) we compare the near-IR SED to the mid-IR SED. The near-IR SED is found to be similar for all HAe stars (Natta et al. 2001), while the major differences occur in the mid-IR SED. The $L_{\text{NIR}}/L_{\text{IR}}$ ratio is smaller for group I than for group II sources. The mid-IR SED of group I sources is “double-peaked” compared to the SED of a group II source. Group I sources are redder than their group II counterparts. The IRAS $m_{12}-m_{60}$ color index quantifies this difference in SED shape.

9.3 Observations and data reduction

Infrared spectra in the $10\mu\text{m}$ atmospheric window were taken in December 2001 and March 2003 with the TIMM12 instrument mounted at the 3.60 m telescope at ESO La Silla observatory. Conditions were clear during all nights. The low resolution ($R \approx 160$) N band grism was used in combination with a 1.2 arcsecond slit. The pixel scale in the

spectroscopic mode of TIMMI2 is 0.45 arcseconds. A log of our observations is given in Table 9.3.1.

9.3.1 Atmospheric correction

Ground-based observations at 10 μm are particularly challenging because of the high atmospheric and instrumental background, and the varying transmission of the earth atmosphere. As proper spectral calibration is essential for the compositional analysis presented in section 9.5.1, we report here in some detail on our data reduction method.

To deal with the high background signal, we employed standard chopping and nodding, using a +10 arcsecond chop throw North-South, and a -10 arcsecond nod throw North-South. For the spectral calibration of our measurements we regularly observed standard stars. These observations are used to determine both the atmospheric extinction per unit airmass (A_v) and the instrumental response (R_v) at all wavelengths. For each science observation, we determine A_v and R_v from two calibration measurements:

$$\begin{aligned} s_{v,1} &= I_{v,1} e^{-\tau_{v,1}} R_v; & \tau_{v,1} &= A_v m_{A,1} \\ s_{v,2} &= I_{v,2} e^{-\tau_{v,2}} R_v; & \tau_{v,2} &= A_v m_{A,2}, \end{aligned} \quad (9.1)$$

where $s_{v,i}$ are the measured calibrator spectra, $I_{v,i}$ are the intrinsic (model) calibrator spectra, $\tau_{v,i}$ are the optical depths of the earth atmosphere during the calibration measurements, and $m_{A,i}$ denote the airmass at which the calibrators were observed. Whenever possible, we chose $m_{A,1}$ or $m_{A,2}$ to be very close to the airmass of the science observation. Both calibrator measurements are chosen as close in time as possible to the science observation. For the intrinsic calibrator spectra we use “spectral templates” by Cohen et al. (1999)¹. Table 9.4 lists the observed calibrators and the applied templates, which are chosen to match the calibrator spectral type as closely as possible. Solving Eq. 1 for A_v and R_v , we find:

$$A_v = \frac{\ln(I_{v,2}/I_{v,1}) + \ln(s_{v,1}/s_{v,2})}{m_{A,2} - m_{A,1}} \quad (9.2)$$

$$R_v = \frac{s_{v,1}}{I_{v,1} e^{-A_v m_{A,1}}} \quad (9.3)$$

The intrinsic spectrum of a science target observed at airmass m_A is then calculated from its measured spectrum s_v as:

$$I_v = \frac{s_v}{R_v} e^{A_v m_A} \quad (9.4)$$

For a number of sources we have ISO spectra available. We generally find very good agreement in spectral shape between the ISO data and our new ground based spectra. A comparison with the ISO spectra of the brighter stars (HD 100546, HD 163296, HD 150193) shows differences at the level of at most a few percent in the shape of the spectra, when the TIMMI2 spectra are scaled such as to most closely match the flux

¹available for download at the TIMMI2 website (<http://www.ls.eso.org/lasilla/sciops/timmi/docs/tables/>)

Table 9.3: Log of the TIMMI2 observations. We list the observing date (defined as the day on which each observing night began), time (U.T.), airmass of the observation, and integration time in seconds (columns 3-6). The calibrators used for the atmospheric correction are also given, with the time and airmass of the measurements (columns 7-12).

(1)	(2)	(3)	(4)	(5)	(6)	(7)	(8)	(9)	(10)	(11)	(12)
#	star	date	time	m_A	T_{int}	calibrator 1	time	$m_{A,1}$	calibrator 2	time	$m_{A,2}$
2	UX Ori	27-12-2001	01:09	1.31	1380	HD 32887	01:59	1.06	HD 32887	00:39	1.25
3	HD 36112	18-03-2003	23:19	1.83	960	HD 48915	00:27	1.04	HD 29139	23:58	1.88
4	HK Ori	19-03-2003	23:21	1.39	960	HD 48915	00:56	1.08	HD 23249	00:04	1.68
5	HD 245185	19-03-2003	00:27	1.56	720	HD 48915	00:56	1.08	HD 23249	00:04	1.68
6	V380 Ori	17-03-2003	00:59	1.37	960	HD 48915	00:21	1.04	HD 58972	01:36	1.34
7	HD 37357	19-03-2003	01:08	1.43	720	HD 48915	00:56	1.08	HD 55865	02:33	1.46
8	HD 37806	27-12-2001	04:04	1.12	690	HD 32887	01:59	1.06	HD 32887	00:39	1.25
9	HD 95881	17-03-2003	02:55	1.37	720	HD 48915	00:21	1.04	HD 107446	02:41	1.32
10	HD 97048	19-03-2003	03:02	1.52	720	HD 98292	04:02	1.28	HD 55865	02:33	1.46
11	HD 100453	18-03-2003	05:24	1.13	960	HD 93813	05:00	1.08	HD 146003	06:38	1.25
12	HD 100546	19-03-2003	05:09	1.34	960	HD 109379	05:36	1.01	HD 98292	06:18	1.37
13	HD 101412	17-03-2003	03:25	1.19	960	HD 48915	00:21	1.04	HD 89388	04:04	1.19
14	HD 104237	17-03-2003	04:57	1.52	480	HD 123139	08:04	1.03	HD 89484	04:37	1.65
15	HD 135344	17-03-2003	05:56	1.13	960	HD 123139	08:04	1.03	HD 107446	06:35	1.20
16	HD 139614	17-03-2003	07:25	1.05	960	HD 123139	08:04	1.03	HD 107446	06:35	1.20
17	HD 142666	18-03-2003	06:07	1.23	720	HD 93813	05:00	1.08	HD 146003	06:38	1.25
18	HD 142527	18-03-2003	06:56	1.11	720	HD 123139	08:07	1.04	HD 146003	06:38	1.25
19	HD 144432	18-03-2003	07:25	1.06	960	HD 123139	08:07	1.04	HD 146003	06:38	1.25
20	HD 144668	17-03-2003	09:15	1.02	720	HD 152334	09:45	1.03	HD 152786	09:01	1.14
21	HD 150193	18-03-2003	08:23	1.04	720	HD 123139	08:07	1.04	HD 146003	06:38	1.25
22	HD 163296	18-03-2003	09:40	1.04	480	HD 123139	08:07	1.04	HD 152786	09:22	1.12
23	HD 169142	17-03-2003	10:07	1.03	960	HD 152334	09:45	1.03	HD 152786	09:01	1.14
24	HD 179218	19-03-2003	09:39	1.78	480	HD 152334	07:59	1.10	HD 187642	10:00	1.68

levels in the ISO spectra. For each HAe star spectrum, the time and airmass of observation, as well as the time and airmass of the two calibration observations are given in Table 9.3.1.

9.3.2 Flux calibration

Our stars have been selected to be *isolated* Herbig stars. Therefore, the IRAS photometry will in most cases not be contaminated by emission from nearby sources or a surrounding remnant cloud. All emission seen in the IRAS data is expected to originate in the disk. We flux-calibrated the spectra using the IRAS 12 μm data, by applying a scaling factor q such that

$$q \int_{\nu=0}^{\infty} I_{\nu} T_{\nu} d\nu = \mathcal{F}_{12} \times 1.35 \times 10^{-10} \quad [\text{erg s}^{-1} \text{cm}^{-2}], \quad (9.5)$$

where T_{ν} is the normalized instrumental response function of the IRAS 12 micron band, and \mathcal{F}_{12} is the 12 micron flux as listed in the IRAS point source catalogue (a source that has a 12 μm flux of $\mathcal{F}_{12}=1$ Jy in the IRAS point source catalogue, yields an inband flux of $1.35 \times 10^{-10} \text{ erg s}^{-1} \text{cm}^{-2}$). The IRAS 12 micron band runs from 8 to 15 μm and is therefore somewhat broader than our spectral coverage. To allow for the calibration we estimate the spectrum between 13.5 and 15 μm , by linearly extrapolating I_{ν} between the continuum points measured at 8 and 13 μm . Our final calibrated spectrum is then $F_{\nu} = qI_{\nu}$. We estimate the absolute photometric accuracy to be 15%.

9.4 Description of the observations

9.4.1 Description of the spectra

The spectra of our sample of HAe stars are shown in Fig. 9.4. All stars show spectral structure on top of a continuum whose slope varies strongly from star to star. The spectral features are due to various kinds of silicates (see section 9.5.1 below). Also, emission from Polycyclic Aromatic Hydrocarbons (PAHs) can be seen, at 7.9, 8.6, 11.3 and 12.7 μm . The relative importance of the silicate and PAH contributions varies strongly. There are sources that show both silicate and PAH emission (e.g. HD 100546, HD 179218), sources that show only silicate emission (e.g. HD 144432), and sources that display only PAH emission (these are the group Ib sources HD 97048, HD 100453, HD 135344, and HD 169142). There are no sources in our sample that have a completely featureless 10 micron spectrum.

ME01 and Acke & van den Ancker (2004) found that the SED correlates with the presence and/or strength of the PAH bands: group I sources tend to show (prominent) PAH emission, while group II sources do not. This trend is confirmed in our sample, but we note that there is considerable scatter. For instance, HD 95881 has little far-IR excess and is thus classified as group II, but, nonetheless, shows clear PAH emission bands.

The silicate band shows very large variations in shape and strength. The bulk of the emission is in most cases due to amorphous silicates, but almost all stars show some

Table 9.4: *Spectral templates used for the calibrators (see section 9.3.1).*

calibrator	spectral type	template file	template sp. type
HD 23249	K0IV	hd123139.tem	K0IIIb
HD 29139	K5III	alp_Tau.dat	K5III
HD 48915	A1V	ν^2 law	ν^2 law
HD 55865	K0III	hd123139.tem	K0IIIb
HD 58972	K3III	hd6805.tem	K2III
HD 89388	K3IIa	hd6805.tem	K2III
HD 89484	K1IIIb	hd169916.tem	K1IIIb
HD 92397	K4.5III	hd32887.tem	K4III
HD 93813	K0/K1III	hd123139.tem	K0IIIb
HD 98292	M2III	alp_Tau.dat	K5III
HD 107446	K3.5III	hd32887.tem	K4III
HD 109379	G5II	hd37160.tem	G8III-IV
HD 123139	K0IIIb	hd123139.tem	K0IIIb
HD 146003	M2III	alp_Tau.dat	K5III
HD 152334	K4III	hd32887.tem	K4III
HD 152786	K3III2	hd6805.tem	K2III
HD 177716	K1IIIb	hd169916.tem	K1IIIb
HD 187642	A7V	HD187642_spec.dat	A7IV-V

spectral structure near $11.3 \mu\text{m}$, which can be attributed to forsterite. Note, however, that this feature blends with the $11.3 \mu\text{m}$ PAH band. There are also prominent narrow emission bands near 9.2 and $10.6 \mu\text{m}$. These are due to crystalline enstatite. The spectrum of HD 100546 is dominated by crystalline forsterite, while that of HD 179218 is dominated by crystalline enstatite. This latter star shows one of the richest $10 \mu\text{m}$ spectra observed to date (see Fig.9.5). The resonances of crystalline enstatite are clearly visible in the spectrum of this source. The ISO spectrum of HD 179218 at longer wavelengths also points to a relatively high abundance of crystalline enstatite (Bouwman et al. 2001). It is obvious that the nature of the crystalline dust in our sample shows very large variations, both in terms of the fraction of the dust that is crystalline, and in composition.

There are four stars (HD 97048, HD 100453, HD 135344 and HD 169142), all classified as group I, that show no detectable silicate emission. Instead, their $10 \mu\text{m}$ spectra are dominated by PAH emission. The lack of silicate emission is most simply explained by assuming that there are no small ($< 3\text{-}5 \mu\text{m}$) silicate grains in the inner 10-20 AU of the disk. Meeus et al. (2002) derive limits on the presence of small silicate grains in HD 100453, and argue that all grains smaller than $4 \mu\text{m}$ must have been removed. The most likely cause for the removal of small silicate grains is grain growth, but apparently this has not affected the population of small carbonaceous grains to the same extent (van Boekel et al. 2004b). Possibly, small grains survive in the outer disk regions. At large distance from the star, the silicate grains may be too cold to contribute to the $10 \mu\text{m}$ spec-

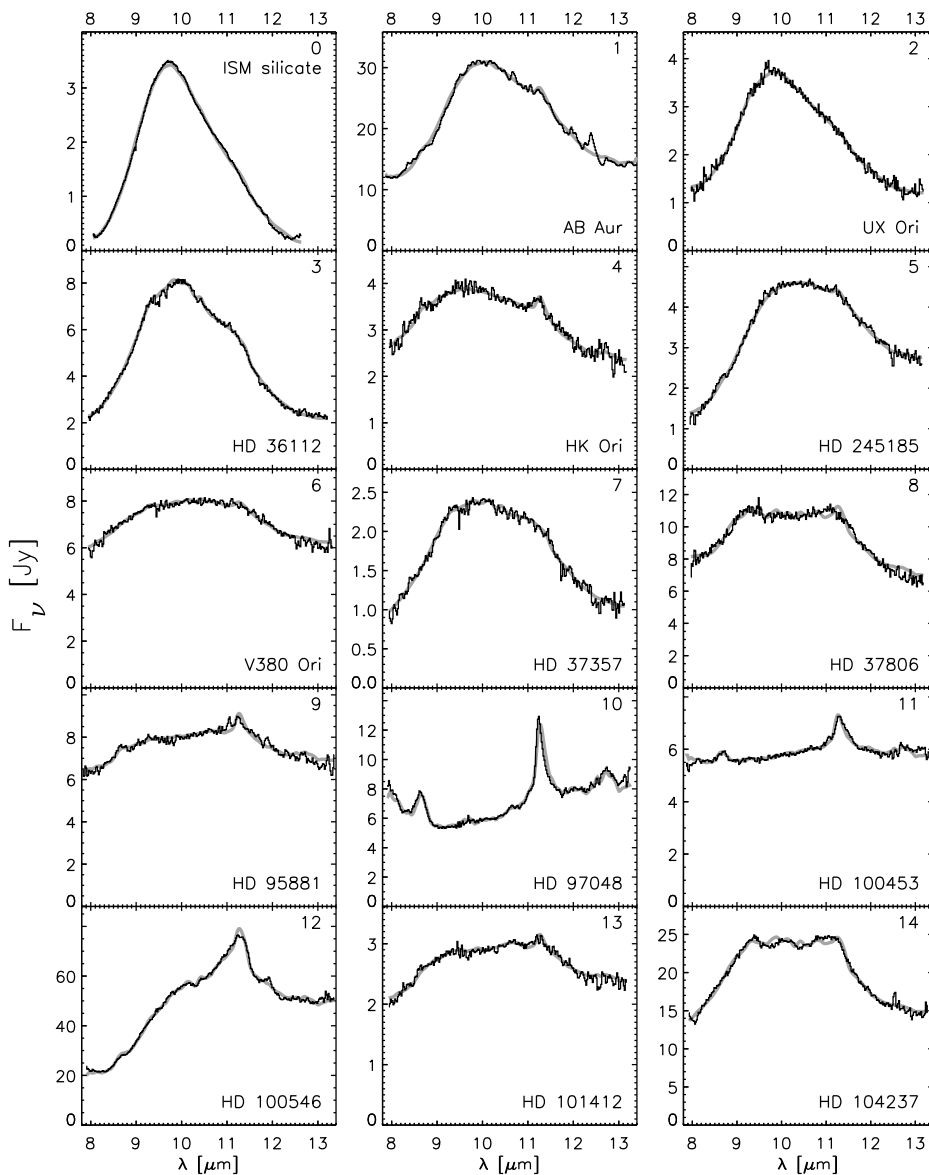


Figure 9.4: N-band spectra of the sources in our sample. The ISM silicate extinction efficiency, plotted in the upper left panel, was taken from Kemper et al. (2004). The AB Aur spectrum was taken by ISO (van den Ancker et al. 2000). Also plotted are the best fits to the spectra (grey curves, see section 9.5.2).

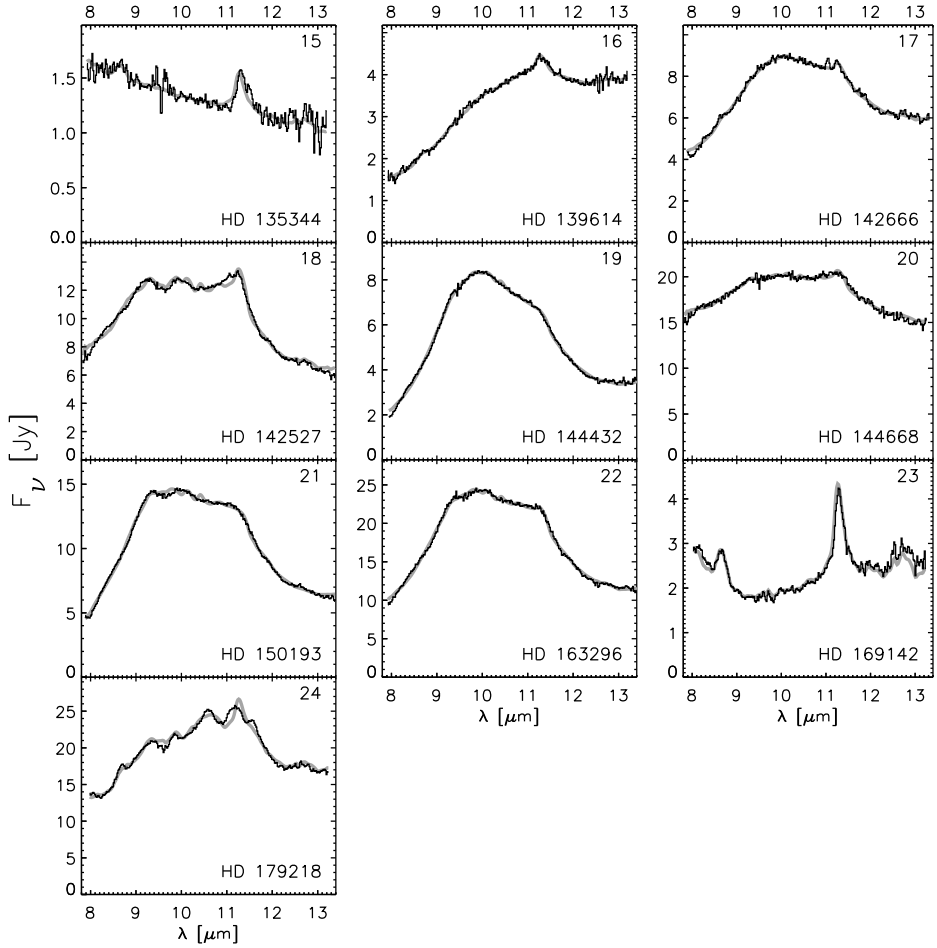


Figure 9.4: (Continued)

trum, while the PAHs can still produce significant emission. This can only occur if the PAHs have not been incorporated into larger grains. Indeed, van Boekel et al. (2004a) find evidence for a distance dependence of the typical silicate grain size in the surface layers of H Ae star disks: in the innermost regions growth has proceeded further than in the outer disk regions.

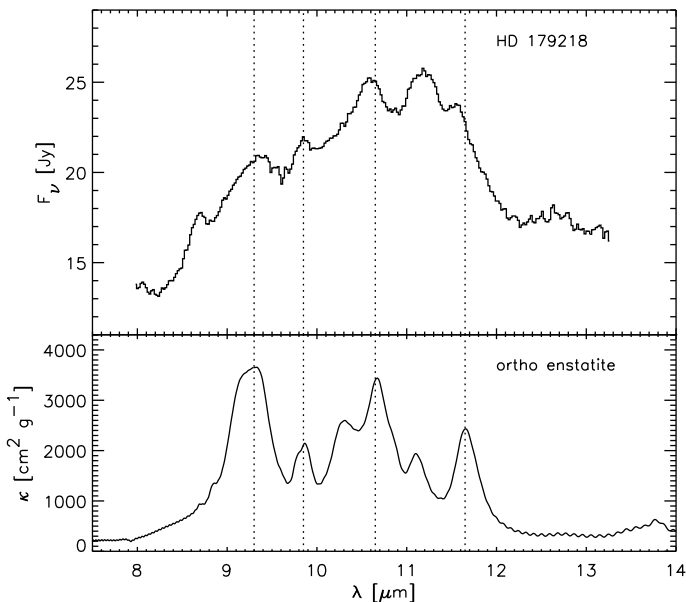


Figure 9.5: The N-band spectrum of HD 179218 (upper panel), and the measured mass absorption coefficients of ortho enstatite taken from Chihara et al. (2002) (lower panel). The wavelengths of the most prominent emission bands are indicated by the dotted lines. In this object, enstatite grains are an important constituent of the grain population that causes the $10\mu\text{m}$ feature.

9.4.2 The shape and strength of the silicate feature

In Fig. 9.6 we show the ratio of the continuum subtracted flux at 11.3 and $9.8\mu\text{m}$, against the silicate peak to continuum ratio (“feature strength”)². Group I sources are indicated with triangles, group II sources with diamonds (the “outlier” # 12 is HD 100546). Sources with a low $11.3/9.8$ ratio have a triangular shaped emission feature, clearly peaked just shortward of $10\mu\text{m}$ (e.g. UX Ori, in Fig. 9.4). Sources with a high $11.3/9.8$ generally have a broad, flat-topped emission band, often showing substructure (e.g. HD 37806, HD 142527). There is a clear correlation between the shape and strength of the silicate feature; stars with a strong feature (i.e. a high peak/continuum ratio) have a low $11.3/9.8$ ratio, whereas stars with weaker silicate features have higher $11.3/9.8$ ratios. This correlation was first demonstrated in Herbig Ae stars by van Boekel et al. (2003). Meeus et al. (2003) and Przygodda et al. (2003) have subsequently shown that the same trend is observed in the silicate feature of T-Tauri stars.

²To estimate the continuum we simply interpolate linearly between 8 and 13 micron. The peak/continuum ratio is the maximum value of the normalized spectrum $F_{norm} = 1 + F_{\nu,cs} / \langle F_{\nu,c} \rangle$, where $F_{\nu,cs}$ is the continuum subtracted spectrum ($F_\nu - F_{\nu,c}$) and $\langle F_{\nu,c} \rangle$ is the mean of the continuum. This definition of F_{norm} preserves the shape of the emission band even if the continuum is not constant. For a constant continuum level it is identical to $F_\nu / F_{\nu,c}$.

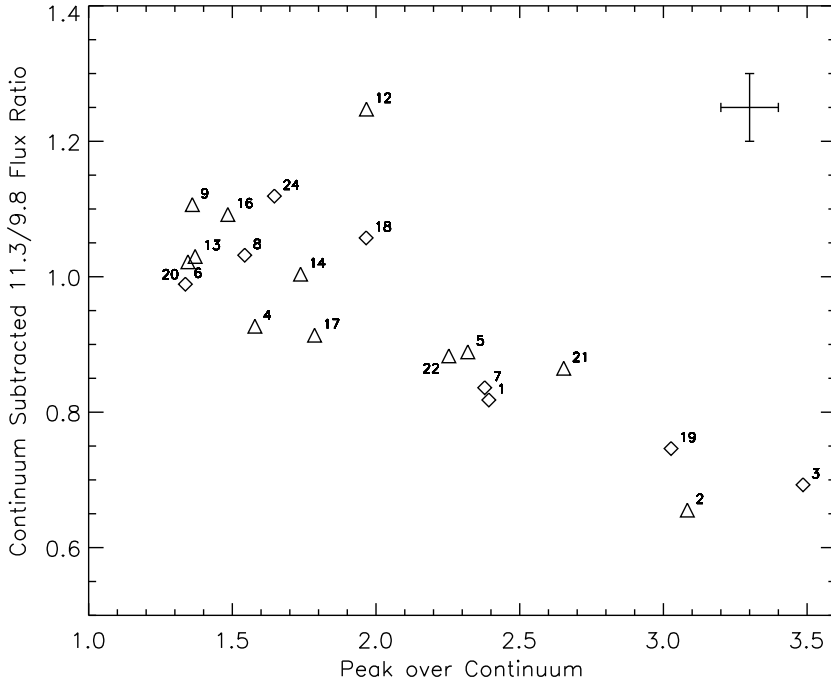


Figure 9.6: The flux ratio of the continuum subtracted spectra at 11.3 and 9.8 micron (a measure for the amount of processing that the material has undergone) versus the peak/continuum ratio of the silicate feature (a measure for the typical grain size). Group I sources are represented by triangles, group II sources by diamonds. In the upper right corner of the figure we have indicated the typical uncertainties in the displayed quantities.

The shape of the emission bands with a low 11.3/9.8 ratio is similar to that of the ISM silicate absorption feature. Such 10 micron features are indicative of small, amorphous silicate grains, i.e. relatively “primitive” dust. The emission bands with high 11.3/9.8 ratios can be explained with on average larger grains, and a higher degree of crystallinity, i.e. relatively “processed” dust. Thus, the silicate feature 11.3/9.8 ratio is a measure of the amount of processing that the material has undergone (Bouwman et al. 2001).

9.5 Analysis

9.5.1 Compositional fits

To derive the composition of the silicate dust causing the 10 micron feature, the observed spectra have been fitted using the most commonly found dust species in circumstellar material that show spectral structure in the 10 micron region (see Fig. 9.7). These are amorphous and crystalline olivine and pyroxene, and amorphous silica (e.g. Bouwman

et al. 2001). Amorphous olivine ($\text{Mg}_{2x}\text{Fe}_{2(1-x)}\text{SiO}_4$, where $0 \lesssim x \lesssim 1$ denotes the magnesium content of the material) is the most commonly found silicate in astrophysical environments. It dominates the 10 micron extinction caused by dust grains in the ISM (Kemper et al. 2004). The 10 micron emission spectrum of small amorphous olivine grains is characterized by a rather broad feature which peaks at $9.8\mu\text{m}$. Small amorphous pyroxene grains ($\text{Mg}_x\text{Fe}_{1-x}\text{SiO}_3$) show an emission feature very similar to that of amorphous olivine grains, though shifted toward shorter wavelengths. The emission spectra from small crystalline olivine and pyroxene grains show strong, narrow resonances that are observed in for example circumstellar disks (Waters & Waelkens 1998; Bouwman et al. 2001) and comets (Crovisier et al. 1997; Bouwman et al. 2003). From the positions of the resonances in the emission spectra of these objects it is clear that the magnesium rich components dominate the emission (see e.g. Jäger et al. 1998). In our fitting procedure we therefore use crystalline olivine and pyroxene with $x = 1$, i.e. forsterite and enstatite respectively. For the amorphous olivine and pyroxene we use $x = 0.5$.

Studies of interplanetary dust particles (Rietmeijer 1989) have shown that some of these particles contain large inclusions of silica (SiO_2). Also, from laboratory experiments it is suggested that when amorphous silicates are annealed to form forsterite, silica will be formed (see e.g. Fabian et al. 2000). The emission spectrum of silica in the 10 micron region has a distinct spectral signature, with a strong feature peaking at $8.9\mu\text{m}$. Therefore, silica is included as one of the possible dust components.

Many of our sources show emission bands at 7.9, 8.6, 11.3 and $12.7\mu\text{m}$ that are attributed to PAHs. In order to include the PAH emission in our compositional fits, we constructed a simple PAH template. This was done by taking our two highest quality spectra of sources without a silicate feature (HD 97048 and HD 169142), subtracting the continuum emission, and averaging over the two spectra. The resulting PAH emission spectrum was added as a fit component, and is shown in the bottom panel of Fig. 9.7.

Dust grains in circumstellar environments are most likely aggregates of many different dust species. However, in order to perform an analysis of the abundances of the various components in a large sample of sources, it is not (yet) feasible to do computations for such complex aggregates. If the aggregates are very fluffy, the constituents of which they are composed will interact with the incident radiation as separate entities. Molster et al. (2003) show that indeed a measurement of the infrared spectrum of a relatively large IDP still displays the spectral structure one would expect from much smaller particles. Therefore, we assume that the emission properties of an aggregated structure can be represented by the sum of the emission properties of the constituents (for a similar approach see e.g. Brucato et al. 1999; Bouwman et al. 2001; Honda et al. 2004).

All dust grains contributing to the $10\mu\text{m}$ region will in principle have their own temperature depending on the grain size and composition as well as on position in the disk. Consequently, the emission function of the dust will be a (weighted) sum over blackbody curves of different temperatures. In order to account for these effects one should use a disk model that self-consistently describes the disk geometry and all relevant radiation processes. This is beyond the scope of the analysis presented here. For state of

the art disk models we refer to Dullemond & Dominik (2004). We add that even these sophisticated models still do not account for many relevant processes, including the settling and (turbulent) mixing of grains leading to spatial gradients in the dust properties. Such spatial gradients have been reported by van Boekel et al. (2004a) to exist in Herbig Ae disks. One should also realize that even if such a detailed modeling approach was attempted, the modest wavelength interval provided by the TIMMI2 data would reveal only very limited information on the temperature distribution. The continuum in the 10 micron region is a very smooth, almost linear function of wavelength. We therefore opted to represent the continuum by a single blackbody curve with a temperature, T_c that is characteristic for the dust emission as a whole. Inherent in this approach is that we essentially assume that the temperature of the individual grains is independent of composition and size, and that there are no gradients in grain properties (per unit mass) throughout the disk.

The disk regions that we study are partially optically thick at $10\ \mu\text{m}$. However, we assume that the disk surface layer from which the observed flux originates is optically thin at this wavelength. This must be the case since we see emission features. The flux emitted by a distribution of dust grains is then given by

$$\mathcal{F}_\nu^{\text{silicate}} \propto B_\nu(T_c) \sum_i w_i \kappa_i, \quad (9.6)$$

where $B_\nu(T_c)$ denotes the Planck function at the characteristic temperature T_c , κ_i is the mass absorption coefficient of dust component i (see also Fig. 9.7), and w_i is a weighting factor which is proportional to the total dust mass in component i . The summation is over all dust components. The mass absorption coefficient of each dust species is determined by the size, shape, structure and chemical composition of the dust grains. The total model spectrum $\mathcal{F}_\nu^{\text{model}}$ is then calculated by adding a continuum and PAH contribution to the silicate emission.

Shape of the dust grains

The shape and structure of the dust grains are very important parameters determining the feature shape of the emission spectrum. Usually it is assumed that the grains are homogeneous and spherical so that Mie theory can be applied to calculate the κ_i . Another widely used assumption is that the grains are much smaller than the wavelength of radiation (“Rayleigh limit”) in which case it is mathematically straightforward to adopt a continuous distribution of ellipsoids (CDE Bohren & Huffman 1983; Bouwman et al. 2003). Since micron sized silicate grains are not in the Rayleigh limit at a wavelength of $10\ \mu\text{m}$, we cannot use CDE calculations to study grain growth. Furthermore, a comparison between calculations of the mass absorption coefficients of small crystalline silicates with measurements shows that we cannot get good agreement using homogeneous spherical particles (see for example Fabian et al. 2001).

Adopting different grain shapes, Min et al. (2003b) showed that the absorption properties can be divided in essentially two categories. One category contains the perfect homogeneous spheres; the other all other investigated shapes, including hollow spheres. Shape effects within the second category do exist, but they are small compared to the

Dust component	Chemical formula	Shape	Reference
Amorphous olivine	$\text{Mg}_{2x}\text{Fe}_{2-2x}\text{SiO}_4$	Homogeneous Spheres	DO
Amorphous pyroxene	$\text{Mg}_x\text{Fe}_{1-x}\text{SiO}_3$	Homogeneous Spheres	DO
Crystalline forsterite	Mg_2SiO_4	Irregular (DHS)	SP
Crystalline enstatite	MgSiO_3	Irregular (DHS)	JA
Amorphous silica	SiO_2	Irregular (DHS)	SK

Table 9.5: Characteristics of the various dust components used in the fitting procedure (see section 9.5.1). The chemical formulas and assumed grain shapes have been indicated in the second and third column. In the fourth column, we give references for the refractive index data used (DO: Dorschner et al. (1995), SP: Servoin & Piriou (1973), JA: Jäger et al. (1998), SK: Spitzer & Kleinman (1960)).

differences with homogeneous spheres. One could say that the difference between perfect homogeneous particles and those having other shapes is essentially a result of a breaking of perfect symmetry (see also Min et al. 2003b). This implies that we have only very limited information on the true (likely irregular) shape of astrophysical dust grains from spectroscopic analysis. However, a practical implication of this result is that one may represent the absorption properties of irregular grains with sufficient accuracy by adopting the average properties of a distribution of shapes other than that of homogeneous spheres. For this purpose, a practical choice is a distribution of hollow spheres (DHS), simply averaging over the volume fraction occupied by the central inclusion, which ranges from 0 to 1. In this shape distribution, the material volume of the particle is kept constant, thus particles with a high value of f will have a large outer radius. This shape distribution has the advantage that it can be applied for all grain sizes using a simple extension of Mie theory. Min et al. (2003b) showed that this indeed gives excellent results for small forsterite grains. Therefore, in this work, the mass absorption coefficients of all crystalline grains (forsterite, enstatite) and silica are calculated with a distribution of hollow spheres. For the amorphous olivine and pyroxene particles we use Mie theory since for these species the effects of shape on absorption properties are minor.

The κ_i are calculated using laboratory measurements of the refractive index as a function of wavelength. References for the measurements used for the various dust species are listed in Table 9.5.

Size of the dust grains

The dust grains in circumstellar disks most likely have a rather broad size distribution. In the 10 micron region the observational data are sensitive to the dust grains with a volume equivalent radius up to a few micron in size. Larger grains mainly contribute to the continuum. In order to minimize the number of free parameters in the fitting procedure, we want to sample the size distribution carefully. We find that the variety of spectral shapes can be best covered using only two distinct particle sizes, a ‘small’ particle size with a material volume equivalent sphere radius $r_V = 0.1 \mu\text{m}$ and a ‘large’ particle size

with $r_V = 1.5 \mu\text{m}$ (for a similar approach see Bouwman et al. 2001; Honda et al. 2004). We have extensively checked that the results of the analysis using three, four or five particle sizes with volume equivalent radii ranging up to $3.5 \mu\text{m}$ do not change significantly. The size of the large grain component, when using only two particle sizes, has to be chosen with care. When it is too large, the difference in absolute value of the mass absorption coefficients of the small and the large grain component will be too big. If, for example, one adopts for the large grain size $r_V = 2 \mu\text{m}$, one would overestimate the abundance of large grains. This is especially so for the large crystalline grains and results in an overestimate of the crystallinity. The differences between the absolute values of the emissivities of a 0.1 and a $2 \mu\text{m}$ amorphous grain are not so big, making $2 \mu\text{m}$ also a reasonable candidate for the large amorphous component. The choice of $1.5 \mu\text{m}$ is in a sense a trade off between the best choice for the crystalline and the amorphous component.

Fitting procedure and error analysis

In order to keep the number of free parameters in the model small, only two grain sizes are used for every silicate dust type (as discussed above). We thus have contributions of five silicate species, of PAHs and of a blackbody continuum of which the absolute level and shape (characteristic temperature) can be varied. The emissivities of the silicates are multiplied by a blackbody spectrum with the same characteristic temperature as the continuum. This results in 13 free parameters. The silicate and PAH templates are shown in Fig. 9.7.

To fit the spectra we minimize the reduced χ^2 of the entire 10 micron region given by

$$\chi^2 = \frac{1}{N_\lambda - M} \sum_{i=1}^{N_\lambda} \left| \frac{\mathcal{F}_v^{\text{model}}(\lambda_i) - \mathcal{F}_v^{\text{observed}}(\lambda_i)}{\sigma_i} \right|^2. \quad (9.7)$$

Here N_λ is the number of wavelength points λ_i , M is the number of fit parameters (in this case $M = 13$) and σ_i is the absolute error on the observed flux at wavelength λ_i . For a given characteristic temperature T_c we can calculate the optimal values for the weights w_i of the individual dust components, using a linear least square fitting procedure.

The measurement errors (σ_i) used in the fitting procedure represent the statistical noise in the spectra. The calibrator spectra all have a very high signal to noise ratio (SNR) and statistical noise of the calibration observations is negligible. The SNR in our Herbig star spectra range from ~ 18 in the faintest source (HD 135344) to approximately 60 in the bright sources (e.g. HD 100546). There are also systematic uncertainties, arising from an imperfect calibration, and the uncertainty in the used spectral templates for the calibrators. Some degree of systematic error is inevitable, since the science target and calibrator cannot be measured at the same time and in the same direction. Since we cannot assess the systematic uncertainties we do not take these into account. We note, however, that agreement between our ground based spectra and high SNR ISO spectra is generally very good. For the faint sources (such as UX Ori), the statistical noise dominates the error budget. For bright sources (e.g. HD 144432) the systematic

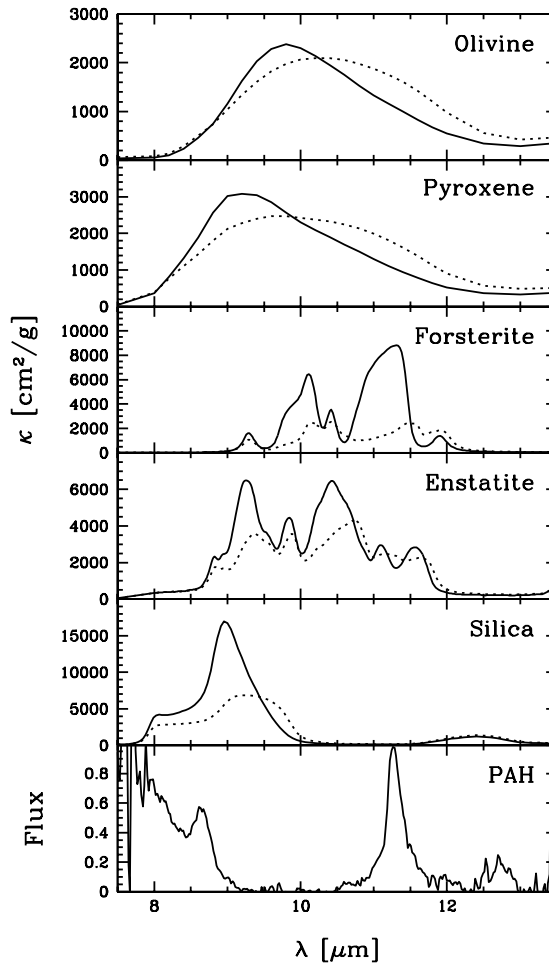


Figure 9.7: The mass absorption coefficients of the various templates used in the fitting procedure (upper 5 panels). We use grains with volume equivalent radii of $0.1\mu\text{m}$ (solid lines) and $1.5\mu\text{m}$ (dotted lines). In the lower panel we show the template used for the PAH emission, which is normalized such that the maximum flux in the 8 to 13 micron region equals unity. For a detailed discussion see section 9.5.1.

uncertainties may be important, implying that we underestimate the errors. This will evidently lead to higher χ^2 values in the fit procedure.

The errors on the fit parameters are calculated using a Monte Carlo method. For every spectrum we generate 1000 synthetic spectra, by randomly adding Gaussian noise to the spectrum with a distribution of width σ_i at each wavelength point. This yields 1000 spectra that are all consistent with our data. On each of these, we perform the exact same compositional fit procedure, yielding (slightly) different values of the fit

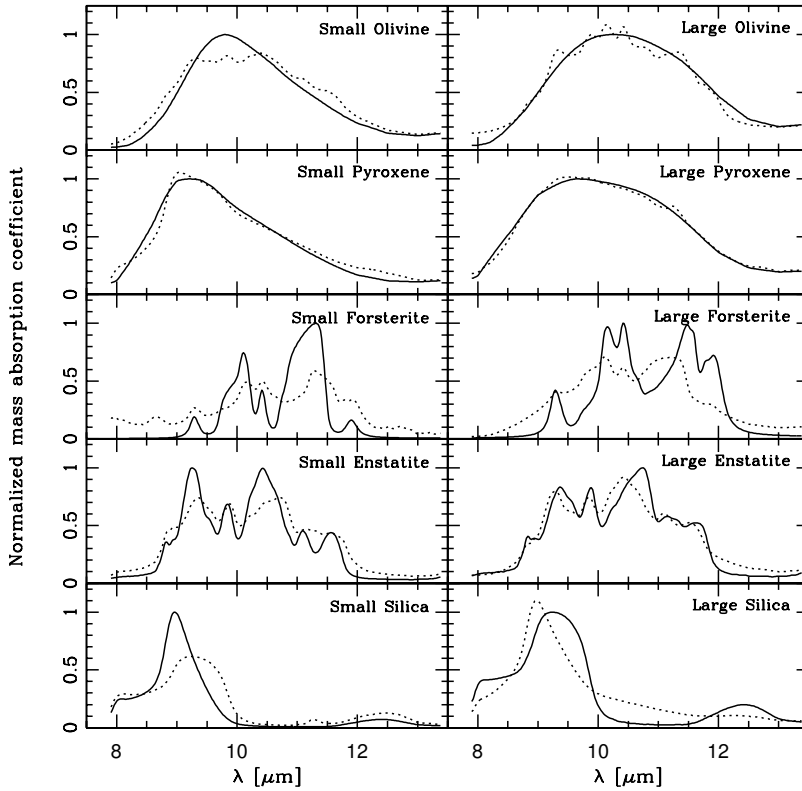


Figure 9.8: The templates used in the fitting procedure (solid curves) together with the resulting best fits using all other templates (dotted curves). The spectra are all normalized such that the maximum value of the template equals unity. In the left column we show the templates for the small grains ($0.1 \mu\text{m}$), in the right column those of the large grains ($1.5 \mu\text{m}$).

parameters. From the resulting distribution of all fit parameters, we calculate the mean (which will be our 'best fit' value) and standard deviation. Besides its simplicity, this method has the advantage that degeneracies between fit parameters automatically show up as large errors in these parameters.

9.5.2 Results

Fig. 9.4 shows the observed spectra together with the best fit model spectra. For comparison we also fit the interstellar extinction as observed towards the galactic center (Kemper et al. 2004). The resulting values of the fit parameters are summarized in Table 9.6. The overall quality of the model fits is very good and we thus conclude that the diversity of the shapes of the observed spectra are well covered by the choice of the spectral templates. We notice that in some sources the model fits show slightly more

Table 9.6: The best fit values of the parameters in our compositional fits. The abundances of small ($0.1\mu\text{m}$) and large ($1.5\mu\text{m}$) grains of the various dust species are given as fractions of the total dust mass, excluding the dust responsible for the continuum emission. If a species was not found, or unconstrained by the spectra, this is indicated by a - symbol.

#	Star	χ^2	T [K]	Olivine		Pyroxene	
				Small	Large	Small	Large
0	Gal. Center	66.8	-	$85.8^{+0.1}_{-0.1}$	-	$12.5^{+0.1}_{-0.1}$	-
1	AB Aur	2.5	$463.8^{+6.3}_{-4.1}$	$49.5^{+2.2}_{-2.4}$	$47.2^{+2.5}_{-2.6}$	-	-
2	UX Ori	0.7	$676.5^{+28.6}_{-37.4}$	$63.6^{+4.9}_{-4.5}$	$30.7^{+6.0}_{-7.9}$	-	$2.0^{+5.8}_{-1.8}$
3	HD 36112	1.7	$669.1^{+19.4}_{-21.2}$	$50.5^{+1.8}_{-1.7}$	$22.4^{+3.2}_{-3.1}$	-	$22.2^{+1.8}_{-1.8}$
4	HK Ori	0.4	$516.0^{+11.9}_{-11.4}$	$7.1^{+7.6}_{-5.4}$	$0.9^{+16.3}_{-0.9}$	$13.7^{+7.2}_{-7.9}$	$75.3^{+9.9}_{-13.3}$
5	HD 245185	0.6	$337.1^{+7.1}_{-9.1}$	$28.5^{+3.5}_{-3.5}$	$57.4^{+7.5}_{-8.8}$	$0.1^{+2.5}_{-0.1}$	$12.2^{+6.5}_{-5.9}$
6	V380 Ori	1.8	$480.6^{+9.4}_{-1.3}$	-	$0.8^{+6.5}_{-0.8}$	-	$74.6^{+2.9}_{-5.0}$
7	HD 37357	0.5	$508.3^{+22.4}_{-24.5}$	$3.9^{+5.9}_{-3.4}$	$39.4^{+11.9}_{-14.8}$	$0.1^{+3.6}_{-0.1}$	$46.0^{+10.4}_{-9.9}$
8	HD 37806	1.8	$524.5^{+6.6}_{-6.0}$	-	$59.8^{+4.6}_{-5.7}$	-	$0.8^{+5.2}_{-0.8}$
9	HD 95881	3.7	$428.5^{+1.5}_{-8.6}$	-	-	-	$79.7^{+4.0}_{-2.7}$
10	HD 97048	1.4	$303.1^{+6.9}_{-3.1}$	-	-	-	-
11	HD 100453	2.1	$429.3^{+0.7}_{-9.3}$	-	-	-	-
12	HD 100546	5.6	$261.4^{+8.6}_{-1.4}$	$2.5^{+1.1}_{-1.6}$	$78.5^{+1.3}_{-1.2}$	-	$0.0^{+0.7}_{-0.0}$
13	HD 101412	0.5	$425.0^{+5.8}_{-5.2}$	-	$0.3^{+9.1}_{-0.3}$	$0.2^{+4.3}_{-0.2}$	$75.2^{+5.4}_{-7.0}$
14	HD 104237	3.9	$446.4^{+3.6}_{-6.4}$	-	-	-	$77.7^{+1.6}_{-1.3}$
15	HD 135344	0.8	$680.4^{+17.7}_{-13.7}$	-	-	-	-
16	HD 139614	0.6	$276.6^{+3.5}_{-6.7}$	$16.0^{+6.2}_{-6.5}$	$47.0^{+11.2}_{-16.7}$	-	$29.7^{+13.8}_{-9.8}$
17	HD 142666	1.6	$396.3^{+3.9}_{-6.3}$	$42.8^{+2.9}_{-2.7}$	$9.7^{+5.0}_{-6.5}$	-	$43.5^{+3.9}_{-2.9}$
18	HD 142527	11.1	$522.5^{+7.5}_{-2.5}$	-	$0.0^{+0.8}_{-0.0}$	-	$73.2^{+0.7}_{-1.0}$
19	HD 144432	3.0	$400.5^{+9.6}_{-0.5}$	$52.7^{+0.7}_{-0.7}$	$0.0^{+1.1}_{-0.0}$	-	$42.3^{+0.7}_{-0.8}$
20	HD 144668	9.6	$516.8^{+3.2}_{-6.8}$	-	$56.9^{+6.8}_{-13.2}$	-	$12.0^{+12.4}_{-6.1}$
21	HD 150193	5.1	$409.9^{+0.1}_{-10.3}$	-	$0.7^{+1.1}_{-0.6}$	-	$82.1^{+0.7}_{-0.8}$
22	HD 163296	10.7	$461.2^{+8.9}_{-1.2}$	$15.3^{+0.7}_{-1.4}$	$29.8^{+3.8}_{-1.4}$	-	$42.2^{+0.8}_{-2.1}$
23	HD 169142	0.9	$348.0^{+3.5}_{-8.0}$	-	-	-	-
24	HD 179218	11.8	$350.0^{+0.0}_{-14.1}$	-	$11.3^{+2.6}_{-2.6}$	-	$58.7^{+2.1}_{-2.0}$

spectral structure between 9 and $11\mu\text{m}$ than the observed spectra. This could be caused by the choice of the shape distribution of the dust grains, which may be too simple to represent the spectral details of realistic particles. We also notice that in, for example, HD 179218 we cannot accurately reproduce the detailed shape of the spectrum. Especially the feature around $11.3\mu\text{m}$ is less sharply peaked in the observed spectrum than

Table 9.6: (continued). The PAH and continuum flux contributions (the last two columns) are listed as percentages of the total integrated flux over the $10\mu\text{m}$ region, contained in these components. These are measures for the relative flux contributions, but cannot be interpreted as relative dust masses.

#	Forsterite		Enstatite		Silica		PAH	Cont.
	Small	Large	Small	Large	Small	Large	contr.	contr.
0	$0.6^{+0.0}_{-0.0}$	-	-	-	-	$1.0^{+0.0}_{-0.0}$	$0.5^{+0.0}_{-0.0}$	-
1	$0.6^{+0.2}_{-0.2}$	$2.7^{+0.7}_{-0.7}$	-	-	-	-	$1.9^{+0.1}_{-0.2}$	$53.1^{+0.5}_{-0.4}$
2	$1.2^{+0.4}_{-0.4}$	$0.3^{+0.9}_{-0.3}$	$0.6^{+0.6}_{-0.4}$	$1.1^{+1.2}_{-0.8}$	-	$0.6^{+0.4}_{-0.4}$	$0.1^{+0.3}_{-0.1}$	$45.2^{+1.3}_{-1.4}$
3	$2.9^{+0.1}_{-0.1}$	$0.0^{+0.1}_{-0.1}$	$1.8^{+0.2}_{-0.2}$	$0.2^{+0.4}_{-0.2}$	-	-	$0.1^{+0.1}_{-0.1}$	$33.9^{+0.4}_{-0.5}$
4	$0.7^{+1.0}_{-0.6}$	$1.4^{+2.7}_{-1.3}$	$0.1^{+1.0}_{-0.1}$	$0.1^{+1.6}_{-0.1}$	-	$0.8^{+1.6}_{-0.8}$	$2.5^{+0.4}_{-0.4}$	$68.5^{+1.4}_{-1.3}$
5	$0.2^{+0.3}_{-0.2}$	$0.7^{+0.9}_{-0.6}$	$0.0^{+0.3}_{-0.0}$	$0.0^{+0.7}_{-0.0}$	-	$0.9^{+0.5}_{-0.5}$	$1.1^{+0.2}_{-0.3}$	$50.6^{+1.1}_{-1.1}$
6	$2.2^{+0.6}_{-0.5}$	$10.8^{+1.5}_{-1.4}$	-	$10.8^{+1.8}_{-1.7}$	$0.8^{+0.3}_{-0.3}$	$0.0^{+0.4}_{-0.0}$	$0.7^{+0.1}_{-0.1}$	$84.9^{+0.5}_{-0.4}$
7	$2.7^{+0.5}_{-0.6}$	$2.2^{+1.8}_{-1.5}$	$0.9^{+0.9}_{-0.7}$	$1.3^{+1.8}_{-1.1}$	$0.0^{+0.2}_{-0.0}$	$3.5^{+0.8}_{-0.8}$	$0.1^{+0.3}_{-0.1}$	$47.5^{+1.6}_{-1.5}$
8	$6.2^{+0.9}_{-0.8}$	$3.5^{+1.9}_{-1.8}$	$0.2^{+0.9}_{-0.2}$	$20.9^{+2.7}_{-2.6}$	$5.0^{+0.4}_{-0.4}$	$3.5^{+0.8}_{-0.8}$	$1.8^{+0.2}_{-0.2}$	$73.7^{+1.0}_{-0.9}$
9	$0.7^{+0.5}_{-0.5}$	$4.7^{+1.6}_{-1.9}$	$0.0^{+0.8}_{-0.0}$	$11.3^{+1.7}_{-2.4}$	$3.0^{+0.3}_{-0.3}$	$0.5^{+0.9}_{-0.5}$	$3.0^{+0.2}_{-0.1}$	$84.2^{+0.4}_{-0.7}$
10	-	-	-	-	-	-	$14.1^{+0.2}_{-0.2}$	$83.1^{+0.6}_{-0.4}$
11	-	-	-	-	-	-	$4.4^{+0.1}_{-0.1}$	$93.5^{+0.2}_{-0.4}$
12	$6.2^{+0.8}_{-0.2}$	$0.1^{+0.4}_{-0.1}$	-	$5.7^{+0.5}_{-0.4}$	$0.2^{+0.1}_{-0.1}$	$6.7^{+0.3}_{-0.6}$	$3.7^{+0.1}_{-0.7}$	$55.3^{+2.9}_{-0.6}$
13	$0.7^{+1.2}_{-0.6}$	$3.4^{+3.1}_{-2.5}$	$0.1^{+1.2}_{-0.1}$	$16.8^{+3.9}_{-3.4}$	$3.2^{+0.6}_{-0.6}$	$0.1^{+1.2}_{-0.1}$	$2.0^{+0.2}_{-0.2}$	$80.2^{+1.1}_{-0.9}$
14	$5.9^{+0.4}_{-0.6}$	-	-	$11.8^{+1.0}_{-1.2}$	$1.7^{+0.2}_{-0.1}$	$2.9^{+0.4}_{-0.4}$	$1.4^{+0.2}_{-0.1}$	$63.4^{+0.6}_{-0.9}$
15	-	-	-	-	-	-	$4.9^{+0.3}_{-0.3}$	$90.3^{+1.0}_{-1.0}$
16	$2.4^{+0.9}_{-0.8}$	$0.7^{+1.7}_{-0.6}$	$0.0^{+0.7}_{-0.0}$	$4.1^{+2.3}_{-2.1}$	-	$0.1^{+0.7}_{-0.1}$	$2.2^{+0.3}_{-0.3}$	$75.9^{+1.3}_{-1.6}$
17	$1.1^{+0.3}_{-0.3}$	$2.3^{+0.8}_{-0.8}$	$0.0^{+0.3}_{-0.0}$	$0.6^{+0.8}_{-0.5}$	-	-	$1.7^{+0.2}_{-0.1}$	$66.8^{+0.5}_{-0.5}$
18	$8.6^{+0.4}_{-0.2}$	-	$0.6^{+0.2}_{-0.2}$	$14.2^{+0.8}_{-0.6}$	$2.4^{+0.1}_{-0.1}$	$1.0^{+0.2}_{-0.3}$	$3.1^{+0.1}_{-0.2}$	$58.8^{+0.7}_{-0.3}$
19	$1.9^{+0.1}_{-0.1}$	$0.7^{+0.3}_{-0.3}$	$0.7^{+0.2}_{-0.2}$	$0.9^{+0.3}_{-0.3}$	-	$0.6^{+0.1}_{-0.1}$	$0.5^{+0.1}_{-0.1}$	$39.7^{+0.5}_{-0.3}$
20	$7.0^{+0.3}_{-0.3}$	$6.3^{+0.9}_{-0.8}$	$0.0^{+0.3}_{-0.0}$	$12.1^{+0.9}_{-0.8}$	$1.5^{+0.2}_{-0.3}$	$4.2^{+0.3}_{-0.3}$	$1.2^{+0.1}_{-0.1}$	$85.3^{+0.2}_{-0.3}$
21	$3.3^{+0.1}_{-0.1}$	$4.1^{+0.3}_{-0.3}$	$0.2^{+0.2}_{-0.2}$	$3.7^{+0.3}_{-0.4}$	-	$5.8^{+0.1}_{-0.1}$	$0.2^{+0.1}_{-0.1}$	$39.7^{+0.2}_{-0.3}$
22	$3.1^{+0.1}_{-0.1}$	$1.3^{+0.3}_{-0.3}$	$0.2^{+0.1}_{-0.1}$	$4.0^{+0.3}_{-0.3}$	-	$4.1^{+0.1}_{-0.1}$	$1.1^{+0.1}_{-0.1}$	$49.6^{+0.2}_{-0.2}$
23	-	-	-	-	-	-	$16.1^{+0.2}_{-0.2}$	$82.0^{+0.4}_{-0.5}$
24	-	$3.5^{+0.6}_{-0.7}$	$6.2^{+0.4}_{-0.4}$	$18.3^{+0.8}_{-0.7}$	$2.0^{+0.1}_{-0.1}$	-	$4.4^{+0.1}_{-0.1}$	$64.8^{+0.2}_{-0.2}$

in the model fit. This effect can also be seen in other sources, albeit in a more modest form, and could be caused by a missing dust component or by the choice of the shape distribution.

As an objective measure for the goodness of fit, the reduced χ^2 of every fit is listed in Table 9.6. For a good fit this parameter should be close to unity. The likely reason

that we have relatively high values of χ^2 for about half of the sources is that we do not take into account the uncertainties on the κ_i . These are mainly caused by uncertainties in the shape, structure and size of the grains, and in the laboratory measurements of the wavelength dependent refractive indices.

To test whether we have degeneracies between the various templates used in the fitting procedure we tried to fit each of the silicate templates using a linear combination of all other templates. The results are shown in Fig. 9.8 where we plot the mass absorption coefficients together with the best fit using the other templates (here the mass absorption coefficients have been normalized such that the maximum value equals unity). The figure shows that almost all of the templates used have a unique spectral structure that cannot be reproduced by the other templates. Only the emission from large pyroxene grains can be reproduced reasonably well by the other templates, although significant differences still exist (e.g. the $11.3\mu\text{m}$ feature that is present in the fit to the large pyroxene opacity in Fig. 9.8). The fit consists of 52% large olivine grains, 43% small pyroxene grains and only 5% of crystalline silicates. This could result in a slight change in the mass fraction of large grains when this template is not used. The crystalline fraction would not be affected significantly. Because the small pyroxene grains are needed in order to reproduce the short wavelength side of some of the spectra, we chose to include also the large pyroxene grains for consistency. The presence of large pyroxene grains can be firmly established only in the highest SNR spectra.

There are a few points one has to keep in mind when interpreting the results of the analysis presented above.

- Since we consider only the 10 micron region of the infrared spectrum our data are sensitive only to grains with a temperature of ~ 200 K or more. This limits our study to the inner disk regions (i.e. $\lesssim 10\text{-}20$ AU).
- Because of the same limitation of the spectral range our data are only sensitive to relatively modest sized grains. In order for the emission to show an observable spectral signature, the dust grains have to be small compared to the wavelength of radiation. $10\mu\text{m}$ measurements are sensitive to grains with a volume equivalent radius $r_V \lesssim 3\mu\text{m}$.
- The disk regions that we study are partially optically thick at $10\mu\text{m}$. This means that we cannot see deep into the disk. We only observe the surface layer.
- Due to the limited spatial resolution of our observations, we observe the integrated spectra of the entire inner disk surface. The observed flux is therefore an average over distance to the star and thus over temperature. Also, we know from spatially resolved observations of the innermost part of a few disks that the mineralogy is not constant as a function of distance to the star (van Boekel et al. 2004a). Close to the star we have higher temperatures and densities which trigger both crystallization and grain growth. The derived parameters therefore represent an average, characteristic temperature and an average dust composition.

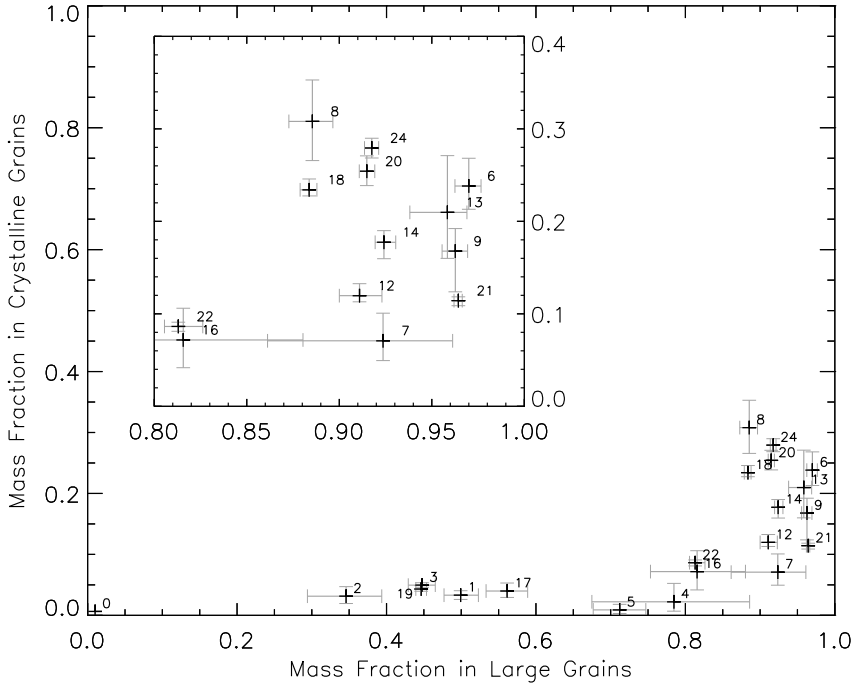


Figure 9.9: The relation between grain size and crystallinity found in our spectral fits. Vertically, we plot the mass fraction of crystalline grains (forsterite and enstatite). Horizontally, the mass fraction of large ($1.5\ \mu\text{m}$) grains is plotted. Since group Ib sources do not display a silicate feature, they are not shown here. For a discussion see sections 9.5.3 and 9.6.

9.5.3 Observed trends in the fits

We will now discuss the trends and correlations observed in the derived fit parameters.

In Fig. 9.9 we visualize the grain growth and crystallinity, as implied by our compositional fits. Horizontally we plot the mass in large ($1.5\ \mu\text{m}$) grains, as a fraction of the total dust mass, *excluding the dust responsible for the continuum component, and the PAHs*. Vertically, we likewise plot the mass fraction contained in crystalline silicates in small and large grains, which is also referred to as the *crystallinity* of the material.

Upon inspection of the figure it is clear that all disks show signs of substantial removal of small grains. There are *no* sources with a mass fraction in large grains below 30%. This infers that none of the sources in our sample contains truly “pristine” dust. All sources have an appreciable amount of large grains at their disk surface, compared to ISM conditions. In addition, all sources have a crystallinity that is higher than the value we derive for the ISM ($\sim 0.6\%$; Kemper et al. 2004 derive an even more stringent upper limit of 0.4%).

The derived mass fraction in large grains ranges from $\approx 30\%$ to $\approx 100\%$, with most sources at high values. *All sources exhibiting a high degree of crystallinity have a high*

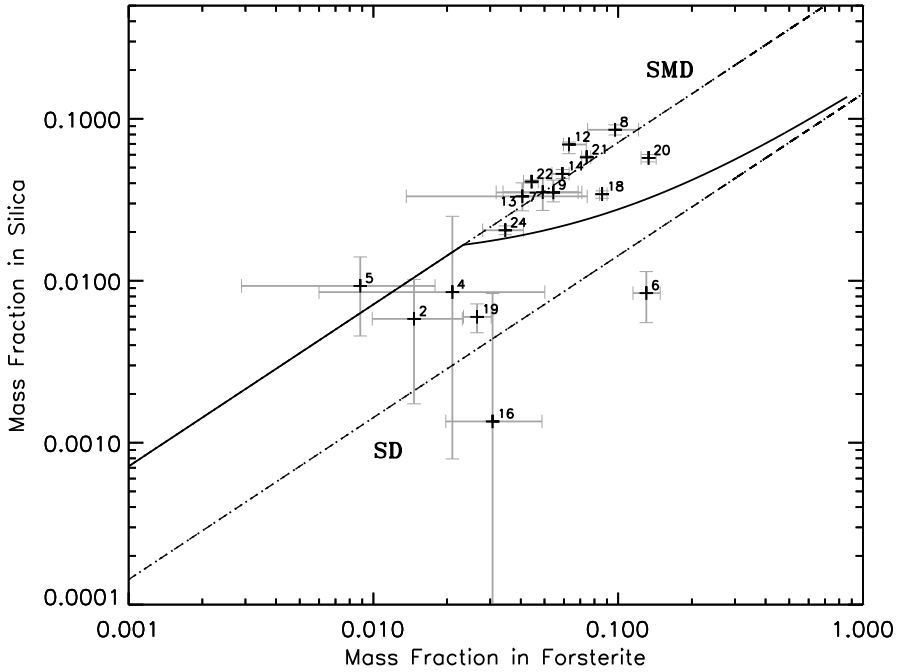


Figure 9.10: The fraction of the dust mass contained in silica grains vs. the mass fraction contained in forsterite grains. Following Bouwman et al. (2001) we also plot the theoretical annealing behavior of two different amorphous magnesium silicates, smectite dehydroxylate (SMD; $\text{Mg}_6\text{Si}_8\text{O}_{22}$; upper dash-dotted line) and serpentine dehydroxylate (SD; $\text{Mg}_3\text{Si}_2\text{O}_7$; lower dash-dotted line). The solid line represents the expected annealing behavior of a mixture of these two silicates, consisting of 4% SMD and 96% SD, which was found by Bouwman et al. (2001) to give the best fit to their data. Our data are in better agreement with a pure SMD initial composition.

mass fraction in large grains. There are *no* highly crystalline sources (crystallinity above 10%) with less than 85% of the dust mass in large grains.

There are no sources with a mass fraction of crystalline material above 35% (see also Table 9.6). It should be kept in mind that the silicate emission we see likely originates in the surface layer of the disk. Van Boekel et al. (2003) argue that the disks are well mixed in the vertical direction, and that therefore the observed silicate emission should be representative of the whole micron and sub-micron sized dust population of the disk. We point out that in this work, “crystallization” refers to the process of crystallizing the material (by whatever means), spreading it over a significant part of the disk region seen at $10\mu\text{m}$, and bringing it up to the disk surface where we can see it spectroscopically. In a scenario where the crystalline silicates are produced by thermal annealing in the innermost disk regions, and transported outward by radial mixing, the degree of crystallization is therefore a measure of the degree of mixing in the disk rather than the actual process of annealing, which is effectively instantaneous at the inner disk edge.

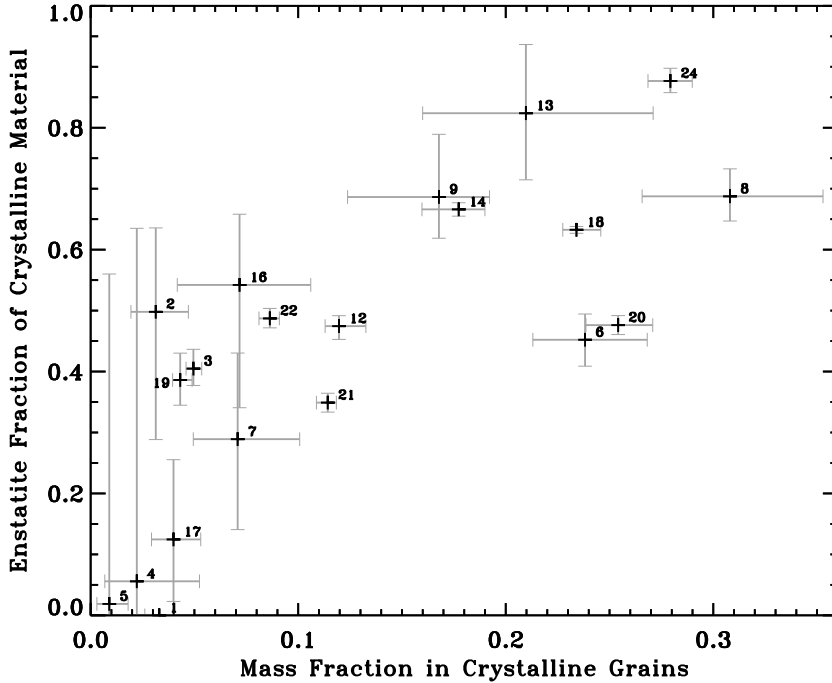


Figure 9.11: The mass fraction of crystalline material contained in enstatite vs. the total mass fraction of crystalline material. A value of 0 on the vertical axis indicates that all the crystalline silicates present in the disk are in the form of forsterite, while a value of 1 means all crystalline silicates are in the form of enstatite.

In Fig. 9.10 we plot the mass fraction of dust contained in forsterite versus that contained in silica grains. It is clear that these mass fractions are correlated. Experiments show that when forsterite is created by annealing of an amorphous silicate, silica is formed as a by-product (Rietmeijer et al. 1986; Hallenbeck & Nuth 1997; Fabian et al. 2000). The amount of silica that is created when forming a certain amount of forsterite depends on the type of amorphous silicate one starts out with. As already suggested by Bouwman et al. (2001), we can try to constrain the composition of the amorphous material by measuring the ratio of forsterite over silica. In the figure we also plot the expected annealing behavior of smectite dehydroxylate (SMD; $\text{Mg}_6\text{Si}_8\text{O}_{22}$) and serpentine dehydroxylate (SD; $\text{Mg}_3\text{Si}_2\text{O}_7$). In low temperature condensation experiments, these are the only magnesium silicates that are formed (Rietmeijer et al. 1999). Whereas Bouwman et al. (2001) found that a mixture of 4% of SMD and 96% of SD yielded the best fit to their data, our results seem to favor an initial composition of pure SMD. Possibly, the discrepancy between the results found by Bouwman et al. (2001) and the results found here is connected to the differences in the dust components used to fit the $10\ \mu\text{m}$ spectra. Notably, Bouwman et al. (2001) do not include large silica and forsterite particles.

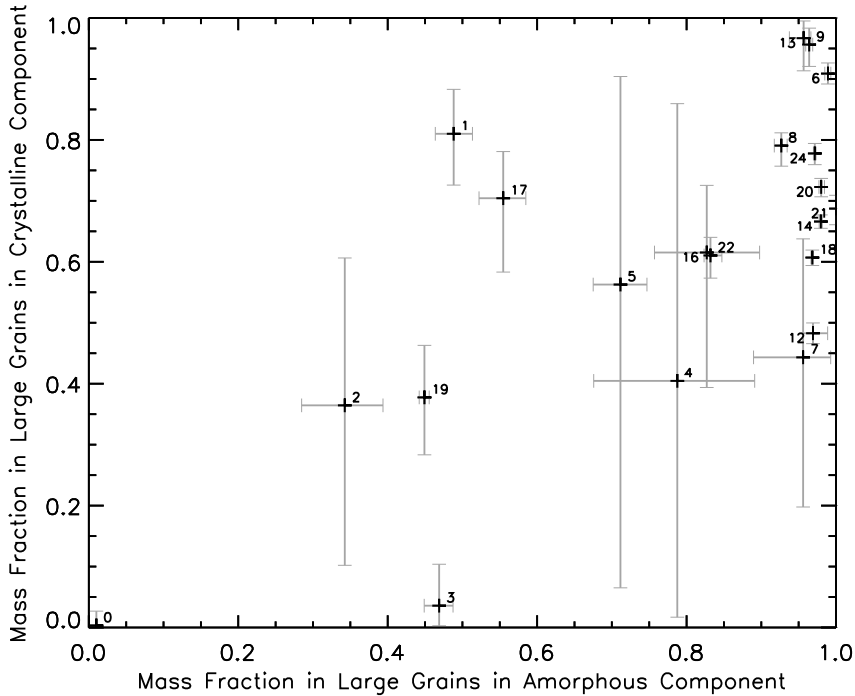


Figure 9.12: The mass fraction of large grains in the crystalline grain population vs. the mass fraction of large grains in the amorphous component. When the average size of the amorphous grains is large, the majority of the crystalline material resides in large grains as well.

In Fig. 9.11 we show the mass fraction of crystalline material contained in enstatite versus the total mass fraction of crystalline material. There is a correlation between the fraction of the total mass contained in crystalline silicates and the composition of these crystalline silicates. In general, for sources with a high degree of crystallinity most crystals are in the form of enstatite, while for the sources with a low crystallinity, forsterite is the dominant crystalline species. We will discuss this further in section 9.6.3.

The amount of growth that the crystalline material has experienced is compared to the growth in the amorphous component in Fig. 9.12. If the amorphous grains are large, also the crystalline grains are large, though the correlation is not tight. In all sources in which the amorphous component has more than 85% large grains, also the crystalline component is dominated by large grains. The sources that have less than 85% large grains in the amorphous component all have a low crystallinity (see Fig. 9.9). Therefore, the ratio of large and small crystals is poorly constrained in these sources, which is reflected in the large errorbars.

The fraction of crystalline silicates is correlated with the mass and luminosity of the central star. This is visualized in Fig. 9.13. The higher mass (higher luminosity) stars have an on average higher crystallinity than the lower mass (lower luminosity) stars.

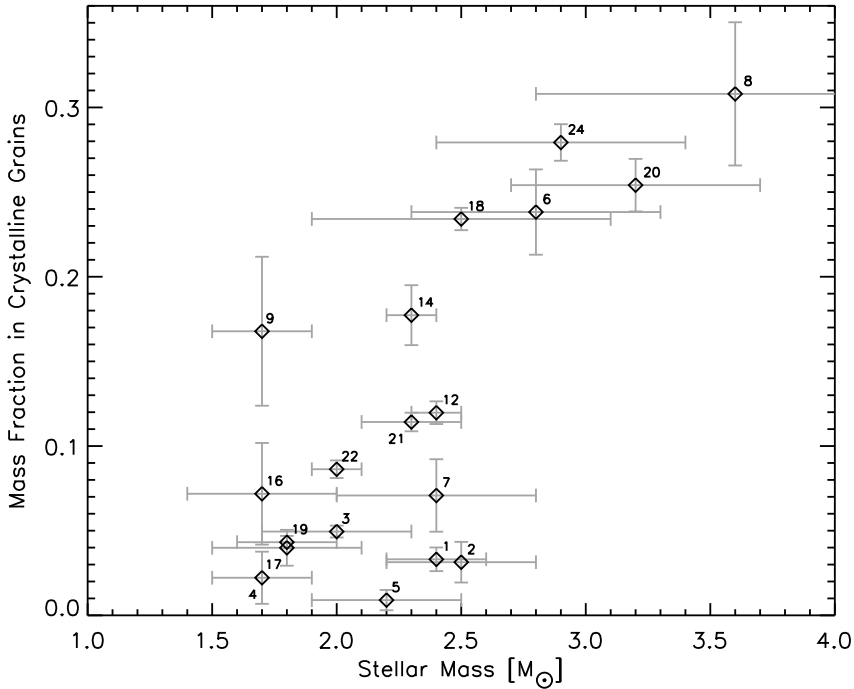


Figure 9.13: The mass fraction of dust in crystalline grains vs. the stellar mass. Higher mass stars show an on average higher fraction of crystalline grains than do lower mass stars.

This correlation will be discussed in section 9.6.3.

All stars with a stellar mass above about $2.5 M_{\odot}$ ($L > 60 L_{\odot}$) have a high fraction ($\geq 85\%$) of large grains (Fig. 9.14). Possibly, conditions in the disks around more massive stars are more favorable for growth than they are in the disks around lower mass stars. An alternative explanation for the observed trend is that the disks around the more massive stars, which are all relatively young (Fig. 9.2), are more turbulent than those around the less massive, older stars. As a consequence the mixing in the young disks will be more efficient. While in the older stars the large grains decouple from the gas and settle to the midplane (and therefore will not be detected in the 10 micron spectrum anymore), in the young stars, larger grains may still reach the disk surface and cause the observed average grain size to be higher.

9.6 Discussion

We now discuss our fit results in terms of the processes that are responsible for the dust evolution. We will first briefly outline the expected conditions that prevailed during the active disk phase (section 9.6.1), i.e. the phase prior to the passive disk phase. For

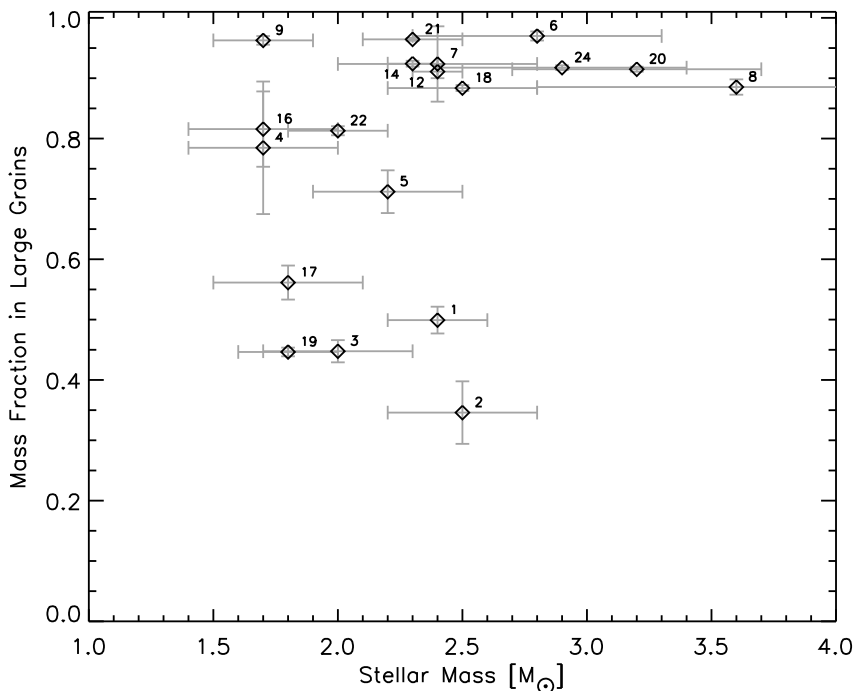


Figure 9.14: The mass fraction of dust residing in large grains vs. the stellar mass. All stars with a mass $M \gtrsim 2.5 M_{\odot}$ have a mass fraction of large grains above 85 %.

a comprehensive review of active disks, see e.g. Calvet et al. (2000). The disks of all stars in our sample are in the passive disk phase. The characteristics of this phase are discussed in section 9.6.2. In section 9.6.3 we summarize the constraints put on dust processing by this work and previous studies. Lastly, in section 9.6.4 we sketch a scenario that is consistent with the current knowledge of dust processing and disk evolution.

9.6.1 The active disk phase

The accretion of matter onto a forming proto-star is believed to be initially spherically symmetric. At some point, as the proto-star contracts, conservation of angular momentum inhibits further spherical accretion. The accretion process then proceeds through a disk, and is accompanied by a bi-polar outflow. The fact that material is radially transported through the disk implies that the disk has viscosity, which is in turn coupled to turbulence.

During this so-called *active disk phase*, gravitational energy of the accreting material is dissipated in the disk, thereby heating it. Accretion rates in the active phase may reach values up to $10^{-5} M_{\odot}\text{yr}^{-1}$ (Calvet et al. 2000). Close to the central star the main energy

source of the disk is accretion luminosity, whereas at larger radii irradiation by the star and hot inner disk regions is expected to be the main heating source of the disk material.

The dust in the disk consists mainly of silicates (studied in this work), and carbon. The dust does not contribute significantly to the disk mass in this phase of the disk evolution (the gas over dust ratio is on the order of 10^2 by mass). However, the thermal radiation emitted by the dust is the dominant cooling process in the disk. In the outer disk regions where the main energy source is irradiation, the dust governs the heating of the disk as well. Therefore, the dust properties determine the disk temperature, except in the innermost disk region where the heating is dominated by viscous dissipation of gravitational energy of the accreting material. The gas, heated by the dust, provides the pressure support of the disk.

The densities in the disk are high, especially near the disk mid-plane, and one may expect coagulation of small dust grains into larger aggregates to occur. Already after $\sim 10^4$ yr of dynamical disk evolution the average mass of a grain can increase by a factor 10^1 to 10^2 , and close to the disk midplane the grains may reach sizes of at least a few times $10\ \mu\text{m}$ up to millimeters (Suttner & Yorke 2001). Close to the central star the temperatures in the disk can reach values in excess of 1000 K. At this temperature the (initially mostly amorphous) silicates are annealed, to form crystalline silicates. Yet closer to the star, temperatures reach values of about 1500 K, and crystalline silicates may form by gas phase condensation of evaporated material.

In some of the stars in our sample, the crystalline silicates appear so prominent that it is unlikely that their emission arises from the innermost disk region only; the abundance of crystalline silicates must be high in a relatively large part of the region of the disk responsible for the $10\ \mu\text{m}$ emission (the innermost 10-20 AU of the disk). There are in essence two possible ways to get crystalline material at ~ 10 AU distance from the star: (1) thermal processing in the hot inner disk and subsequent radial transport of this material outward, and (2) local production of crystalline material at large distance from the star in transient heating events caused by shocks (e.g. Harker & Desch 2002) or lightning (e.g. Pilipp et al. 1998; Desch & Cuzzi 2000). During the active disk phase the accretion rate in the viscous disk is high and the disk will be turbulent. This is expected to enable radial mixing of material (Bockelée-Morvan et al. 2002; Gail 2004).

9.6.2 The passive disk phase

When the supply of fresh material from the maternal cloud has exhausted, further accretion onto the star proceeds only on a very low level (order $10^{-8}\ \text{M}_\odot\text{yr}^{-1}$). Under these conditions the energy production by viscous dissipation can be fully neglected. Throughout the disk the temperature of the material is determined by absorption of stellar radiation; this is referred to as the *passive disk phase*. The stars that we study are in this evolutionary phase. In the observed SEDs of sources in the passive disk phase, the infrared excess typically becomes noticeable above the photospheric emission at a wavelength of about $1\ \mu\text{m}$. The excess emission in the near-infrared indicates that the inner radius of the disk is determined by the evaporation temperature of silicates (at about 1500 K). At wavelengths longward of $2\ \mu\text{m}$ the infrared emission from a gas rich disk completely dominates the SED.

The formation of planets and planetesimals is thought to occur during the passive disk phase. As the disk dissipates on a timescale of 10^7 yr, the infrared excess fades. The inner disk regions become devoid of gas and dust first. When the system has evolved into the *debris disk phase* (e.g. β Pictoris, Aumann 1984; Smith & Terrile 1984) excess emission can be seen above the stellar photospheric emission only at wavelengths above $\sim 10\ \mu\text{m}$.

The era of crystallization

During the passive disk phase there is a region in the inner disk where the temperature is above 1000 K, and therefore the silicates will be crystallized. As there is no significant accretion luminosity, this region will be smaller than in the active disk phase. It is unclear whether the disk will be turbulent enough for significant radial mixing to take place during the passive phase. Also the proposed mechanisms for local production of crystalline silicates in the outer disk regions are more efficient in the active disk phase. Theoretically therefore, the active disk phase is the preferred era for the crystallization of the dust. Nonetheless it has, from an observational point of view, been suggested that the crystallinity of HAe disks gradually evolves from low to high values during the passive phase (Grady et al. 2000).

9.6.3 New constraints on dust processing

We first briefly repeat the results that follow directly from our spectral modeling:

1. All disks have already substantial removal of the smallest grains (in our fits represented by the $0.1\ \mu\text{m}$ grains). The mass fraction of large (in our fits $1.5\ \mu\text{m}$) grains ranges from about 35 to almost 100 percent.
2. The crystallinity ranges from about 5 to 30 percent. Disks with a high crystallinity are always dominated by large grains.
3. Vice versa, disks with more than 85 percent large grains show a crystallinity above 10 percent; disks with less than 85 percent large grains show a crystallinity below 10 percent.
4. Large crystals are found when large amorphous grains are abundant. We do not find disks in which the bulk of the grains is large, and the crystalline silicates are small.
5. In disks with a crystallinity below 15 percent, more than 45 percent of the crystalline silicates consist of forsterite. Above 15 percent crystallinity, more than 45 percent of the crystalline silicates consist of enstatite.

When the stellar parameters of our sample stars (see Table 9.1) are taken into account, several additional conclusions can be drawn:

6. The disks with the highest degree of crystalline material (between 20 and 30 percent) all belong to stars with a mass above $2.5\ M_{\odot}$, and a luminosity above $60\ L_{\odot}$.

7. Below a crystallinity of 20 percent, there does not appear to be a correlation between stellar parameters (mass, luminosity, age) and crystallinity. Separate studies of the 10 micron spectra of T Tauri stars (Przygodda et al. 2003; Honda, private communication) indicate that the crystallinities of T Tauri star disks are similar to those observed in the disks of those H Ae stars in our sample that have $M \lesssim 2.5 M_{\odot}$ (i.e. $\lesssim 10$ percent). We note that a small subset of the T Tauri star disks shows a significantly higher crystallinity, deviating from the general trend (Honda et al. 2003).
8. The stars in our sample with masses below $2.5 M_{\odot}$ have ages ranging from 2×10^6 to $\sim 10^7$ yr (see Fig. 9.2). If we consider only this subgroup, we find no relation between the stellar age and the disk crystallinity.
9. The stars that lack a 10 micron silicate emission band (HD 97048, HD 100453, HD 135344 and HD 169142) tend to be old, with ages of 5-10 Myr.

A number of previous studies have been concerned with the crystalline silicates in H Ae star disks. Here we briefly recall some of the results that are of relevance for this study:

10. Recent observations using the $10 \mu\text{m}$ instrument MIDI (Leinert et al. 2003) on the VLT Interferometer (Glindemann et al. 2003) have enabled the extraction of the spectra of the innermost ~ 2 AU of three H Ae stars (van Boekel et al. 2004a), showing that:
 - HD 144432 has virtually all its crystals in the inner 2 AU.
 - HD 163296 has a flatter crystallinity "gradient" and has a higher overall crystallinity than HD 144432.
 - HD 142527 has the highest crystallinity of the three stars studied, virtually the entire inner disk is crystallized. Also at radii larger than 2 AU, the abundance of crystalline silicates is relatively high.
 - The innermost regions of the disks have experienced more grain growth than the outer disk regions. Small grains are mostly found at larger distance from these stars.
11. ISO observations of HD 179218 and HD 100546 show the presence of cold (100-150 K) crystalline silicates. This implies a substantial crystallinity even at distances between 20 and 40-50 AU (Malfait et al. 1998b; Bouwman et al. 2001, ME01).
12. A $33.5 \mu\text{m}$ forsterite band is tentatively detected in the ISO spectrum of HD 100453 (Vandenbussche et al. 2004).

We will now discuss the implications of the points mentioned above. For clarity, we have labeled each of the implications with the index number(s) of the point(s) that lead to it.

- 1, 2, 3:** The dust in the circumstellar disks coagulates more easily than it crystallizes. This is likely due to the fact that the circumstances enabling grain growth (i.e. high densities) prevail in a much larger part of the disk than the circumstances needed for crystallization of silicates (i.e. high temperatures). Once a certain level of coagulation is reached, crystallinity becomes a lot more obvious in the upper layers of the disk.
- 4:** This observation is consistent with crystallization occurring as the grains grow: whatever population of grains is present, is crystallized. Most of the crystallization occurs when the average grain size is already large (micron sized).
- 1, 2, 3, 10, 12:** Coagulation is more efficient in the inner disk regions than in the outer disk regions. In the sources that lack a silicate band coagulation must have proceeded furthest. Our relation between grain growth and crystallization (Fig. 9.9) then implies that these disks must have a substantial fraction of crystalline silicates, certainly above 10 percent and perhaps more than 20 percent. However, we do not find the usual forsterite band at $11.3\ \mu\text{m}$ nor the $23.5\ \mu\text{m}$ forsterite band. So, also the crystalline silicates must on average be large. Indeed this is what was concluded for HD 100453 (Vandenbussche et al. 2004). Again, it seems that whatever (inner disk) grain population is present, is crystallized.
- 4:** Micron sized crystalline grains are present in the disks. It is hard to produce crystalline grains of these sizes via shock heating. At any rate, our data put severe limits on the efficiency of shock heating, as the shock mechanism must be able to produce sufficiently strong shocks to crystallize micron sized grains.
- 5:** If we consider two possible sources of crystalline silicates, i.e. chemical equilibrium reactions (gas phase condensation and subsequent gas-solid reactions) and thermal annealing, then we can note the following (Gail 2004):
- Enstatite is expected to be the dominant crystalline species formed by chemical equilibrium processes in most of the inner disk, apart from the hottest, innermost region, which is dominated by forsterite.
 - Since most likely amorphous olivine is the most abundant species entering the disk from the ISM, forsterite (or better, crystalline olivine) is expected to be the dominant crystalline species formed by thermal annealing.

In disks with a low crystallinity, forsterite is the dominant crystalline species, suggesting that this material is formed by thermal annealing. The high abundance of enstatite observed in the highly crystalline disks indicates that the production of crystalline material has occurred by means of chemical equilibrium processes in these sources.

- 1, 2, 3, 4, 10:** The TIMMI2 and MIDI data taken together are consistent with crystallization starting in the innermost regions. Disks with a high crystallinity in the TIMMI2 data have a substantial fraction of crystalline grains in the 5-10 AU area (or even in the 20-50 AU region, see e.g. the ISO spectra of HD 100546,

HD 179218 (Malfait et al. 1998b; Bouwman et al. 2001)), i.e. well outside the regions where thermal annealing and chemical equilibrium processes are expected to be effective.

- 5, 11:** HD 179218 has a high abundance of cold enstatite. In the context of the above reasoning, this enstatite must have been produced either locally in transient heating events, or transported outward from the inner disk to observable cold disk regions. If chemical equilibrium processes are an important means of producing enstatite, the HD 179218 data point to enstatite production in the inner regions and transport to larger distance by radial mixing.
- 6:** Crystallization is more efficient in disks around higher mass, higher luminosity stars. Several possible explanations for this trend can be identified:
1. during the active phase, the region in which the disk material is sufficiently hot for thermal annealing (and chemical equilibrium processes) to occur is larger in high mass stars, since the energy dissipated in the disk per unit mass accreted material is higher. If this is the dominant effect, our results favor crystallization in the active phase.
 2. during the passive phase, when the extent of the region where annealing (and chemical equilibrium processes) can occur is set by irradiation from the central star, the higher luminosity of the more massive stars causes this region to be larger than in the low mass stars. If this is the dominant effect, our results favor crystallization in the passive phase.
 3. the disks around more massive, more luminous stars may be more turbulent, both during the active and passive phase. The outward mixing of processed material will then be more efficient in the high mass stars, causing a more prominent appearance of this dust in the spectrum.

It is currently unclear which of the above effects is dominant. The study of young ($\tau < 10^6$ yr), low mass stars may allow to answer this question.

- 8:** This observation suggests that whatever caused the observed range of crystallinities in stars with a mass below about $2.5 M_{\odot}$, occurred before 2×10^6 yr. This puts the epoch of crystallization in the active and/or early passive phase.

9.6.4 Global picture that emerges

The $10 \mu\text{m}$ emission is emitted by the surface layer of the disk at radii below 20 AU from the central star. In the midplane of this region (and presumably even at larger radii), dust coagulation takes place. Vertical mixing ensures that the coagulated, micron-sized grains reach the disk surface layer and become apparent in the spectrum. Growth is most efficient in the innermost disk regions where the densities are highest. Crystallization by

means of thermal annealing and chemical equilibrium processes occurs in the hot innermost disk region. In many disks there are significant amounts of crystalline material at larger ($\gtrsim 5$ AU) distances from the star, where thermal annealing and chemical equilibrium processes are ineffective. The combined evidence presented in section 9.6.3 seems to favor radial transport from the innermost disk regions as the source of these crystals, above local production mechanisms (e.g. shock annealing).

Crystallization is most efficient in the disks surrounding the more massive, more luminous stars ($M \gtrsim 2.5 M_{\odot}$, $L \gtrsim 60 L_{\odot}$). In these disks, the region in which thermal annealing and chemical equilibrium processes can produce crystalline silicates is larger than in the disks surrounding lower mass stars. Additionally, the disks around the more massive stars may be more turbulent, enabling more efficient radial mixing. It is unclear whether the crystallization of the dust in the disks occurs predominantly in the active disk phase, or in the passive phase that follows. Our data do suggest that the disks reach their final crystallinity relatively early in the passive phase ($\tau \lesssim 2$ Myr). Therefore, crystallization happens during the active and/or early passive phase.

9.7 Conclusions

We have undertaken a large spectroscopic survey of Herbig Ae stars in the $10\mu\text{m}$ atmospheric window, and have presented new spectra of 23 stars. The correlation between the shape and the strength of the $10\mu\text{m}$ silicate emission band reported by van Boekel et al. (2003) is reconfirmed with a larger sample. We have performed compositional fits to the silicate feature using opacities of minerals commonly found in circumstellar disks (amorphous olivine and pyroxene, crystalline olivine and pyroxene, and amorphous silica) and polycyclic aromatic hydrocarbons. For all minerals we have allowed both “small” ($0.1\mu\text{m}$) and “large” ($1.5\mu\text{m}$) grains in order to study the effects of grain growth. This set of materials is sufficient to reproduce the wide variety of observed spectral shapes.

We find a trend between the mass fraction in large grains and the mass fraction in crystalline grains: *all sources with a high crystallinity have a high mass fraction in large grains*. There are no highly crystalline sources which are dominated by small grains. Most sources have a mass fraction in large grains of more than 80 percent.

We note that there is an important bias in our sample (and probably in most samples of Herbig stars studied in the literature): the more massive sample stars ($\sim 3 M_{\odot}$, “high mass”) are younger than the less massive ($\lesssim 2.5 M_{\odot}$, “low mass”) stars. There are no low mass stars younger than 1 Myr in our sample. In order to establish the disk conditions at the end of the active disk phase, which precedes the passive phase, it is essential that such very young, low mass stars are found and studied. Since these stars may still be enshrouded in circumstellar material, they may have to be selected using infrared data.

We find a trend between the derived crystallinity of the dust and the mass (and luminosity) of the central star: the disks around stars with a mass larger than $2.5 M_{\odot}$ (a luminosity above $60 L_{\odot}$) have a higher crystallinity ($\gtrsim 20\%$) than the less massive, less luminous stars. Within the subset of sources with a stellar mass below $2.5 M_{\odot}$, no correlation between crystallinity and stellar parameters (mass, luminosity, age) is seen. These

lower mass stars in our sample are all older than ~ 2 Myr. Since in this subset there is no correlation between age and crystallinity, we conclude that the crystallization of the material predominantly happens in the active or early passive disk phase (before 2 Myr).

The evidence presented in this paper combined with conclusions from other studies seems to favor a scenario in which crystalline silicates are produced in the innermost regions of the disk and transported outwards. Spatially resolved spectra of these disks, as can be obtained using for example the MIDI instrument on the Very Large Telescope Interferometer, will provide crucial information on the radial dependence of the mineralogy of the dust in these disks. In addition, measurements at longer wavelengths can probe colder regions (further out) in the disk which can provide further constraints on the temperature structure and spatial distribution of the dust.

Acknowledgments

This research has made use of the SIMBAD database, operated at CDS, Strasbourg, France. We gratefully acknowledge J. W. Hovenier for thorough reading and valuable comments on an earlier version of the manuscript.

10

The building blocks of planets in the ‘terrestrial’ region of protoplanetary disks

*R. van Boekel, M. Min, Ch. Leinert, L. B. F. M. Waters, A. Richichi, O. Chesneau, W. Jaffe, C. Dominik, A. Dutrey, U. Graser, Th. Henning, J. de Jong, R. Köhler, A. de Koter, B. Lopez, F. Malbet, S. Morel, F. Paresce, G. Perrin, Th. Preibisch, F. Przygodda, M. Schöller, and M. Wittkowski
Nature, v.432, p.479-482 (2004)*

Abstract

Our solar system was formed from an interstellar cloud of gas and dust. Most of the interstellar dust mass is contained in amorphous silicates (Kemper et al. 2004). In contrast, crystalline silicates are abundant throughout the solar system, reflecting thermal and chemical alteration of solids during planet formation. Even primitive bodies such as comets contain crystalline silicates (Hanner et al. 1994). Little is known about the nature of the dust that served to form Earth-like planets. Infrared spectroscopy of vibrational resonances in the lattice of small dust particles provides information about dust properties, such as chemical composition, size and shape. Here we report the first spatially resolved detection and compositional analysis of these building blocks in the innermost two astronomical units of three protoplanetary disks. We find the dust in these regions to be highly crystallized, more than any other dust observed in young stars to date. In addition, the outer region of one star has equal amounts of pyroxene and olivine while the inner regions are dominated by olivine. The spectral shape of the inner disk spectra shows surprising similarity with solar system comets. Radial mixing models naturally explain this resemblance as well as the gradient in chemical composition. Our observations imply that silicates crystallize before any terrestrial planets are formed, consistent with the composition of meteorites in the solar system.

Most young stars are surrounded by a disk of gas and dust which is a remnant of the star formation process. This disk is formed due to conservation of angular momentum in the collapsing proto-stellar cloud, and channels material from the cloud to the protostar. When the material in the surrounding molecular cloud is exhausted, the disk dissipates within approximately 10^7 years (Haisch et al. 2001). Planet formation is believed to result from the growth of sub-micron sized interstellar dust particles (Beckwith et al. 2000). Therefore, changes in size but also in the chemical nature of the dust grains

Star	Crystallinity [%]		Fraction large grains [%]		Crystalline olivine to pyroxene ratio	
	Inner D.	Outer D.	Inner D.	Outer D.	Inner D.	Outer D.
HD 163296	40 ⁺²⁰ ₋₂₀	15 ⁺¹⁰ ₋₁₀	95 ⁺⁵ ₋₁₀	65 ⁺²⁰ ₋₂₀	2.3 ^{+3.7} _{-0.5}	-
HD 144432	55 ⁺³⁰ ₋₂₀	10 ⁺¹⁰ ₋₅	90 ⁺¹⁰ ₋₁₀	35 ⁺²⁰ ₋₂₀	2.0 ^{+1.8} _{-0.6}	-
HD 142527	95 ⁺⁵ ₋₁₅	40 ⁺²⁰ ₋₁₅	65 ⁺¹⁵ ₋₁₀	80 ⁺¹⁰ ₋₃₀	2.1 ^{+1.3} _{-0.7}	0.9 ^{+0.2} _{-0.1}

Table 10.1: The fractional abundances of large and crystalline grains as well as the ratio of crystalline olivine to pyroxene in the inner (1-2 AU) and outer (2-20 AU) disk regions of three Herbig Ae stars. The dust components used in the model spectra are amorphous and crystalline olivine ($Mg_{2x}Fe_{2-2x}SiO_4$), amorphous and crystalline pyroxene ($Mg_xFe_{1-x}SiO_3$), and amorphous silica (SiO_2). For the crystalline components we used the magnesium rich silicates ($x = 1$) and for the amorphous components we used $x = 0.5$. The crystallinity is defined as the percentage of the total dust mass contributing to the 10 micron feature, contained in crystalline olivine and pyroxene. Since the signature of crystalline silicates in the outer disk spectra of HD 163296 and HD 144432 is not very clear, the ratio of crystalline olivine over pyroxene in these spectra is not very well determined. Especially the abundance of crystalline pyroxene in these spectra is poorly constrained. All dust species are considered with two different grain sizes, $0.1 \mu m$ (small grains) and $1.5 \mu m$ (large grains). temperature. Since we are looking at a coagulating environment where the various dust species are expected to be in thermal contact, we assume that all components have the same temperature.

The opacities of the dust species are calculated from refractive indices obtained by laboratory measurements by Dorschner et al. (1995); Servoin & Piriou (1973); Jäger et al. (1998); Spitzer & Kleinman (1960), using the method of Min et al. (2003b). The abundances of the various dust species are determined using a linear least squares fitting procedure assuming the dust emission comes from an optically thin part of the disk. The errors on the fit parameters include both uncertainties in the data and in the modeling method, and are 1σ . As the dominant part of the error budget is due to systematic uncertainties that are the same in the inner and outer disk spectra, the relative difference between the two is much more significant than the error bars suggest. For details on the fitting procedure and the error analysis we refer to supplementary information provided at the end of this chapter.

in the nebular disk environment trace the first steps in planet formation. For instance, crystalline silicates are formed as a result of thermal annealing of amorphous grains, or by vaporisation and subsequent gas-phase condensation in the innermost disk regions. These are referred to as *primary processes*. After inclusion of dust in larger parent bodies such as asteroids and planets, so-called *secondary processing* occurs, which includes oxidation, aqueous alteration and thermal metamorphism. Asteroids and comets contain pristine interstellar dust as well as dust which has seen substantial processing (Bradley 2003). The reconstruction of the formation history of our solar system depends on a better understanding of the nature of primary and secondary processes, and when and where they occurred in the proto-solar nebula.

We observed three Herbig Ae stars with the Mid-Infrared Interferometric Instrument MIDI (Leinert et al. 2003) installed at the Very Large Telescope Interferometer (VLTI).

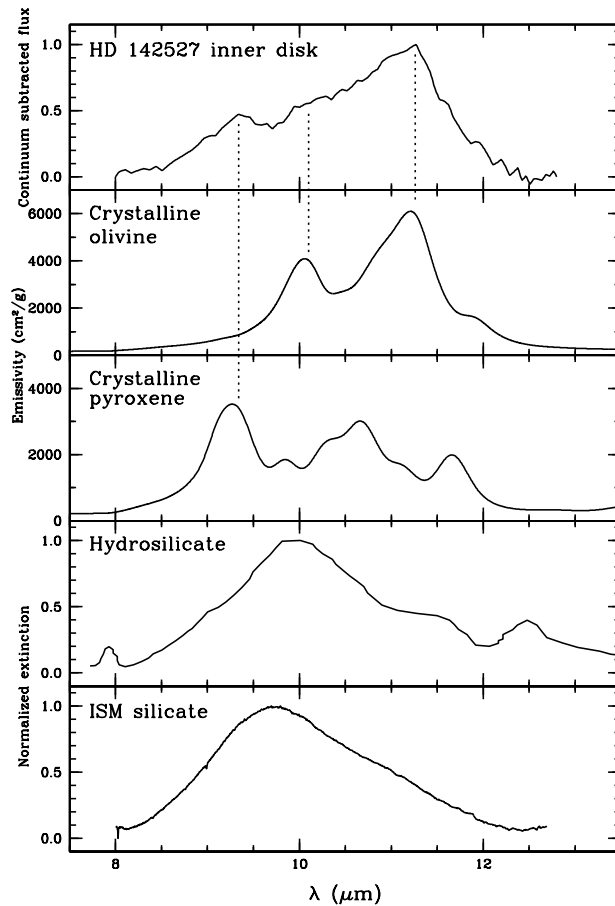


Figure 10.1: The spectrum of the innermost disk regions of HD 142527 compared to spectra of typical dust species. From top to bottom we plot the observed inner disk spectrum of HD 142527, the laboratory spectra of crystalline olivine and pyroxene (Chihara et al. 2001), a laboratory spectrum of an IDP consisting of hydrated silicates (Sandford & Walker 1985), and the interstellar medium silicate spectrum (Kemper et al. 2004). The resolution of the laboratory data is reduced to that of the interferometric spectrum. The main resonances of crystalline pyroxene at 9.2 micron and crystalline olivine at 11.3 micron are clearly seen in the HD 142527 spectrum. We can exclude that there is a significant contribution of hydrated silicates to the spectrum in the inner disk regions of HD 142527, suggesting that we see primary, rather than secondary dust.

The light from two 8.2 meter Unit Telescopes separated by 103 meters on the ground was combined, providing a spatial resolution of about 20 milli-arcseconds. This corresponds to ~ 1 -2 Astronomical Units (AU) at the distance of the observed stars; an improvement of more than a factor of 10 in spatial resolution compared to the largest modern day telescopes, in this wavelength regime. The MIDI instrument measures spectrally dispersed

visibilities with $\lambda/\Delta\lambda = 30$ in the 7.5 to 13.5 μm atmospheric window. Since the intensity distribution of circumstellar disks is strongly centrally peaked (Eisner et al. 2003; Leinert et al. 2004), the correlated spectra measured by the interferometer are dominated by the inner 1-2 AU of the disks. We refer to these as the *inner disk spectra*. In addition, spectra were obtained with a single 8.2 meter telescope, in which the objects are spatially unresolved (Leinert et al. 2004). We refer to these spectra as the *total disk spectra*. The difference between the total and the inner disk spectra arises mainly from a region between approximately 2 and 20 AU. We will refer to these spectra as the *outer disk spectra*.

In Fig. 10.1 we show the inner disk spectrum of HD 142527. The spectrum is clearly dominated by crystalline olivine and pyroxene. These minerals are also the most common ones in solar system objects. No contribution from amorphous silicates is evident. As shown below, the spectrum is in fact consistent with 100 percent crystalline material, making it the most crystalline dust ever observed in young stars (Molster & Waters 2003). Clearly, the mechanism responsible for crystallization must be highly efficient. Fig. 10.2 shows the inner and outer disk spectra for all three stars. We have fitted the observations using laboratory measurements of materials which are the dominant species found in circumstellar disks (Bouwman et al. 2001) and interplanetary dust particles (Bradley 2003). The derived mass fraction of crystalline silicates, the olivine over pyroxene ratio in the inner and outer disk spectra, as well as the fraction of material that resides in large grains, are listed in Table 1.

Both in the solar system and in circumstellar disks crystalline silicates are found at large distances from the star. The origin of these silicates is a matter of debate. While in the hot inner disk regions crystalline silicates can be produced by means of gas phase condensation or thermal annealing, the typical grain temperatures in the outer (2-20 AU) disk regions are far below the glass temperature of silicates of ~ 1000 K. The crystals in these regions may have been transported outward through the disk (Gail 2004) or in an outward flowing wind (Nuth et al. 2002). An alternative source of crystalline silicates in the outer disk regions is *in situ* annealing by e.g. shocks (Harker & Desch 2002) or lightning (Pilipp et al. 1998; Desch & Cuzzi 2000). A third way to produce crystalline silicates is the collisional destruction of large parent bodies in which secondary processing has taken place. We can use the mineralogy of the dust to derive information about the nature of the primary and/or secondary processes the small grain population has undergone.

Models of disks accounting for the chemical equilibrium of a solid-gas mixture at high temperatures as well as the radial mixing of material (Gail 2004) predict that the innermost disk region consists entirely of forsterite (the Mg-rich end member of the olivine family). At slightly lower temperatures, a reaction with gas-phase silicon efficiently converts this to enstatite (the Mg-rich end member of the pyroxene family). At larger distance from the star, the predicted crystalline olivine over pyroxene ratio reaches about 0.5. Our observations qualitatively confirm these predictions. The inner disk spectrum of HD 142527 puts the strongest constraints since it is the most processed one in our data. Assuming equal temperatures for all dust species, we find that the ratio of olivine to pyroxene in the inner disk spectrum is 2.1, while it is 0.9 in the outer disk spectrum.

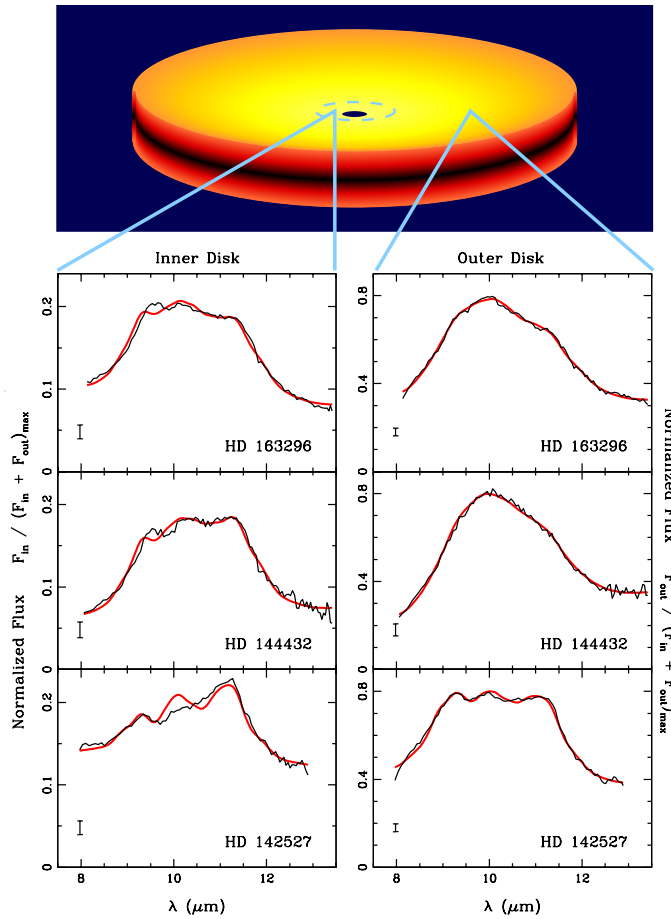


Figure 10.2: Infrared spectra of the inner (1-2 AU) and outer (2-20 AU) disk regions of three Herbig Ae stars. The outer disk spectrum of each source has been constructed by subtracting the correlated spectrum from the total disk spectrum (presented in Leinert et al. (2004)). The regions that dominate the inner and outer disk spectra are indicated in the schematic representation of a protoplanetary disk at the top of the figure (not to scale). The flux levels are scaled such that the sum of the inner and outer disk spectrum, i.e. the total disk spectrum, is normalized to unity. This allows the relative contributions of the inner and outer disk to the total spectrum to be easily estimated from this figure. The uncertainties in the spectra are indicated by the error bars in the lower left corner of each graph. The differences in shape between the inner and outer disk spectra are clearly visible in all three sources, indicating a difference in dust mineralogy. The broadening of the feature as seen in the inner disk spectra indicates grain growth, while the resonance at $11.3 \mu\text{m}$ indicates the presence of crystalline silicates (see also Fig. 10.1). Also shown are the best fit model spectra for the inner and outer disk regions (grey lines, see also Table 10.1). The model spectra reproduce the observed spectral shapes, though the fits to the inner disk spectra are of somewhat lesser quality than the fits to the outer disk spectra.

This is the first direct measurement of a gradient in the chemical composition of the dust in protoplanetary disks. The measured gradient is smaller than predicted by radial mixing models. This could be due to non-equilibrium chemistry, or due to the assumed stoichiometry in the amorphous silicates prior to annealing.

For all three stars the inner disk regions have a substantially higher degree of crystallinity than the outer regions. However, these outer regions show a crystalline silicate abundance that clearly exceeds limits derived for the interstellar medium (Kemper et al. 2004). Therefore, these crystalline silicates have to be produced in the disk. It is not clear that the local processes that have been proposed to produce these crystals can account for the observed degree of crystallinity. Models for radial mixing of protoplanetary disks (Gail 2004) can produce a crystalline fraction of several tens of percent at distances of 5-10 AU (which is the relevant scale for our observations) provided that a reservoir of crystalline material is present in the innermost disk regions. Our data prove that this reservoir exists.

Secondary processing of dust in large parent bodies produces hydrous silicates by means of aqueous alteration. Studies of meteorites have shown that the fine-grained matrix material of chondrites often consists of hydrous silicates (Brearley & Jones 1998). However, we can exclude the possibility that the grains in our sources are predominantly hydrosilicates, since these show a fairly sharp peak near 10 μm , as seen in Interplanetary Dust Particles (IDPs) rich in hydrosilicates (Sandford & Walker 1985). We conclude that aqueous alteration, followed by parent body destruction, has not yet resulted in the production of a large abundance of small hydrosilicate grains in HD 142527. Therefore, parent body processing can be excluded as the main source of crystalline silicates.

Fig. 10.3 shows a remarkable similarity between the inner disk spectra of our objects and those of solar system comets, suggesting that also the composition of the dust is comparable. Therefore, the building blocks of comets in our solar system have been processed in a similar way and to the same degree as in the inner disks of our programme stars. This is surprising since comets formed in the icy regions of the solar nebula, beyond 5 AU distance from the sun. Cometary crystalline silicates are Mg-rich (Crovisier et al. 1997). Chemical equilibrium models indeed predict the formation of Mg-rich crystalline silicates at very high temperatures (Gail 2004). Measurements of the composition of crystalline silicates that form in the outflows of red giants (Molster et al. 2002b) support such chemical models. In addition, crystalline silicates found in fluffy, chondritic IDPs have a whisker or platelet morphology and internal crystallographic defects, indicative of gas-phase condensation (Bradley 2003). This latter process is unlikely to occur in the outer regions of protoplanetary disks, but is expected to be important in the innermost regions. The most natural explanation for the presence of these materials in comets therefore seems to be transport by radial mixing from the rich reservoir of processed, Mg-rich crystalline silicate grains in the inner disk. Furthermore, radial mixing models can account for the presence of cold crystalline silicates in the outer (> 20 AU) regions of some protoplanetary disks (Malfait et al. 1998b; Bouwman et al. 2001) as well as the occurrence of large (10-20 μm) FeS crystals in IDPs of cometary origin (Bradley 2003).

It has been suggested that the degree of crystallinity of protoplanetary disks slowly

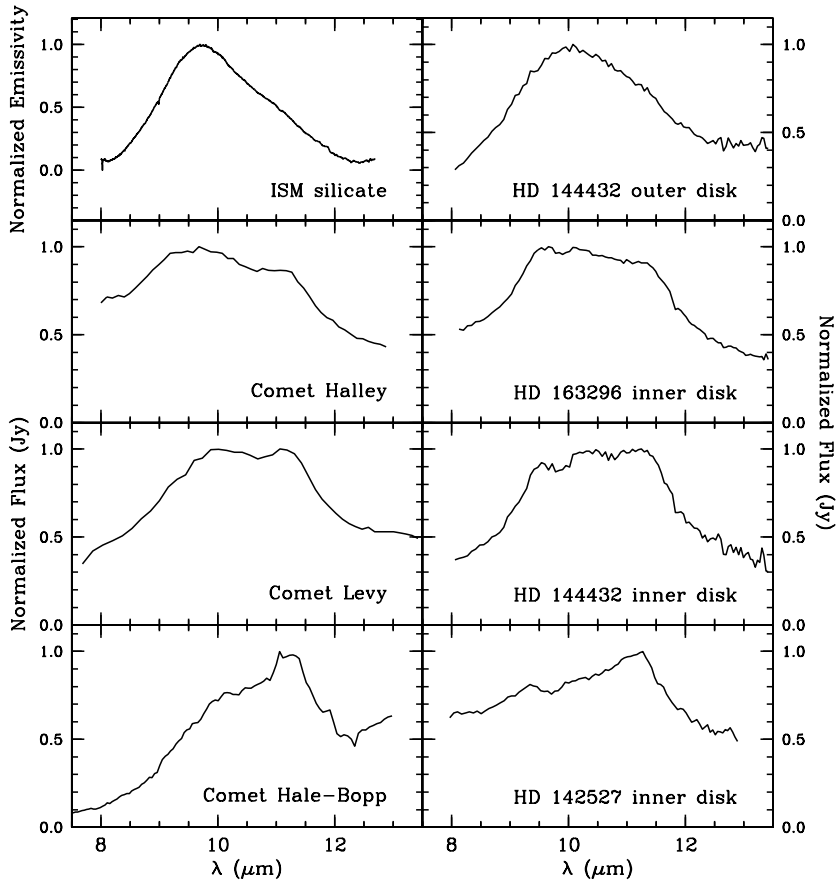


Figure 10.3: A comparison between the spectral shapes of various astronomical objects (left column) with those of the inner and outer disk regions of our three Herbig Ae stars (right column). In the first row, we compare the silicate feature of the interstellar medium (ISM, Kemper et al. 2004) with the outer disk spectrum of HD 144432. The silicate grains in the ISM are small ($<0.1 \mu\text{m}$) and amorphous. This results in a spectrum that has a typical triangular shape, peaking at $9.7 \mu\text{m}$. The outer disk spectrum of HD 144432 is very similar, although a very weak shoulder at $11.3 \mu\text{m}$ can be seen, indicating the presence of small amounts of processed material. In the second through last row, we compare the inner disk spectra of our three Herbig stars with three solar system comets (Hanner et al. 1994; Crovisier et al. 1997). The shapes of these spectra are very different from that of the ISM, indicating a higher degree of crystallinity, and on average larger dust grains. Grain growth makes the silicate emission band broader. Crystalline silicates have several bands in the 8–13 micron spectral region, the strongest of which is at $11.3 \mu\text{m}$. Modest crystallinity causes the the silicate feature to have rather sharp shoulders around 9.5 and $11.5 \mu\text{m}$, in highly crystalline sources the crystalline silicates show prominent peaks (see Hale-Bopp and HD 142527). The spectra are shown here in order of increasing crystallinity from top to bottom.

increases with time after the accretion of matter on the star has stopped (Grady et al. 2000). This evidence is based on the lack of crystalline silicates in infrared spectra of embedded young stars in the active phase, which are still accreting gas and dust from an interstellar cloud (Acke & van den Ancker 2004). In contrast, passive protoplanetary disks around optically visible stars that are no longer accreting matter can show strong crystalline silicate emission (Malfait et al. 1998b). The star with the highest degree of crystalline silicates in our sample, HD 142527, is also the youngest one, with an age of approximately 1 Myr (van den Ancker, private communication). Our observations thus imply that crystallization of almost the entire inner disk and a substantial part of the outer disk must have occurred very early in the evolution of the disk. Since dust processing - both radial mixing and shock processing - is more efficient during the active disk phase, our observations provide strong evidence that crystallization occurred in the active disk phase. The formation of the planets and asteroids in the inner solar system is believed to have occurred on a much longer timescale (Wetherill 1990), during the passive disk phase. Therefore, our observations indicate that, as was the case in the early solar system (Brearley & Jones 1998), the silicate dust in the inner regions of protoplanetary disks is highly crystalline before planet formation occurs.

Acknowledgments

Based on observations obtained at the European Southern Observatory (ESO), Chile. The authors would like to thank all those involved in building VLTI and MIDI. We thank V. Icke for providing the illustration shown in Fig. 10.2. C. P. Dullemond is acknowledged for many interesting discussions.

Supplementary material of chapter 10

Fitting procedure

We have modeled the 10 micron emission from small silicate dust particles using calculated emissivities of irregularly shaped, chemically homogeneous dust grains. We use a statistical approach, i.e. we simulate the optical properties of irregularly shaped particles by those of a shape distribution of particles with various simple shapes. We use a distribution of hollow spheres which successfully reproduces laboratory measurements of absorption spectra of small particles (Min et al. 2003b). Note that it is *not* assumed that the particles actually are hollow spheres. Rather, a *distribution* of hollow spheres with *varying inner hole size* can be used as a calculation method to derive the optical properties of irregular grains. The dust materials included are amorphous and crystalline olivine ($\text{Mg}_{2x}\text{Fe}_{2-2x}\text{SiO}_4$), amorphous and crystalline pyroxene ($\text{Mg}_x\text{Fe}_{1-x}\text{SiO}_3$), and amorphous silica (SiO_2). Here x determines the Mg/Fe ratio. In the 10 micron region at the spectral resolution that we have, the spectra are not very sensitive to the iron over magnesium ratio. We use the magnesium end members ($x = 1$) for the crystalline silicates and for the amorphous material we adopt $x = 0.5$. The dust components we consider are the most important ones that give rise to spectral signature in the 10 micron region. We also add a continuum contribution which accounts for the large grain component and for the featureless dust components such as amorphous carbon and metallic iron. In order to fit the data we make the following assumptions:

1. The emissivity of dust is represented by the emissivities of only two particle sizes, with a volume equivalent radius of $0.1\ \mu\text{m}$ (“small”) and $1.5\ \mu\text{m}$ (“large”). We have extensively tested that indeed we can describe the size distribution of the grains with this minimum number of free parameters. Silicate particles smaller than 0.1 micron are spectroscopically identical to 0.1 micron grains (i.e. they have the same mass absorption coefficients, such that the total derived dust mass does not depend on the size of the grains). Grains that are larger than a few microns quickly lose their emission band at $10\ \mu\text{m}$. The spectra of intermediate grain sizes can be reproduced by a linear combination of our small and large grains. We found that a “large” grain size of $1.5\ \mu\text{m}$ is the optimum value, i.e. it gives the best fits of the spectra at the spectral resolution of our data (even slightly better than a $2.0\ \mu\text{m}$ grain used by Bouwman et al. 2001).
2. The thermal radiation we analyze comes from the optically thin part of the disk, which allows us to add the contributions from the various components linearly.
3. Since we observe a relatively small wavelength range we represent the continuum emission by a single temperature blackbody. All dust components have the same single temperature. This is justified because it is very likely that the dust grains have coagulated, implying thermal contact between the various dust components.

The emissivities of the various dust components for the two sizes are plotted in Fig. 10.4. The abundances of the dust components are determined by using a linear

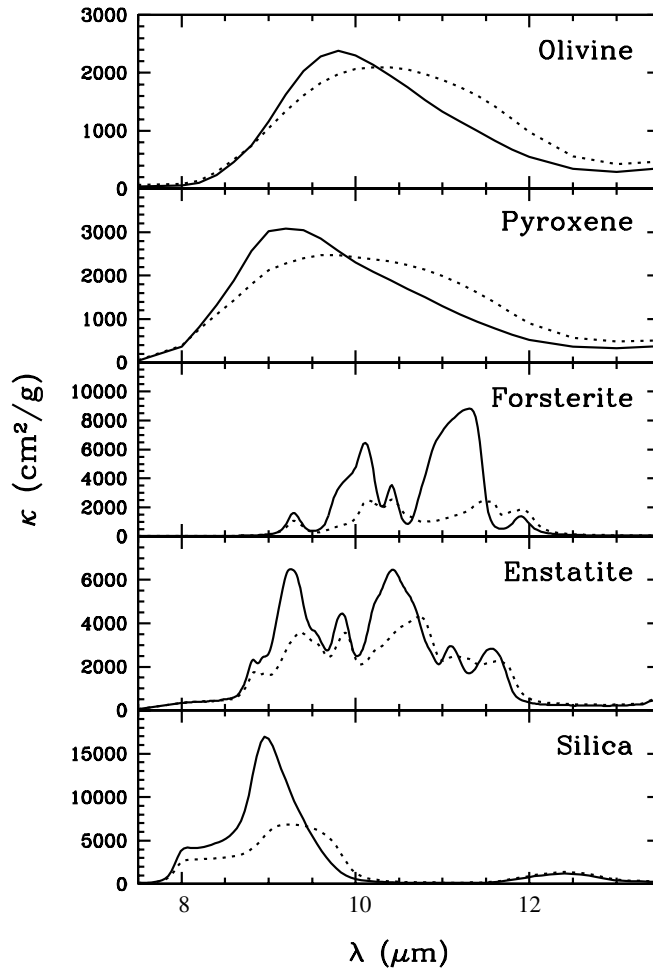


Figure 10.4: The emissivities of the various dust components and particle sizes used in the fitting procedure. The solid lines are for $0.1 \mu\text{m}$ grains, the dotted lines for $1.5 \mu\text{m}$ grains. The opacities of the dust species are calculated from refractive indices obtained by laboratory measurements by Dorschner et al. (1995); Servoin & Piriou (1973); Jäger et al. (1998); Spitzer & Kleinman (1960).

least square fitting procedure. The temperature of the grains is varied until a best fit is obtained.

The emission in the 10 micron region is dominated by small ($< 3 \mu\text{m}$), warm dust grains. Therefore, the derived abundances using the method described above are for this dust population.

Error analysis

The following sources of errors can be identified: (1) statistical noise in the spectra, (2) systematic errors in the data, and (3) errors in the model calculations.

1. *Statistical noise on the spectra.*

The spectra are obtained with high signal to noise ratios, so the statistical noise will contribute a minor part to the total error budget.

2. *Systematic errors in the data.*

First of all a systematic error is introduced by the varying spatial resolution of the interferometer between 8 and 13 μm . Because the spatial resolution at short wavelengths is higher than at longer wavelengths, we see a slightly larger part of the disk at longer wavelengths. This introduces a slope in the spectrum. The magnitude of this effect depends on the exact geometry of the innermost disk regions. The effect was modeled by assuming various disk geometries and turns out to have only minor influence on the derived abundances ($\sim 5\%$ level). Another source of systematic errors is introduced by the imperfect beam overlap in the interferometer. This effect also causes a slope in the spectrum. The effects of an erroneous slope in the spectrum on the derived abundances are negligible ($\sim 1\%$ level). Third, the uncertainties arising from the atmospheric calibration are less than 10%, which is a conservative estimate. The estimated total errors in the measurements have been indicated in the lower left corner of the panels in Fig. 10.2.

3. *Errors in the model calculations.*

The main source of error in the model arises from uncertainties in the emissivities and the limited number of dust species included. Also, we make the assumption that laboratory measurements of cosmic dust analogs are representative for materials observed in astronomical objects. The spectra obtained with the Infrared Space Observatory have shown that the overall agreement is good. The laboratory measurements are reproduced reasonably well by the model calculations of emissivities of small particles. The errors in the model calculations limit the accuracy of the absolute value of the derived abundances. However, since all spectra are fitted using the same procedure, the relative trends, on which our discussion is based, are not affected much.

Estimation of the errors on the fitting parameters.

In order to estimate the sensitivity of the derived fitting parameters to the above mentioned statistical and systematic errors, we use a Monte Carlo method, in which we generate a large number of synthetic data sets (1000) by adding random noise to the spectra. All these data sets are then fitted using the same fitting procedure. The spread in the derived parameters then gives an estimate of the sensitivity of these parameters to the exact shape of the spectra. We determine the strength of the random noise by requiring that the best fit model to the original data set has a reduced χ^2 of unity. In this way we simulate the added contributions of all above mentioned error sources, *including systematic errors*.

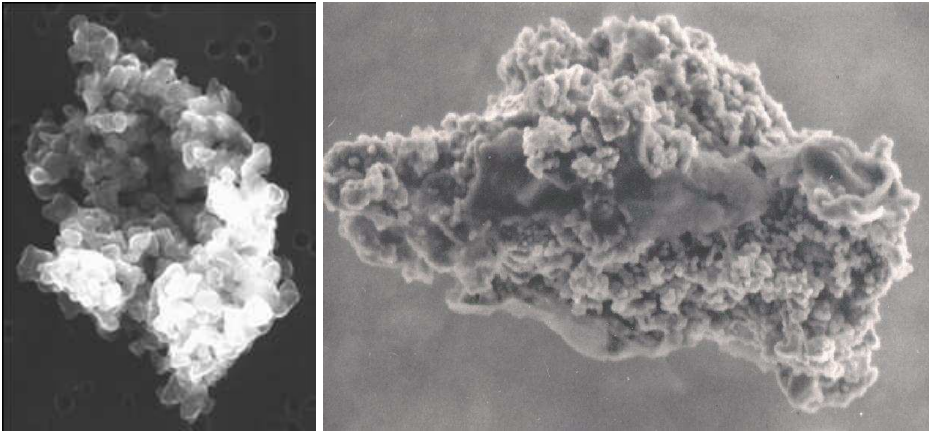
Samenvatting in het Nederlands

De titel van dit proefschrift is: 'Optische eigenschappen van vaste deeltjes in circumstellaire schijven en kometen'. Met de optische eigenschappen van een stofdeeltje bedoelen we de manieren waarop het stofdeeltje een wisselwerking aangaat met licht. Wat dit inhoudt wordt verderop in meer detail besproken. Eerst zullen we bespreken wat we bedoelen met stof in circumstellaire schijven en kometen, wat we weten over de eigenschappen van deze stofdeeltjes, en waarom het interessant is om deze stofdeeltjes te bestuderen.

Kosmisch stof

Als we het in de sterrenkunde over stof hebben gaat het niet over het bekende stof dat je in huis vindt. Dit huisstof bestaat onder andere uit textielresten, overblijfselen van insecten, menselijk en dierlijk haar, voedselresten, huidschilfers, plantendeeltjes en schimmelsporen. Voor zover we weten komen geen van deze bestanddelen elders voor in het heelal. De stofdeeltjes die in het heelal voorkomen noemen we kosmisch stof. Het kosmisch stof waar we het over hebben bestaat uit microscopisch kleine deeltjes samengesteld uit, onder andere, silicaten en koolstof. Voorbeelden zijn te zien in figuur 1. De cyclus van vorming en vernietiging van het stof in het heelal gaat ongeveer als volgt in zijn werk.

De geboorte van een groot gedeelte van het stof in het heelal vindt plaats op het sterfbed van relatief lichte sterren, d.w.z. sterren die ongeveer evenveel massa bevatten als de Zon. Als zo'n relatief lichte ster het einde van haar leven nadert, verliest zij een heleboel van haar massa. Het materiaal dat de ster verliest zal in eerste instantie gasvormig zijn, maar als het van de ster wegstroomt en afkoelt zullen in het gas kleine stofdeeltjes gevormd worden, met een typische diameter van ongeveer een tienduizendste van een millimeter. Deze stofdeeltjes komen uiteindelijk terecht in het *interstellaire medium*, de ruimte tussen de sterren. Het interstellaire medium is erg leeg. Ruwweg zul je slechts één zo'n microscopisch klein stofdeeltje aantreffen in een ruimte van een miljoen kubieke meter. Ter vergelijking: dit komt overeen met een paar stofdeeltjes in een ruimte ter grootte van de Amsterdam Arena. In het interstellaire medium kunnen ook dichtere wolken gevormd worden. Zo'n wolk kan ineensorten onder zijn eigen zwaartekracht, wat het begin inluidt van de vorming van een nieuwe ster. In het centrum van deze ineenstortende wolk wordt een jonge ster gevormd met om zich heen een roterende, platte schijf van stof en gas. Deze schijf noemen we een *protoplanetaire* of *circumstellaire* schijf. In zo'n schijf is de dichtheid van de stofdeeltjes hoog genoeg om ze te laten samenklonteren tot grotere stofdeeltjes. Deze samenklontering leidt uiteindelijk tot de vorming van grotere lichamen zoals kometen, asteroïden en wellicht planeten. De planeten en kometen in ons zonnestelsel zijn zo'n viereeneenhalf miljard jaar geleden op deze manier gevormd uit het stof in de schijf rond de jonge Zon. Om de stofcyclus compleet te maken zal de ster, dus ook onze Zon, aan het eind van haar leven opzwellen en een



Figuur 1: Voorbeelden van interplanetaire stofdeeltjes. Deze stofdeeltjes zijn afkomstig uit ons zonnestelsel en zijn opgeveegd door de Aarde in haar baan rond de Zon. De afgebeelde deeltjes zijn ingevangen door detectoren op de vleugels van speciale vliegtuigen op ongeveer 20 km hoogte in de stratosfeer. De grootte van de deeltjes is ongeveer een honderdste van een millimeter. Bron: NASA

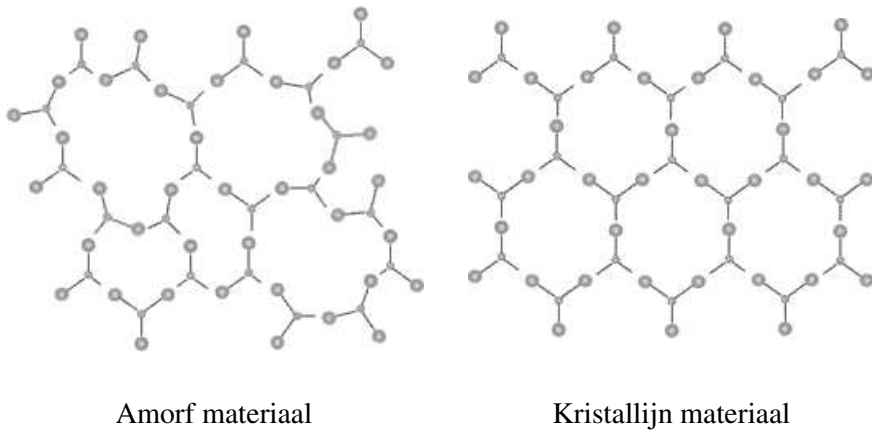
heleboel materie verliezen waaruit een nieuwe generatie stof gevormd kan worden.

Eigenschappen van stof

De methoden beschreven in dit proefschrift zijn gericht op het achterhalen van de eigenschappen van kosmische stofdeeltjes, zoals hun samenstelling, grootte en vorm. Al deze eigenschappen hebben invloed op de manier waarop het stof een interactie aangaat met licht.

Samenstelling

Kosmisch stof bestaat voor een belangrijk deel uit silicaten. Silicaten vormen ook een belangrijk deel van het materiaal waaruit de Aarde is opgebouwd. Er zijn twee belangrijke groepen te onderscheiden, *kristallijne* en *amorfe* silicaten. Het verschil tussen deze twee groepen zit hem niet in de atomaire samenstelling van het materiaal, maar in de ordening van de atomen. In een amorf silicaat zitten de atomen in een rooster op een ongeordende manier, terwijl de atomen in een kristallijn silicaat volgens een perfecte roosterstructuur geordend zijn (zie ook figuur 2). Om van een amorf silicaat een kristallijn silicaat te maken moet het materiaal opgewarmd worden tot boven ongeveer 700 °C. Dit kan bijvoorbeeld door het materiaal dicht bij een ster te brengen. Als we dus ergens kristallijne silicaten vinden betekent dit dat het materiaal ooit heel warm geweest is. Dit vertelt ons iets over de geschiedenis van het stof, zoals waar het is gevormd en waar het zich bevindt of geweest is.



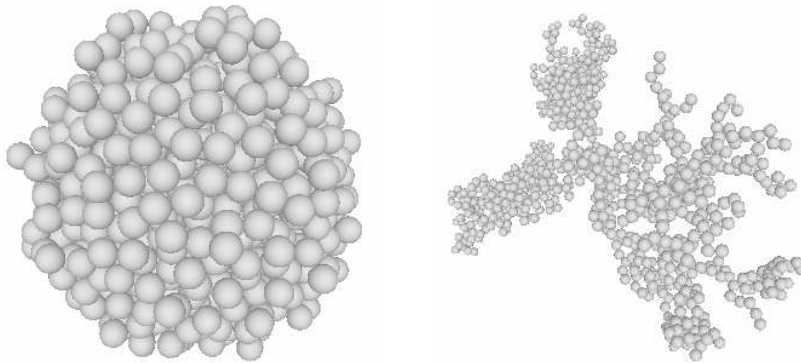
Figuur 2: Schematisch voorbeeld van het verschil in ordening van de atomen in het rooster van een amorf materiaal (links) en een kristallijn materiaal (rechts).

Grootte

Een andere belangrijke eigenschap van de stofdeeltjes is hun grootte. De stofdeeltjes in de interstellaire ruimte zijn zeer klein. Als de stofdeeltjes gaan samenklonteren in bijvoorbeeld een circumstellaire schijf zal hun grootte toenemen. Dit is het begin van de vorming van grotere objecten, zoals bijvoorbeeld planeten. Het is dus heel interessant om te weten te komen waar en hoe snel de grootte van de stofdeeltjes verandert.

Vorm en structuur

De vorm en structuur is een andere eigenschap van de stofdeeltjes. Als men een probleem in natuurkunde of sterrenkunde wil oplossen wordt het vrijwel altijd eerst gesimplificeerd. De eerste pogingen om de interactie van licht met stofdeeltjes te modelleren waren dan ook gebaseerd op de aanname dat de stofdeeltjes perfecte, homogene bolletjes zijn. Dit maakt het probleem relatief eenvoudig en is voor het begrijpen van een belangrijk deel van de relevante processen een zeer leerzame exercitie. Echter, zoals figuur 1 al laat zien is een homogene bol geen accurate beschrijving van de werkelijke vorm van een stofdeeltje. Steeds meer drong het besef dan ook door dat het beter modelleren van de vorm en structuur van de stofdeeltjes belangrijk is voor de interpretatie van sterrenkundige waarnemingen. Resultaten van laboratoriummetingen van lichtverstrooiing door natuurlijke deeltjes leidden er eind jaren zeventig toe dat de eerste workshop op het gebied van lichtverstrooiing aan niet-bolvormige deeltjes werd gehouden. Tegelijkertijd zorgde de snelle ontwikkeling op het gebied van computers ervoor dat numerieke methoden om de optische eigenschappen van niet-bolvormige deeltjes te berekenen konden worden ontwikkeld en toegepast. Vandaag de dag is er een grote gemeenschap van wetenschappers uit verschillende gebieden in de natuur- en sterrenkunde die zich met dit onderwerp bezighoudt. Het werk dat gepresenteerd wordt in dit proefschrift is voor een groot deel gericht op het berekenen van de optische eigenschappen van stofdeeltjes met



Figuur 3: Twee voorbeelden van met een computer gesimuleerde aggregaten. Links een vrij compact aggregaat, rechts een vrij open aggregaat.

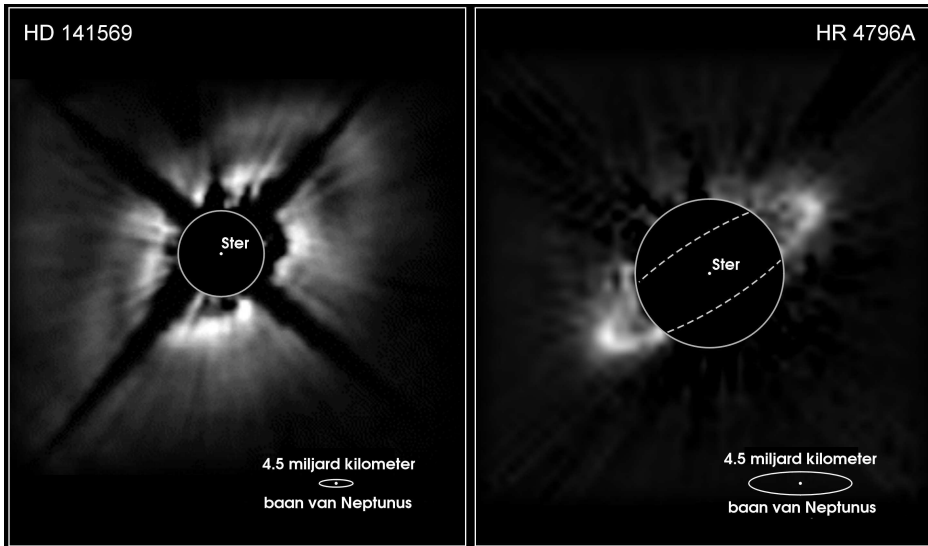
een realistische vorm en structuur, toegespitst op sterrenkundige toepassingen.

Ruwweg kunnen we de vorm en structuur van de stofdeeltjes onderverdelen in twee klassen; enkelvoudige deeltjes en samengestelde deeltjes. Een samengesteld deeltje, ook wel een aggregaat genoemd, ontstaat als kleine deeltjes samenklonteren tot een groter deeltje. Dit kan op een compacte manier gebeuren, zodat alle afzonderlijke componenten dicht op elkaar komen te zitten, of erg open, met veel loze ruimte tussen de componenten in. In figuur 3 is een voorbeeld te zien van een compact en een open aggregaat.

Circumstellair stof

Zoals hierboven reeds is gezegd vormen de schijven rondom jonge sterren de kraamkamers van asteroïden, kometen en planeten. Ook de planeten en andere objecten in ons zonnestelsel zijn gevormd in een circumstellaire schijf die de toen nog jonge Zon omringde. Het is dan ook buitengewoon interessant om de schijven rondom andere sterren te bestuderen, omdat dat een uniek zicht geeft op hoe ons zonnestelsel er waarschijnlijk viereneenhalf miljard jaar geleden uitgezien heeft. In figuur 4 zijn voorbeelden te zien van waarnemingen van circumstellaire schijven rondom twee jonge sterren.

Een logische vraag die opkomt als je de bouwstenen van planeten wilt bestuderen is ‘Waarom graaf je niet een gat in de Aarde en bestudeer je dat materiaal?’. Het antwoord is dat het materiaal dat we nu op Aarde vinden een aantal malen is vernietigd en weer opnieuw gevormd. Dit is gebeurd toen de jonge Aarde een grote vloeibare bal lava was, en het gebeurt nog steeds in het binnenste van de Aarde waar ten gevolge van de grote massa van de Aarde temperatuur en druk hoog zijn oplopen. Dit betekent dat de materialen die we nu op Aarde vinden niet meer de oorspronkelijke bouwstenen zijn. Een van de weinige manieren om deze bouwstenen te bestuderen is dus het onderzoeken van zonnestelsels in wording rondom andere sterren.



Figuur 4: Waarnemingen van stofschijven rondom twee jonge sterren. De centrale ster is afgedekt om te voorkomen dat de ster de zwakke emissie van de schijf overstraalt. Bron: A. Weinberger e.a., NASA (links), en B. Smith e.a., NASA (rechts).

Stof in kometen

Een komeet is eigenlijk een grote vuile sneeuwbal. Een groot gedeelte van de komeet bestaat namelijk uit ijs dat vervuild is met kleine stofdeeltjes. Een komeet is relatief klein, gemiddeld ca. 10 kilometer in doorsnede. Ter vergelijking: de doorsnede van de Aarde is bijna 13 duizend kilometer. Wegens haar geringe afmetingen en massa is een komeet nooit gesmolten geweest. Het is dus aannemelijk dat het stof dat opgesloten zit in het ijs van een komeet vrijwel niet veranderd is sinds de vorming van de komeet. Dat maakt stof in kometen een waardevolle bron van informatie over het stof dat aanwezig was in het vroege zonnestelsel.

Als een komeet dicht bij de Zon komt smelt het ijs en komt een grote hoeveelheid gas en stof vrij. Dit kan een spectaculair beeld opleveren, zoals bijvoorbeeld het geval was met de komeet Hale-Bopp in 1997 (zie ook figuur 5). Het gas en stof omringt de komeet en vormt de *coma*. Deze kan vele malen groter zijn dan de kern van de komeet. Het gas en het stof worden door de Zon weggeblazen van de komeet. Het gas is het meest gevoelig hiervoor en vormt een staart die direct van de Zon afwijkt. Het stof is iets minder gevoelig voor dit wegblazen en vormt een tweede staart die ongeveer de baan van de komeet volgt. Wat we met het blote oog kunnen waarnemen van een komeet is licht van de Zon dat wordt verstrooid door de stofdeeltjes en het gas in de coma en de staarten van de komeet.



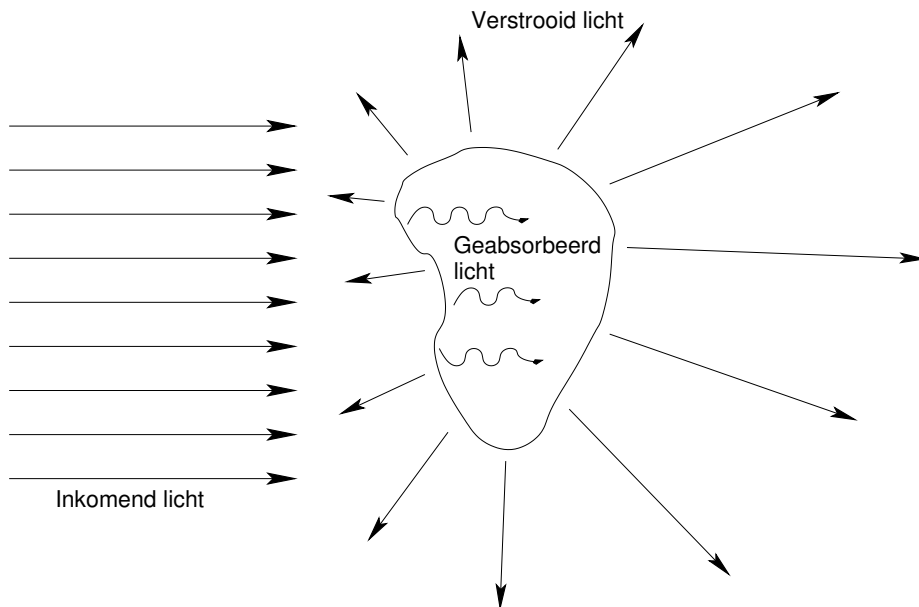
Figuur 5: De heldere komeet Hale-Bopp zoals hij zichtbaar was in Californië in april 1997. Bron: W. Pacholka

De wisselwerking van straling en stof

Vrijwel alle informatie over objecten in het heelal komt tot ons via de *elektromagnetische straling* (zoals zichtbaar licht, infrarood straling, ultraviolet straling, röntgenstraling enz.) die deze objecten uitzenden of verstrooien en die kan worden waargenomen met behulp van telescopen. Als we dus de eigenschappen van kosmische stofdeeltjes willen bestuderen, zullen we moeten begrijpen hoe de interactie van straling en stofdeeltjes in zijn werk gaat. Elektromagnetische straling is een golfverschijnsel. De golflengte van de straling bepaalt de kleur en de soort. Er zijn drie processen die van belang zijn voor de wisselwerking van straling en stof, namelijk *absorptie*, *verstrooiing* en *emissie*. Deze zullen we hieronder verder bespreken.

Absorptie en verstrooiing

Een bundel straling die op een stofdeeltje valt kan op twee manieren beïnvloed worden. Een deel van de straling wordt geabsorbeerd door het stofdeeltje en een deel wordt verstrooid (zie ook figuur 6). De straling die wordt geabsorbeerd wordt in het stofdeeltje in andere vormen van energie, zoals warmte, omgezet. De verstrooide straling wordt door het deeltje in alle richtingen verspreid. Hoeveel straling wordt geabsorbeerd en verstrooid door een stofdeeltje hangt af van de hoeveelheid en golflengte van de inkomende



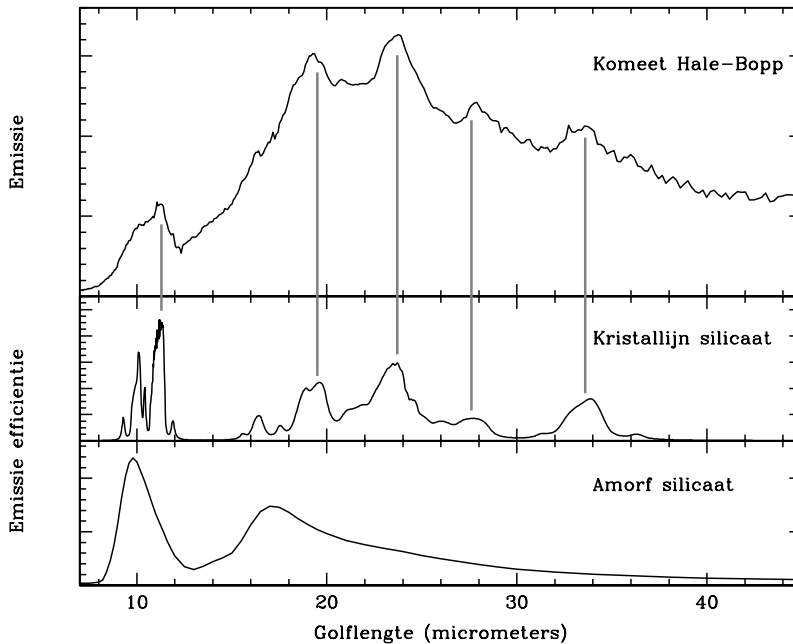
Figuur 6: Schematische weergave van de verstrooiing en absorptie van licht door een stofdeeltje.

straling en van de eigenschappen van het stofdeeltje.

Een belangrijke eigenschap van het verstrooide licht is *polarisatie*. De graad van lineaire polarisatie is de mate van voorkeur voor een bepaalde trillingsrichting van de stralingsgolf. Direct licht van de Zon is ongepolariseerd; alle trillingsrichtingen komen evenveel voor. Als het zonlicht wordt verstrooid kan het gedeeltelijk of geheel gepolariseerd worden; een bepaalde trillingsrichting krijgt een sterke voorkeur. Dit verschijnsel kan in het dagelijks leven worden waargenomen in bijvoorbeeld licht dat is weerkaatst door een nat wegdek. Een polaroid zonnebril maakt gebruik van de polarisatie van het gereflecteerde licht door een bepaalde richting te blokkeren om zo hinderlijke reflecties weg te filteren. Straling die wordt verstrooid aan een verzameling stofdeeltjes kan ook gepolariseerd worden. De mate van polarisatie kan worden gemeten en bevat belangrijke informatie over de grootte en de structuur van de verstrooiende deeltjes.

Emissie

Ieder object zendt straling uit. Dit noemen we *emissie*. De hoeveelheid en de golflengteverdeling van de uitgezonden straling zijn afhankelijk van de temperatuur van het object. De Zon bijvoorbeeld is heel erg warm en zendt daardoor veel straling uit in het zichtbare deel van het spectrum, waar (niet toevallig) onze ogen gevoelig zijn. Koudere objecten, bij kamertemperatuur bijvoorbeeld, zenden een groot gedeelte van hun straling uit bij langere golflengtes, in het *infrarood*. Ook de stofdeeltjes die we bestuderen in dit proefschrift zenden het grootste deel van hun straling uit in het infrarode deel van het



Figuur 7: De emissie als functie van de golflengte van komeet Hale-Bopp (bovenste paneel) samen met de emissie efficiëntie als functie van de golflengte voor kleine kristallijne en amorf silicaat deeltjes (onderste twee panelen). Het is duidelijk dat de prominente pieken die in het spectrum van kristallijne silicaat deeltjes gezien worden ook waar te nemen zijn in het spectrum van Hale-Bopp.

spectrum.

Hoeveel straling een stofdeeltje bij een bepaalde golflengte uitzendt is naast de temperatuur van het deeltje ook afhankelijk van zijn grootte, vorm en samenstelling. De golflengteafhankelijkheid van de emissie, het emissiespectrum, is een soort 'vingerafdruk' die karakteristiek is voor de eigenschappen van het stofdeeltje. Dit emissiespectrum kunnen we waarnemen en gebruiken om te bepalen wat de eigenschappen van de stofdeeltjes in circumstellaire schijven of kometen zijn. In figuur 7 zien we het emissiespectrum van komeet Hale-Bopp vergeleken met de spectra van een kristallijn en een amorf silicaat. Beide materialen zijn aanwezig in het stof van deze komeet. De signatuur van het kristallijne silicaat is prominent aanwezig in het emissiespectrum van Hale-Bopp.

Het berekenen van de optische eigenschappen van stofdeeltjes

Voor het berekenen van de optische eigenschappen van een stofdeeltje kun je twee extreme benaderingen onderscheiden. In de eerste benadering gaat men ervan uit dat het deeltje te beschrijven is als een homogene bol. Dit heeft als voordeel dat het probleem

eenvoudig op te lossen is en de berekeningen snel en efficiënt gedaan kunnen worden. Het nadeel van deze benadering is dat de stofdeeltjes meestal helemaal niet bolvormig zijn en dat de resultaten vaak niet overeenkomen met waarnemingen en experimentele resultaten. Het tweede extreem is om de vorm en structuur van de stofdeeltjes zo nauwkeurig mogelijk te modelleren. Het voordeel van deze aanpak is dat het nauwkeurige uitkomsten geeft die goed overeenkomen met de werkelijkheid. Een nadeel is echter dat het zeer complex en rekenintensief werk met zich meebrengt en dat het door de complexiteit weinig inzicht verschaft. Een derde benadering, die een belangrijk deel van dit proefschrift beslaat, zoekt de gulden middenweg tussen de twee extremen. Dit is de *statistische benadering*. In de statistische benadering proberen we de optische eigenschappen van een verzameling onregelmatig gevormde stofdeeltjes te simuleren d.m.v. de optische eigenschappen van een verzameling stofdeeltjes met relatief simpele vormen. Op deze manier breken we de perfecte symmetrie van een homogene bol, terwijl we de complexiteit van het probleem zoveel mogelijk beperken.

Dit proefschrift

In dit proefschrift worden de optische eigenschappen van stofdeeltjes van verschillende vormen, groottes en samenstellingen onderzocht. De beschikbare diagnostiek om deze stofeigenschappen te achterhalen uit sterrenkundige waarnemingen wordt bestudeerd. Ook wordt de ontwikkelde theorie toegepast op waarnemingen van stof in circumstellaire schijven en kometen.

In hoofdstuk 2 wordt de statistische benadering voor heel kleine deeltjes behandeld. We laten zien dat deze benadering goed werkt voor de emissie- en absorptie-eigenschappen van zulke minuscule deeltjes. In hoofdstuk 3 presenteren we een methode om de optische eigenschappen van zeer kleine deeltjes met willekeurige vormen te berekenen. Ook laten we in dit hoofdstuk zien dat de absorptie- en emissie-eigenschappen van *elk willekeurig gevormd deeltje*, zolang het maar klein genoeg is, beschreven kunnen worden door de gemiddelde absorptie- en emissie-eigenschappen van een verzameling uitgerekte en afgeplatte bollen (zogenaamde *omwentelingsellipsoïden*).

In hoofdstuk 4 en 5 bestuderen we de optische eigenschappen van twee relatief eenvoudige deeltjesvormen. In hoofdstuk 4 bestuderen we verzamelingen van omwentelingsellipsoïden van verschillende groottes en vormen en in hoofdstuk 5 verzamelingen van holle bollen. We laten zien dat het gebruik van een verzameling holle bollen in veel gevallen een effectieve en nauwkeurige manier is om de optische eigenschappen van onregelmatig gevormde deeltjes te berekenen.

In hoofdstuk 6 bestuderen we het emissiespectrum van aggregaten en vergelijken dat met die van enkelvoudige deeltjes. We bestuderen het effect van de aggregaatstructuur (open of compact, zie figuur 3) op het emissiespectrum. In de open structuren is nog veel van de emissiesignatuur van de aparte, kleine deeltjes waaruit het aggregaat bestaat te zien, terwijl de emissiespectra van de compacte aggregaten meer de signatuur laat zien van een groot deeltje.

In hoofdstuk 7 onderzoeken we de emissiespectra van heel grote deeltjes. Als de deeltjesgrootte toeneemt wordt over het algemeen het contrast van de pieken in het

emissiespectrum kleiner. Daarom zou men verwachten dat alle structuur uit het spectrum verdwijnt als men de deeltjes maar groot genoeg maakt. Daarmee zou de mooie diagnostiek, zoals die zichtbaar is voor kleine deeltjes (zie ook figuur 7), verdwijnen. In hoofdstuk 7 laten we echter zien dat voor de kristallijne silicaten er altijd structuur in het spectrum aanwezig blijft die karakteristiek is voor het materiaal, hoe groot je de deeltjes ook maakt. Dit zorgt ervoor dat we in principe ook de samenstelling van heel grote deeltjes kunnen bepalen aan de hand van emissiespectra.

De theorie die in de voorgaande hoofdstukken ontwikkeld is, is toegepast op waarnemingen van stof in circumstellaire schijven en kometen in hoofdstukken 8, 9 en 10. In hoofdstuk 8 modelleren we het emissiespectrum en de graad van polarisatie van komeet Hale-Bopp voor verschillende fasehoeken en golflengtes. Door de piek-verhoudingen in het emissiespectrum van de kristallijne silicaten te bestuderen, concluderen we dat de kristallijne silicaatdeeltjes in komeet Hale-Bopp veel kleiner zijn dan de amorfe silicaatdeeltjes. We concluderen ook dat de fractie kristallijne silicaten verrassend laag is, hoewel de signatuur van kristallijne silicaatdeeltjes heel duidelijk aanwezig is in het spectrum van Hale-Bopp.

Hoofdstuk 9 gaat over een onderzoek van de emissiespectra van een groot aantal jonge sterren. Deze sterren hebben allemaal een circumstellaire schijf. In deze studie concentreren we ons op de fractie kristallijn materiaal en de fractie grote stofdeeltjes die in de schijven aanwezig zijn. We vinden dat in alle schijven die een hoge fractie kristallijn materiaal hebben de gemiddelde grootte van de deeltjes hoog is. Echter, we vinden ook schijven die een hoge mate van stofgroei hebben gehad zonder dat er veel kristallijn materiaal is gevormd. Dit betekent dat het groeien van stofdeeltjes makkelijker is dan het kristalliseren ervan. Dit komt waarschijnlijk doordat de omstandigheden die nodig zijn voor stofgroei in een groter deel van de schijf aanwezig zijn dan de omstandigheden om kristallijn materiaal te maken.

In hoofdstuk 10 bestuderen we het gecombineerde licht van twee telescopen van ieder ruim acht meter in doorsnede. Door het licht van deze twee telescopen te combineren kunnen we inzoomen op de binnenste delen van een circumstellaire schijf. Normaliter ontvangen we de totale emissie van al het stof uit de hele schijf. Met de techniek die gebruikt wordt in hoofdstuk 10 nemen we alleen het stof in de binnendelen van de schijf waar, waar in ons zonnestelsel de terrestrische planeten zijn gevormd. Zo hebben we dus een unieke kijk op de bouwstenen van terrestrische planeten. Wat we vinden is dat in de schijven die we bestudeerd hebben alle materialen om planeten te maken aanwezig zijn in de binnendelen van de schijf en dat de groei van het stof daar reeds begonnen is. Ook vinden we dat het stof in dit gebied van de schijf een veel hogere fractie kristallijn materiaal bevat dan in de buitendelen van de schijf. Het lijkt er dus op dat de bouwstenen van terrestrische planeten, inclusief de Aarde, hoofdzakelijk uit kleine kristalletjes bestaan.

Het werk gepresenteerd in dit proefschrift verschaft een aantal praktische en robuuste methoden om sterrenkundige waarnemingen van stof te analyseren. De toepassingen op sterrenkundige waarnemingen van stof in kometen en rondom jonge sterren hebben ons veel geleerd over de evolutie en geschiedenis van stof in circumstellaire schijven en kometen. Ook zullen resultaten van dit proefschrift ons in de toekomst helpen bij

de interpretatie van nieuwe waarnemingen. Dit zal ons ongetwijfeld vele antwoorden opleveren, maar zoals altijd in de wetenschap zullen deze antwoorden nieuwe vragen opwerpen. De puzzel is nog lang niet af, maar een klein stukje is toegevoegd.

Bibliography

- Acke, B. & van den Ancker, M. E. 2004, *ISO spectroscopy of disks around Herbig Ae/Be stars*. A&A, 426, 151
- Acke, B., van den Ancker, M. E., Dullemond, C. P., van Boekel, R., & Waters, L. B. F. M. 2004, *Correlation between grain growth and disk geometry in Herbig Ae/Be systems*. A&A, 422, 621
- Aden, A. L. & Kerker, M. 1951, *Scattering of electromagnetic waves from two concentric spheres*. Journal of Applied Physics, 22, 1242
- Andre, P., Ward-Thompson, D., & Barsony, M. 2000, *From Prestellar Cores to Protostars: the Initial Conditions of Star Formation*. Protostars and Planets IV, 59
- Artymowicz, P. 1988, *Radiation pressure forces on particles in the Beta Pictoris system*. ApJ, 335, L79
- Augereau, J. C., Lagrange, A. M., Mouillet, D., & Ménard, F. 2001, *HST/NICMOS2 coronagraphic observations of the circumstellar environment of three old PMS stars: HD 100546, SAO 206462 and MWC 480*. A&A, 365, 78
- Aumann, H. H. 1984, *IRAS Observations of Nearby Main-Sequence Dwarfs*. BAAS, 16, 483
- Ball, R. C. & Witten, T. A. 1984, *Causality Bond on the Density of Aggregates*. PRA, 29, 2966
- Battaglia, A., Muinonen, K., Nousiainen, T., & Peltoniemi, J. I. 1999, *Light scattering by Gaussian particles: Rayleigh-ellipsoid approximation*. J. Quant. Spectrosc. Radiat. Transfer, 63, 277
- Beckwith, S. V. W., Henning, T., & Nakagawa, Y. 2000, *Dust Properties and Assembly of Large Particles in Protoplanetary Disks*. Protostars and Planets IV, 533
- Begemann, B., Dorschner, J., Henning, T., Mutschke, H., & Thamm, E. 1994, *A laboratory approach to the interstellar sulfide dust problem*. ApJ, 423, L71
- Blum, J., Wurm, G., Kempf, S., et al. 2000, *Growth and Form of Planetary Seedlings: Results from a Microgravity Aggregation Experiment*. Physical Review Letters, 85, 2426
- Bockelée-Morvan, D., Gautier, D., Hersant, F., Huré, J.-M., & Robert, F. 2002, *Turbulent radial mixing in the solar nebula as the source of crystalline silicates in comets*. A&A, 384, 1107
- Bohren, C. F. & Huffman, D. R. 1983, *Absorption and scattering of light by small particles* (New York: Wiley)
- Bouchet, P., Schmider, F. X., & Manfroid, J. 1991, *JHKLM standard stars in the ESO system*. A&AS, 91, 409
- Bouwman, J., de Koter, A., Dominik, C., & Waters, L. B. F. M. 2003, *The origin of crystalline silicates in the Herbig Be star HD 100546 and in comet Hale-Bopp*. A&A, 401, 577
- Bouwman, J., Meeus, G., de Koter, A., et al. 2001, *Processing of silicate dust grains in Herbig Ae/Be systems*. A&A, 375, 950
- Bradley, J. 2003, *The Astromineralogy of Interplanetary Dust Particles*. LNP Vol. 609:

- Astromineralogy, 217, ed. Henning
- Bradley, J. P., Brownlee, D. E., & Veblen, D. R. 1983, *Pyroxene whiskers and platelets in interplanetary dust - Evidence of vapour phase growth*. *Nature*, 301, 473
- Bradley, J. P., Humecki, H. J., & Germani, M. S. 1992, *Combined infrared and analytical electron microscope studies of interplanetary dust particles*. *ApJ*, 394, 643
- Bradley, J. P., Snow, T. P., Brownlee, D. E., & Hanner, M. S. 1999, *Solid Interstellar Matter: The ISO Revolution*, ed. L. d'Hendecourt, C. Joblin, & A. Jones, Centre de Physique des Houches No. 11 (Berlin: Springer), 297
- Brearley, A. & Jones, R. H. 1998, *Chondritic meteorites*. in *Planetary Materials*, ed. J. Papike (The Mineralogical Society of America), Chapter 3
- Brucato, J. R., Colangeli, L., Mennella, V., Palumbo, P., & Bussoletti, E. 1999, *Silicates in Hale-Bopp: hints from laboratory studies*. *Planet. Space Sci.*, 47, 773
- Burns, J. A., Lamy, P. L., & Soter, S. 1979, *Radiation forces on small particles in the solar system*. *Icarus*, 40, 1
- Calvet, N., Hartmann, L., & Strom, S. E. 2000, *Evolution of Disk Accretion*. *Protostars and Planets IV*, 377
- Carter, B. S. 1990, *Southern JHKL standards*. *MNRAS*, 242, 1
- Charbonneau, P. 1995, *Genetic Algorithms in Astronomy and Astrophysics*. *ApJS*, 101, 309
- Chihara, H., Koike, C., & Tsuchiyama, A. 2001, *Low-Temperature Optical Properties of Silicate Particles in the Far-Infrared Region*. *PASJ*, 53, 243
- Chihara, H., Koike, C., Tsuchiyama, A., Tachibana, S., & Sakamoto, D. 2002, *Compositional dependence of infrared absorption spectra of crystalline silicates. I. Mg-Fe pyroxenes*. *A&A*, 391, 267
- Christensen, P. R., Bandfield, J. L., Hamilton, V. E., et al. 2000, *A thermal emission spectral library of rock-forming minerals*. *J. Geophys. Res.*, 105, 9735
- Chýlek, P., Videen, G., Geldart, D. J. W., Dobbie, J. S., & Tso, H. C. W. 2000, *Effective Medium Approximations for Heterogeneous Particles*. in *Light Scattering by Non-spherical Particles, Theory, Measurements and Applications*, ed. M. I. Mishchenko, J. W. Hovenier, & L. D. Travis (San Diego: Academic Press), 273–308
- Cohen, M. 1973, *Infra-red observations of young stars. II. T Tau stars and the ORI population*. *MNRAS*, 161, 97
- Cohen, M., Walker, R. G., Carter, B., et al. 1999, *Spectral Irradiance Calibration in the Infrared. X. A Self-Consistent Radiometric All-Sky Network of Absolutely Calibrated Stellar Spectra*. *AJ*, 117, 1864
- Crovisier, J., Leech, K., Bockelee-Morvan, D., et al. 1997, *The spectrum of Comet Hale-Bopp (C/1995 01) observed with the Infrared Space Observatory at 2.9 AU from the Sun*. *Science*, 275, 1904
- Cutri, R. M., Skrutskie, M. F., van Dyk, S., et al. 2003, *2MASS All-Sky Catalog of Point Sources (Cutri+ 2003)*. *VizieR Online Data Catalog*, 2246, 0
- de Winter, D., van den Ancker, M. E., Maira, A., et al. 2001, *A photometric catalogue of southern emission-line stars*. *A&A*, 380, 609
- de Winter, D., van den Ancker, M. E., Perez, M. R., et al. 1996, *The peculiar B[e] star HD 45677. I. Photometric observations*. *A&AS*, 119, 1

- Demyk, K., Dartois, E., Wiesemeyer, H., et al. 2000, *Composition of the Silicates around Evolved Stars and Protostars*. ISO beyond the peaks: The 2nd ISO workshop on analytical spectroscopy. Eds. A. Salama, M.F.Kessler, K. Leech & B. Schulz. ESA-SP 456., 456, 183
- Dent, W. R. F., Walker, H. J., Holland, W. S., & Greaves, J. S. 2000, *Models of the dust structures around Vega-excess stars*. MNRAS, 314, 702
- Desch, S. J. & Cuzzi, J. N. 2000, *The Generation of Lightning in the Solar Nebula*. Icarus, 143, 87
- Dominik, C. & Decin, G. 2003, *Age Dependence of the Vega Phenomenon: Theory*. ApJ, 598, 626
- Dominik, C., Dullemond, C. P., Cami, J., & van Winckel, H. 2003, *The dust disk of HR 4049. Another brick in the wall*. A&A, 397, 595
- Dominik, C. & Nübold, H. 2002, *Magnetic Aggregation: Dynamics and Numerical Modeling*. Icarus, Volume 157, Issue 1, pp. 173-186 (2002)., 157, 173
- Dorschner, J., Begemann, B., Henning, T., Jäger, C., & Mutschke, H. 1995, *Steps toward interstellar silicate mineralogy. II. Study of Mg-Fe-silicate glasses of variable composition*. A&A, 300, 503
- Draine, B. T. 1988, *The discrete-dipole approximation and its application to interstellar graphite grains*. ApJ, 333, 848
- Draine, B. T. 2000, *The Discrete Dipole Approximation for Light Scattering by Irregular Targets*. in *Light Scattering by Nonspherical Particles: Theory, Measurements, and Applications*, ed. M. I. Mishchenko, J. W. Hovenier, & L. D. Travis (San Diego: Academic Press), 131–145
- Draine, B. T. & Flatau, P. J. 1994, *Discrete-dipole approximation for scattering calculations*. Optical Society of America Journal A, 11, 1491
- Draine, B. T. & Goodman, J. 1993, *Beyond Clausius-Mossotti - Wave propagation on a polarizable point lattice and the discrete dipole approximation*. ApJ, 405, 685
- Draine, B. T. & Lee, H. M. 1984, *Optical properties of interstellar graphite and silicate grains*. ApJ, 285, 89
- Dullemond, C. P. & Dominik, C. 2004, *Flaring vs. self-shadowed disks: The SEDs of Herbig Ae/Be stars*. A&A, 417, 159
- Dullemond, C. P. & Dominik, C. 2005, *Dust coagulation in protoplanetary disks: a rapid depletion of small grains*. A&A in press
- Dullemond, C. P., Dominik, C., & Natta, A. 2001, *Passive Irradiated Circumstellar Disks with an Inner Hole*. ApJ, 560, 957
- Dwek, E. 1997, *Can Composite Fluffy Dust Particles Solve the Interstellar Carbon Crisis?* ApJ, 484, 779
- Eiroa, C., Garzón, F., Alberdi, A., et al. 2001, *EXPORT: Near-IR observations of Vega-type and pre-main sequence stars*. A&A, 365, 110
- Eisner, J. A., Lane, B. F., Akeson, R. L., Hillenbrand, L. A., & Sargent, A. I. 2003, *Near-Infrared Interferometric Measurements of Herbig Ae/Be Stars*. ApJ, 588, 360
- Fabian, D., Henning, T., Jäger, C., et al. 2001, *Steps toward interstellar silicate mineralogy. VI. Dependence of crystalline olivine IR spectra on iron content and particle shape*. A&A, 378, 228

- Fabian, D., Jäger, C., Henning, T., Dorschner, J., & Mutschke, H. 2000, *Steps toward interstellar silicate mineralogy. V. Thermal Evolution of Amorphous Magnesium Silicates and Silica*. A&A, 364, 282
- Filippov, A. V., Zurita, M., & Rosner, D. E. 2000, *Fractal-like Aggregates: Relation between Morphology and Physical Properties*. Journal of Colloid and Interface Science, 229, 261
- Fogel, M. E. & Leung, C. M. 1998, *Modeling Extinction and Infrared Emission from Fractal Dust Grains: Fractal Dimension as a Shape Parameter*. ApJ, 501, 175
- Forrest, W. J., Sargent, B., Furlan, E., et al. 2004, *Mid-infrared Spectroscopy of Disks around Classical T Tauri Stars*. ApJS, 154, 443
- Fouque, P., Le Bertre, T., Epchtein, N., Guglielmo, F., & Kerschbaum, F. 1992, *Near-infrared photometry of a sample of IRAS point sources*. A&AS, 93, 151
- Gail, H.-P. 2004, *Radial mixing in protoplanetary accretion disks. IV. Metamorphosis of the silicate dust complex*. A&A, 413, 571
- Galdemard, P., Lagage, P. O., Dubreuil, D., et al. 1999, *Mid-Infrared Spectro-Imaging Observations Of Comet Hale-Bopp*. Earth Moon and Planets, 78, 271
- Ganesh, S., Joshi, U. C., Baliyan, K. S., & Deshpande, M. R. 1998, *Polarimetric observations of the comet Hale-Bopp*. A&AS, 129, 489
- Geiss, J. 1987, *Composition measurements and the history of cometary matter*. A&A, 187, 859
- Glass, I. S. & Penston, M. V. 1974, *An infrared survey of RW Aurigae stars*. MNRAS, 167, 237
- Glindemann, A., Algomedo, J., Amestica, R., et al. 2003, *The VLTI – A Status Report*. in Interferometry for Optical Astronomy II. Edited by Wesley A. Traub. Proceedings of the SPIE, Volume 4838, pp. 89-100 (2003), 89–100
- Goncharenko, A. V., Semenov, Y. G., & Venger, E. F. 1999, *Effective scattering cross section of an assembly of small ellipsoidal particles*. J. Opt. Soc. Am. A, 16, 517
- Goodman, J. J., Draine, B. T., & Flatau, P. J. 1991, *Application of fast-Fourier-transform techniques to the discrete-dipole approximation*. Optics Letters, 16, 1198
- Grady, C. A., Polomski, E. F., Henning, T., et al. 2001, *The Disk and Environment of the Herbig Be Star HD 100546*. AJ, 122, 3396
- Grady, C. A., Sitko, M. L., Russell, R. W., et al. 2000, *Infalling Planetesimals in Pre-Main Stellar Systems*. Protostars and Planets IV, 613
- Gray, D. E. 1963, American Institute of Physics (AIP). Handbook (New York: McGraw-Hill, 1963, 2nd ed., edited by Gray, Dwight E.)
- Greenberg, J. M. & Li, A. 1996, *What are the true astronomical silicates?* A&A, 309, 258
- Grevesse, N. & Sauval, A. J. 1998, *Standard Solar Composition*. Space Science Reviews, 85, 161
- Hage, J. I. & Greenberg, J. M. 1990, *A model for the optical properties of porous grains*. ApJ, 361, 251
- Haisch, K. E., Lada, E. A., & Lada, C. J. 2001, *Disk Frequencies and Lifetimes in Young Clusters*. ApJ, 553, L153
- Hales, T. C. 1992, *The sphere packing problem*. Journal of Computational and Applied

- Mathematics, 44, 41
- Hallenbeck, S. & Nuth, J. 1997, *Infrared Observations of the Transition from Chaotic to Crystalline Silicates via Thermal Annealing in the Laboratory*. *Ap&SS*, 255, 427
- Hanner, M. S., Gehrz, R. D., Harker, D. E., et al. 1999, *Thermal Emission from the Dust Coma of Comet Hale-Bopp and the Composition of the Silicate Grains*. *Earth Moon and Planets*, 79, 247
- Hanner, M. S., Lynch, D. K., & Russell, R. W. 1994, *The 8-13 micron spectra of comets and the composition of silicate grains*. *ApJ*, 425, 274
- Hansen, J. E. & Hovenier, J. W. 1974, *Interpretation of the Polarization of Venus*. *Journal of Atmospheric Sciences*, 31, 1137
- Harker, D. E. & Desch, S. J. 2002, *Annealing of Silicate Dust by Nebular Shocks at 10 AU*. *ApJ*, 565, L109
- Harker, D. E., Wooden, D. H., Woodward, C. E., & Lisse, C. M. 2002, *Grain Properties of Comet C/1995 O1 (Hale-Bopp)*. *ApJ*, 580, 579
- Hasegawa, H., Ichikawa, T., Abe, S., et al. 1999, *Near-Infrared Photometric and Polarimetric Observations Of Comet Hale-Bopp*. *Earth Moon and Planets*, 78, 353
- Hayward, T. L., Hanner, M. S., & Sekanina, Z. 2000, *Thermal Infrared Imaging and Spectroscopy of Comet Hale-Bopp (C/1995 O1)*. *ApJ*, 538, 428
- Heinrichsen, I., Walker, H. J., & Klaas, U. 1998, *Infrared mapping of the dust disc around VEGA*. *MNRAS*, 293, L78
- Henning, T., Chan, S. J., & Assendorp, R. 1996, *The nature of objects with a 21- μ m feature*. *A&A*, 312, 511
- Henning, T. & Stognienko, R. 1993, *Porous grains and polarization of light: The silicate features*. *A&A*, 280, 609
- Henning, T. & Stognienko, R. 1996, *Dust opacities for protoplanetary accretion disks: influence of dust aggregates*. *A&A*, 311, 291
- Herbig, G. H. 1960, *The Spectra of Be- and Ae-TYPE Stars Associated with Nebulosity*. *APJS*, 4, 337
- Hildebrand, R. H. & Dragovan, M. 1995, *The Shapes and Alignment Properties of Interstellar Dust Grains*. *ApJ*, 450, 663
- Hill, S. C., Hill, A. C., & Barber, P. W. 1984, *Light scattering by size/shape distributions of soil particles and spheroids*. *Appl. Opt.*, 23, 1025
- Hillenbrand, L. A., Strom, S. E., Vrba, F. J., & Keene, J. 1992, *Herbig Ae/Be stars - Intermediate-mass stars surrounded by massive circumstellar accretion disks*. *ApJ*, 397, 613
- Hoekstra, A. G., Grimminck, M. D., & Sloot, P. M. A. 1998, *Large scale simulations of elastic light scattering by fast discrete dipole approximation*. *International Journal of Modern Physics*, 9, 87
- Holland, W. S., Greaves, J. S., Zuckerman, B., et al. 1998, *Submillimetre images of dusty debris around nearby stars*. *Nature*, 392, 788
- Honda, M., Kataza, H., Okamoto, Y. K., et al. 2004, *Crystalline Silicate Feature of the Vega-like Star HD 145263*. *ApJ*, 610, L49
- Honda, M., Kataza, H., Okamoto, Y. K., et al. 2003, *Detection of Crystalline Silicates around the T Tauri Star Hen 3-600A*. *ApJ*, 585, L59

- Hony, S., Waters, L. B. F. M., & Tielens, A. G. G. M. 2002, *The carrier of the “30” mu m emission feature in evolved stars. A simple model using magnesium sulfide.* A&A, 390, 533
- Hoogzaad, S. N., Molster, F. J., Dominik, C., et al. 2002, *The circumstellar dust shell of the post-AGB star HD 161796.* A&A, 389, 547
- Hovenier, J. W., van der Mee, C., & Domke, H. 2004, *Transfer of Polarized Light in Planetary Atmospheres* (Dordrecht: Kluwer Academic Publishers)
- Hovenier, J. W. & van der Mee, C. V. M. 2000, *Basic Relationships for Matrices Describing Scattering by Small Particles.* in *Light Scattering by Nonspherical Particles: Theory, Measurements, and Applications*, ed. M. I. Mishchenko, J. W. Hovenier, & L. D. Travis (San Diego: Academic Press), 61–85
- Hovenier, J. W., Volten, H., Muñoz, O., van der Zande, W. J., & Waters, L. B. 2003, *Laboratory study of Scattering Matrices for Randomly Oriented Particles: Potentials, Problems, and Perspectives.* *Journal of Quantitative Spectroscopy and Radiative Transfer*, 79, 741
- Iatì, M. A., Cecchi-Pestellini, C., Williams, D. A., et al. 2001, *Porous interstellar grains.* MNRAS, 322, 749
- Jäger, C., Dorschner, J., Mutschke, H., Posch, T., & Henning, T. 2003, *Steps toward interstellar silicate mineralogy. VII. Spectral properties and crystallization behaviour of magnesium silicates produced by the sol-gel method.* A&A, 408, 193
- Jäger, C., Molster, F. J., Dorschner, J., et al. 1998, *Steps toward interstellar silicate mineralogy. IV. The crystalline revolution.* A&A, 339, 904
- Jewitt, D. & Matthews, H. 1999, *Particulate Mass Loss from Comet Hale-Bopp.* AJ, 117, 1056
- Jockers, K., Rosenbush, V. K., Bonev, T., & Credner, T. 1999, *Images of Polarization and Colour in the Inner Coma of Comet Hale-Bopp.* *Earth Moon and Planets*, 78, 373
- Joint IRAS Science Working Group. 1988, *Infrared Astronomical Satellite Catalogs, 1988. The Point Source Catalog, version 2.0, NASA RP-1190.* in *IRAS Point Source Catalog (1988)*
- Jones, A. P. 1988, *Modelling interstellar extinction. I - Porous grains.* MNRAS, 234, 209
- Jones, T. J. & Gehrz, R. D. 2000, *Infrared Imaging Polarimetry of Comet C/1995 O1 (Hale-Bopp).* *Icarus*, 143, 338
- Kahnert, F. M. & Stamnes, J. J. 2002, *Can simple particle shapes be used to model scalar optical properties of an ensemble of wavelength-sized particles.* *J. Opt. Soc. Am. A*, 19, 521
- Kahnert, F. M., Stamnes, J. J., & Stamnes, K. 2002, *Using simple particle shapes to model the Stokes scattering matrix of ensembles of wavelength-sized particles with complex shapes: possibilities and limitations.* *Journal of Quantitative Spectroscopy and Radiative Transfer*, 74, 167
- Kahnert, M. 2003, *Numerical methods in electromagnetic scattering theory.* *Journal of Quantitative Spectroscopy and Radiative Transfer*, 79, 775
- Kahnert, M. 2004, *Reproducing the optical properties of fine desert dust aerosols using ensembles of simple model particles.* *Journal of Quantitative Spectroscopy and*

- Radiative Transfer, 85, 231
- Kattawar, G. W. & Eisner, M. 1970, *Radiation from a Homogeneous Isothermal Sphere*. *Appl. Opt.*, 9, 2685
- Keller, L., Hony, S., Bradley, J. P., et al. 2002, *Identification of iron sulphide grains in protoplanetary disks*. *Nature*, 417, 148
- Kemper, F., Vriend, W. J., & Tielens, A. G. G. M. 2004, *The Absence of Crystalline Silicates in the Diffuse Interstellar Medium*. *ApJ*, 609, 826
- Kempf, S., Pfalzner, S., & Henning, T. K. 1999, *N-Particle-Simulations of Dust Growth*. *Icarus*, 141, 388
- Koike, C., Shibai, H., & Tsuchiyama, A. 1993, *Extinction of Olivine and Pyroxene in the Mid Infrared and Far Infrared*. *MNRAS*, 264, 654
- Kokhanovsky, A. A. 2001, *Optics of Light Scattering Media: Problems and Solutions*, 2nd edn. (New York: Wiley)
- Kolokolova, L. & Gustafson, B. A. S. 2001, *Scattering by inhomogeneous particles: microwave analog experiments and comparison to effective medium theories*. *Journal of Quantitative Spectroscopy and Radiative Transfer*, 70, 611
- Kolokolova, L., Hanner, M. S., Levasseur-Regourd, A. C., & Gustafson, B. A. S. 2004, *Physical properties of cometary dust from light scattering and thermal emission*, *Comets II* (Arizona Press)
- Kolokolova, L., Jockers, K., Gustafson, B. S., & Lichtenberg, G. 2001, *Color and polarization as indicators of comet dust properties and evolution in the near-nucleus coma*. *J. Geophys. Res.*, 106, 10113
- Krotkov, N. A., Flittner, D. E., Krueger, A. J., et al. 1999, *Effect of particle nonsphericity on satellite monitoring of drifting volcanic ash clouds*. *J. Quant. Spectrosc. Radiat. Transfer*, 63, 613
- Kurucz, R. 1993, *Model Atmospheres*, CD-ROM Nos. 1-18, Cambridge, Mass.: Smithsonian Astrophysical Observatory
- Lakhtakia, A. 1992, *General theory of the Purcell-Pennypacker scattering approach and its extension to bianisotropic scatterers*. *ApJ*, 394, 494
- Lakhtakia, A. & Mulholland, G. W. 1993, *On two numerical techniques for light scattering by dielectric agglomerated structures*. *Journal of Research of the National Institute of Standards and Technology*, 98, 699
- Lawrence, G., Jones, T. J., & Gehrz, R. D. 1990, *Photometry of masing and nonmasing OH/IR stars*. *AJ*, 99, 1232
- Leinert, C., Graser, U., Waters, L. B. F. M., et al. 2003, *Ten-micron instrument MIDI: getting ready for observations on the VLTI*. in *Interferometry for Optical Astronomy II*. Edited by Wesley A. Traub. *Proceedings of the SPIE*, Volume 4838, 893–904
- Leinert, C., van Boekel, R., Waters, L. B. F. M., et al. 2004, *Mid-infrared sizes of circumstellar disks around Herbig Ae/Be stars measured with MIDI on the VLTI*. *A&A*, 423, 537
- Lellouch, E., Crovisier, J., Lim, T., et al. 1998, *Evidence for water ice and estimate of dust production rate in comet Hale-Bopp at 2.9 AU from the Sun*. *A&A*, 339, L9
- Levasseur-Regourd, A. C. 1999, *Polarization of Light Scattered by Cometary Dust Particles: Observations and Tentative Interpretations*. *Space Science Reviews*, 90,

163

- Levasseur-Regourd, A. C. 2004, Polarimetry of dust in the solar system: remote observations, in-situ measurements and experimental simulations, Photopolarimetry in Remote Sensing (Kluwer Academic Publishers)
- Li, A. & Draine, B. T. 2001, *On Ultrasmall Silicate Grains in the Diffuse Interstellar Medium*. ApJ, 550, L213
- Li, A. & Greenberg, J. M. 1998, *From Interstellar Dust to Comets: Infrared Emission from Comet Hale-Bopp (C/1995 O1)*. ApJ, 498, L83
- Li, A., Greenberg, J. M., & Zhao, G. 2002, *Modelling the astronomical silicate features - I. On the spectrum subtraction method*. MNRAS, 334, 840
- Lynch, D. K. & Mazuk, S. 2000, *Adventures in Modeling Thermal Emission Spectra of Comets*. ASP Conf. Ser. 196: Thermal Emission Spectroscopy and Analysis of Dust, Disks, and Regoliths, 127
- MacKinnon, I. D. R. & Rietmeijer, F. J. M. 1987, *Mineralogy of chondritic interplanetary dust particles*. Reviews of Geophysics, 25, 1527
- Mackowski, D. W. 1995, *Electrostatic analysis of radiative absorption by sphere clusters in the Rayleigh limit: application to soot particles*. Appl. Opt., 34, 3535
- Malfait, K., Bogaert, E., & Waelkens, C. 1998a, *An ultraviolet, optical and infrared study of Herbig Ae/Be stars*. A&A, 331, 211
- Malfait, K., Waelkens, C., Waters, L. B. F. M., et al. 1998b, *The spectrum of the young star HD 100546 observed with the Infrared Space Observatory*. A&A, 332, L25
- Mannings, V. & Sargent, A. I. 1997, *A High-Resolution Study of Gas and Dust around Young Intermediate-Mass Stars: Evidence for Circumstellar Disks in Herbig AE Systems*. ApJ, 490, 792
- Manset, N. & Bastien, P. 2000, *Polarimetric Observations of Comets C/1995 O1 Hale-Bopp and C/1996 B2 Hyakutake*. Icarus, 145, 203
- Markel, V. A., Muratov, L. S., Stockman, M. I., & George, T. F. 1991, *Theory and numerical simulation of optical properties of fractal clusters*. Phys. Rev. B, 43, 8183
- Mason, C. G., Gehrz, R. D., Jones, T. J., et al. 2001, *Observations of Unusually Small Dust Grains in the Coma of Comet Hale-Bopp C/1995 O1*. ApJ, 549, 635
- Mathis, J. S. 1996, *Dust Models with Tight Abundance Constraints*. ApJ, 472, 643
- Meeus, G., Bouwman, J., Dominik, C., Waters, L. B. F. M., & de Koter, A. 2002, *The absence of the 10 μ m silicate feature in the isolated Herbig Ae star HD 100453*. A&A, 392, 1039
- Meeus, G., Sterzik, M., Bouwman, J., & Natta, A. 2003, *Mid-IR spectroscopy of T Tauri stars in Chamealeon I: Evidence for processed dust at the earliest stages*. A&A, 409, L25
- Meeus, G., Waters, L. B. F. M., Bouwman, J., et al. 2001, *ISO spectroscopy of circumstellar dust in 14 Herbig Ae/Be systems: Towards an understanding of dust processing*. A&A, 365, 476
- Mendoza, E. E. 1967, *Multicolor photometry of stellar aggregates*. Boletín de los Observatorios Tonantzintla y Tacubaya, 4, 149
- Mie, G. 1908, *Beiträge zur Optik trüber Medien speziell kolloidaler Metallösungen*. Ann Phys., 25, 377

- Min, M., Dominik, C., & Waters, L. B. F. M. 2004, *Spectroscopic diagnostic for the mineralogy of large dust grains*. A&A, 413, L35
- Min, M., Hovenier, J. W., & de Koter, A. 2003a, *Scattering and absorption cross sections for randomly oriented spheroids of arbitrary size*. Journal of Quantitative Spectroscopy and Radiative Transfer, 79, 939
- Min, M., Hovenier, J. W., & de Koter, A. 2003b, *Shape effects in scattering and absorption by randomly oriented particles small compared to the wavelength*. A&A, 404, 35
- Min, M., Hovenier, J. W., & de Koter, A. 2005, *Modeling optical properties of cosmic dust grains using a distribution of hollow spheres*. A&A, 432, 909
- Mishchenko, M. & Travis, L. D. 1994, *Light scattering by polydispersions of randomly oriented spheroids with sizes comparable to wavelengths of observation*. Appl. Opt., 33, 7206
- Mishchenko, M. I. 1991, *Infrared absorption by shape distributions of NH₃ ice particles - an application to the Jovian atmosphere*. Earth Moon and Planets, 53, 149
- Mishchenko, M. I., Hovenier, J. W., & Travis, L. D., eds. 2000, *Light Scattering by Non-spherical Particles, Theory, Measurements and Applications* (San Diego: Academic Press)
- Mishchenko, M. I. & Travis, L. D. 1998, *Capabilities and limitations of a current FORTRAN implementation of the T-matrix method for randomly oriented, rotationally symmetric scatterers*. J. Quant. Spectrosc. Radiat. Transfer, 60, 309
- Mishchenko, M. I., Travis, L. D., Kahn, R. A., & West, R. A. 1997, *Modeling phase functions for dust-like tropospheric aerosols using a shape mixture of randomly oriented polydisperse spheroids*. J. Geophys. Res., 102, 13543
- Mishchenko, M. I., Travis, L. D., & Lacis, A. A. 2002, *Scattering, Absorption and Emission of Light by Small Particles* (Cambridge: Cambridge University Press)
- Mishchenko, M. I., Travis, L. D., & Macke, A. 1996, *Scattering of light by polydisperse, randomly oriented, finite circular cylinders*. Appl. Opt., 35, 4927
- Mishchenko, M. I., Travis, L. D., & Mackowski, D. W. 1996, *T-matrix computations of light scattering by nonspherical particles: a review*. J. Quant. Spectrosc. Radiat. Transfer, 55, 535
- Molster, F. J., Demyk, A., D'Hendecourt, L., & Bradley, J. P. 2003, *The First 2-50 μm Infrared Spectrum of an Interplanetary Dust Particle (IDP)*. in Lunar and Planetary Institute Conference Abstracts, 1148
- Molster, F. J. & Waters, L. B. F. M. 2003, *The Mineralogy of Interstellar and Circumstellar Dust*. LNP Vol. 609: Astromineralogy, 121
- Molster, F. J., Waters, L. B. F. M., & Tielens, A. G. G. M. 2002a, *Crystalline silicate dust around evolved stars. II. The crystalline silicate complexes*. A&A, 382, 222
- Molster, F. J., Waters, L. B. F. M., Tielens, A. G. G. M., Koike, C., & Chihara, H. 2002b, *Crystalline silicate dust around evolved stars. III. A correlations study of crystalline silicate features*. A&A, 382, 241
- Molster, F. J., Waters, L. B. F. M., Trams, N. R., et al. 1999a, *The composition and nature of the dust shell surrounding the binary AFGL 4106*. A&A, 350, 163
- Molster, F. J., Yamamura, I., Waters, L. B. F. M., et al. 1999b, *Low-temperature crystal-*

- lization of silicate dust in circumstellar disks. *Nature*, 401, 563
- Moreno, F., Muñoz, O., Vilaplana, R., & Molina, A. 2003, *Irregular Particles in Comet C/1995 O1 Hale-Bopp Inferred from its Mid-Infrared Spectrum*. *ApJ*, 595, 522
- Muñoz, O., Volten, H., de Haan, J. F., Vassen, W., & Hovenier, J. W. 2000, *Experimental determination of scattering matrices of olivine and Allende meteorite particles*. *A&A*, 360, 777
- Muñonen, K., Nousiainen, T., Fast, P., Lumme, K., & Peltoniemi, J. 1996, *Light scattering by Gaussian random particles: ray optics approximation*. *Journal of Quantitative Spectroscopy and Radiative Transfer*, 55, 577
- Nübold, H., Poppe, T., Rost, M., Dominik, C., & Glassmeier, K. 2003, *Magnetic aggregation II. Laboratory and microgravity experiments*. *Icarus*, 165, 195
- Natta, A., Prusti, T., Neri, R., et al. 2001, *A reconsideration of disk properties in Herbig Ae stars*. *A&A*, 371, 186
- Nuth, J. A., Rietmeijer, F. J. M., & Hill, H. G. M. 2002, *Condensation processes in astrophysical environments: The composition and structure of cometary grains*. *Meteoritics and Planetary Science*, 37, 1579
- Palla, F. & Stahler, S. W. 1993, *The Pre-Main-Sequence Evolution of Intermediate-Mass Stars*. *ApJ*, 418, 414
- Palla, F. & Stahler, S. W. 1999, *Star Formation in the Orion Nebula Cluster*. *ApJ*, 525, 772
- Pilipp, W., Hartquist, T. W., Morfill, G. E., & Levy, E. H. 1998, *Chondrule formation by lightning in the Protosolar Nebula?* *A&A*, 331, 121
- Preibisch, T., Ossenkopf, V., Yorke, H. W., & Henning, T. 1993, *The influence of ice-coated grains on protostellar spectra*. *A&A*, 279, 577
- Press, W. H., Teukolsky, S. A., Vetterling, W. T., & Flannery, B. P. 1992, *Numerical Recipes in FORTRAN*, 2nd edn. (Cambridge: Cambridge University Press)
- Przygodda, F., van Boekel, R., Àbrahàm, P., et al. 2003, *Evidence for grain growth in T Tauri disks*. *A&A*, 412, L43
- Purcell, E. M. 1969, *On the Absorption and Emission of Light by Interstellar Grains*. *ApJ*, 158, 433
- Purcell, E. M. & Pennypacker, C. R. 1973, *Scattering and Absorption of Light by Non-spherical Dielectric Grains*. *ApJ*, 186, 705
- Rayleigh, Lord, J. W. S. 1871, *On the light from the sky, its polarization and colour*. *Phil. Mag.*, 41, 107
- Reimann, H., Weinert, U., & Wagner, S. 1998, *TIMMI 2: a new MIR multimode instrument for ESO*. in Proc. SPIE Vol. 3354, p. 865-876, *Infrared Astronomical Instrumentation*, Albert M. Fowler; Ed., Vol. 3354, 865–876
- Rietmeijer, F. J. M. 1989, *Ultrafine-grained mineralogy and matrix chemistry of olivine-rich chondritic interplanetary dust particles*. in *Lunar and Planetary Science Conference*, 513–521
- Rietmeijer, F. J. M., Nuth, J. A., & Karner, J. M. 1999, *Metastable Eutectic Condensation in a Mg-Fe-SiO-H₂-O₂ Vapor: Analogs to Circumstellar Dust*. *ApJ*, 527, 395
- Rietmeijer, F. J. M., Nuth, J. A., & MacKinnon, I. D. R. 1986, *Analytical electron microscopy of Mg-SiO smokes - A comparison with infrared and XRD studies*. *Icarus*,

- 66, 211
- Sandford, S. A. & Walker, R. M. 1985, *Laboratory infrared transmission spectra of individual interplanetary dust particles from 2.5 to 25 microns*. *ApJ*, 291, 838
- Servoin, J. L. & Piriou, B. 1973, *Infrared Reflectivity and Raman Scattering of Mg₂SiO₄ Single Crystal*. *Phys. Stat. Sol. (b)*, 55, 677
- Shu, F. H., Adams, F. C., & Lizano, S. 1987, *Star formation in molecular clouds - Observation and theory*. *ARA&A*, 25, 23
- Siess, L., Dufour, E., & Forestini, M. 2000, *An internet server for pre-main sequence tracks of low- and intermediate-mass stars*. *A&A*, 358, 593
- Skinner, S. L., Brown, A., & Stewart, R. T. 1993, *A high-sensitivity survey of radio continuum emission from Herbig Ae/Be stars*. *ApJS*, 87, 217
- Smith, B. A. & Terrile, R. J. 1984, *A circumstellar disk around Beta Pictoris*. *Science*, 226, 1421
- Snow, T. P. & Witt, A. N. 1995, *The Interstellar Carbon Budget and the Role of Carbon in Dust and Large Molecules*. *Science*, 270, 1455
- Spitzer, W. G. & Kleinman, D. A. 1960, *Infrared lattice bands of quartz*. *Physical Review*, 121, 1324
- Stognienko, R., Henning, T., & Ossenkopf, V. 1995, *Optical properties of coagulated particles*. *A&A*, 296, 797
- Strom, K. M., Strom, S. E., Wilkin, F. P., et al. 1990, *A study of the stellar population in the LYNDs 1641 dark cloud. IV - The Einstein X-ray sources*. *ApJ*, 362, 168
- Suttner, G. & Yorke, H. W. 2001, *Early Dust Evolution in Protostellar Accretion Disks*. *ApJ*, 551, 461
- Sylvester, R. J., Skinner, C. J., Barlow, M. J., & Mannings, V. 1996, *Optical, infrared and millimetre-wave properties of Vega-like systems*. *MNRAS*, 279, 915
- Tanaka, H., Inaba, S., & Nakazawa, K. 1996, *Steady-State Size Distribution for the Self-Similar Collision Cascade*. *Icarus*, 123, 450
- Toon, O. B. & Ackerman, T. P. 1981, *Algorithms for the calculation of scattering by stratified spheres*. *Appl. Opt.*, 20, 3657
- Vaidya, D. B. & Gupta, R. 1999, *Interstellar extinction by porous grains*. *A&A*, 348, 594
- van Boekel, R., Min, M., Leinert, C., et al. 2004a, *The building blocks of planets within the 'terrestrial' region of protoplanetary disks*. *Nature*, 432, 479
- van Boekel, R., Waters, L. B. F. M., Dominik, C., et al. 2003, *Grain growth in the inner regions of Herbig Ae/Be star disks*. *A&A*, 400, L21
- van Boekel, R., Waters, L. B. F. M., Dominik, C., et al. 2004b, *Spatially and spectrally resolved 10 μm emission in Herbig Ae/Be stars*. *A&A*, 418, 177
- van de Hulst, H. C. 1957, *Light Scattering by Small Particles* (New York: Wiley)
- van den Ancker, M. E., Bouwman, J., Wesselius, P. R., et al. 2000, *ISO spectroscopy of circumstellar dust in the Herbig Ae systems AB Aur and HD 163296*. *A&A*, 357, 325
- van den Ancker, M. E., de Winter, D., & Tjin A Dje, H. R. E. 1998, *HIPPARCOS photometry of Herbig Ae/Be stars*. *A&A*, 330, 145
- Vandenbussche, B., Dominik, C., Min, M., et al. 2004, *Tentative detection of micron-sized forsterite grains in the proto-planetary disk surrounding HD 100453*. *A&A*,

- 427, 519
- Volten, H., Muñoz, O., Rol, E., et al. 2001, *Scattering matrices of mineral aerosol particles at 441.6 nm and 632.8 nm*. J. Geophys. Res., 17375
- Volten, H., Muñoz, O., Hovenier, J. W., et al. 2005, *WWW scattering matrix database for small mineral particles at 441.6 and 632.8nm*. Journal of Quantitative Spectroscopy and Radiative Transfer, 90, 191
- Voshchinnikov, N. V. & Farafonov, V. G. 1993, *Optical properties of spheroidal particles*. Ap&SS, 204, 19
- Vrba, F. J., Strom, S. E., & Strom, K. M. 1976, *Infrared surveys of dark- cloud complexes. III. The R CrA dark cloud*. AJ, 81, 317
- Walker, H. J. & Wolstencroft, R. D. 1988, *Cool circumstellar matter around nearby main-sequence stars*. PASP, 100, 1509
- Warren, J. L., Barret, R. A., Dodson, A. L., Watts, L. A., & Zolensky, M. E., eds. 1994, *Cosmic Dust Catalog*, Vol. 14, NASA Johnson Space Center, Houston
- Waters, L. B. F. M., Cote, J., & Geballe, T. R. 1988, *51 Ophiuchi (B9.5 Ve) - A Be star in the class of Beta Pictoris stars?* A&A, 203, 348
- Waters, L. B. F. M., Molster, F. J., de Jong, T., et al. 1996, *Mineralogy of oxygen-rich dust shells*. A&A, 315, L361
- Waters, L. B. F. M. & Waelkens, C. 1998, *Herbig Ae/Be Stars*. ARA&A, 36, 233
- Waters, L. B. F. M., Waelkens, C., van der Hucht, K. A., & Zaal, P. A., eds. 1997/1998, *ISO's View on Stellar Evolution* (Dordrecht: Kluwer Academic Publishers)
- Wehrstedt, M. & Gail, H.-P. 2002, *Radial mixing in protoplanetary accretion disks. II. Time dependent disk models with annealing and carbon combustion*. A&A, 385, 181
- Weidenschilling, S. J. 1997, *The Origin of Comets in the Solar Nebula: A Unified Model*. Icarus, 127, 290
- Weiler, M., Rauer, H., Knollenberg, J., Jorda, L., & Helbert, J. 2003, *The dust activity of comet C/1995 O1 (Hale-Bopp) between 3 AU and 13 AU from the Sun*. A&A, 403, 313
- Weitz, D. A., Huang, J. S., Lin, M. Y., & Sung, J. 1985, *Limits of the fractal dimension for irreversible kinetic aggregation of gold colloids*. Physical Review Letters, 54, 1416
- West, R. A., Orton, G. S., Draine, B. T., & Hubbell, E. A. 1989, *Infrared absorption features for tetrahedral ammonia ice crystals*. Icarus, 80, 220
- Wetherill, G. W. 1990, *Formation of the earth*. Annual Review of Earth and Planetary Sciences, 18, 205
- Wooden, D. H. 2002, *Comet Grains: Their IR Emission and Their Relation to ISM Grains*. Earth Moon and Planets, 89, 247
- Wooden, D. H., Harker, D. E., Woodward, C. E., et al. 1999, *Silicate Mineralogy of the Dust in the Inner Coma of Comet C/1995 O1 (Hale-Bopp) Pre- and Postperihelion*. ApJ, 517, 1034
- Wriedt, T. 2002, *Using the T-matrix method for light scattering computations by non-axisymmetric particles: superellipsoids and realistically shaped particles*. Part. Part. Syst. Charact., 19, 256

Dankwoord

En dan is nu het moment aangebroken om alle mensen te bedanken die hebben bijgedragen aan het mogelijk maken van dit proefschrift. Nou zeg ik hier wel optimistisch ‘alle mensen’, maar ik vrees dat mijn geheugen niet toereikend is om recht te doen aan eenieder die dat verdient. Mocht je je naam niet op deze twee pagina’s terugvinden, dan bied ik daarvoor mijn welgemeende excuses aan en wil ik je bedanken voor je steun, hulp of commentaar.

Allereerst wil ik mijn twee promotores bedanken, Joop Hovenier en Rens Waters. Iedere promovendus zou zich gelukkig prijzen met één promotor die zo enthousiast en betrokken is, dus ik prijs mezelf dubbel gelukkig. Beste Joop, dankzij jouw uitgebreide kennis, toewijding en onovertroffen nauwkeurigheid heb ik veel van je geleerd over lichtverstrooiing en wetenschap in het algemeen. Ik zal je wijze lessen, ook de velen die niets met wetenschap van doen hebben, niet gauw vergeten. Iedere discussie die we hadden leverde weer nieuwe, interessante vragen op waar ik niet bij had stilgestaan en eindigde steevast met de bemoedigende uitspraak: ‘We gaan voort met de strijd!’. Beste Rens, elke keer verbaas ik me weer over jouw brede visie en uitgebreide kennis van het vakgebied. Ook je schijnbaar onbreekbare optimisme en enthousiasme zijn erg inspirerend. Door de grote hoeveelheid ideeën die jij steeds weer aandraagt, en die zorgen voor steeds nieuwe en interessante inzichten, heb je mij geleerd hoe leuk en aansprekend wetenschap kan zijn. Ook wil ik hier graag mijn co-promotor, Alex de Koter, bedanken voor alle goede adviezen en scherpe vragen. Menige discussie die in dit proefschrift staat is aanzienlijk aangescherpt door jouw kritische blik en rake vragen die je, ongeacht het onderwerp, immer paraat blijkt te hebben.

Dit proefschrift is tot stand gekomen uit vele discussies en gesprekken. Roy, het was me een waar genoegen om met jou samen te mogen nadenken en discussiëren. Het lijstje ‘Wat Roy en Michiel nog niet snappen’ zou, vrees ik, langer moeten zijn dan het momenteel is, maar we gaan het vast ooit begrijpen. Carsten, jouw uitgebreide kennis over stof, circumstellaire schijven en andere zaken, samen met je aanstekelijke enthousiasme over de resultaten van het onderzoek, zijn van groot belang geweest voor het totstandkomen van dit proefschrift; mijn dank daarvoor. *Hester and Olga, the scattering sisters, thank you for sharing your insights in light scattering with me, and especially for introducing me to the light scattering community.*

I also like to express my gratitude to the thesis committee for careful reading of my thesis and for useful comments and suggestions. I especially wish to thank Michael Mishchenko for constructive comments on nearly every paper I submitted.

The ‘Anton Pannekoek’ institute is a very nice place to work, so I wish to thank you all for making this institute what it is. In het bijzonder wil ik hier een klein aantal mensen noemen. Rien, Rohied, Martin en Arjen: ik dank jullie voor je steun, hulp en gezellige uren rond de kofftietafel en bij de lunch. Ook wil ik graag een woord van dank uitspreken voor de mensen van het secretariaat, jullie geweldige en immer vrolijke ondersteuning houdt dit instituut draaiende. *I also wish to thank the people that I had the pleasure to share the office with: Annique, Wing-Fai and Tom. I thank you for your enjoyable*

company. Annique, a special thanks goes to you for all your advice on life, science and supervisors, and for teaching me the magic handshake.

Iedere wetenschapper weet dat zonder een goede basis niets overeind blijft staan. Ik wil dan ook graag mijn ouders heel erg bedanken voor de stevige, fijne basis die ze mij gegeven hebben. Maar ook nu zijn jullie nog steeds een grote steun en staan jullie altijd klaar als dat nodig is. Erik en Rogier, jullie zijn allebei geweldige broers. Ik wil jullie bedanken voor jullie vriendschap en voor het feit dat ik altijd op jullie kan rekenen. Ook wil ik mijn schoonzusjes, Janneke en Mariska, bedanken voor alle gezelligheid en vriendschap.

Rutger, als eerste van mijn vrienden wil ik graag jou bedanken. De vele serieuze, zinloze, natuurkundige en diepgaande gesprekken die we hebben gehad tijdens onze studie, wandelvakanties, feesten, dinsdagavonden en andere gelegenheden zijn me erg dierbaar. Ook zijn een aantal van de ideeën die in dit proefschrift staan op dinsdagavond bij een biertje en een goed gesprek gevormd. Bedankt voor je kameraadschap.

Beste vrienden, het is erg fijn om me zo nu en dan te realiseren hoe ik het getroffen heb met jullie. Dat ik dankzij jullie bijvoorbeeld af en toe volledig alle mogelijke vormen van wetenschap kon vergeten voor een weekend heeft dit proefschrift absoluut veel goed gedaan. Maar ook is het goed om gewoon een avond, of een dag, gezellig te praten over alles en niets. Jullie zijn allen op je eigen manier bijzondere mensen. Roelof, Jasper, Jacco, Blerik, Verik, Margot, Christiaan, Lourens, Ingrid, Monique, Marijn en de anderen: bedankt!

Lieve Dorien, graag wil ik dit dankwoord, en daarmee dit proefschrift, besluiten met jou uit de grond van mijn hart te bedanken voor al je steun, liefde en vriendschap. Zonder jou was ik nooit op dit punt gekomen. Wat we verder ook verzinnen in het leven, of wat het leven verder ook verzint voor ons, jij maakt dat ik er het volste vertrouwen in heb. Bedankt voor alles.

dis.

